Analysing Gas Kinematics in Star-Forming Galaxies using Disc Modelling

Mathew R. Varidel

Submitted in fulfillment of the requirements for the degree of Doctor of Philosophy

June 11, 2021

Faculty of Science
University of Sydney

Abstract

The work in this thesis aims to accurately determine the gas kinematics in disc galaxies and relate those inferences to their drivers. For this thesis a Bayesian disc modelling technique, known as BLOBBY3D, was developed to infer the gas kinematics of galaxies while limiting the effects of beam smearing. BLOBBY3D was applied to samples of galaxies from the SAMI Galaxy Survey, DYnamics of Newly Assembled Massive Objects (DYNAMO) survey, and the KMOS Redshift One Spectroscopic Survey (KROSS). The results of these analyses were used to gain accurate measures of the velocity dispersion and rotational velocity in galaxies from $z \sim 0.1$ to $z \sim 1$ with wide ranging galaxy properties.

Using these results it was found that the gas velocity dispersion in galaxies at $z \sim 0.1$ slowly increases from $\sigma_v \sim 17\pm3$ km s^{-1} to $\sigma_v \sim 24\pm5$ km s^{-1} across the range $\log_{10}(\mathrm{SFR}/\mathrm{M}_\odot\ \mathrm{yr}^{-1}) \in$ [-3, 0]. A sharper increase in velocity dispersion occurs for $\log_{10}(\mathrm{SFR}/\mathrm{M}_\odot\ \mathrm{yr}^{-1}) > 0$, where the velocity dispersion increases to as high as $\sigma_v \sim 80$ km s^{-1}. The SFR–σ_v relation was found to be consistent with turbulence driven by models that incorporated both star-formation feedback processes and gravitational transport of gas through the disc.

Comparisons of the results from KROSS at $z \sim 1$ to those from the SAMI Galaxy Survey and DYNAMO survey were used to determine the change in gas kinematics across epochs. The typical velocity dispersion at $z \sim 1$ was found to be consistent with galaxies from the DYNAMO survey that have similar galaxy properties. This suggests that the galaxy properties rather than time are playing a major factor in the intrinsic velocity dispersion of the galaxy. It was then shown that disc galaxies are consistent with being marginally stable from gravitational collapse. The consistency of SFR–σ_v with the theoretical models that include star-formation feedback and gas transport are also shown to extend to galaxies at $z \sim 1$.

The usefulness and future applicability of using BLOBBY3D in future studies is then outlined in the conclusion.

Acknowledgements

This thesis is the culmination of studying for the last 9 years, since I took mathematics and science bridging courses at The University of Sydney. My marks from high school were not good enough to go to university given poor application to school work at that time. I have many people to thank along that journey.

First I would like to thank The University of Sydney for providing me with a position to study at this great institution throughout my education. I've had great teachers along the way in science, mathematics, and a little philosophy. Being able to study in my home city has allowed me to maintain a balance between studying with work, family and social commitments.

Of course my PhD supervisors, Scott Croom and Geraint Lewis, require a great deal of thanks. For allowing me the appropriate mentorship and understanding while balancing work with university. They have both provided me with a lot of their time over the last four years with weekly meetings, lots of reading/re-reading of all of my work, plus significant advice and discussions. I would also like to add Brendon Brewer, who acted as a mentor particularly earlier on in my PhD, and without whom the concept of BLOBBY3D would not exist. The many discussions and meetings with other members of the SAMI and Gravitational Astrophysics Group have both improved my work and my breadth of understanding of the various fields in astrophysics.

I thank those that have had to deal with me prioritising studying over other events and responsibilities. Particularly my incredibly patient partner Alison Loh, who has provided me ample time and space to complete my university work. She also patiently dealt with some ups and downs when I thought I would fail a particular course or get stressed out about exams and assignments. She has also had to forego several trips due to my university schedule and we've braced the Northern Hemisphere twice during mid-winter so that it fell during university holidays – when she'd rather be in the Sun. Also, thanks to the several managers that have been willing to allow me time to study over the last 9 years, which includes Ed Ramshaw from PokerStars and Matthew Freebury from Real World Analytics. Without the patience of those people I would not have made it this far.

I would also like to dedicate this thesis to my father David Varidel, who I lost in May of 2020. Dad was proud of me when I received my undergraduate degree and I'm sure he would be proud of me for completing my PhD.

Statement of Originality

This is to certify that to the best of my knowledge, the content of this thesis is my own work. This thesis has not been submitted for any degree or other purposes.

I certify that the intellectual content of this thesis is the product of my own work and that all the assistance received in preparing this thesis and sources have been acknowledged.

Name: ..... Signed: .....

Date: .....

Statement of Attribution

The following papers have been reproduced in this work. In both cases I was the lead and corresponding author. The following details my contribution to these papers.

Chapter 2 of this thesis is published as *The SAMI Galaxy Survey: Bayesian Inference for Gas Disk Kinematics using a Hierarchical Gaussian Mixture Model*. It appeared in Number 3 of Volume 485 of the Monthly Notices of the Royal Astronomical Society in 2019. Declaration of work within this paper:

- I wrote the model parameterisation code for BLOBBY3D within the DNEST4 framework. DNEST4 is a publicly available sampling code written by Brendon Brewer.
- I wrote the code to construct toy models used for testing. I also performed the testing of BLOBBY3D on the toy models.
- Testing of ^{3D}BAROLO was performed jointly by myself and Enrico Di Teodoro.
- I applied BLOBBY3D to data from the SAMI Galaxy Survey. This includes data selection and writing code to clean and mask the data for modelling by BLOBBY3D.
- I wrote the paper in consultation with supervisors; Scott Croom and Geraint Lewis. Further feedback on the paper was provided by Brendon Brewer, Enrico Di Teodoro and the wider SAMI Galaxy Survey team.

Chapter 3 is published as *The SAMI Galaxy Survey: Gas velocity dispersions in low-z star-forming galaxies and the driver of turbulence*. It appeared in Number 2 of Volume 495 of the Monthly Notices of the Royal Astronomical Society in 2020. Declaration of work for the aforementioned paper:

- I performed the modelling including the data preparation and running of BLOBBY3D for all the galaxies selected for this paper. I also perform the subsequent analysis of these results.
- I wrote the paper in consultation with supervisors Scott Croom and Geraint Lewis. The exception being Section 3.5, which was written by Barbara Catinella, due to her work on the observations for the HI gas mass measurements. Further feedback on the paper was provided by Deanne Fisher, Karl Glazebrook, Mark Krumholz, and the wider SAMI Galaxy Survey Team.

I certify that the above statements are true.

Name: ..... Signed: .....

Date: .....

As supervisor for the candidature upon which this thesis is based, I can confirm that the authorship attribution statements above are correct.

Name: ..... Signed: .....

Date: .....

Contents

1 Introduction **1**
- 1.1 Disc galaxies . . . 2
  - 1.1.1 Galaxy classification . . . 2
  - 1.1.2 Galaxy morphological evolution . . . 3
  - 1.1.3 Gas accumulation of disc galaxies . . . 4
- 1.2 Disc kinematics . . . 5
  - 1.2.1 Rotation of disc galaxies . . . 6
  - 1.2.2 Velocity dispersion in disc galaxies . . . 6
  - 1.2.3 Potential drivers of turbulence in discs . . . 8
- 1.3 Spectroscopy . . . 11
  - 1.3.1 Single fibre spectroscopy . . . 13
  - 1.3.2 Integral field spectroscopy . . . 13
  - 1.3.3 Multi-object IFS . . . 13
- 1.4 Beam smearing . . . 17
- 1.5 This Thesis . . . 18

2 Construction of Blobby3D **20**

3 Applications of Blobby3D: The Drivers of Ionised Gas Turbulence in Low-z Galaxies **44**

4 Applications of Blobby3D: The Drivers of Ionised Gas Turbulence Across Epochs **72**

5 Conclusions **88**
- 5.1 Future work . . . 89

1 Introduction

Observations of the movements of celestial objects have contributed significantly to our understanding of our place in the Universe. As far back as oral and written tradition has existed, there is evidence that humans were aware that various objects moved in the sky relative to the Earth and each other. Evidence for astronomical observation from oral tradition goes as far back as tens of thousands of years with the Aboriginal and Torres Strait Islander people (e.g. Hamacher & Banks, 2018). Numerous engraved objects and stone artefacts provide tentative evidence for the knowledge of celestial objects dating back tens of thousands of years (e.g. Hamacher et al., 2012). Systematically recorded observations go back to circa 700 BC with the Babylonians and Indians (Sachs, 1974; Kak, 2003).

The cosmological implications of these observations were not realised initially. As natural philosophy and then science emerged, from Plato to Galileo, it became clear that the implications of the movements of these objects placed us in a much larger Universe than we may have first thought, and perhaps more dauntingly, that humans were not at the centre of it. The first attempt to explain the movements of celestial objects resulted in a geocentric worldview, where the Sun and planets orbited around the Earth. The moon and inner planets were placed before the Sun as solar eclipses by these objects were known, with the outer planets placed beyond the Sun as ancient astronomers had observed those planets to pass behind the Sun.

While Aristarchus introduced the concept of a Heliocentric model in circa 300 BC (Heath & Aristarchus of Samos, 1913), this model did not initially have much influence. At the time, the geocentric model was a reasonable explanation of the observations. For one, humans can't feel that they are travelling through space. The concept that objects stay in motion unless a force acts upon it would not be discovered until much later. Also, the relative motion of stars to other stars as a result of the change of the position of Earth was not observable. Furthermore, the movement of the planets was not known with the precision required to precisely determine their orbits.

Evidence for the scientific process, by which models were updated to account for observational data, can be seen very early in the thought processes of those studying the movements of celestial objects. Epicycles, where a planet orbits a point which in itself is orbiting the centre of the Universe, were proposed to explain the retrograde motion of the planets from the viewpoint of Earth. Refinement of these models through improved mathematics and rudimentary model fitting were completed by Ptolemy in circa 100 AD (Ptolemy & Taliaferro, 1948).

The realisation that the Earth was not the centre of the Universe was due to the improved observational data from better instrumentation and careful cataloguing by Brahe and Galileo. Johannes Kepler realised that the best model to fit Brahe's data was one that had the Sun at the centre with the planets travelling on ellipses (Aiton, 1975). Using his own telescopes, Galileo observed that moons orbited other planets (Galilei, 1653), disproving that objects only orbited the centre of the Universe, which was generally perceived to be the Earth. Together, these two thoughts eventually led to the establishment of our current heliocentric view of the Solar System.

We now know that the Universe is a much larger place than the Solar System. Telescopic observations by Galileo were able to determine that the Milky Way is a collection of stars. The realisation that the Milky Way was only one galaxy of many occurred across a period from the 1820s to 1920s. The discovery that other galaxies (or 'island universes') existed was in part due to observations of galaxies moving with respect to the stars. In the 1910s, Vesto Slipher was the first to measure the redshift of 'spiral nebulae'. Slipher was able to use this to determine that the spiral nebulae were moving an order of magnitude faster than the stars. He noted that this provided significant evidence for 'island universes' (Slipher, 1917). Further evidence that the spiral nebulae were distinct objects came from large internal rotations of the objects themselves, which was found by Slipher and confirmed by Pease (1915, 1916), although it's not clear that either Slipher or Pease considered this as evidence for the 'island universe' theory. In work published in 1929, Edwin Hubble showed that distance of variable stars within Andromeda was too great to be within our galaxy (Hubble, 1929). Current estimates suggest that our Galaxy is only one in a sea of 10^{12} galaxies in the visible Universe (Conselice et al., 2016), and it is possible that there are many more outside of that.

Modern instrumentation now allow us to study large numbers of galaxies in great detail. For example, the Sloan Digital Sky Survey (SDSS, York et al., 2000) has observed millions of galaxies alone. We can also observe galaxies in such detail that the content and kinematics of both stellar and gas components can be spatially resolved within an individual galaxy. Such studies have yielded significant information about the systemic and internal rotations of galaxies, which has led to significant increases in our understanding of our place in the Universe. However, we are only at the beginning of leveraging information from the significant number of observed and future observable galaxies that will be completed over the coming decades.

1.1 Disc galaxies

The focus of this thesis will be on disc galaxies. The spiral nebulae that were first studied by Slipher and others are examples of these galaxies. Discs can be broadly described as galaxies with their contents rotating in a flattened structure. However, it's important to place disc galaxies in the larger context of the range of galaxies.

1.1.1 Galaxy classification

First attempts at understanding the range of galaxies were primarily based on morphological classifications. Morphological classifications were attempted prior to the determination that other galaxies existed. Initial attempts of cataloguing by William and John Herschel used sizes and brightness (Herschel, 1864). Improvements in photography allowed for a determination of two distance morphological classes of galaxies: ellipticals and spirals. Hubble was the first to provide a systematic morphological classification of these galaxy types (Hubble, 1926, 1927). He placed the ellipticals and spirals on a continuous sequence (Figure 1.1). Ellipticals ranged from spheroidal (E0) to more flattened (E6) galaxies. The spiral galaxies were split into two groups of galaxies based on the presence of a bar. Spirals ranged from those with tight (Sa/SBa) to loose bounded spiral arms (Sc/SBc). The transition galaxies are S0/SB0 galaxies that have flattened discs with a centralised bulge but with no spiral arms. A smaller set of galaxies were irregular galaxies that have unusual morphologies.

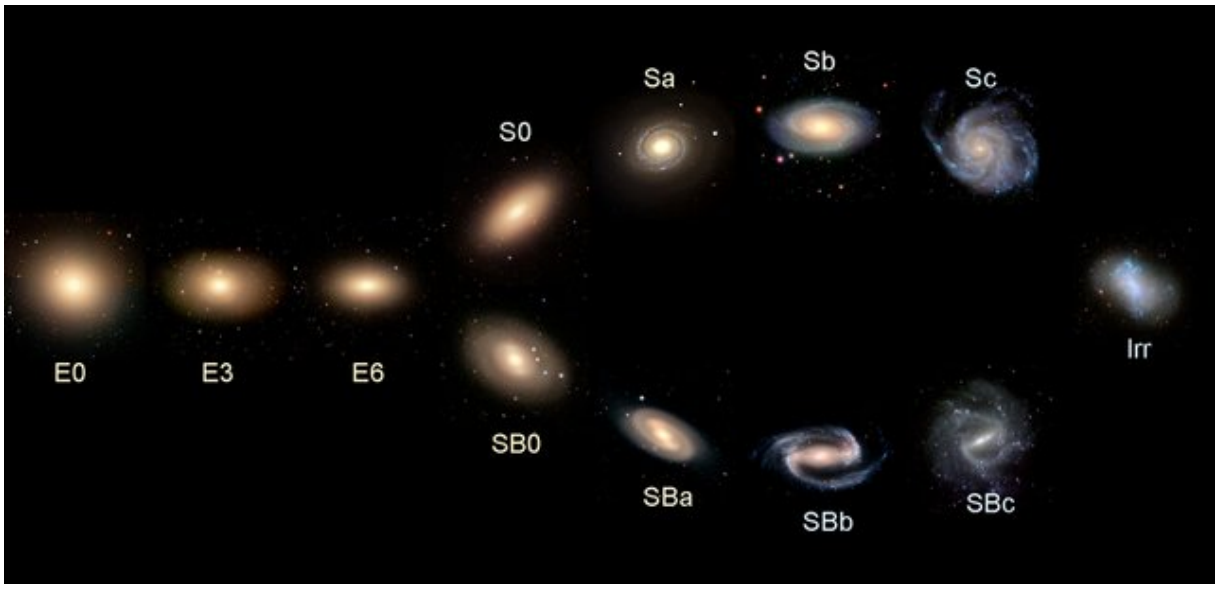

Figure 1.1: Hubble tuning fork used for the original classification of galaxies (Masters et al., 2019). The galaxies progress from elliptical to more flattened structures from E0 to E6. The spiral galaxies transition from tightly to loosely bound spiral arms from S0/SB0 to Sc/SBc. 'B' represents the presence of a bar. Irregular galaxies are shown on the right and have unusual morphologies.

Another way to classify nearby galaxies is by their colour. In the nearby Universe there is a clear dichotomy between red and blue galaxies. Spirals are typically bluer representing a galaxy that is still star-forming. Whereas ellipticals are typically redder with little star-formation. These populations are quite distinct in the nearby Universe with a small fraction of galaxies in the 'green valley' between them (Strateva et al., 2001; Baldry et al., 2004). Combining the morphology and colour classifications suggests that there are two dominant types of galaxies; star-forming discs and passive (non star-forming) ellipticals.

1.1.2 Galaxy morphological evolution

The advent of the Hubble Space Telescope allowed for the study of galaxy morphology at higher redshifts. One of the most interesting discoveries was that the proportion of morphological classes changed with lookback time. In fact, the Hubble sequence appears to be less applicable at earlier times in the Universe.

First evidence for this was found by the increased fraction of irregular galaxies in the earlier Universe. Initial analyses showed that the number counts of irregular galaxies decreased with increasing brightness, which suggested that their was a larger fraction of irregular galaxies in the earlier Universe (Glazebrook et al., 1995; Driver et al., 1995). The ability to quantify the change in galaxy types became possible as redshifts were able to be determined in high redshift galaxies (see Figure 1.2). The latest approaches suggest that morphological disc-like galaxies decrease by an order of magnitude by $z \sim 2$ and are very rare by $z \sim 3$. While the morphologically ellipsoidal-like fraction decreases slowly as a function of redshift. The fraction of irregular galaxies increases significantly up to $z \sim 3$.

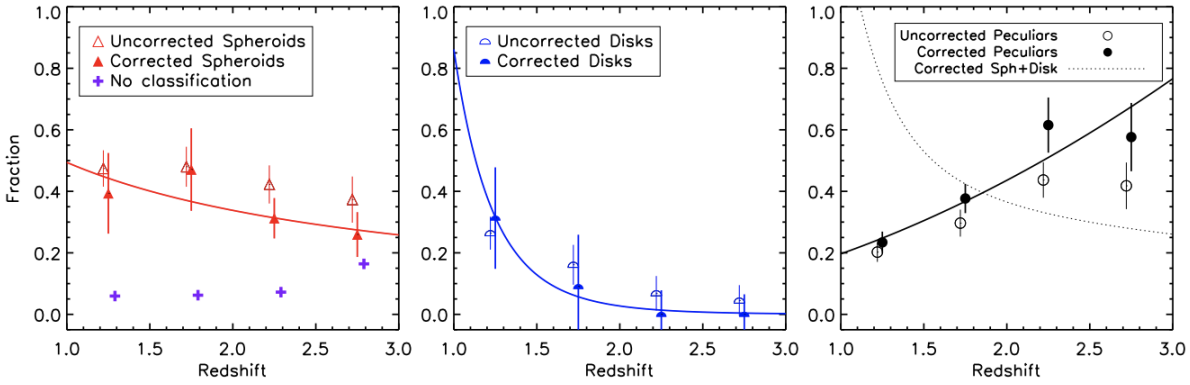

Figure 1.2: The evolution in morphological galaxy classes across cosmic time (Mortlock et al., 2013). In this case, spheroids represents galaxies that would have historically been referred to as ellipsoidals. A slight distinction has also been made where peculiars represent higher mass galaxies with irregular morphologies.

Within the specific morphological classes it is also clear that significant changes occurred. In particular spiral structures decrease drastically at earlier times. Bars are also absent at these higher redshifts (van den Bergh et al., 1996). Instead, the earliest samples of discs shows that disc galaxies typically had clumpier morphologies (Genzel et al., 2011; Wisnioski et al., 2011).

A well known increase in size with decreasing redshift also exists. This was initially shown with limited samples of massive ($\log(M_*/M_\odot) \gtrsim 11$) galaxies that were shown to be smaller in size at $z \sim 1$ - 3 compared to similar mass present day galaxies (Daddi et al., 2005; Trujillo et al., 2006). Larger samples were used to quantify the size evolution for massive galaxies (Trujillo et al., 2007; Buitrago et al., 2008; van Dokkum et al., 2010; Weinzirl et al., 2011; Conselice, 2014). These studies found that elliptical galaxies grew in size faster than disc-like galaxies. Then van der Wel et al. (2014) was able to show that the size evolution exists for galaxies of mass down to $\log(M_*/M_\odot) \sim 9$, suggesting that the size evolution is ubiquitous.

Observations much earlier than $z \sim 3$ are rare but looking in detail at the earliest times, galaxies are significantly different to those observed in the nearby Universe. The earliest confirmed galaxies were typically compact with centralised star-formation. A study of 16 galaxies by Oesch et al. (2010) $z \sim 7$ - 8 found an average size of 0.7±0.3 kpc with little size evolution up to $z \sim 4$. Only 2 out of the 16 galaxies studied by galaxies exhibited morphologies with non-centralised star-formation. Another example is that the earliest observed galaxy at $z \sim 11.1$ has a half-light radius of 0.6±0.3 kpc (Oesch et al., 2016). This provides evidence of size evolution from the earliest times till the present day.

1.1.3 Gas accumulation of disc galaxies

This thesis will focus on the gas in disc galaxies. It is suspected that the current day spiral galaxies evolved from the earlier smaller and clumpier galaxies. This must have occurred via significant accumulation of gas that was subsequently converted to stars.

Galaxies have long been thought to form via hierarchical mechanisms. In this scenario the halo forms initially via gravitational mechanisms and then collapses into a disc-like

object (Eggen et al., 1962). The initial seeds for these galaxies are also set by the initial dark matter density fluctuations in the Universe (Blumenthal et al., 1984). The accretion onto those seeds is now discussed.

The two processes for gas accretion are split into a 'hot' or 'cold' scenario. The hot process occurs by gas accumulating in a spherically symmetric manner. As the gas collapses it becomes heated via shocks. The heat of the gas acts as an outward force slowing the collapse of the gas. The gas requires time to cool thus collapsing slowly into a disc (Rees & Ostriker, 1977). The 'cold' process occurs via preferential accretion along filaments (Kereš et al., 2005). This process avoids the gas overheating and thus allows for an increased efficiency in gas build up in the disc.

Simulations suggest that both hot and cold gas accretion occur (Kereš et al., 2005, 2009; Dekel et al., 2009). Typically galaxies with high stellar masses are dominated by spherical collapse and have centralised hot haloes within their galaxies. Whereas galaxies with stellar masses $\lesssim 2 \times 10^{10}$ $M_{\odot}$ are typically dominated by cold gas accretion.

Observational evidence of efficient star-formation via cold gas accretion has been shown recently by the observation of disc galaxies at significant lookback times. Two early disc galaxies at $\sim$ 1.5 billion years after the big bang ($z \sim 4.2$) have been discovered in 2020 (Neeleman et al., 2020; Rizzo et al., 2020). Furthermore, a significant fraction of galaxies at $z \sim 1$ - 2 can be classified as discs. Förster Schreiber et al. (2009) argued that approximately 1/3rd of galaxies at $z \sim 2$ can be classified as discs. More recent studies by Stott et al. (2016) and Wisnioski et al. (2015) argue that 50% - 80% of galaxies are disc galaxies depending on the exact criteria used. As such, it is likely that a significant proportion of gas accretion is efficient.

Even though the formation of disc galaxies was well advanced by $z \sim 2$ there are still significant differences between those galaxies and nearby disc galaxies. As noted previously, most of the nearby galaxies exhibit spiral structures and some exhibit bars. The formation of these structures is still under significant debate and given that it is not the focus of this thesis, it won't be discussed further. Instead, the focus will be on the difference in gas kinematics of disc galaxies.

1.2 Disc kinematics

The gas kinematics of a disc are measured using emission lines. The most prominent emission lines are from hydrogen. To trace ionised hydrogen the most studied lines are Hα due to the transition from the 3rd to 2nd shell, Hβ due to the 4th to 2nd shell transition, and Hγ from the 5th to 2nd shell. Tracing neutral hydrogen is performed by measuring HI due to the transition in spin states of the hydrogen atom. Emission lines from other elements include nitrogen, oxygen, and carbon.

The kinematics of a galaxy are studied by quantifying the line-of-sight velocity distribution (LOSVD). A mock emission line profile is shown in Figure 1.3. Emission line profiles are naturally measured in wavelength or frequency space but using our understanding of the doppler effect this can be converted into velocity space. The integrated LOSVD is equal to the total amplitude and provides a measure of the gas content. The mean of the LOSVD is a measure of the typical LoS velocity of the gas. The width of the LOSVD, often referred to as the velocity dispersion, provides a measure for the random motions within the gas. By measuring these emission line profiles across a galaxy, we can gain significant understanding about the kinematics of the gas across the disc.

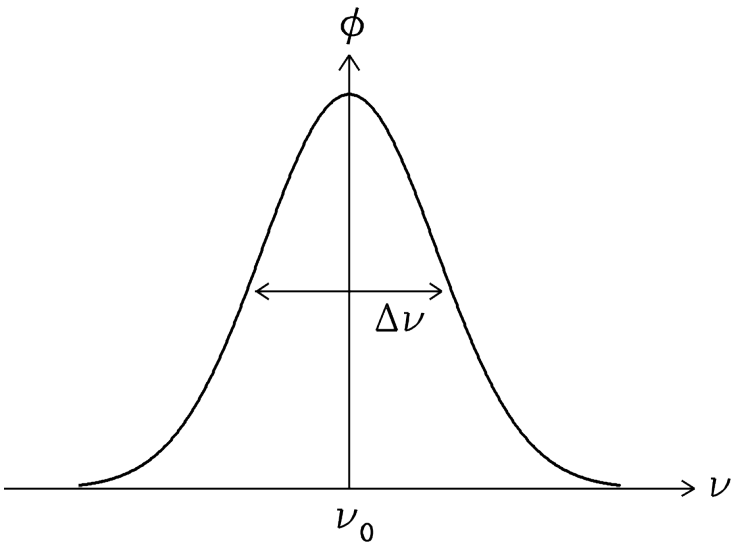

Figure 1.3: A mock emission line profile that measures the luminosity of light (ϕ) as a function of frequency (ν). Image taken from cv.nrao.edu/~sransom/web/Ch7.html.

1.2.1 Rotation of disc galaxies

The study of gas rotation in disc galaxies has been an important field in astronomy over the last century since Slipher and Pease confirmed the rotation of spiral nebulae. A major area of study has been the determination of rotation curves, which are representations of the rotational velocity as a function of radius. Pease found that the rotation velocity increased for increasing radii within the inner regions of the galaxy. However, later studies by Rubin found that rotation curves plateau at increasing radii (e.g. Rubin & Ford, 1970).

Using Newton's laws it can be derived that the rotation velocity is proportional to $\sqrt{M/r}$, where M is the mass enclosed within a given radius r from the centre of the galaxy. As such, it should be expected that the rotational velocity increases in the centre of the galaxy but eventually decreases as the incremental mass at larger radii decreases. The discovery of plateauing velocity fields suggested that there was missing matter that was unobservable (see Figure 1.4 as an example). Thus, the study of rotation curves was the first significant evidence for dark matter. We now suspect that dark matter constitutes 25% of the mass-energy budget of the Universe (Planck Collaboration et al., 2018).

Rotation curves still underpin a significant portion of study into the kinematics of disc galaxies. This is often used to understand the mass distribution of the galaxy. This makes rotation a fundamentally important characteristic. Given this, studies of more detailed kinematics properties are often compared to the rotational velocity of the galaxy.

1.2.2 Velocity dispersion in disc galaxies

A primary goal of the work in this thesis is to accurately estimate the velocity dispersion within disc galaxies. Velocity dispersion is the width of the velocity distribution from the mean. It can be thought of as motions that deviate from the bulk rotation of the disc. In general velocity dispersion can be thought of as a three-dimensional quantity with (σ_R, σ_θ, σ_z) in cylindrical coordinates. σ_R provides pressure support to limit the ability of the galaxy to collapse radially. Whereas σ_z provides vertical pressure support. Thus, it can provide us with insight with respect to the settling of the disc and the pressure support

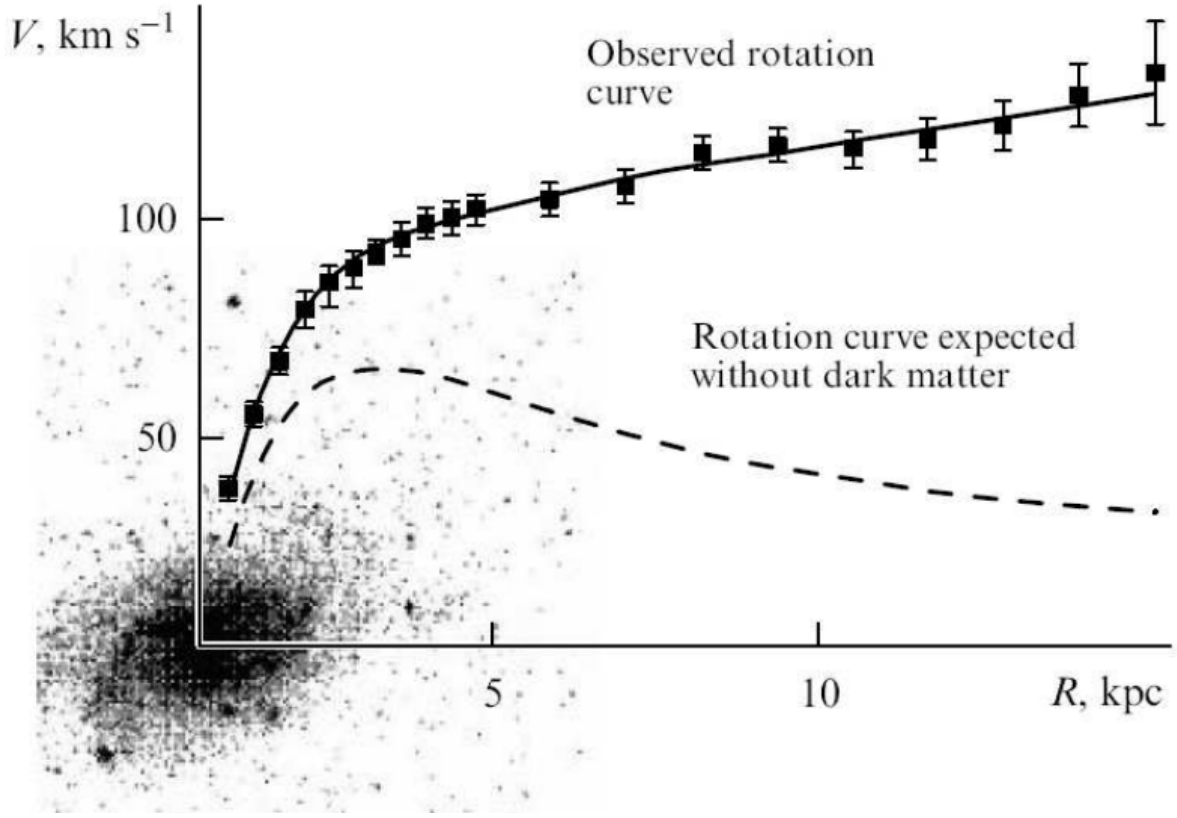

Figure 1.4: Example of a rotation curve for M33 (Zasov et al., 2017). The rotation velocity does not decrease as expected given the observed matter, providing evidence for dark matter.

provided by random motions.

The measured velocity dispersion has several contributing components. One is the thermal component that is due to the characteristic temperature of the gas. For example, discs are often measured using the Hα emission that has a characteristic temperature of 10^4 K resulting in an expected velocity dispersion of $\sim$9 km s^{-1} (Glazebrook, 2013). HI observations do not suffer from this effect due to measuring the neutral hydrogen component of the disc.

Studies in the 1980s and 1990s of HII regions in the Milky Way and Magellanic clouds provide a further mechanism. These studies found that HII regions expand at speeds up to $\sigma \sim 10$ km s^{-1}. The large 30 Doradus complex in the Large Magellanic Cloud (LMC) was found to expand even faster at $\sigma \sim 13$ - 17 km s^{-1} (Chu & Kennicutt, 1994). As such, this needs to be taken into account when determining the velocity dispersion in the ionised gas.

The final component is due to turbulence. Turbulent motions can be thought of as the chaotic motions within the galaxy. Observations consistently find velocity dispersions that are higher than can be explained by the contributions from the thermal and expansion components. In low redshift galaxies, HI discs, which are independent of significant thermal and expansion effects, typically have velocity dispersions $\sigma \sim 10$ km s^{-1}. Using the Hα emission line at low redshift, studies consistently find velocity dispersions that are higher than can be explained by the contributions from the thermal and expansion components. Typical Hα gas velocity dispersions in nearby galaxies are in the range 10 - 30 km s^{-1}.

Studies of galaxies at $z \gtrsim 1$ consistently find supersonic velocity dispersions. Genzel et al. (2006) found a single rotating disc with intrinsic velocity dispersion across the disc of 30 - 60 km s^{-1}. Law et al. (2007) found three galaxies at $z \sim 2$ - 3 with global $\sigma \sim 80$ km s^{-1}. As larger studies of galaxies at high redshift were performed it became clear that global velocity dispersions at $z \gtrsim 1$ were 30 - 100 km s^{-1} (e.g. Förster Schreiber et al., 2006, 2009).

Using consistent samples and methodologies to estimate velocity dispersion across epochs has also found that velocity dispersion increases as a function of redshift. Kassin et al. (2012) found clear trends of velocity dispersion decreasing from $z \sim 1$ to today. Using KMOS^{3D} survey data with a consistent approach, Wisnioski et al. (2015) were able to confirm an evolution from $z \sim 1$ to $z \sim 2$. These results using KMOS^{3D} data have since been confirmed by Übler et al. (2019), although with a shallower evolution. Thus, observations suggest that there is a trend in increasing turbulence at higher redshift.

1.2.3 Potential drivers of turbulence in discs

The ubiquity of supersonic velocity dispersions in discs raises the question of the drivers of such chaotic motions. In the late 90s it was shown that gas turbulence would decay on the order of $\mathcal{O}(100$ Myr) for the whole galaxy to $\mathcal{O}(< 10$ Myr) for individual giant molecular clouds (Mac Low et al., 1998; Stone et al., 1998; Mac Low, 1999). Without an ongoing mechanism to drive turbulence these results suggests that we should rarely observe galaxies with supersonic turbulence. There are numerous methods that have been proposed to drive turbulence. These methods can be broadly split up into star-formation feedback or gravitational instabilities.

Star-formation feedback

Star-formation feedback mechanisms include supernova, stellar winds, and ionising radiation. Theoretical studies suggest that supernova would dominate compared to other star-formation feedback mechanisms (Norman & Ferrara, 1996; Mac Low & Klessen, 2004). As such, supernova have typically been the focus of studies on star-formation feedback processes.

Catalogues of supernova remnants (SNRs) were constructed from the late 1960s (Aizu & Tabara, 1967; Poveda & Woltjer, 1968; Milne, 1970). It was found that supernovae leave distinctive expanding shells. The basic theoretical understanding of the momentum contribution from a single supernova was known very early on (Woltjer, 1970, 1972). When a supernova occurs it results in a sudden expansion of gas at supersonic velocities on the order of thousands of km s^{-1}. This results in an expanding shell of gas forced outwards by a shock. The volume upstream of the shock is cleared and has significantly higher velocities than downstream of the shock. As the shock expands it loses momentum and integrates into the surrounding interstellar medium (ISM).

Despite the basic process of momentum injection of a single supernova into the ISM being well known, there are still significant details being studied. Some of these include adding realistic conditions such as gas phases (e.g. Federrath, 2015), magnetic fields (e.g. Kim & Ostriker, 2015), and understanding the contribution of clustered supernova (e.g. Walch & Naab, 2015; Gentry et al., 2017). As such, there are still significant gaps in our understanding that need to be resolved with respect to star-formation feedback processes.

The contribution from supernova to the observed velocity dispersion requires further thought. In typical extragalactic observations we only have access to properties such as

integrated luminosity, which is related to the star-formation rate, across portions of the galaxy rather than individual supernova. Assumptions need to be made to incorporate these quantities into our theoretical understanding.

Observational analysis has typically related integrated star-formation to the gas velocity dispersion. Star-formation rate has consistently been found to correlate with velocity dispersion (e.g. Figure 1.5, also see Lehnert et al., 2009, 2013; Green et al., 2010, 2014; Le Tiran et al., 2011). This adds further evidence that star-formation feedback processes could drive the turbulence within disc galaxies across epochs.

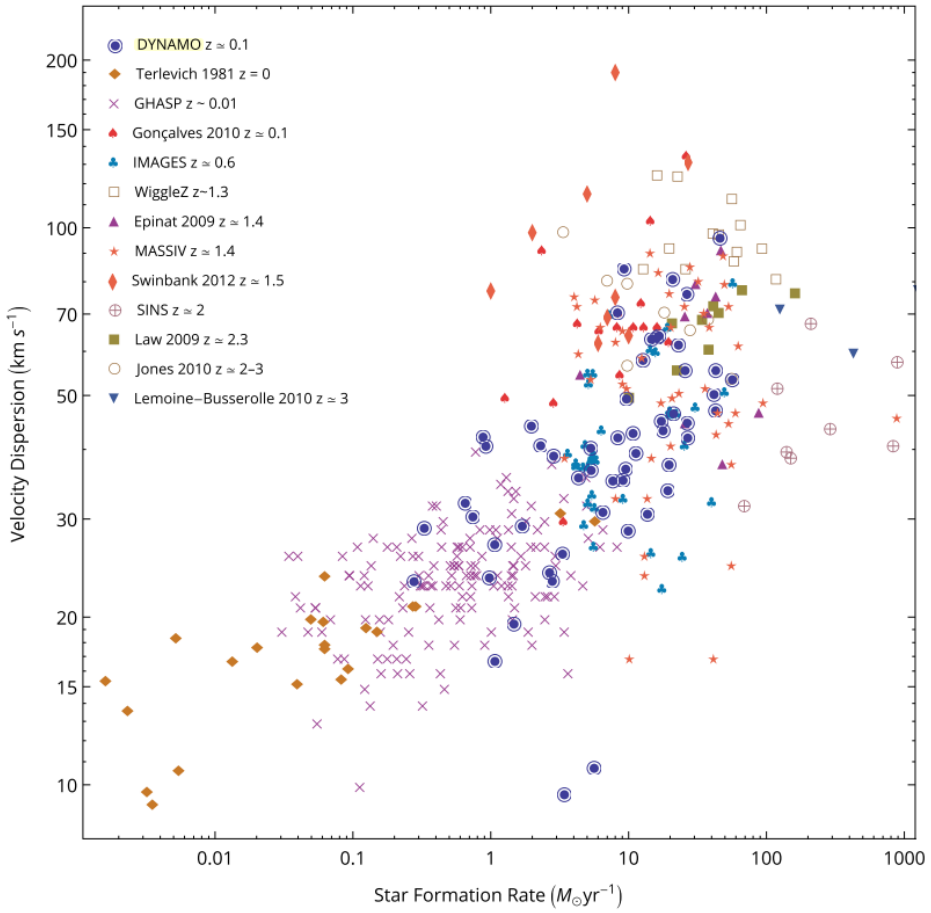

Figure 1.5: The correlation between SFR and velocity dispersion as found by Green et al. (2014).

It can also be argued that star-formation feedback provides a mechanism to explain the highly turbulent galaxies at $z \gtrsim 1$ as mentioned previously. This is due to star-formation rate increasing from today to $z \sim 3$ (Hopkins & Beacom, 2006). Thus, if star-formation feedback processes drive turbulence we would expect a correlation between velocity dispersion and redshift.

Gravitational instabilities

Gravitational instabilities can be caused by numerous mechanisms. This includes galaxy mergers, unstable disc formation, accretion of gas onto or through the disc, or differential large-scale kinematics. I will outline these mechanisms below.

Mergers have been considered as a potential driver of turbulence. At earlier times we see an increased fraction of galaxy mergers (see a review in Conselice, 2014) which corresponds to irregular morphologies and increased turbulence. However, simulations suggest that mergers are unlikely to be a significant ongoing mechanism of turbulence. Major mergers, where galaxies of similar masses collide, typically form elliptical rather than disc galaxies. Minor mergers, where a smaller galaxy collides with a larger one, still result in an increase in the height of the disc which is inconsistent with observations (Bournaud et al., 2009). Therefore, it is unlikely that mergers play a significant role in the turbulence observed in disc galaxies.

Simulations suggest that galaxies undergo unstable disc formation that leads to clumpy turbulent disc galaxies (Noguchi, 1999; Immeli et al., 2004; Bournaud et al., 2007; Agertz et al., 2009). These studies suggest that the gravitational instability leads to clumps that eventually spiral into the centre of the galaxy to form a bulge (although recent simulations show that clumps can have stable orbits (e.g. Greif et al., 2012; Chon & Hosokawa, 2019)). Under the typical unstable disc formation process scenario, newly formed galaxies will typically have velocity dispersions of $\sigma \sim 50$ km s^{-1}, although the supersonic velocity dispersions tend to decay on the order of the disc formation time ($\mathcal{O}$(100 Myr), Aumer et al., 2010). While this may account for some of the turbulence in newly formed disc galaxies at higher redshifts an ongoing mechanism is required to sustain the turbulence that is initially set in newly formed discs.

Several theoretical works have argued that supersonic velocity dispersions across all epochs can be explained by gravitational instabilities alone. Krumholz & Burkert (2010) showed that a steady state solution exists between the turbulent energy due to accretion and transport of gas through the disc and energy lost through turbulence. Predictions for the redshift dependence of velocity dispersion suggest that supersonic velocity dispersions can be maintained on the order of $\mathcal{O}$(Gyr). Goldbaum et al. (2015, 2016) also showed that galaxies will maintain supersonic velocity dispersions using transport of gas through the disc in simulations.

On sub-galactic scales it has been argued that turbulence can be driven by interactions between galaxy components. This includes the compression between spiral arms and clumps (Dobbs & Bonnell, 2008; Tasker & Tan, 2009; Aumer et al., 2010; Oliva-Altamirano et al., 2018). These analyses are well suited to simulations or individual galaxies but the contribution to a typical galaxy is not well understood.

Another proposal is based on differential large scale dynamics and thermal properties of the gas. Dynamical instabilities can result from differential rotation at different radii causing gravitational or magnetorotational instabilities (Balbus & Hawley, 1991; Piontek & Ostriker, 2004, 2007). Similarly, differential temperature phases of the gas has also been argued to contribute to the turbulence (Field, 1965; Balbus, 1986; Koyama & Inutsuka, 2002; Kritsuk & Norman, 2002).

It is likely that all of these mechanisms contribute to the supersonic velocity dispersions typically observed in the interstellar medium. However, the physics of the interstellar medium is complex and as such it remains unclear which mechanisms dominate. Significant research is still needed to resolve this problem.

Models that combine star-formation feedback and gravitational instabilities

Research has also been performed to combine models where star-formation feedback and gravitational instabilities. Krumholz et al. (2018) constructed a model assuming that a disc galaxy is in vertical hydrostatic and energy equilibrium. Where the energy contribution from accretion and transport of gas through the disc is balanced by the pressure

induced by turbulent motions from supernovae.

This model predicts that star-formation feedback processes and gravitational instabilities drive turbulence in different regimes (see Figure 1.6). Star-formation feedback processes drive turbulence at the ∼10 - 20 km s^{-1} for galaxies with integrated star-formation rate (SFR) $\lesssim$ 1 $M_\odot$ yr^{-1}. Whereas velocity dispersion increases rapidly up to ∼100 km s^{-1} for SFR $\gtrsim$ 1 $M_\odot$ yr^{-1}. This model will be tested in Chapters 3 and 4.

1.3 Spectroscopy

The bulk of the analysis within this thesis has been performed on spectroscopic observations of galaxies. Spectroscopy involves the study of the interaction between an object and electromagnetic radiation. The constituents of an object can be determined by the emission and absorption of electromagnetic radiation at particular wavelengths.

Spectral lines were first discovered from observations of the Sun, when Wollaston (1802) first observed several dark lines in a continuous spectrum. Fraunhofer (1817) then improved the analysis of the Solar spectrum with more sophisticated instrumentation. Fraunhofer replaced the previously used prisms with numerous slits to construct a grating to disperse the light. Gratings allow for higher spectral resolution such that the wavelength of the dark lines could be quantified. Kirchhoff & Bunsen (1860b,a) showed that the dark lines observed by Fraunhofer were related to the absorption of particular elements.

Quantification of spectral lines led to the construction of mathematical models to describe them. Balmer (1885) constructed an empirical model to describe the spectral lines in the visible spectrum. Rydberg (1890) subsequently found a generalised formula to describe spectral line series in many elements, that is $1/\lambda = R_{\rm H}(1/n_1^2 - 1/n_2^2)$, where λ is the wavelength of the electromagnetic radiation, n_1 and n_2 correspond to the energy levels relating to the transition, and $R_H = 1.097{\times}10^7$ m^{-1} is the Rydberg constant. The commonly observed Hα line that will be studied extensively in this thesis is part of the Balmer series when $n_1 = 2$ and $n_2 = 3$.

The physical explanation for spectral lines was improved upon the realisation of quantum mechanics. Einstein discovered that electromagnetic radiation could only be emitted in discrete units (Einstein, 1905). This led to many discoveries including an explanation for the atom. Bohr (1913) used a semi-classical approach assuming that electrons travelled on discrete orbits. Bohr's model explained spectral lines assuming that electrons could only travel on orbits of a particular radius. The energy emitted was equal to the energy lost when the atom jumped from a higher to lower orbit. The same argument can be made for the absorption of light with the electron jumping from a lower to higher orbit. This model was appropriate to explain the Balmer and Rydberg series. However, the model has been superceded by a fully quantum mechanical model for the atom.

Our understanding of spectral lines can also be applied to galaxies. Similar to the Sun, a continuous spectrum with absorption features corresponds to the stellar contribution of light from a galaxy. Whereas emission features correspond to the ionised gas within that galaxy. In this way, we can determine the stellar and gas contribution for a given galaxy and study those components separately.

Instrumentation to perform spectroscopy have taken numerous forms over the years. The basic requirements of a spectroscopic observational instrument are an aperture to receive the light, an instrument to disperse the light which is typically a grating, and a detector to receive and record the light. Various other components are involved to focus and direct the light within the instrument. Below I will focus particularly on fibre optics based systems as data throughout this thesis uses those instruments.

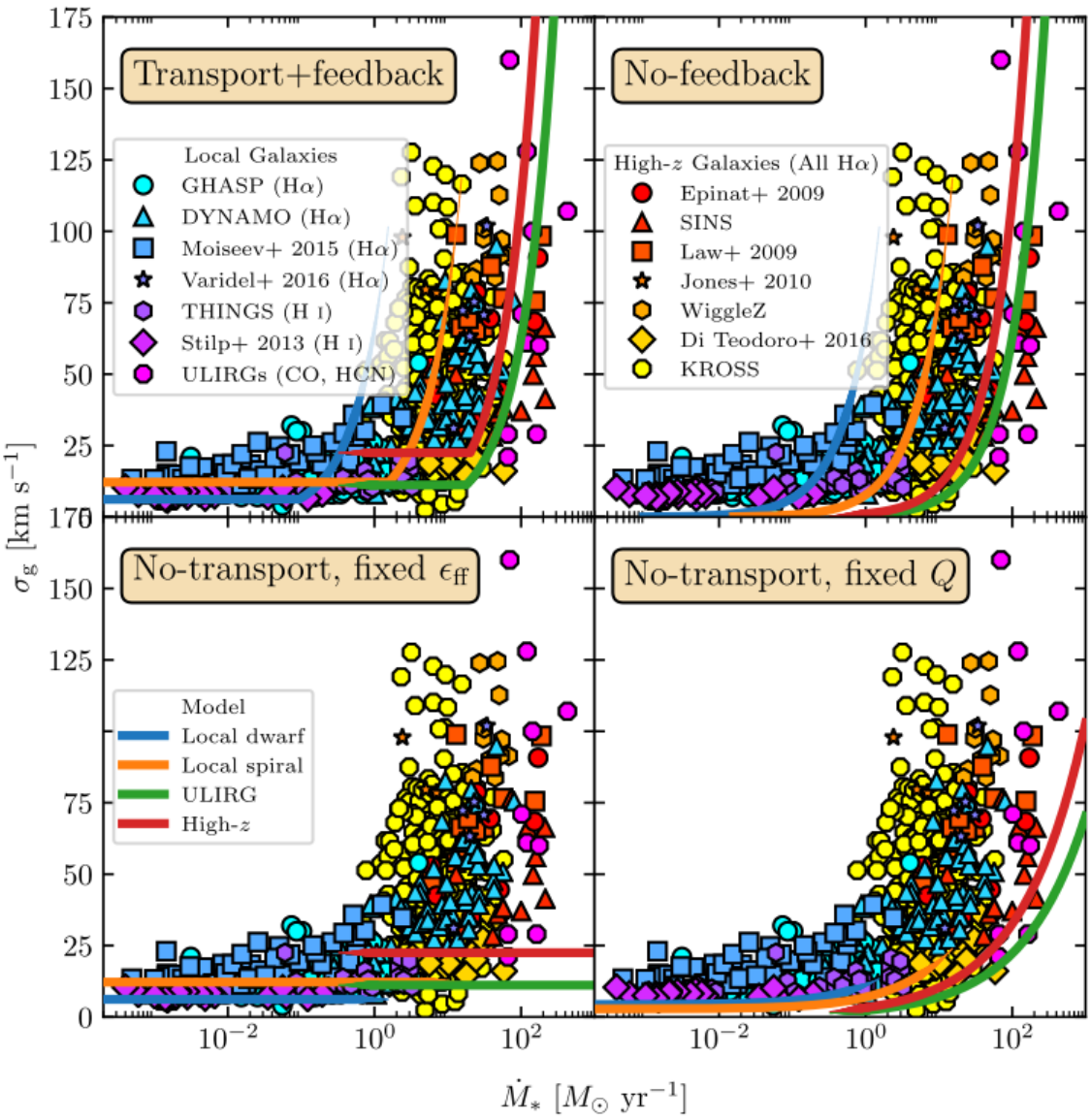

Figure 1.6: Predictions for velocity dispersion (σ_g) compared to SFR ($\dot{M}_*$) using various models as shown by Krumholz et al. (2018). Top left shows a model that has both star-formation feedback and gas transport through the disc as drivers of turbulence. Top right shows a model with just gas transport. Models without gas transport but assume steady-state solutions with fixed Toomre-Q or fixed star-formation rate ($\epsilon_{\rm ff}$) across the disc.

1.3.1 Single fibre spectroscopy

Optical fibres were first discussed and implemented in the 1970s (Angel et al., 1977; Hubbard et al., 1979) with the first direct observations via fibre in the Medusa spectrograph (Hill et al., 1980). Medusa was initially used to simultaneously observe multiple galaxies using a single fibre per galaxy. Thus Medusa allowed for the efficient observation of many galaxies.

Another advantage for fibres is that they are easily maneuverable. This allows for the reconfiguration of the instrument to observe many different layouts of objects. The ability to perform observations of objects simultaneously plus easily reconfigure the layout makes large sample surveys feasible. Surveys using single fibre options include the 2dF Galaxy Redshift Survey (2dFGRS, Colless et al., 2001), 6dF Galaxy Survey (Jones et al., 2004), and the Sloan Digital Sky Survey (SDSS, York et al., 2000). These surveys have provided an array of important information about the arrangement of galaxies across the sky, the distribution of galaxies at different redshifts, as well as global galaxy properties. The limitation of single fibre spectroscopy is that it can only observe a point of the galaxy at any given time.

1.3.2 Integral field spectroscopy

The goal of Integral Field Spectroscopy (IFS) is to obtain three-dimensional (3D) data cubes of a given object. The 3D observation consists of two spatial dimensions and one spectral dimension. Thus, we get spatially resolved spectral information for a given object.

At similar times to the construction of Medusa, proposals for IFS instruments via observations using fibre bundles was proposed by Vanderriest (1980). This was implemented in the DensPak instrument shortly thereafter (Barden & Wade, 1988). A fibre bundle is placed in line with the object, such that light from various locations of the object can be observed.

A disadvantange of fibre bundles is that each fibre requires a protective material around it known as a 'cladding'. This cladding is often thick enough that the fill-factor (the light collecting fraction compared to the total fibre bundle area) is $\sim 50\%$ (Eisenhauer & Raab, 2015). Several other IFS configurations have been suggested, in part to avoid this low fill-factor issue.

Image slicers (Content, 1997) and lenslet arrays (Courtes, 1982) have been used instead of fibre bundles. A third approach is to couple a lenslet array with fibres. See Figure 1.7 for qualitative examples of these instruments. As these approaches split the observation in an adjacent manner they solve the issue surrounding the fill-factor for fibre bundles.

The first surveys using an IFS instrument was SAURON in 2001 (Bacon et al., 2001). However, initial surveys were limited due to observing single objects at a time. Through considerable effort a number of surveys of several hundreds of galaxies exist using single IFS instruments. This includes ATLAS^{3D} (Cappellari et al., 2011) with 260 galaxies and the Calar Alto Legacy Integral Field Area survey (CALIFA, Sánchez et al., 2012) that observed 600 galaxies. To scale IFS up to thousands or even tens of thousands of galaxies new ideas were required.

1.3.3 Multi-object IFS

Scaling IFS to higher galaxies numbers was achieved by constructing instruments that observed multiple galaxies simultaneously. The first instrument built with this capabil-

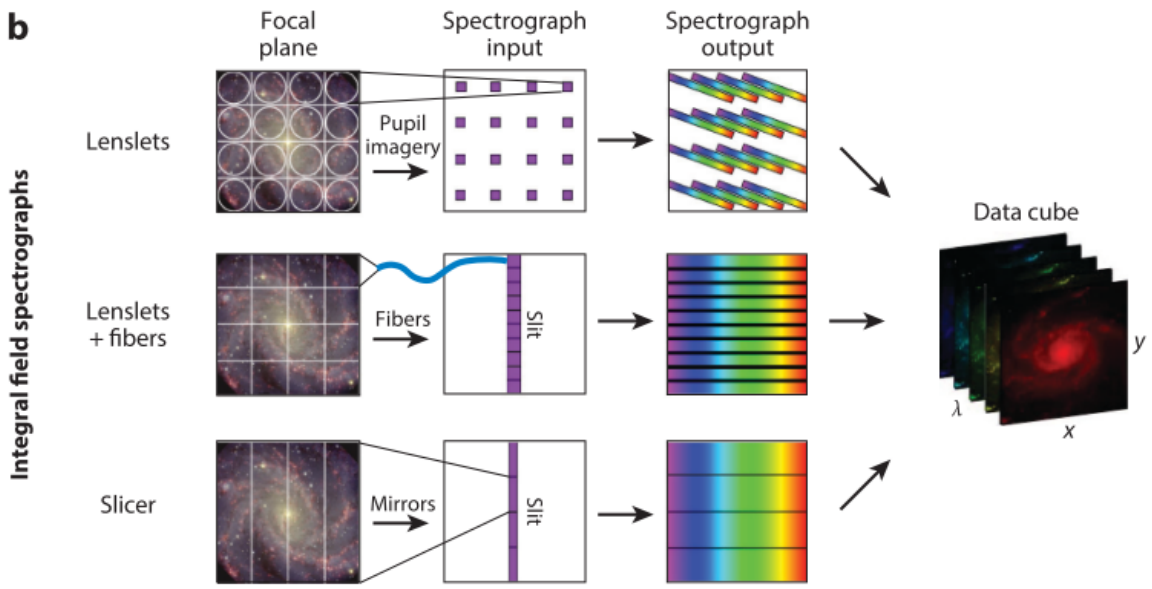

Figure 1.7: Integral Field Spectroscopy configurations (Eisenhauer & Raab, 2015).

ity was the Fibre Large Array Multi Element Spectrograph (FLAMES, Pasquini et al., 2002). FLAMES allows for the observation of 15 objects simultaneously. It has a $2'' \times 3''$ Field of View (FoV) and limited spectral resolution of $R \geq 9000$. FLAMES has since been superceded by multi-object IFS instruments that have a greater FoV. Two of these instruments are the Sydney-AAO Mutli-object Integral field spectrograph (SAMI, Croom et al., 2012) and the K-band Multi-Object Spectrograph (KMOS, Sharples et al., 2004, 2013).

SAMI

SAMI is a multi-object IFS instrument on the Anglo-Australia Telescope. It allows for the spatially resolved observation of 13 objects simultaneously. This capability is implemented by having 13 fused fibre hexabundles (Bland-Hawthorn et al., 2011; Bryant et al., 2014) that are drilled into plates that are mapped to the objects of interest (see Figure 1.8).

Hexabundles were a novel approach applied to SAMI. They consist of 61 fibres that are tightly bundled together with a minimal 5μm cladding. This improves the typical fill-factor to 75% compared to 50% for earlier approaches (Eisenhauer & Raab, 2015). The individual fibres in SAMI have a $1.6''$ diameter for a total FoV of $15''$.

While hexabundles improve the fill-factor of comparable fused bundles, SAMI observes a galaxy in multiple slightly different locations (dithers) to adequately get a full image of the galaxy. Typically there are 7 dithers for each galaxy field. A data cube is constructed from these dithers by using a weighted sampling methodology (Sharp et al., 2015). The data cubes have a mean spatial resolution of $2.06''$ (Scott et al., 2018).

SAMI is a high spectral resolution instrument connected to the double beam AAOmega Spectrograph (Sharp et al., 2006). For the blue arm the 580V grating was used, which has a spectral coverage range of 3700 - 5700 Å providing a nominal resolution of $R = 1730$ (σ = 74 km s^{-1}). Whereas for the red arm the the R1000 grating was used with a spectral range of 6250 - 7350 Å providing a nominal resolution of $R = 4500$ (σ = 29 km s^{-1}). This high spectral resolution is ideal to study gas kinematics given velocity dispersions can be

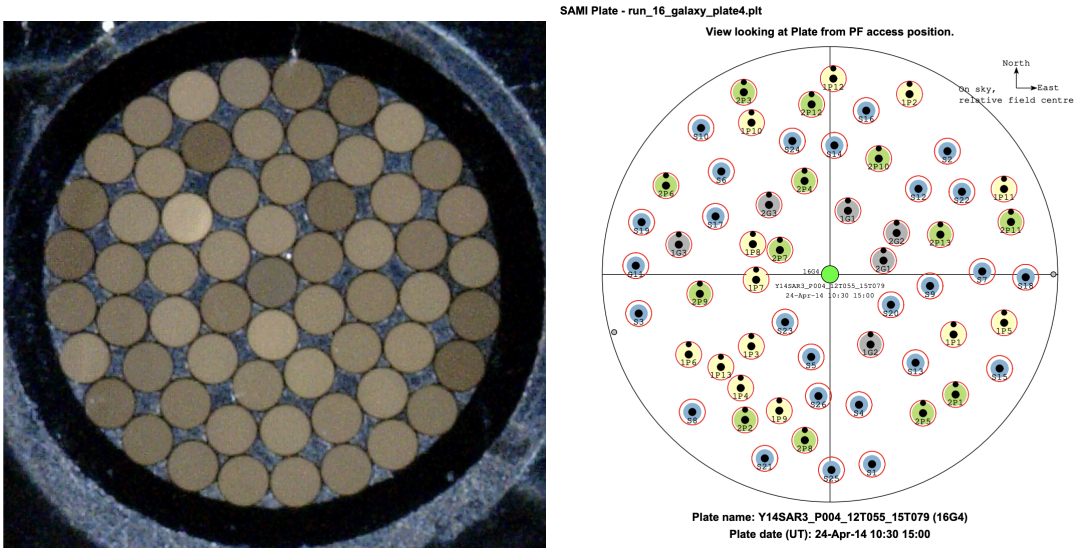

Figure 1.8: Left: A 61-core fused hexabundle (Bryant et al., 2014). Right: An example of a SAMI plate that allows for the observations of multiple objects simultaneously (Bryant et al., 2015). Each plate is equiped for two galaxy fields with 2×13 galaxy locations (yellow, green), 2 sets of guide stars (grey), plus 26 sky fibres for calibration (blue).

as low as ∼10 km s^{-1}.

The SAMI instrument was used for the SAMI Galaxy Survey. The observational time for the SAMI Galaxy Survey was completed in 2018 with over 3000 galaxies observed. These galaxies are relatively nearby ($z \lesssim 0.1$), have a wide range of stellar masses ($7.5 < \log_{10}(M_*/M_\odot) < 11.6$) and star-formation rates ($-4 < \log_{10}(SFR\ /\ M_*\ yr^{-1} < 1$) (Bryant et al., 2015; Green et al., 2018; Scott et al., 2018).

The SAMI Galaxy Survey features throughout this thesis as it is an ideal galaxy survey for studying the kinematics in nearby galaxies. The wide range of stellar masses and star-formation rates allows for the exploration of kinematics as a function of these properties. The stellar mass shapes the gravitational potential and has clear effects on the rotation curves and velocity dispersion within the galaxy. Observations and theoretical models suggest that velocity dispersion and star-formation are correlated, therefore the ability to probe this correlation across several orders of magnitude in star-formation rate is ideal.

The high spectral resolution of the SAMI Galaxy Survey is appropriate to study the ionised gas kinematics. The spectral resolution in the red arm of 29 km s^{-1} makes it possible to probe the velocity dispersion at a similar order to the ionised gas velocity dispersion which is often 10 - 30 km s^{-1}. Several papers have already used the high spectral resolution to their advantage. For example, SAMI data has been fit with multiple components (e.g. Figure 1.9 and also see Hampton et al., 2017) or with higher-order moments (van de Sande et al., 2017). Thus SAMI is an ideal data set to use for a detailed study of the velocity dispersion in galaxies at low redshift.

KMOS

KMOS is a multi-object IFS on the European Southern Observatory Very Large Telescope (ESO/VLT) in Chile. 24 objects can be observed across a 7.2′ field using KMOS (Sharples et al., 2004, 2013). Each IFU has a 2.8″ × 2.8″ FoV. KMOS has been used on several surveys including the KMOS Redshift One Spectrograph Survey (KROSS, Stott et al.,

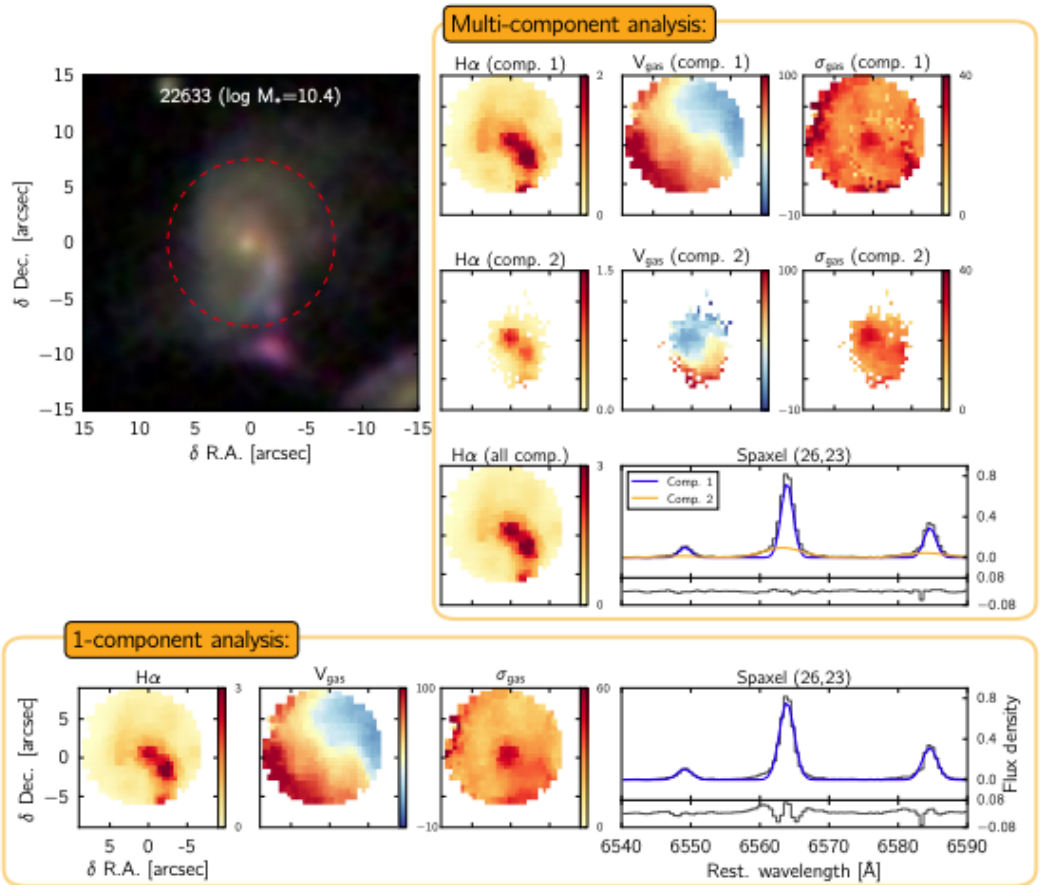

Figure 1.9: An example of fitting single and multiple components to GAMA 22887 from SAMI data (Green et al., 2018). The high spectral resolution of SAMI allows for these detailed fits to be performed.

2016) and KMOS^{3D} (Wisnioski et al., 2015).

Gas kinematics is studied for galaxies observed in KROSS in Chapter 4. KROSS is designed to study a sample of star-forming galaxies at $z \sim 1$ (Stott et al., 2016). The survey design was focused on the Hα emission line, which is a good tracer of the star-forming gas in disc galaxies.

The total sample consists of 795 galaxies with typical properties of galaxies at the targeted redshift. Observed galaxy properties were redshifts of $0.8 \lesssim z \lesssim 1.0$, stellar mass range of $9 < \log_{10}(M_* \ / \ M_\odot) < 11$, and star-formation rates of $0 \lesssim \log_{10}(\mathrm{SFR} \ / \ M_\odot \ \mathrm{yr}^{-1}) \lesssim 2$ (Stott et al., 2016; Harrison et al., 2017).

Observed galaxies with KROSS have properties of interest for this thesis. KROSS have typical properties of galaxies observed at $z \sim 1$ that can be used for the analysis of the evolution of galaxy properties and their kinematics across epochs. Furthermore, SAMI and KROSS have overlapping galaxy property ranges, thus allowing for the potential to distinguish between the contribution to the gas kinematics with respect to their physical properties and lookback time. For example, Tiley et al. (2019) argued that there is minimal evolution of the rotational velocity of a galaxy as a function of mass from $z \sim 1$ to today using comparisons between KROSS and SAMI. (Johnson et al., 2018) also used KROSS and SAMI to compare the velocity dispersion of these epochs, although with a different approach than what is explored in this thesis. Thus KROSS provides an interesting sample for the study of gas kinematics at $z \sim 1$, which allows for the potential

to answer important questions with respect to galaxy evolution across epochs.

1.4 Beam smearing

While spatially resolved sprectroscopy is required to estimate the intrinsic velocity dispersion for disc galaxies it can be misleading. This is due to an effect referred to as beam smearing which is the spatial blurring of the 3D data cube. Beam smearing acts to spatially blur gradients that affect the observed velocity dispersion.

All telescopes have a finite spatial resolution that results in smearing out the object of interest by the Point Spread Function (PSF). Mathematically, this can be seen as a convolution of the object by the PSF:

$$I = O * P, \tag{1.1}$$

where I is the observed image, O is the 2D projection of the object of interest, and P is the 2D convolution kernel.

Three dimensional IFS observations are the construction of numerous 2D images at several wavelengths. Thus, each 2D image is convolved by this beam. As each wavelength corresponds to a different Line-of-Sight (LoS) velocity this results in a smearing out of the galaxy kinematics. Measuring the kinematics from this beam smeared cube results in a smeared out image of the galaxy, a smoothed mean velocity map, and a velocity dispersion profile that peaks in the centre (Figure 1.10).

This smearing effect has been well known when constructing telescopes. It was also known in the HI community when the determination of rotation curves became popular (e.g. Höglund & Roberts, 1965; Roberts, 1968; Rubin & Mezger, 1970). There were even quite sophisticated techniques that resemble modern approaches to correct for beam smearing.

One of the initial attempts to correct for beam smearing was to construct a three-dimensional (3D) model of the galaxy that is convolved by the PSF. Roberts (1968) modelled observations of NGC 4631 with a parametric velocity profile and a constant velocity dispersion across the disc, that was then inclined with respect to the LoS. This model was convolved by the PSF prior to performing a comparison to the observations. There were twelve parameters in this model that needed to be fit. 60 different parameter sets were considered with the smallest root-mean square error chosen as the best fit. The best fit is shown in Figure 1.11.

Even though three-dimensional modelling was well known early on it has not always been used. Possible detractors to 3D modelling techniques are the complexity in creating them, difficulty in fitting numerous parameters, and the computational time it takes to fit such models. As such, simpler approaches have been common.

Researchers often use 2D or 1D modelling techniques for the rotation curves. These models are typically much easier and quicker to fit given the removal of the convolution step. In regimes where the beam is much smaller than the disc of the galaxy, heuristic approaches can also be used to estimate the velocity dispersion. The simplest heuristic approach is to measure the velocity dispersion in the outskirts of the galaxy where beam smearing will be less severe due to shallower velocity gradients (e.g. Wisnioski et al., 2015).

Improvements in computational power and fitting algorithms has improved the implementations of 3D modelling techniques, while recent code sharing abilities has allowed implementations to be widely distributed. The first widely available 3D modelling package known was GALMOD (Sicking, 1997) although it required a by-eye fitting approach.

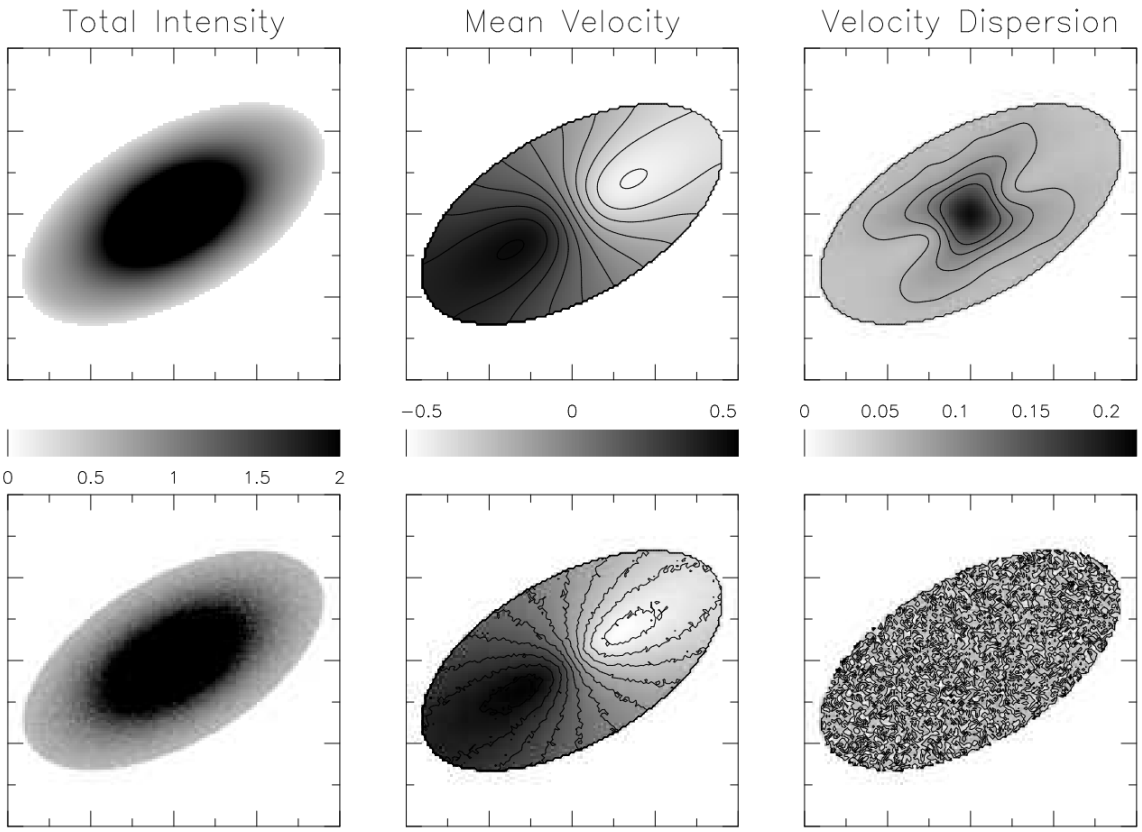

Figure 1.10: The effects of beam smearing on an idealistic disc (Teuben, 2002). Total intensity (left), mean velocity (middle), and velocity dispersion (right) for a disc with (top) and without beam smearing (bottom).

Recent algorithms are typically packaged with fitting procedures (e.g. Bouché et al., 2015; Di Teodoro & Fraternali, 2015; Bekiaris et al., 2016). In the next chapter, I will introduce a new fitting algorithm that was developed with the aim of modelling optical data while also taking into account the spatial flux substructure in galaxies.

1.5 This Thesis

This thesis aims to study the gas turbulence in disc galaxies. In Chapter 2 the issue of accurately inferring the gas kinematics in IFU observations is addressed. This chapter outlines the development of a novel technique referred to as BLOBBY3D that aims to infer the underlying velocity dispersion. I show that estimates of both the global and local velocity dispersion is effected by beam smearing. Then BLOBBY3D is applied to a small sample of galaxies from the SAMI Galaxy Survey.

In Chapters 3 and 4 BLOBBY3D is applied to samples of star-forming disc galaxies from the SAMI Galaxy Survey, DYNAMO survey, and KROSS. The inferences of the gas kinematics from BLOBBY3D are then used to study the correlation of gas kinematics with other galaxy properties, the evolution of gas kinematics from $z \sim 1$ to $z \sim 0.1$, as well as for comparisons to theoretical models of the drivers of turbulence. In Chapter 5 the results are summarised and future work is considered.

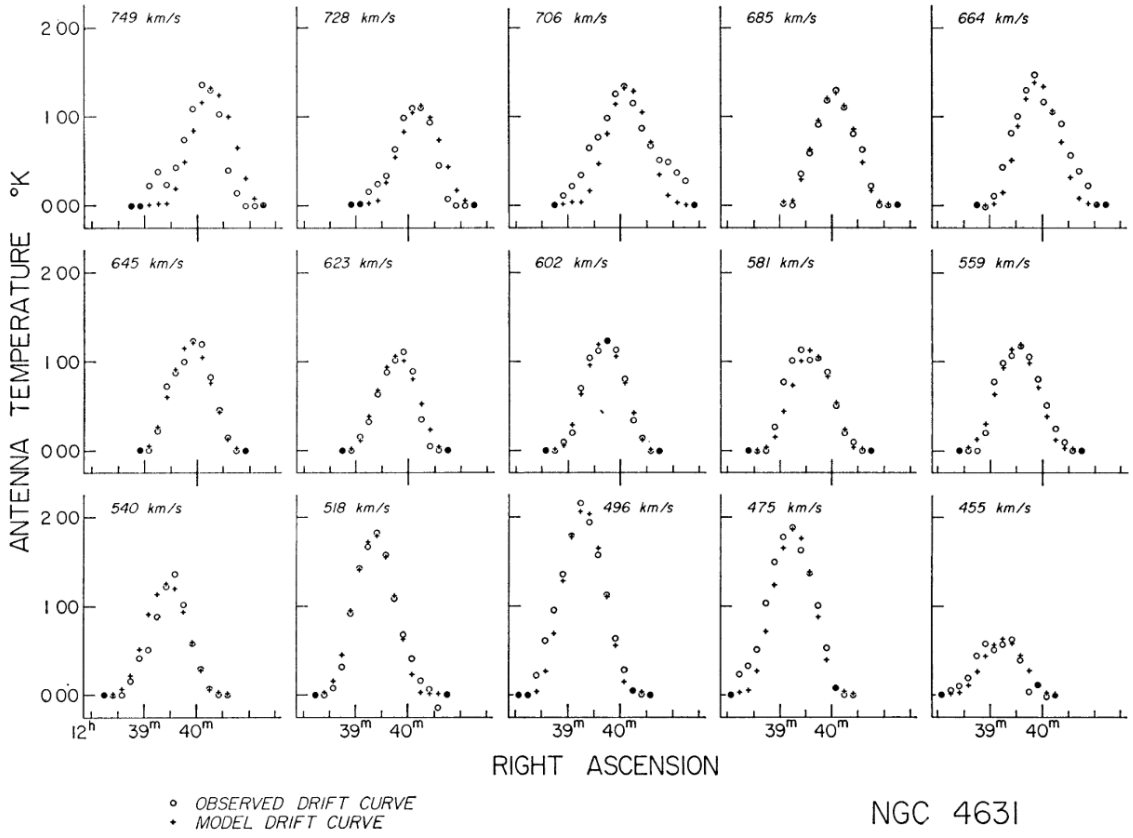

Figure 1.11: An early 3D fitting algorithm to HI observations of NGC 4631 (Roberts, 1968). Each plot shows the line-of-sight velocity distribution for a given velocity channel. The observed (open circles) are compared to the modelled (filled circles) in each plot.

2 Construction of Blobby3D

The first paper in this thesis is entitled *The SAMI Galaxy Survey: Bayesian Inference for Gas Disk Kinematics using a Hierarchical Gaussian Mixture Model*. It appeared in the Monthly Notices of the Royal Astronomical Survey (MNRAS) in May 2019. The paper is a description of the development of a novel 3D forward-fitting galaxy modelling technique, referred to as Blobby3D. Blobby3D was applied to different data sets in subsequent chapters. We outline the model parameterisation, tests of Blobby3D compared to toy models, plus applying Blobby3D to a sample of 20 star-forming galaxies from the SAMI Galaxy Survey.

MNRAS **000**, 1–23 (2019) Preprint 11 June 2021 Compiled using MNRAS LATEX style file v3.0

The SAMI Galaxy Survey: Bayesian Inference for Gas Disk Kinematics using a Hierarchical Gaussian Mixture Model

Mathew R. Varidel[1,2,3]★, Scott M. Croom[1,2,3], Geraint F. Lewis[1], Brendon J. Brewer[4], Enrico M. Di Teodoro[5], Joss Bland-Hawthorn[1,3], Julia J. Bryant[1,2,3,6], Christoph Federrath[5], Caroline Foster[1,3], Karl Glazebrook[3,7], Michael Goodwin[8], Brent Groves[2,3,5], Andrew M. Hopkins[9], Jon S. Lawrence[9], Ángel R. López-Sánchez[9,10], Anne M. Medling[5,11]†, Matt S. Owers[10,12], Samuel N. Richards[13] Richard Scalzo[14], Nicholas Scott[1,2,3], Sarah M. Sweet[3,8], Dan S. Taranu[2,15,16], Jesse van de Sande[1,3]

[1] *Sydney Institute for Astronomy (SIfA), School of Physics, A28, The University of Sydney, NSW 2006, Australia*
[2] *ARC Centre of Excellence for All-Sky Astrophysics (CAASTRO)*
[3] *ARC Centre of Excellence for All Sky Astrophysics in 3 Dimensions (ASTRO 3D)*
[4] *Department of Statistics, The University of Auckland, Private Bag 92019, Auckland 1142, New Zealand*
[5] *Research School of Astronomy and Astrophysics, Australian National University, Canberra, ACT 2611, Australia*
[6] *Australian Astronomical Optics, AAO-USydney, School of Physics, University of Sydney, NSW 2006, Australia*
[7] *Centre for Astrophysics and Supercomputing, Swinburne University of Technology, PO Box 218, Hawthorn, VIC 3122*
[8] *Australian Astronomical Observatory, 105 Delhi Rd, North Ryde, NSW 2113, Australia*
[9] *Australian Astronomical Optics, Faculty of Science and Engineering, Macquarie University, 105 Delhi Rd, North Ryde, NSW 2113, Australia*
[10] *Department of Physics and Astronomy, Macquarie University, NSW 2109, Australia*
[11] *Ritter Astrophysical Research Center, University of Toledo, Toledo, OH 43606, USA*
[12] *Astronomy, Astrophysics and Astrophotonics Research Centre, Macquarie University, Sydney, NSW 2109, Australia*
[13] *SOFIA Science Center, USRA, NASA Ames Research Center, Building N232, M/S 232-12, P.O. Box 1, Moffett Field, CA 94035-0001, USA*
[14] *Centre for Translational Data Science, University of Sydney, Darlington NSW 2008, Australia*
[15] *International Centre for Radio Astronomy Research, University of Western Australia, 35 Stirling Highway, Crawley WA 6009, Australia*
[16] *Department of Astrophysical Sciences, Princeton University, 4 Ivy Lane, Princeton, NJ 08544, USA*

Accepted XXX. Received YYY; in original form ZZZ

ABSTRACT

We present a novel Bayesian method, referred to as BLOBBY3D, to infer gas kinematics that mitigates the effects of beam smearing for observations using Integral Field Spectroscopy (IFS). The method is robust for regularly rotating galaxies despite substructure in the gas distribution. Modelling the gas substructure within the disk is achieved by using a hierarchical Gaussian mixture model. To account for beam smearing effects, we construct a modelled cube that is then convolved per wavelength slice by the seeing, before calculating the likelihood function. We show that our method can model complex gas substructure including clumps and spiral arms. We also show that kinematic asymmetries can be observed after beam smearing for regularly rotating galaxies with asymmetries only introduced in the spatial distribution of the gas. We present findings for our method applied to a sample of 20 star-forming galaxies from the SAMI Galaxy Survey. We estimate the global Hα gas velocity dispersion for our sample to be in the range $\bar{\sigma}_v \sim [7, 30]$ km s^{-1}. The relative difference between our approach and estimates using the single Gaussian component fits per spaxel is $\Delta\bar{\sigma}_v/\bar{\sigma}_v = -0.29 \pm 0.18$ for the Hα flux-weighted mean velocity dispersion.

Key words: methods: statistical, methods: data analysis, galaxies: kinematics and dynamics, techniques: imaging spectroscopy

★ E-mail: mathew.varidel@sydney.edu.au

† Hubble Fellow

1 INTRODUCTION

Accurately estimating the intrinsic gas kinematics is vital to answer specific science questions. For example, an open question remains about the drivers of turbulence within disk galaxies (eg. Tamburro et al. 2009; Federrath et al. 2017a). There is much evidence for higher velocity dispersions in $z > 1$ galaxies compared to nearby galaxies (Epinat et al. 2010; Förster Schreiber et al. 2009; Genzel et al. 2006; Law et al. 2007; Wisnioski et al. 2011). While the physical drivers of turbulence are not well understood, possibilities include one or more of the following; unstable disk formation (Bournaud et al. 2010), Jeans collapse (Aumer et al. 2010), star-formation feedback processes (Green et al. 2010, 2014), cold-gas accretion (Aumer et al. 2010), ongoing minor mergers (Bournaud et al. 2009), interactions between clumps (Dekel et al. 2009a,b; Ceverino et al. 2010), interactions between clumps and spiral arms (Dobbs & Bonnell 2007), or interactions between clumps and the interstellar medium (Oliva-Altamirano et al. 2018).

To gain a better understanding of the drivers of gas turbulence within the disk, it is important to accurately determine the intrinsic velocity dispersion of the galaxy. However, a known issue of observations using spatially resolved spectroscopy is beam smearing. Beam smearing is the effect of spatially blurring the flux profile due to the atmospheric seeing. For observations using spectroscopy, beam smearing acts to spatially blend spectral features. The blending of spectral features at different Line of Sight (LoS) velocities acts to flatten the observed velocity gradient and increase the observed LoS velocity dispersion. For single-component disk models, this has been shown to greatly exacerbate the observed LoS velocity dispersion in the middle of the galaxy (Davies et al. 2011).

Several heuristic approaches have been used to estimate the intrinsic velocity dispersion of a galaxy. A popular approach is to estimate the velocity dispersion away from the centre of the galaxy (eg. Johnson et al. 2018). Another approach is to apply corrections to the observed velocity dispersion as a function of properties that exacerbate the effect of beam smearing such as the seeing width and rotational velocity (Johnson et al. 2018). The local velocity gradient (Varidel et al. 2016) has also been used to ignore spaxels with high local velocity gradient (Zhou et al. 2017; Federrath et al. 2017b) as well as provide corrections for the global (Varidel et al. 2016) and local velocity dispersion (Oliva-Altamirano et al. 2018).

Forward modelling approaches have also been used to simultaneously model the flux and kinematic profiles. In these algorithms, a 3D modeled cube is constructed for the galaxy and then spatially convolved per spectral slice to simulate the effect of beam smearing. The convolved cube is compared to the observed data. In this way, the galaxy properties are fitted to the original data while accounting for the effects of beam smearing. There are several publicly available cube-fitting algorithms designed for optical observations known to the authors. Those are GalPak3D (Bouché et al. 2015), GBKFit (Bekiaris et al. 2016), and ^{3D}Barolo (Di Teodoro & Fraternali 2015).

GalPak3D and GBKFit assume parametric radial flux and velocity profiles with constant velocity dispersion. These algorithms have been used to infer the intrinsic global velocity dispersion and bulk rotation properties (eg. Contini et al. 2016; Oliva-Altamirano et al. 2018). However, due to the parametric construction of the galaxy models, the residuals often exhibit significant substructure. This will usually be dominated by the gas distribution as it often exhibits more complex structure than the idealised radial profiles.

An implementation of non-parametric radial profiles has been constructed in tilted ring models. These models decompose the galaxy into a series of rings each with independent flux and kinematic properties. Tilted ring models are appropriate for analysing galaxies that are well represented by non-parametric radial profiles. In particular, they produce exquisitely detailed non-parametric radial profiles for high-resolution data (eg. Fig. 4, Di Teodoro & Fraternali 2015).

A pioneering 3D tilted ring model was implemented in Galmod (Sicking 1997) in the Gronigen Image Processing SYstem (GIPSY, van der Hulst et al. 1992). Examples of modern implementations of tilted-ring models are ^{3D}Barolo and TiRiFiC (Józsa et al. 2007). TiRiFiC has received considerable development allowing for increased flexibility on a standard tilted ring model. However, it has solely been used for HI radio observations. This is at least partially due it assuming the spectral dimension is frequency. While it would be possible to transform the optical wavelength dimension of the data to frequency for use in TiRiFiC, we are not aware of researchers that have used TiRiFiC on optical data. Instead, ^{3D}Barolo has been used on both optical (eg. Di Teodoro et al. 2016, 2018) and radio observations (eg. Iorio et al. 2017).

A typical assumption used in previous methods is that the gas substructure can be well modelled using a radial profile. However, the distribution of gas within a galaxy is often more complex including rings, spiral arms, or individual clumps. In this paper, we will outline a 3D method to model the gas distribution and kinematic profiles robustly despite substructure of the gas distribution within the disk. This algorithm is inspired by the works of Brewer et al. (2011b, 2016), who modelled the photometry of lensed galaxies with substructure by decomposing galaxies into a number of blobs using mixture models of a positive definite basis function. Our method (referred to as Blobby3D) decomposes the gas distribution into a mixture model of a positive definite basis function while simultaneously fitting the gas kinematics. Our method assumes radial velocity and velocity dispersion profiles across the galaxy.

The outline of this paper is as follows. In Section 2 we will frame the inference problem in terms of Bayesian reasoning and describe the model parameterisation. In Section 3 we will discuss applications of our method to several toy data sets. In Section 4 we will apply the method to a sample of galaxies from the SAMI Galaxy Survey. In Section 5 we will discuss the implications of our results. We then make our concluding statements in Section 6.

2 MODEL DESCRIPTION

The problem of inferring the underlying galaxy properties can be formulated within the Bayesian framework as an inference for the galaxy parameters ($\mathbf{G}$), convolution parameters from the seeing and instrumental broadening ($\mathbf{\Sigma}$), and any

systematic effects ($\mathbf{S}$) given some data (D),

$$p(\mathbf{G}, \Sigma, \mathbf{S}|D) \propto p(\mathbf{G}, \Sigma, \mathbf{S})p(D|\mathbf{G}, \Sigma, \mathbf{S}) \quad (1)$$

$$\propto p(\Sigma)p(\mathbf{S}|\Sigma)p(\mathbf{G}|\Sigma, \mathbf{S})p(D|\mathbf{G}, \Sigma, \mathbf{S}). \quad (2)$$

Bayes' theorem relates the inference for the parameters $\mathbf{G}$, Σ, and $\mathbf{S}$ to our prior understanding in $p(\mathbf{G}, \mathbf{\Sigma}, \mathbf{S})$ and the data using the likelihood function, $p(D|\mathbf{G}, \mathbf{\Sigma}, \mathbf{S})$. All galaxy inferences can be summarised in this way.

In this work, we will assume that the convolution parameters are known. That is, $p(\mathbf{\Sigma})$ is a delta function that peaks at the assumed convolution parameters. The Point Spread Function (PSF), representing the seeing, is typically estimated by modelling stars that are observed at the same time as the galaxies. Whereas the instrumental broadening is estimated by taking calibrations of the spectrograph using arc frames. Assuming that the convolution parameters are known will probably result in narrower posterior distributions than if we propagated our uncertainty in the convolution parameters.

Furthermore, we only consider systematic effects that are independent of the galaxy parameterisation. Making the above assumptions, we approximate the problem represented in equation (2) to,

$$p(\mathbf{G}, \mathbf{S}|D, \Sigma) \propto p(\mathbf{G}, \mathbf{S})p(D|\mathbf{G}, \mathbf{\Sigma}, \mathbf{S}) \quad (3)$$

$$\propto p(\mathbf{G})p(\mathbf{S})p(D|\mathbf{G}, \mathbf{\Sigma}, \mathbf{S}). \quad (4)$$

The following sections will outline the assumptions made about the parameterisation of $\mathbf{G}$, $\mathbf{\Sigma}$, and $\mathbf{S}$.

2.1 Galaxy parameterisation (G)

Our choice of galaxy parameterisation is constructed with the aim to model the gas distribution and kinematics for a wide range of regularly rotating galaxies. We parameterise the gas distribution with respect to a single emission line.

A simplistic prior assumption for the gas distribution of a galaxy, is that it consists of an unknown number of gas clouds that are gravitationally bound. The gas distribution will be centred and rotate around a single kinematic centre. The velocity profile is assumed to be radial with a gradient that is steep near the kinematic centre and plateaus at increasing radius. The velocity dispersion profile is assumed to follow a smoothly varying radial profile across the galaxy.

We will now describe the parameterisation of the above prior assumption in accordance with Bayes' theorem. Note that we also describe the joint prior distribution including the assumed constants, parameters, hyper-parameters, and data in Table 1.

2.1.1 The galaxy coordinate system

The galaxy coordinate system is described by a kinematic centre at (x_c, y_c), an inclination angle i, and the semi-major axis position angle θ. This describes a thin plane for the gas to lie in. The set of parameters required to define the coordinate system are referred to as $\mathbf{C}$. The prior distribution for each parameter is assumed to be independent such that,

$$p(C) = p(x_c)p(y_c)p(i)p(\theta) \quad (5)$$

The kinematic centre of the galaxy is typically in the centre of the Field-of-View (FoV). We weakly incorporate this information by placing a wide-tailed Cauchy distribution centred in the middle of the image with a Full-Width Half-Maximum (FWHM) of $0.1 \times$ `ImageWidth`. `ImageWidth` is defined to be the geometric mean length of the FoV. The prior distribution for the kinematic centre is truncated such that it cannot lie outside of the FoV.

We assume that the kinematic position angle follows a uniform distribution in the range $\theta \in [0, 2\pi]$. The inclination angle is typically constrained by the observed morphology and the kinematic profiles. However, it is often not possible to observe the full extent of the galaxy in IFS surveys. For example, a typical galaxy observed in the SAMI Galaxy Survey, which we will be using to test our methodology, is observed out to $\sim 2R_e$, where R_e is the half-light radius. This limits our ability to infer the inclination from the observed gas distribution. The LoS kinematic profiles are known to be approximately degenerate for varying inclination angles as well (eg. Fig. 9, Glazebrook 2013). We did test our methodology with a uniform prior for the inclination angle in the range $i \in [0, \pi/2]$. However, when applying our methodology to the sample galaxies in Section 4, we found that the inferred inclination angle could differ significantly from the estimated inclination angle when converting the observed ellipticity to an inclination angle assuming a thin disk. With this in mind, we assume that the inclination can be estimated from previous observations of the same galaxy with a wider FoV. The inclination is then set as a constant. The inclination and kinematic position angle are incorporated into the LoS velocity profile and define a plane that the gas lies in.

Setting the inclination angle as a constant will have several implications for our inferences. The inferred posterior distributions will probably be narrower than if we incorporated our uncertainty of the inclination angle into our model parameterisation. Also, the effect of beam smearing on kinematic properties is a function of the LoS velocity profile which is affected by the inclination angle assumption. As such, we will introduce a systematic bias when our assumptions about the inclination are incorrect.

2.1.2 The spatial gas distribution

To incorporate our prior understanding within the galaxy parameterisation, we decomposed the gas distribution into a sum of positive definite basis functions. We use positive definite basis functions as the integrated flux of a gas cloud should always be positive. Decomposing the gas distribution into a sum of positive definite basis functions is an approach to model complex structures such as spirals, rings, and clumps that are observed in galaxies. We refer to each component as a 'blob'.

We do not claim that a single blob represents an individual gas cloud. This is due to the following:

- The resolution of the data in many IFS studies is typically too low to resolve individual gas clouds.
- The choice of parameterisation for the positive definite basis function will lead to more or less blobs. This is due to the shape of the blob not perfectly matching the individual gas cloud. As such, several blobs may be required to model the shape of the gas cloud.

There are cases where an individual blob or a set of blobs

Table 1. The hyperparameters, parameters, and data (i.e. all of the quantities involved in the inference), along with the prior distributions for each quantity. Taken together, these specify the joint prior distribution for the hyperparameters, parameters, and data, from which we obtain the posterior distribution. Where parameters are assumed to be known we represent the prior as a Dirac delta function with a user-input defined as $\mathcal{U}$. The notation $T(a, b)$ (written after a probability distribution) denotes truncation to the interval $[a, b]$. `ImageWidth` and `PixelWidth` refer to the geometric mean of the spatial dimensions for the cube and a single pixel, respectively. Note that flux units are 10^{-16} erg s^{-1} cm^{-2}.

Quantity	Meaning	Prior
Galaxy coordinate system (C)		
x_c	x-coordinate for centre of galaxy	Cauchy(`XImageCentre`, $0.1 \times$ `ImageWidth`)$T(x_{\rm min}, x_{\rm max})$
y_c	y-coordinate for centre of galaxy	Cauchy(`YImageCentre`, $0.1 \times$ `ImageWidth`)$T(y_{\rm min}, y_{\rm max})$
θ	Galaxy semi-major axis angle (anti-clockwise w.r.t. East)	Uniform(0, 2π)
i	Galaxy inclination ($i = 0$ for face-on)	$\delta(i - \mathcal{U})$
Number of blobs		
N	Number of blobs comprising the galaxy	Loguniform$\{1, 2, ..., 300\}$
Blob hyperparameters (α)		
μ_r	Typical distance of blobs from (x_c, y_c)	Loguniform(0.03″, 30″)
μ_F	Typical flux of blobs	Loguniform(10^{-3}, 10^3)
σ_F	Deviation of log flux from μ_F	Loguniform(0.03, 3)
$W_{\rm max}$	Maximum width of blobs	Loguniform(`PixelWidth`, 30″)
$q_{\rm min}$	Cutoff axis ratio	Uniform(0.2, 1)
Blob parameters ($\mathbf{B}_j$)		
F_j	Integrated flux	Lognormal(μ_F, σ_F^2)
r_j	Distance of centre from (x_c, y_c)	Exponential(μ_r)
θ_j	Polar angle of centre w.r.t. θ	Uniform(0.0, 2π)
w_j	Width of blob	Loguniform(`PixelWidth`, $W_{\rm max}$)
q_j	Axis ratio ($q = b/a$)	Triangular($q_{\rm min}$, 1)
ϕ_j	Orientation angle (anti-clockwise w.r.t. $\theta + \theta_j$)	Uniform(0, π)
Velocity profile parameters (V)		
$v_{\rm sys}$	Systemic velocity	Cauchy(0 km s^{-1}, 30 km s^{-1}) T(-150 km s^{-1}, 150 km s^{-1})
v_c	Asymptotic velocity	Loguniform(40 km s^{-1}, 400 km s^{-1})
r_t	Turnover radius for velocity profile	Loguniform(0.03″, 30″)
γ_v	Shape parameter for velocity profile	Loguniform(1, 100)
β_v	Shape parameter for velocity profile	Uniform(-0.75, 0.75)
Velocity dispersion profile parameters ($\mathbf{\Sigma_V}$)		
$\sigma_{v,0}$	Velocity dispersion at the kinematic centre	Loguniform(1 km s^{-1}, 200 km s^{-1})
$\sigma_{v,1}$	Log velocity dispersion gradient	Normal(0, 0.2^2)
Convolution parameters ($\mathbf{\Sigma}$)		
$A_{k,\rm PSF}$	Weight for each Gaussian representing the PSF	$\delta(A_{k,\rm PSF} - \mathcal{U})$
FWHM$_{k,\rm PSF}$	Seeing FWHM for each Gaussian representing the PSF	δ(FWHM$_{k,\rm PSF} - \mathcal{U}$)
FWHM$_{\rm lsf}$	Instrumental broadening	δ(FWHM$_{\rm lsf} - \mathcal{U}$)
Systematic parameters (S)		
σ_0	Constant Gaussian noise component	Loguniform(10^{-12}, 10)
Data (D)		
D_{ijk}	Flux for each velocity bin	Normal(M_{ijk}, $\sigma^2_{\rm obs} + \sigma_0^2$)

may be assigned a particular classification such as an individual clump, spiral arm, or ring. However, such processing of the model output must be performed by the user after the modelling has been completed. For the majority of cases, the individual blobs should be seen as nuisance parameters. The primary reason for using blobs is to construct a flexible model of the gas distribution, rather than to derive properties of individual gas clouds.

There have been previous 3D approaches that decomposed galaxies into a series of sources (ie. clouds or blobs). An example of this are the Monte Carlo integration techniques used in tilted ring models such as GALMOD (Sicking 1997). In these algorithms, the 3D tilted ring model is integrated using Monte Carlo sampling of point sources within a ring with a given gas column density and kinematics. However, the primarily goal is not to derive the individual parameters of the clouds, but rather to perform the integration of the 3D tilted ring model.

An alternative flexible approach, that has been applied to lensing data, is to use pixelated flux profiles. In these models, each pixel has an independent flux value. The pixelated flux profile is often regularised such that the resulting profile is smooth (eg. Suyu et al. 2006). The advantage of this approach is that it can theoretically model any flux distribution at the observed scale, prior to performing the convolution. The disadvantage of the pixelated approach, is that the prior distribution assigns high prior probability to flux profiles that look like noise and the regularisation approach typically does not enforce the flux to be positive definite (Brewer et al. 2011b). As such, we have chosen to use the approach of modelling the gas distribution using a sum of positive definite basis functions.

We chose a Gaussian basis function where the integrated flux for each blob is always positive. Using a Gaussian basis function to represent the spatial gas distribution is not the only possibility. For example, generic Sèrsic profiles and

quadratic polynomials with negative curvature calculated where the flux is positive have been used to model lensed galaxies by Brewer et al. (2011b, 2016). Other paramaterisations of positive definite functions would also be feasible.

Each blob is defined by a set of parameters $\mathbf{B}_j$ that describe its integrated flux (F_j), central position (r_j, θ_j) with respect to the galaxy centre (x_c, y_c) and semi-major axis position angle (θ), width (w_j), axis ratio ($q_j = b/a$), and orientation (ϕ_j) with respect to $\theta + \theta_j$. The spatial component of the blob flux is then,

$$F(x', y') = \frac{F_j}{2\pi w_j^2} \exp\left(-\frac{1}{2w_j^2}\left(q_j x'^2 + \frac{y'^2}{q_j}\right)\right). \quad (6)$$

The coordinate system (x', y') is transformed with respect to the galaxy coordinate system defined by $\mathbf{C} = \{x_c, y_c, i, \theta\}$ and subsequently rotated with respect to the blob orientation (ϕ_j). To construct the flux map in the original coordinate system (ie. $F(x, y)$), we calculate the flux per spaxel in the rotated coordinates and sum the flux contribution for each blob.

The blob parameters F_j, r_j, w_j, and q_j are hierarchically constrained. Hierarchical Gaussian mixture models refer to models that are a sum of Gaussians where the Gaussian parameters are hierarchically constrained. For a hierarchical Gaussian mixture model, a joint prior is constructed for the Gaussian parameters $\{\mathbf{B}_j\}_{j=1}^N$ for N Gaussians conditional on a set of hyperparameters $\boldsymbol{\alpha}$ (ie. the parameters for the prior distribution). The joint prior distribution for N Gaussians is then described as,

$$p(\boldsymbol{\alpha}, \{\mathbf{B}_j\}_{j=1}^N) = p(\boldsymbol{\alpha}) \prod_{j=1}^{N} p(\mathbf{B}_j|\boldsymbol{\alpha}). \quad (7)$$

Where $p(\boldsymbol{\alpha})$ refers to the prior distribution for the hyperparameters. The prior distribution for the blob parameters $\mathbf{B}_j$ are dependent on the hyperparameters encoded in $p(\mathbf{B}_j|\boldsymbol{\alpha})$.

The number of Gaussians required to adequately model the gas distribution is unknown prior to performing the inference. We can explicitly incorporate this within the joint prior distribution such that,

$$p(N, \boldsymbol{\alpha}, \{\mathbf{B}_j\}_{j=1}^N) = p(N)p(\boldsymbol{\alpha}|N) \prod_{j=1}^{N} p(\mathbf{B}_j|\boldsymbol{\alpha}, N) \quad (8)$$

$$= p(N)p(\boldsymbol{\alpha}) \prod_{j=1}^{N} p(\mathbf{B}_j|\alpha). \quad (9)$$

The last step assumes the hyperparameters ($\boldsymbol{\alpha}$) and blob parameters $\{\mathbf{B}_j\}_{j=1}^N$ are independent from the number of Gaussians (N). We defined the prior distribution for the number of blobs $p(N)$ to be a loguniform distribution in the range $\{1, 2, 3, ..., N_{\max}\}$. We have set $N_{\max} = 300$ for all examples in this paper. Given 6 parameters per blob and a potential for up to 300 blobs, the total number of parameters to describe the full set of Gaussians is between 6 – 1,800.

Hierarchical Gaussian mixture models are preferred when the parameters for the Gaussians follow a prior distribution where the hyperparameters are unknown. In our case, the hyperparameters are descriptors for the distribution of blobs which are specific for the observed galaxy. In this way the galaxy shape, typical blob shape, and individual blob parameters are inferred simultaneously.

We assume the integrated flux of the blobs follows a lognormal distribution suggesting that the blob has a typical integrated flux (μ_F) and deviation (σ_F). The lognormal distribution also ensures the integrated flux is positive.

The distance of the blobs (r_j) is assumed to follow an exponential distribution from the kinematic centre (x_c, y_c). This imparts a typical distance μ_r from the kinematic centre which is fitted per galaxy.

The width of the blobs (w_j) is assumed to follow a loguniform distribution. The choice of a loguniform distribution is chosen to avoid imparting a typical scale length as both disk and clumpy features may be required to model a given galaxy. The minimum width is defined by the `PixelWidth` which is the geometric mean of the x and y dimensions for a pixel. Restricting the minimum width of the blobs has been incorporated for several reasons. It limits the problem of accurately integrating and spatially convolving blobs that are much smaller than the pixel width. It also limits the possibility of overfitting the gas substructure. The maximum width ($W_{\max}$) is a free hyperparameter that is fitted for the galaxy.

The typical axis ratio ($q_j = b/a$) for a blob is also unknown prior to performing the inference. We chose a right-angled triangular prior distribution for q_j of the form,

$$p(q_j) = \frac{2(q_j - q_{\min})}{(1 - q_{\min})^2}. \quad (10)$$

The hyperparameter $q_{\min}$ is the minimum axis ratio. This prior imparts a preference for circular Gaussians.

2.1.3 *The Velocity Profile*

In the spectral dimension, we assume a single Gaussian emission line component per spaxel. The mean position per spaxel describes the rotational velocity profile across the galaxy. We assumed a continuous velocity profile across the blobs with a mean LoS velocity defined by the Courteau (1997) empirical model,

$$v(r) = v_c \frac{(1 + r_t/r)^\beta}{(1 + (r_t/r)^\gamma)^{1/\gamma}} \sin(i)\cos(\theta) + v_{\rm sys}. \quad (11)$$

r is defined as the distance in the galaxy plane to the kinematic centre. $v_{\rm sys}$ is a systemic velocity term, v_c is the asymptotic velocity, and r_t is the turnover radius. β is a shape parameter that describes the gradient for $r > r_t$, where positive results in a decreasing velocity profile and negative results in a increasing profile. γ describes how sharply the velocity profile turns over. We refer to the set of parameters describing the velocity profile as $\mathbf{V}$.

The prior distribution for these parameters are assumed to be independent such that,

$$p(\mathbf{V}) = p(v_{\rm sys})p(v_c)p(r_t)p(\beta)p(\gamma). \quad (12)$$

It is assumed that the data cube is de-redshifted, but we allow for offsets for a non-zero systemic velocity by applying a prior that follows a wide-tailed Cauchy distribution with FWHM of 30 km s^{-1} and is truncated to the interval [-150 km s^{-1}, 150 km s^{-1}]. For all examples explored in this paper, the systemic velocity was well within these ranges. However, the range can be increased to account for a greater offsets if required.

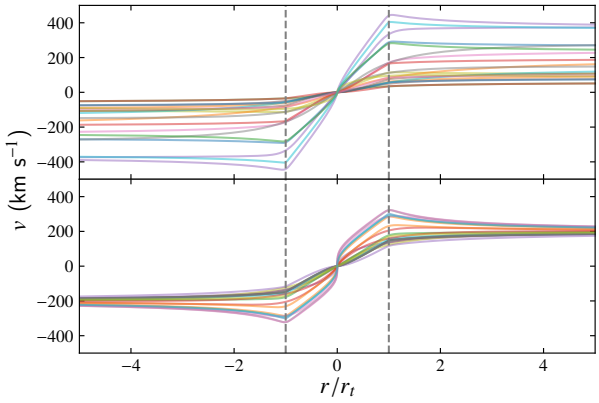

Figure 1. Prior samples of the radial velocity profile. Samples where all velocity parameters vary except $v_{\rm sys} = 0$ km s^{-1} (top) and with $v_c = 200$ km s^{-1} (bottom). Vertical lines indicate the turnover radius at $r = \pm r_t$. Our choice of priors for the velocity profile parameters were chosen to yield realistic radial velocity profiles.

The remaining parameters v_c, r_t, β, and γ are set with limits that yield a reasonable prior distribution by observing samples of the profiles. See Fig. 1 for velocity profiles using random samples from the prior for the velocity parameters. We assume loguniform prior for v_c in the range [40 km s^{-1}, 400 km s^{-1}]. The lower bound of 40 km s^{-1} for v_c was adequate for the test galaxies in this paper, but it can be easily lowered to take into account a larger sample of galaxies. The turnover radius (r_t) is assumed to follow a loguniform distribution in the range [0.03″, 30″].

Our velocity profile assumption yields a reasonably flexible radial profile, but we do not claim that this represents all galaxy velocity profiles. In particular, warps and asymmetries are not taken into account. Further flexibility may be required when the method is applied to larger data sets.

2.1.4 The velocity dispersion profile

The width of the Gaussian in the spectral dimension describes velocity dispersion per spaxel. The velocity dispersion profile is assumed to be a log-linear radial profile of the form,

$$\sigma_v(r) = \exp\Big(\log(\sigma_{v,0}) + \sigma_{v,1} r\Big). \tag{13}$$

Where $\sigma_{v,0}$ represents the velocity dispersion at the kinematic centre (x_c, y_c) and $\sigma_{v,1}$ represents the log radial velocity dispersion gradient. We refer to the set of parameters that describe the galaxy velocity dispersion profile as $\mathbf{\Sigma_V}$. We used a log-linear profile such that $\sigma_v > 0$ at all radii. A disadvantage of this parameterisation is that for large $\sigma_{v,1}$, the observed σ_v can be much higher than is realistic. We use a normal prior distribution with mean 0 and variance 0.2^2 for $\sigma_{v,1}$ to limit unrealistically high velocity dispersion gradients. We assume independence of the prior distributions for $\mathbf{\Sigma_V}$ such that,

$$p(\mathbf{\Sigma_V}) = p(\sigma_{v,0})p(\sigma_{v,1}). \tag{14}$$

During testing we also explored the possibility of having a single velocity dispersion per blob. While this would be ideal, it can lead to over-fitting systematics that have not been corrected for appropriately. In particular, blobs with unrealistically high velocity dispersion would often be required to account for systematic offsets in the continuum. This can occur in the log-linear model as well, but it is less affected due to the parameterisation across the galaxy. Therefore, we have opted for a simplified parametric model which is more robust but less flexible.

2.1.5 The full galaxy parametersisation

The flux distribution including a Gaussian instrumental broadening ($\sigma_{\rm lsf}$) within velocity space for a blob is defined as,

$$F(x, y, v) = \frac{F(x, y)}{\sqrt{2\pi(\sigma^2_{v(r(x,y))} + \sigma^2_{\rm lsf})}} \exp\left(\frac{(v - v(r(x, y)))^2}{\sqrt{\sigma^2_{v(r(x,y))} + \sigma^2_{\rm lsf}}}\right). \tag{15}$$

Equations 6, 11, 13, and 15 fully define the flux distribution of a blob for a given emission line for the spatial and velocity dimensions. The above model is converted from velocity to wavelength space such that the model can be compared to the data.

The full joint prior distribution for our galaxy model parameterisation is described as,

$$p(\mathbf{G}) = p(\mathbf{C}, \mathbf{V}, \mathbf{\Sigma_V}, N, \boldsymbol{\alpha}, \{\mathbf{B}_j\}_{j=1}^N) \tag{16}$$

$$= p(\mathbf{C})p(\mathbf{V})p(\mathbf{\Sigma_V})p(N, \boldsymbol{\alpha}, \{\mathbf{B}_j\}_{j=1}^N) \tag{17}$$

$$= p(\mathbf{C})p(\mathbf{V})p(\mathbf{\Sigma_V})p(N)p(\boldsymbol{\alpha}) \prod_{j=1}^{N} p(\mathbf{B}_j|\alpha). \tag{18}$$

The first step expands the galaxy parameterisation ($\mathbf{G}$) to the sets of parameters describing the galaxy coordinate system ($\mathbf{C}$), velocity profile ($\mathbf{V}$), velocity dispersion profile ($\mathbf{\Sigma_V}$), number of blobs (N), the hyperparameters for the blobs ($\boldsymbol{\alpha}$), and the blob parameters ($\{\mathbf{B}_j\}_{j=1}^N$). The second step assumes independence between the various parameter sets where applicable. The third step expands the joint prior for N, $\boldsymbol{\alpha}$, and ($\{\mathbf{B}_j\}_{j=1}^N$) to state the dependence of the blob parameters ($\{\mathbf{B}_j\}_{j=1}^N$) on the blob hyperparameters ($\boldsymbol{\alpha}$) as in Equation 9.

2.2 Sampling the prior for G

The galaxy model parameterisation is complex, including hierarchical constraints and a variable number of parameters dependent on the number of blobs. For such high dimensional model parameterisations, it is often difficult to gain an intuitive understanding of the prior distribution. A common approach to check that a complex prior distribution is reasonable, is to visually check randomly drawn samples from the prior. As an example of this approach, we show 2D maps for 10 randomly drawn samples from the joint prior distribution in Fig. 2.

The 2D maps are constructed with a 15″ and 0.5″ square FoV and pixel width. These limits were constructed with the SAMI Galaxy Survey in mind, which has a FoV with typical diameter of ∼ 15″ and 0.5″ square pixels. We set

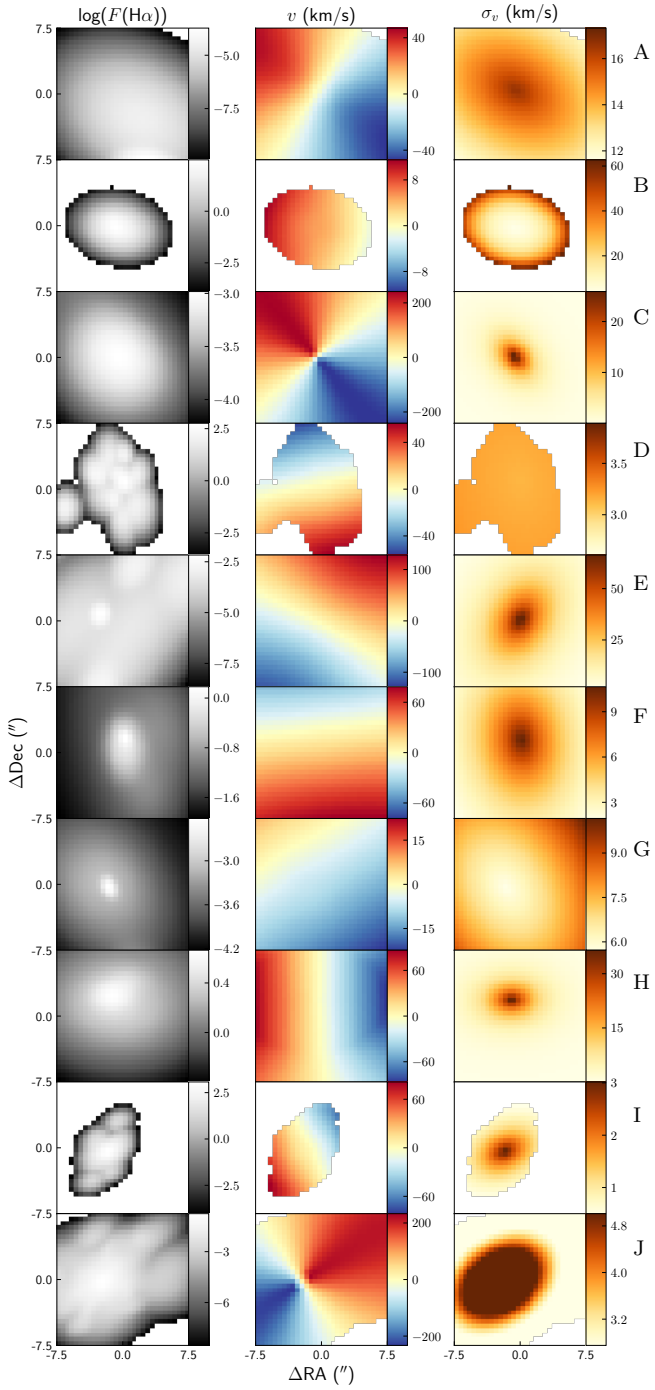

Figure 2. 2D maps of randomly drawn samples from the prior distribution for the Hα flux (left), LoS velocity (middle), and LoS velocity dispersion (right). For illustrative purposes, we show samples with inclination $i = \pi/4$, systemic velocity $v_{\rm sys} \in [-10\ {\rm km\ s^{-1}}, 10\ {\rm km\ s^{-1}}]$, and the kinematic centre $x_c, y_c \in [-3'', 3'']$. These maps show the flexibility of modelling the spatial gas distribution using a Gaussian mixture model. We also chose priors to yield realistic gas distributions and kinematic profiles.

the inclination $i = \pi/4$. For illustrative purposes, we also limit the prior samples shown in Fig. 2 such that $v_{\rm sys} \in [-10\ {\rm km\ s^{-1}}, 10\ {\rm km\ s^{-1}}]$ and $x_c, y_c \in [-3'', 3'']$.

In all samples there is a clear photometric and kinematic centre. These properties are constrained by the global parameters controlling the plane for the gas to lie in (i, θ) as well as the centre and typical distance for the blob centres (x_c, y_c, μ_r). Similarly, we avoid unusually shaped blobs by hierarchically constraining the width and axis-ratio of the blobs.

Several samples add increased complexity with centralised peaks (eg. F and G) and others with non-centralised clumps (eg. D, E, F, I, J). The most unusual clump is probably in D on the west-side of the image, but individual gas clumps similar to this are possible in real data (eg. Richards et al. 2014).

The LoS velocity and velocity dispersion profiles are reasonable radial velocity profiles. Increased flexibility such as warps and asymmetries could be added to increase the realism of the profiles in the future.

We note that the prior distribution is a balance between flexibility and realism. As such, not all samples from the prior will represent realistic galaxies. Instead, the data is required to constrain the prior distribution via posterior sampling.

2.3 PSF convolution

The PSF convolution kernel is assumed to be well represented by a decomposition of concentric circular 2D Gaussians. Each Gaussian is described by $\Sigma_k = \{A_{k,\rm PSF}, {\rm FWHM}_{k,\rm PSF}\}$ corresponding to the weight and FWHM for the k-th component. Each Gaussian has the separability property such that it can be deconstructed into two orthogonal vectors. Therefore, the 2D convolution is performed by convolving consecutively along each axis. Linear convolution using this method scales as $O(N_{\rm col,image}N_{\rm col,kern} + N_{\rm row,image}N_{\rm row,kern})$ for each Gaussian. Further speed-up is gained by only constructing each Gaussian kernel out to $2.12 \times {\rm FWHM}_{\rm PSF}$, which is equivalent to $5\sigma_{\rm PSF}$.

Convolution is also a distributive operation. As such, we perform the convolution by each Gaussian component on the original image and then sum the convolved images. This method will scale linearly with the number of Gaussians required to model the kernel. We have only used 1–2 Gaussian components to represent the PSF as that was an acceptable number in our case.

In all examples in this paper, we have used representations of the kernel to be a Gaussian or Moffat profile. We do this as the pipeline for the SAMI Galaxy Survey provides estimates for the PSF for both the Gaussian and Moffat profiles. The PSF profile parameters are estimated by fitting observations of stars that have been taken simultaneously to observing the galaxies. In cases where the PSF is represented by a Moffat profile, we fit the 2D Moffat kernel with a sum of 2 Gaussians. The fitted parameters are then passed to the code implementation of our method.

2.4 Data

Our method assumes that the data cube has been isolated to a single emission line and the continuum has been subtracted.

For optical IFS observations, this requires accurate modelling of the stellar continuum. In low signal-to-noise observations this may not be possible and thus signal-to-noise cuts of the data cube are required. While it may be ideal to parameterise the systematics in the continuum corrections, we avoided modelling the systematics to avoid introducing a high number of nuisance parameters to our model.

To isolate an emission line, typical optical IFS observations will need to be cut in the spectral dimension around the emission line of interest. This may be difficult in the spectral regions where there are multiple emission lines. In our examples, we will be focusing on the Hα emission line at 6562.8 Å which is adjacent to the two [NII] lines at 6548.1 Å and 6583.1 Å. Isolating the Hα emission line from the surrounding [NII] lines may be impossible for galaxies with high LoS velocity dispersions. In such cases, it will be a requirement to model the [NII] lines as this will cause systematics which we have not taken into account in our current parameterisation. Adding the [NII] lines could be introduced to our method by modelling the [NII]/Hα per blob, then constraining the doublet using the theoretical ratio between the lines.

To construct the likelihood function, we assume the data follows a normal distribution. The mean is equal to an input data cube file ($D_{ijk,\mathrm{obs}}$). The variance is given by the sum of an input variance cube ($\sigma^2_{ijk,\mathrm{obs}}$) and an additional constant variance (σ^2_0),

$$\sigma^2_{ijk} = \sigma^2_{ijk,\mathrm{obs}} + \sigma^2_0, \tag{19}$$

σ^2_0 is a systematic noise parameter corresponding to $\mathbf{S}$ in our generic inference problem in Equation 4. σ^2_0 helps take into account under-estimated variance within the continuum subtracted data cube and some systematics that may arise due to limitations in the galaxy model parameterisation. The additional variance term will not account for significant unresolved structures between the data and model. Under those circumstances, the posterior distributions can be systematically biased.

The non-diagonal elements of the covariance cube have not been incorporated. Including the non-diagonal elements of the covariance would require an inversion of the covariance matrix which scales as $O(n^3)$. Data cubes cut around Hα typically have $O(10^3)$ data points, which results in a highly time consuming calculation. As such, we have avoided implementing the covariance matrix in the likelihood function. The likelihood function is then given by,

$$p(D|\mathbf{G},\Sigma,\mathbf{S}) = \prod^{n_i}\prod^{n_j}\prod^{n_k} \frac{1}{\sqrt{2\pi\sigma^2_{ijk}}} \exp\left(-\frac{(M_{ijk}-D_{ijk})^2}{2\sigma^2_{ijk}}\right). \tag{20}$$

where M_{ijk} represents the model convolved by the PSF.

2.5 Posterior sampling

The posterior density function (PDF) is defined by Equation 4, where the joint prior for the galaxy parameterisation is given in Equation 18, the prior for our systematic parameters is defined as $p(\mathbf{S}) = p(\sigma_0)$, and the likelihood function is given in Equation 20. Table 1 also summarises the joint prior distribution and data. The galaxy model is described by 4 global parameters, 5 blob hyperparameters, 5 velocity parameters, 2 velocity dispersion parameters, 1 systematic noise parameter, and 6 blob parameters for N blobs. For typical galaxies 10s–100s of blobs are required to sufficiently model the galaxy assuming our joint prior distribution. As such, the number of parameters required to model the galaxy is typically $O(100)$, making this a high parameter model. It is also required to fit both the number of blobs as well as the parameters for those blobs.

With these requirements in mind, we use DNest4 (Brewer et al. 2011a; Brewer & Foreman-Mackey 2018). DNest4 expands the nested sampling aglorithm (Skilling 2004) by constructing future levels via a multi-level exploration of the posterior density function. The multi-level exploration is performed using an implementation of the Metropolis algorithm in the the Markov-Chain Monte-Carlo (MCMC) class. DNest4 is typically more robust to local maxima as it has the ability to walk up and down nested sampling levels to explore the posterior distribution. Furthermore, as DNest4 is a nested sampling algorithm it can be used to calculate the evidence Z (ie. the normalisation constant for a given model), and subsequently perform model comparison.

DNest4 also has an in-built reversible jump object (Brewer 2014). A reversible jump is a proposal step that allows for a change in components. We use this to propose steps that add or remove blobs such that we can perform posterior sampling for the number of blobs (N). An inference problem with a varying number of components is referred to as transdimensional inference. Such problems are notoriously difficult to explore, but DNest4 has been used to successfully perform inferences on such problems as modelling lensed galaxies with a variable number of blobs (Brewer et al. 2011b, 2016), similar to our approach. Other applications within astronomy have been to estimate the number of stars in a crowded stellar field (Brewer et al. 2013) and modelling star-formation histories (Walmswell et al. 2013).

3 TESTING THE METHOD

The remaining sections of this paper are devoted to demonstrating the methodology on a number of examples. We have tested the method on idealised toy models and real data. In this section, we will describe the applications of our method applied to a set of toy models.

3.1 Simple toy models

The toy models were constructed as a thin disk with an exponential flux profile. The velocity dispersion was set to a constant across the disk. We used an Universal Rotation Curve (URC, Persic et al. 1996) to model the velocity profile.

The URC was chosen as this profile relates the flux profile to the velocity profile via the parameter $v(R_{\mathrm{opt}})$, where R_{opt} is equal to the 83%-light radius. Another consideration in choosing the URC was to avoid using the same velocity profile in our toy models and our method. This way, we could test the ability of our method to infer the underlying kinematics despite having different velocity profile assumptions. The URC is defined as,

$$v(x) = \sqrt{v^2_d(x) + v^2_h(x)}, \tag{21}$$

where $v_d(x)$ and $v_h(x)$ represent the disk and halo velocity component contributions with $x = r/R_{\rm opt}$. The disk and halo components are defined as,

$$v_d^2(x) = v^2(R_{\rm opt})\beta \frac{1.97x^{1.22}}{(x^2 + 0.78^2)^{1.43}} \quad (22)$$

$$v_h^2(x) = v^2(R_{\rm opt})(1-\beta)(1+\alpha^2)\frac{x^2}{x^2+\alpha^2} \quad (23)$$

where the shape parameters are,

$$\alpha = 1.5\left(\frac{L}{L^*}\right)^{1/5} \quad \text{and} \quad \beta = 0.72 + 0.44\log_{10}\left(\frac{L}{L^*}\right). \quad (24)$$

We set $L/L^* = 1$ for all toy models. A systemic velocity term was omitted for simplicity. The galaxies were inclined by 45° such that the LoS velocity was observable.

The spatial edge of the cube was assumed set at 2 R_e. The cubes were oversampled by a factor of 5 elements in the spatial and wavelength directions. Emission lines were broadened by a Gaussian line-spread function (LSF) with $\mathrm{FWHM_{LSF}} = 1.61$ Å similar to the SAMI Galaxy Survey (van de Sande et al. 2017) and convolved by the seeing per wavelength slice. The over-sampled data cube was integrated to the desired resolution. The resulting cubes have a $15'' \times 15''$ FoV with 30×30 elements and a wavelength range of [6554 Å, 6571 Å] with 31 elements. The above choices were aimed at replicating a cube cut around the Hα emission line for a typical galaxy observed with the Sydney Australian-Astronomical-Observatory Multi-object Integral-Field Spectrograph (SAMI) instrument (Croom et al. 2012).

To check for systematics in the kinematic inferences for different methods, we constructed the toy models with negligible noise. A grid of toy models was constructed with $\sigma_{v,\rm input} = \{10, 20, 30, 40, 50\}$ km s^{-1}, $v(R_{\rm opt}) = \{50, 100, 150, 200, 300\}$ km s^{-1}. The toy models were convolved with a Gaussian PSF with $\mathrm{FWHM_{PSF}} = \{1'', 2'', 3''\}$ or a Moffat PSF with $\{\mathrm{FWHM_{PSF}}, \beta_{\rm PSF}\} = \{2'', 3\}$.

3.1.1 *Estimating the velocity dispersion*

In Fig. 3, we show the relative difference between the estimated mean velocity dispersion ($\sigma_{v,\rm out}$) and the input velocity dispersion ($\sigma_{v,\rm input}$). The relative differences are shown compared to $v(R_{\rm opt})\mathrm{FWHM_{PSF}}/\sigma_{v,\rm input}$. This relationship yielded the clearest trend for the relative difference estimates using a single component Gaussian fit per spaxel. The intuitive reasoning for this relationship is that increasing $v(R_{\rm opt})/\sigma_{v,\rm input}$ increases the velocity gradient at the centre of the galaxy with respect to the input velocity dispersion. This exacerbates the effect of beam smearing due to blending velocity profiles that have significantly different mean velocity compared to their width. Similarly, increasing the $\mathrm{FWHM_{PSF}}$ acts to blend velocity gradients across wider regions of the galaxy.

We started by comparing a single component Gaussian fit to each each spaxel, a tilted ring model using ^{3D}Barolo, and our method. For the single-component Gaussian fits, we calculated the mean velocity dispersion of the spaxels across the FoV. The results for ^{3D}Barolo were calculated using the area-weighted mean velocity dispersion across the rings. For our method, we constructed the 2D velocity dispersion map for each posterior sample and then calculated the mean velocity dispersion of the spaxels. All posterior samples are shown on this plot, but due to the negligible noise applied to the toy models the posterior distributions for the mean velocity dispersion are negligible at this scale.

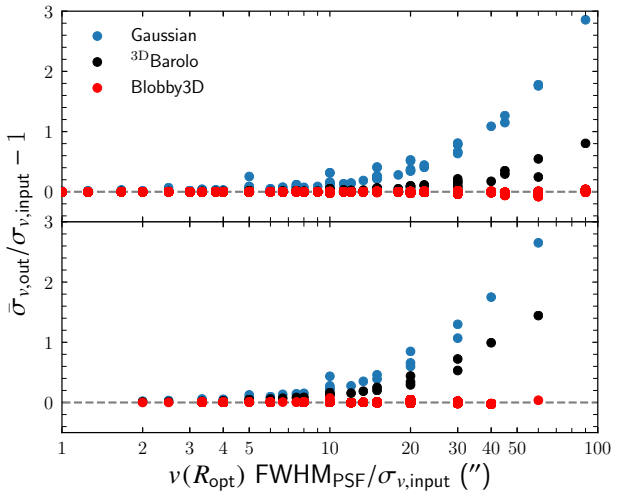

Figure 3. Relative difference between the estimated mean velocity dispersion ($\bar{\sigma}_{v,\rm out}$) and the input velocity dispersion ($\bar{\sigma}_{v,\rm input}$). This is shown as a function of $v(R_{\rm opt})$, the $\mathrm{FWHM_{PSF}}$, and the input velocity dispersion. The methods compared were a single-component Gaussian fit to each spaxel (blue), ^{3D}Barolo (black), and our method (red). The model inputs are a grid of $\sigma_{v,\rm input} = \{10, 20, 30, 40, 50\}$ km s^{-1} and $v(R_{\rm opt}) = \{50, 100, 150, 200, 300\}$ km s^{-1}. The PSF profiles used are a Gaussian (top) with $\mathrm{FWHM_{PSF}} = \{1'', 2'', 3''\}$ and Moffat (bottom) with $\{\mathrm{FWHM_{PSF}}, \beta_{\rm PSF}\} = \{2'', 3\}$. Using the mean velocity dispersion after fitting a single-component Gaussian fit per spaxel, we found that the estimated velocity dispersion increased as a function of $v(R_{\rm opt})\mathrm{FWHM_{PSF}}/\sigma_{v,\rm input}$. ^{3D}Barolo improves the estimates for the intrinsic mean velocity dispersion, yet still results in a trend similar to the estimates using the single-component Gaussian fit per spaxel. Blobby3D reliably infers the mean intrinsic velocity dispersion for our full grid of toy models.

To further illustrate the effect of beam smearing on the observed velocity dispersion, we show radial profiles across a grid of input $\sigma_{v,\rm input}$ and $v(R_{\rm opt})$ assuming a Gaussian convolution kernel with $\mathrm{FWHM_{PSF}} = 2''$ in Fig. 4. This shows that the effect of beam smearing increases significantly in the centre of the galaxy where the velocity gradient is highest. Increasing $v(R_{\rm opt})$ also acts to increase the velocity gradient, and thus the offsets increase as well. The effect of beam smearing decreases as the input velocity dispersion increases, suggesting that the relative relationship between $v(R_{\rm opt})/\sigma_{v,\rm input}$ is more indicative of the effects of beam smearing.

^{3D}Barolo provides partial corrections for beam smearing. However, the relative difference is $\sigma_{v,\rm out}/\sigma_{v,\rm input} - 1 \sim 0.1$ at $v(R_{\rm opt})\mathrm{FWHM_{PSF}}/\sigma_{v,\rm input} = 30''$ and increases with $v(R_{\rm opt})\mathrm{FWHM_{PSF}}/\sigma_{v,\rm input}$. The effect of beam smearing increases towards the centre of the galaxy as well. We suspected that the observed bias was due to ^{3D}Barolo interpreting the unresolved velocity gradient across the discretised rings as increased velocity dispersion. Yet we found no significant difference for the estimated velocity dispersion profile when

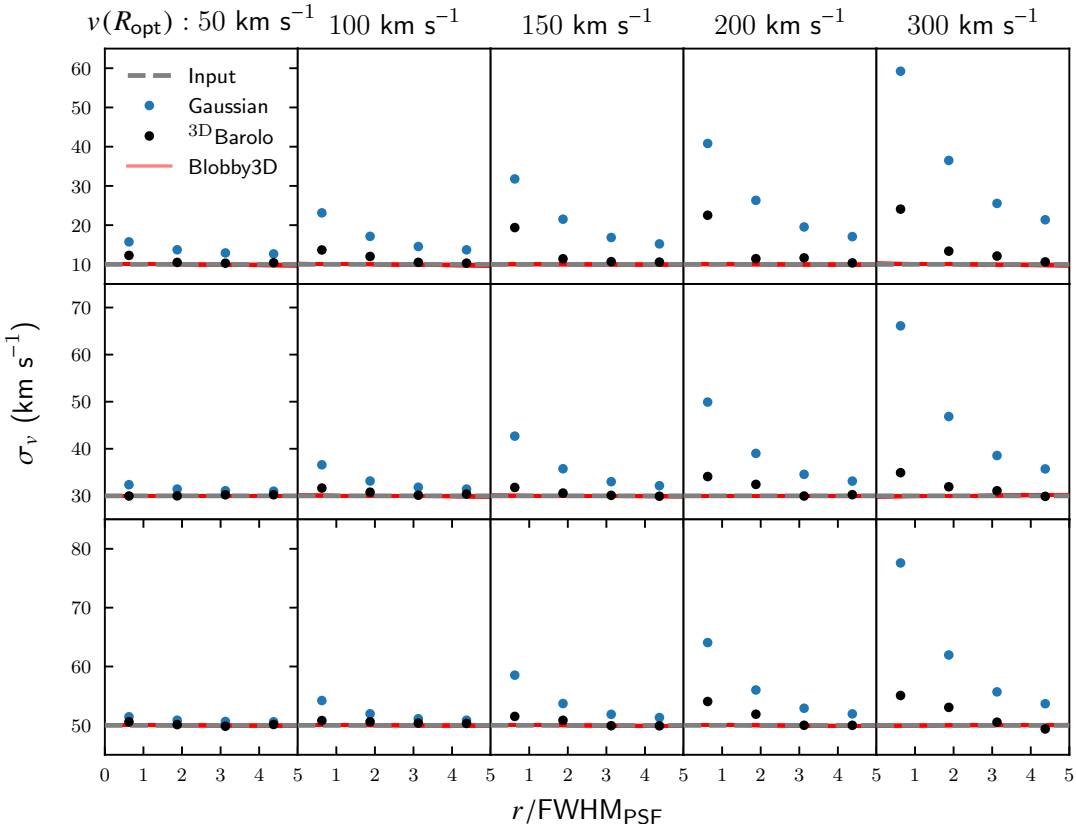

Figure 4. Recovering the LoS intrinsic radial velocity dispersion profiles for our toy models convolved by a Guassian PSF with FWHM$_{PSF}$ = 2″. We show different $v(R_{opt})$ and $\sigma_{v,input}$ per column and row, respectively. Blue points correspond to single component Gaussian fits to each spaxel and then averaged for each radial bin. Black points correspond to the velocity dispersion estimates per ring using the 3DBarolo fitting code, and Blobby3D shows the posterior samples for the radial velocity dispersion profiles. We found that the relative difference between the estimated and actual LoS velocity dispersion increased towards the centre of the centre of the galaxy where the LoS velocity gradient is greatest. Similarly, these effects increased as $v(R_{opt})/\sigma_{v,input}$ increased. The estimates using 3DBarolo improve on the single-component Gaussian fit, while Blobby3D accurately infers the LoS velocity dispersion across the grid of toy models.

using a different number of rings. As such, the observed biases observed for 3DBarolo appears to be fundamental for low resolution data. Di Teodoro & Fraternali (2015) also found that 3DBarolo over-estimated the velocity dispersion at the centre of the galaxy for low-resolution observations (see Fig. 8 in their paper).

3DBarolo is further affected when used for toy models convolved by a Moffat kernel. The divergence in the relative difference is $\sigma_{v,out}/\sigma_{v,input} - 1 \sim 0.1$ at $v(R_{opt})$FWHM$_{PSF}/\sigma_{v,input} = 10''$. In this case, we assumed the Gaussian convolution kernel used by 3DBarolo had a FWHM equal to that of the Moffat profile. As 3DBarolo assumes a Gaussian PSF, we expected that using it for a toy model convolved by a Moffat kernel would affect the estimates. Bouché et al. (2015) also pointed out that significant differences for the velocity dispersion estimates can be caused by not accurately modelling the PSF axis ratio. Similar issues are likely to arise when our PSF modelling assumptions are not met. We suggest that researchers keep in mind that assumptions about the PSF will affect the velocity dispersion estimates.

Our method accurately estimates the intrinsic velocity dispersion, as shown in both the relative differences in Fig. 3 and the radial profiles in Fig. 4. We also show the posterior distribution of the log relative difference $\log(\sigma_{v,0}/\sigma_{v,in})$ and $\sigma_{v,1}$ in Fig. 5. These plots are marginalised over all toy models and the remaining parameters. The marginalised distributions remain consistent with zero for both parameters as $\log(\sigma_{V,0}/\sigma_{v,in}) = 0.3 \pm 1.7 \times 10^{-2}$ and $\sigma_{v,1} = -1 \pm 4 \times 10^{-3}$. There is a slight tendency for higher $\sigma_{v,0}$ with negative gradients, but this was negligible as the difference in velocity dispersion compared to the input values was < 1 km s^{-1} in all cases.

3.1.2 *Estimating the velocity profiles*

We show the inferred velocity profiles for varying $v(R_{opt})$ and FWHM$_{PSF}$ in Fig. 6 and Fig. 7 respectively. We only show the velocity profiles for $\sigma_{v,in} = 20$ km s^{-1} as we did not observe any dependency on the inferred velocity profiles as a function of the input velocity dispersion.

Once again, considering the Gaussian fits as indicative for the effects of beam smearing, we note that the velocity is typically under-estimated in regions of high velocity gradient. This relative effect on the observed velocity compared to $v(R_{opt})$ is approximately constant. Instead, the differences

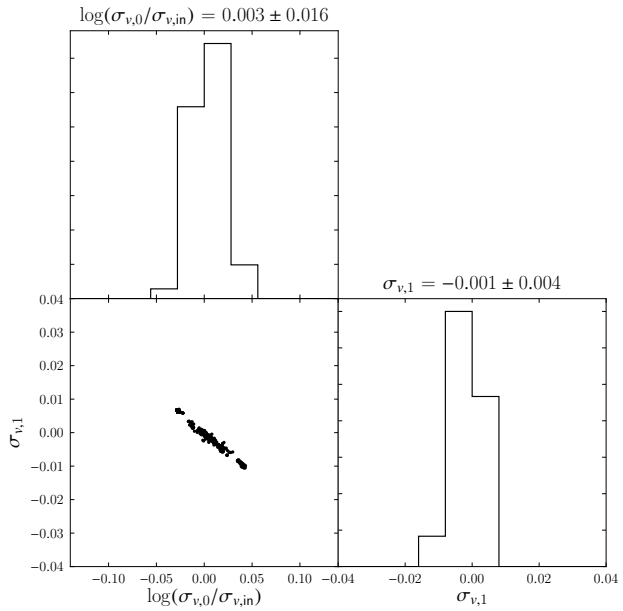

Figure 5. Marginalised posterior distributions for the log relative difference between the modelled central velocity dispersion ($\sigma_{v,0}$) and the input velocity dispersion ($\sigma_{v,\mathrm{true}}$) (top), plus the log velocity dispersion gradient ($\sigma_{v,1}$) (bottom right). We also show the conditional posterior distribution between these parameters (bottom left). We found that the distribution of our inferred intrinsic velocity dispersion parameters was consistent with our inputs.

are greatly affected by increasing the $\mathrm{FWHM_{PSF}}$. These effects are consistent with the modelling performed by Davies et al. (2011).

The effects of beam smearing remain when using ^{3D}BAROLO. We did not find any significant difference for the inferred velocity profiles when we changed the number of rings.

Our method typically estimates the velocity profile well for $v(R_{\mathrm{opt}}) \geq 150$ km s^{-1}. For $v(R_{\mathrm{opt}}) < 150$ km s^{-1}, there are issues estimating the shape of the velocity profile, particularly in the centre of the galaxy and the outskirts. The effects for $v(R_{\mathrm{opt}}) = 100$ km s^{-1} are minimal both in relative and absolute terms. For $v(R_{\mathrm{opt}}) = 50$ km s^{-1} the relative difference is ~ 0.05 corresponding to a few km s^{-1}.

The reasoning for the difference at low $v(R_{\mathrm{opt}})$ remains unclear as better 1D fits for the Courteau (1997) empirical model to the input Universal Rotation Curve are within the prior distribution. We suspect that the differences are driven by performing the full 3D modelling where the differences in model parameterisation and integration are slightly different for the toy modelling compared to the BLOBBY3D approach. However, given the negligible difference compared to systematic and variance that will be involved in modelling real data, we do not consider this to be a significant issue.

3.2 A toy model with gas substructure

We then constructed a more realistic toy model. First, we constructed a toy model as defined above with $\sigma_v = 20$ km s^{-1} and $v_c = 200$ km s^{-1}. We rotated the position angle of the disk by $\pi/4$ and added 10 Gaussian blobs to the gas distribution. All blobs were defined to be circular in the plane of the disk. The integrated flux for each blob was set to 10% of the disk flux. The width for each blob was set to $w = 0.2R_e$. The centre of the blobs were randomised uniformly with distance to the centre as $r/R_e = [0, 2]$ in the plane of the disk. We distributed the polar angle uniformly in the range $\phi_c = [0, \pi]$. We add independent and identically distributed (iid) Gaussian noise corresponding to mean S/N = 20 per wavelength bin. The cube was oversampled then convolved as per all of our previous toy models.

The distribution of ϕ in the range $[0, \pi]$ introduces an asymmetry in the flux profile as blobs are only placed on one side of the disk. We do this to show that our method is capable of recovering asymmetric gas distributions. We also note that such substructures are common in real observations.

We show the toy model and our results in Fig. 8. An interesting consequence of introducing asymmetries in the flux profile is that convolving the model by the PSF introduces asymmetries in the velocity dispersion profile. In this case, the 2D velocity dispersion map for the convolved data shows two tails on the side where the blobs are located.

Modelling to the convolved data is performed well with no outlying structure remaining in the residual maps. Recovery of the preconvolved model is also performed reasonably well. The maximum relative difference in the map is ~ 0.1 whereas the velocity profile is within several km s^{-1} and the maximum difference in velocity dispersion is less than 1 km s^{-1}. While this posterior sample shows a very shallow positive velocity dispersion gradient (< 1 km s^{-1} difference across the FoV), there is no observed bias in the gradients in the full marginalised posterior distribution with $\sigma_{v,0} = 0.03 \pm 0.11$.

4 APPLICATIONS TO REAL DATA

We then applied the method to a sample of 20 galaxies from the SAMI Galaxy Survey. The SAMI Galaxy Survey uses SAMI (Croom et al. 2012). SAMI uses 13 fibre bundles known as hexabundles which consist of 61 fibres with 75% filling factor that subtend 1.6″ for a total FoV with width 15″ (Bland-Hawthorn et al. 2011; Bryant et al. 2014). The IFUs, as well as 26 sky fibres, are plugged into pre-drilled plates using magnetic connectors. SAMI fibres are fed to the double-beam AAOmega spectrograph (Sharp et al. 2006). The SAMI Galaxy survey uses the 570V grating at 3700-5700 Å giving a resolution of $R \sim 1730$, and the R1000 grating from 6250-7350 Å giving a resolution of $R \sim 4500$.

4.1 Sample selection

The SAMI Galaxy Survey has observed $> 3{,}000$ galaxies. We aim to present initial results for a small sample of galaxies that are representative of typical star-forming galaxies within the parent sample. Star-forming galaxies were chosen as their gas kinematics typically have smoothly varying kinematic profiles. This is in contrast to galaxies with Hα emission associated non-starforming mechanisms. A common example are galaxies with Active Galactic Nuclei (AGN), as they typically have significantly higher velocity dispersion in the centre of the galaxy compared to the outskirts.

Star-forming galaxies were selected by applying a cutoff

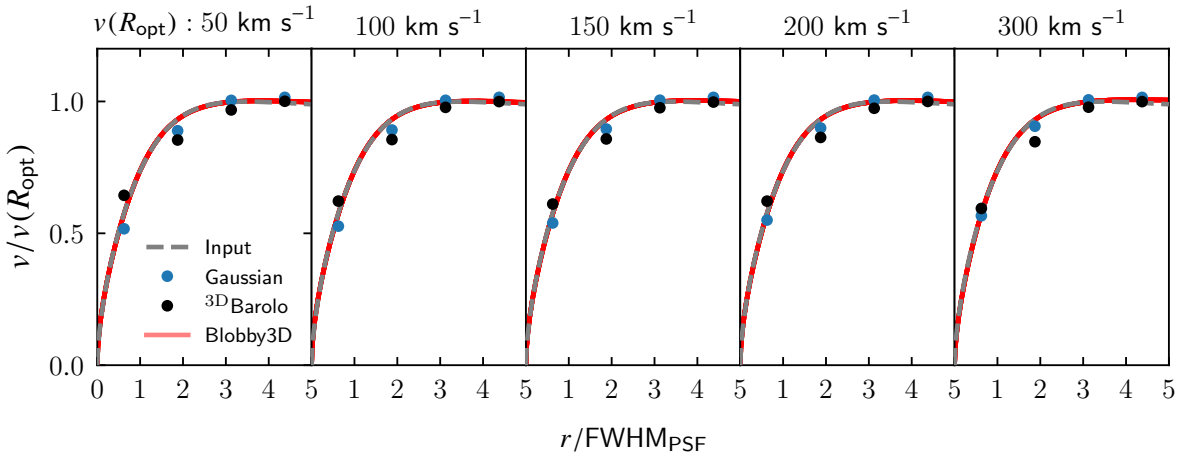

Figure 6. Recovering the velocity profile for our toy models with exponential flux distribution, universal rotation curve with different $v(R_{opt})$, and σ_v = 20 km s^{-1}. The toy models were convolved with a Gaussian profile with FWHM$_{PSF}$ = 2″. The toy models were constructed with negligible noise to check for systematic biases in the methodologies. Blue dots correspond to a single component Gaussian fit to each spaxel where the mean has been calculated for 4 equally space bins. ^{3D}Barolo (black) show the radial velocity in each radial bin. Blobby3D (red) shows 12 posterior samples for the velocity profile, although the difference for each posterior sample is negligible due to zero noise applied to the toy models. ^{3D}Barolo does not fully recover the velocity profile at $v(R_{opt})$ = 50 km s^{-1}.

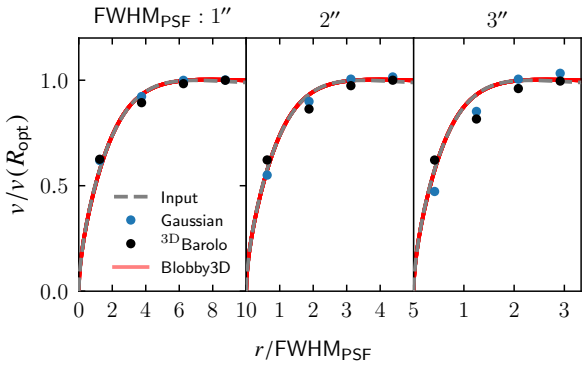

Figure 7. Similar to Fig. 6 but setting $v(R_{opt})$ = 200 km s^{-1} and varying the FWHM$_{PSF}$. In this case, we found that the inferred LoS velocity gradient is flattened for both the single component Gaussian fits to each spaxel and ^{3D}Barolo as FWHM$_{PSF}$ increases. Blobby3D is not affected by increasing the FWHM$_{PSF}$.

integrated Hα equivalent width > 3 Å. The equivalent width cutoff is consistent with the star-forming main sequence cutoff applied by Cid Fernandes et al. (2011) using single-fibre SDSS data. The equivalent width was measured as the width in the spectral dimension of a rectangle with width and height equal to a measure of the integrated continuum and Hα flux, respectively. We used the mean continuum across the wavelength range [6500 Å, 6540 Å] as the estimate for the continuum per spaxel.

We removed galaxies with Hα emission contaminated by AGN or LINERs using the AGN classification proposed by Kauffmann et al. (2003). Under this classifcation, we removed galaxies under the condition that,

$$\log([\mathrm{OIII}]/\mathrm{H}\beta) > 0.61/(\log([\mathrm{NII}]/\mathrm{H}\alpha) - 0.05) + 1.3, \quad (25)$$

where [OIII] and [NII] represent the emission lines at 5007 Å and 6583 Å, respectively. For each emission line, we used the integrated flux estimates in the 1.4″ aperture spectra data provided in the SAMI Galaxy Survey DR2 (Scott et al. 2018). The 1.4″ aperture spectra data are the innermost aperture spectra data provided in SAMI Galaxy Survey DR2, and thus should be the most appropriate to find galaxies with AGN or LINER emission which is typically centrally concentrated.

We selected galaxies with an intermediate inclination angle ($i \in [30°, 60°]$). Galaxies with low inclination were avoided as it is difficult to infer the velocity profile. Whereas galaxies close to edge-on will be difficult to model as our method assumes a thin-disk. Furthermore, galaxies observed close to edge-on are typically optically thick, such that the entire disk cannot be observed. The inclination estimates were calculated by converting an estimate for the observed ellipticity assuming a thin-disk. Similarly, we selected galaxies with intermediate effective radius ($R_e \in [2.5'', 22.5'']$). This avoids small galaxies that are not well resolved. It also ignores large galaxies which may be difficult to infer their velocity profile. Estimates for the ellipticity and effective radius were taken from the SAMI Galaxy Survey parent catalogue (Bryant et al. 2015), who in turn used the single Sérsic fits to the r-band Sloan Digital Sky Survey images by Kelvin et al. (2012).

There are 330 galaxies that meet the above criteria in the SAMI Galaxy Survey DR2. We chose 20 galaxies with our final galaxy sample shown in Table 2.

4.2 Data cubes

The data cubes we used were from the SAMI internal data release v0.10.1 (Scott et al. 2018). Data cubes were redshift corrected by the spectroscopic redshift which was taken from the SAMI parent catalogue (Bryant et al. 2015) who used the estimates from the Galaxy and Mass Assembly (GAMA) survey (Driver et al. 2011).

The data cubes were then cut around the Hα emission line by ±500 km s^{-1}. In our sample, this was wide enough to

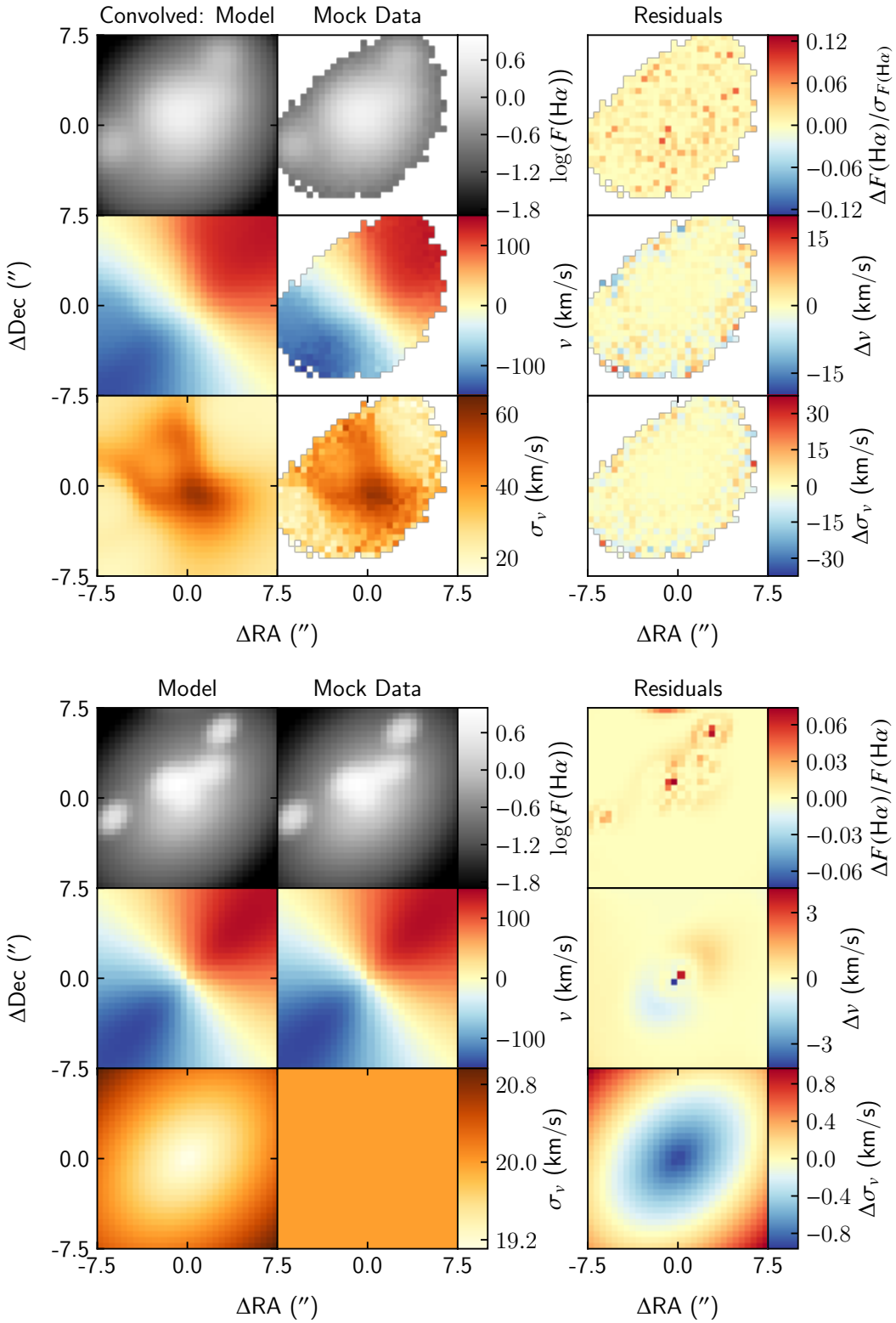

Figure 8. 2D maps for a posterior sample for a toy model with asymmetric gas substructure. For the top three rows, we show the convolved model compared to the convolved mock data (ie. toy model). The preconvolved BLOBBY3D model and preconvolved mock data are compared in the bottom three rows. In both cases the rows show the Hα flux, LoS velocity profile, and LoS velocity dispersion. The columns show the respective BLOBBY3D output, data, and residuals. The absolute residuals are shown for the velocity and velocity dispersion maps. In the top panel we show the flux map residuals normalised with respect to the modelled Gaussian noise, whereas in the bottom panel we show the relative flux difference. The convolved mock data is shown where Hα flux S/N > 10. We found that convolving a model with gas substructure and radial kinematic profiles introduced kinematic asymmetries. BLOBBY3D was able to model the gas and kinematic profile asymmetries and recover the intrinsic gas kinematics accurately.

Table 2. Summary statistics for our sample of galaxies from the SAMI galaxy survey. All values are sourced from the SAMI parent catalogue described by Bryant et al. (2015). We also show the estimated SAMI Galaxy Survey pipeline estimated values for the PSF assuming a Moffat profile.

GAMA ID	RA (°)	Dec (°)	$z_{\rm spec}$	$\log(M_*/M_\odot)$	R_e ($''$)	e	FWHM$_{\rm PSF}$ ($''$)	$\beta_{\rm PSF}$
214245	129.52446	0.60896	0.014	9.40	4.46	0.32	2.12	3.65
220371	181.23715	1.50824	0.020	9.53	6.97	0.35	3.37	6.78
220578	182.17817	1.45636	0.019	8.98	2.96	0.41	2.34	2.71
238395	214.24319	1.64043	0.025	9.87	4.11	0.18	3.29	4.76
273951	185.93037	1.31109	0.026	8.72	4.34	0.45	1.62	2.77
278804	133.85939	0.85818	0.042	9.82	2.65	0.38	2.87	4.03
298114	218.40091	1.30590	0.056	10.25	4.84	0.41	2.26	4.01
30346	174.63865	-1.18449	0.021	10.45	11.25	0.32	1.89	2.48
30377	174.82286	-1.07931	0.027	8.22	3.81	0.35	3.30	3.81
30890	177.25796	-1.10260	0.020	9.79	7.56	0.43	2.92	3.94
422366	130.59560	2.49733	0.029	9.62	8.86	0.49	1.78	2.49
485885	217.75790	-1.71721	0.055	10.25	5.04	0.16	2.27	5.19
517167	131.16137	2.41098	0.030	9.24	3.67	0.31	2.01	2.81
55367	181.79334	-0.25959	0.022	8.40	6.71	0.30	1.56	3.64
56183	184.85245	-0.29410	0.039	9.50	3.58	0.23	2.18	3.19
592999	215.06156	-0.07938	0.053	10.26	4.24	0.47	1.53	2.98
617655	212.63506	0.22418	0.029	9.07	5.08	0.14	2.85	8.67
69620	175.72473	0.16189	0.018	9.30	4.45	0.25	2.53	4.49
84107	175.99843	0.42801	0.029	9.71	5.05	0.23	2.53	4.49
85423	182.27832	0.47328	0.020	8.63	3.56	0.18	2.90	3.55

observe the full Hα emission line while avoiding significant influence from the adjacent [NII] emission lines.

The continuum model used to subtract from the data cubes were the single-component LZIFU (Ho et al. 2016) data products from the SAMI Galaxy Survey internal data release v0.10.1. LZIFU uses the penalised pixel-fitting routine (pPXF, Cappellari & Emsellem 2004) to model the continuum using a combination of spectral stellar population templates.

Poor continuum modelling can cause systematics in the data cube that are not well represented in the galaxy model parameterisation. While we could extend the systematic parameterisation to account for systematics introduced by poor continuum modelling, such corrections would likely require a large number of nuisance parameters that would be difficult to marginalise over. Instead, we masked pixels with Hα flux signal-to-noise < 3 and performed a secondary fit to the data using a Gaussian plus linear continuum estimate to the region cut around the Hα line. The continuum estimated from this fit was then subtracted from the data.

4.3 Results

For completeness, we show our estimates of the marginalised distributions for all parameters, omitting individual blob parameters, in Tables 3 and 4. We also show 2D maps of an example posterior sample for GAMA 485885 and 220371 in Fig. 9. A galaxy with asymmetric substructure observed in the gas kinematics is shown in 10. These example posterior samples show the ability of our method to fit complex substructure. Note that the exact shape of each blob does change per posterior sample, so these should only be considered for illustrative purposes.

For GAMA 485885, we see the ability of our approach to resolve a classic spiral gas distribution. The 2D residuals between the convolved model and data exhibit significant differences on scales less than the FWHM$_{\rm PSF}$. The 2D maps for the LoS gas kinematics suggest that the gas is approximately regularly rotating around a kinematic centre, potentially with a small warp in the kinematic position angle. The Hα gas velocity dispersion is peaked within the centre of the galaxy as expected for most regularly rotating galaxies that have been affected by beam smearing.

We show 2D maps for GAMA 220371 in Fig. 9. This galaxy has a clumpy Hα gas profile. We are still able to construct an adequate model to the data using our approach. The 2D residual maps for the Hα flux show greater differences for three clumps in the North-East, South-East, and South-West regions. However, the general structure of the clumps is reasonably well resolved. The maps for the gas kinematics suggest an approximately regularly rotating galaxy. The velocity dispersion map does not show a significant peak in the centre of the galaxy compared to GAMA 485885. This is likely driven by having a shallower LoS velocity gradient and less centralised Hα gas flux compared to GAMA 485885.

An example posterior sample for GAMA 30890 is shown in Fig. 10. This galaxy exhibits asymmetries and substructure in the LoS Hα gas kinematic maps. We are able to partially recover the Hα gas kinematics despite only introducing asymmetries in the gas Hα gas distribution. Some substructure in the residuals remain with a patch of Hα gas flux that is lower in the convolved model compared to data. There is also a slight warp in the LoS velocity profile as a function of radius, and differences in the velocity dispersion on the order of 5 km s^{-1}. However, the convolved model still performs reasonably well at resolving the gas flux and kinematics. Our ability to partially resolve the gas kinematic asymmetries, suggests that the Hα gas distribution plus beam smearing can result in gas substructures that are not necessarily present in the underlying data. This is similar to the results we saw in Fig. 8, where we showed that introducing asymmetric substructure in the gas distribution for a regularly rotating

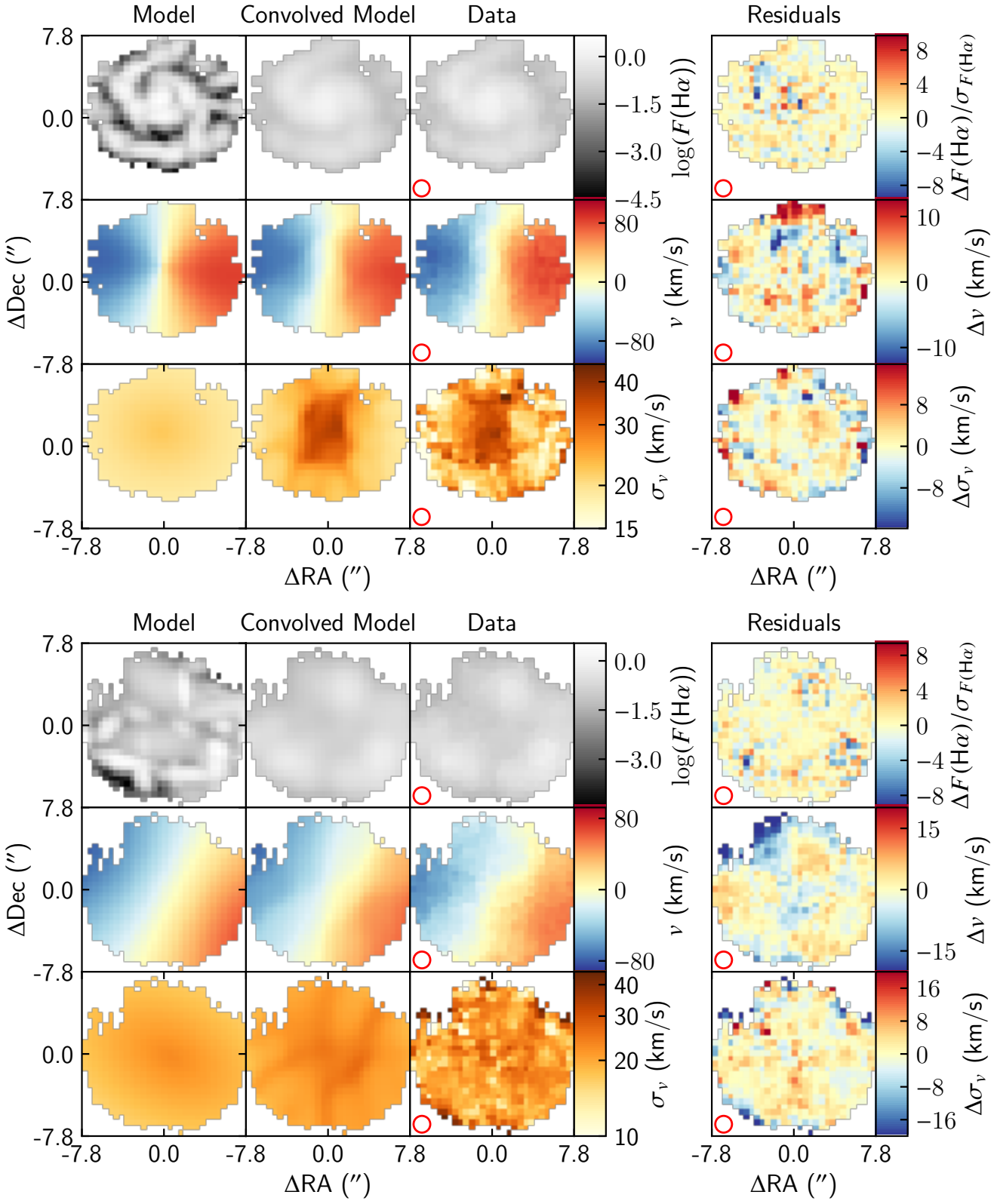

Figure 9. 2D maps for a single posterior sample for GAMA 485885 (top) and 220371 (bottom). For each galaxy we show from left to right the model, convolved model, single-component Gaussian fits to the data, and 2D residuals where $\Delta F(\mathrm{H}\alpha) = F(\mathrm{H}\alpha, \text{Convolved Model}) - F(\mathrm{H}\alpha, \text{Data})$. The flux map residuals have been normalised with respect to the modelled Gaussian noise, whereas the absolute difference is shown for the velocity and velocity dispersion maps. Red circles with $r = \mathrm{FWHM_{PSF}}$ indicate the seeing width. The rows show the Hα flux, LoS velocity profile, and LoS velocity dispersion. Spaxels are shown where the data Hα flux S/N > 10. These examples show the ability of BLOBBY3D to model galaxies with spirals and clumpy profiles. Parameterising complex gas distributions such as observed in the these galaxies is typically difficult, but they are a natural output of our approach.

Table 3. Inferences for global parameters and blob hyperparameters for our sample of galaxies from the SAMI Galaxy Survey. We show the mean and standard deviation for the marginalised distribution for each parameter. Note that flux units are 10^{-16} erg s^{-1} cm^{-2}.

GAMA ID	N	PA (°)	μ_r (″)	μ_F	σ_F	$W_{\rm max}$ (″)	$q_{\rm min}$	$\log(\sigma_0)$
214245	79±17	304.4±0.2	24±5	2.5±0.6	1.2±0.3	1.05±0.07	0.206±0.007	-3.43±0.04
220371	117±20	332.05±0.09	25±4	4.2±1.0	1.3±0.2	1.81±0.06	0.25±0.02	-3.09±0.01
220578	20±7	22.2±0.1	13±7	46±7	0.4±0.2	0.504±0.004	0.29±0.04	-2.445±0.004
238395	173±45	163.11±0.07	21±6	20±11	1.9±0.4	0.5009±0.0008	0.36±0.02	-1.569±0.002
273951	15±4	30.2±0.7	5±3	28±14	1.8±0.4	0.5005±0.0005	0.22±0.02	-1.508±0.003
278804	18±3	209±1	1.9±0.7	4±1	1.0±0.2	0.51±0.02	0.28±0.07	-2.07367±0.00003
298114	112±25	272.80±0.03	21±6	15.4±0.7	0.32±0.05	1.92±0.04	0.203±0.004	-2.461±0.005
30346	70±9	304.32±0.02	26±5	72±5	0.46±0.08	2.31±0.04	0.23±0.01	-2.009±0.003
30377	79±23	173±1	21±6	1.1±0.4	1.0±0.3	0.51±0.01	0.7±0.2	-8±2
30890	100±17	19.35±0.03	22±5	23±2	0.71±0.08	2.31±0.05	0.24±0.01	-2.587±0.003
422366	159±29	258.37±0.10	26±3	5±1	0.9±0.2	0.6±0.1	0.23±0.03	-2.2229±0.0002
485885	130±33	353.0±0.1	19±6	2.8±0.4	0.79±0.09	0.5007±0.0008	0.202±0.002	-3.38±0.03
517167	59±16	359.58±0.10	21±6	7±3	1.5±0.3	1.2±0.1	0.203±0.004	-2.634±0.004
55367	177±46	182.8±0.1	24±4	0.5±0.2	1.5±0.2	0.79±0.04	0.202±0.002	-8±2
56183	115±34	264.27±0.07	15±7	1.9±0.7	1.9±0.3	1.18±0.03	0.42±0.03	-2.760±0.004
592999	98±22	223.90±0.05	20±6	7±1	1.0±0.1	2.24±0.05	0.207±0.005	-2.362±0.003
617655	117±26	316.5±0.1	23±5	1.9±0.4	1.0±0.1	1.29±0.04	0.42±0.02	-8±2
69620	152±25	300.20±0.07	23±4	17±2	0.65±0.06	0.5002±0.0002	0.28±0.03	-2.072±0.002
84107	110±23	274.66±0.04	23±5	19±4	1.2±0.2	0.5001±0.0001	0.544±0.010	-1.775±0.002
85423	87±24	251.2±0.3	23±5	1.1±0.7	1.6±0.4	1.09±0.05	0.48±0.06	-8±2

Table 4. Inferences for galaxy kinematic parameters for our sample of galaxies from the SAMI Galaxy Survey. We show the mean and standard deviation for the marginalised distribution for each parameter.

GAMA ID	$v_{\rm sys}$ (km s^{-1})	v_c (km s^{-1})	r_t (″)	γ_v	β_v	$\sigma_{v,0}$ (km s^{-1})	$\sigma_{v,1}$
214245	-11.5±0.1	71±1	3.69±0.04	81±12	-0.36±0.03	25.7±0.6	-0.087±0.005
220371	-5.03±0.08	178±5	8.0±0.3	1.43±0.08	-0.24±0.03	23.0±0.5	-0.031±0.003
220578	-15.6±0.3	72±1	6.2±0.1	58±22	0.71±0.01	20.6±0.5	-0.104±0.009
238395	-3.58±0.08	147±3	2.5±0.4	1.03±0.03	0.31±0.05	27.3±0.2	0.023±0.002
273951	5.95±0.08	242±81	15±3	17±24	-0.71±0.04	33.0±0.9	-0.17±0.03
278804	-16.4±0.8	140±2	6.5±0.2	3.8±0.5	0.662±0.008	26±2	-0.21±0.05
298114	5.19±0.07	180.6±0.4	2.051±0.009	93±8	-0.149±0.006	21.4±0.3	0.001±0.002
30346	2.09±0.08	183.7±0.2	0.684±0.009	94±6	-0.08±0.02	12.3±0.3	0.051±0.003
30377	5.4±0.3	274±55	13±2	21±24	-0.70±0.04	18.1±0.5	0.023±0.006
30890	-7.64±0.05	134.0±0.4	1.20±0.07	1.24±0.02	-0.47±0.06	23.7±0.1	0.001±0.001
422366	-12.8±0.3	78±1	5.53±0.07	17±8	0.52±0.02	18.3±0.4	0.018±0.003
485885	-5.6±0.1	129±6	4.3±0.1	2.8±0.4	0.67±0.03	21.8±0.3	-0.017±0.003
517167	-9.80±0.10	73.5±0.5	4.38±0.02	92±8	0.593±0.009	13.8±0.2	0.075±0.004
55367	-10.2±0.1	70±5	27±2	32±26	0.40±0.02	14.9±0.7	-0.15±0.01
56183	-6.99±0.09	111±2	4.8±0.3	1.21±0.03	0.58±0.01	31.6±0.2	-0.076±0.002
592999	-17.00±0.10	185±3	7.5±0.1	1.85±0.06	0.601±0.009	33.8±0.5	-0.061±0.003
617655	8.07±0.09	86±3	3.9±0.1	10±3	0.26±0.06	14.0±0.4	0.039±0.006
69620	3.86±0.08	106±3	19.5±0.9	2.7±0.2	0.590±0.008	20.6±0.1	0.021±0.001
84107	7.25±0.06	99.5±0.6	3.62±0.01	96±4	0.34±0.01	25.1±0.3	0.017±0.003
85423	94±2	177±5	5.33±0.09	32±22	-0.68±0.03	19±1	-0.07±0.02

toy model plus beam smearing led to substructure in the gas kinematics.

The SAMI Galaxy Survey provides gas kinematic data products estimated using the LZIFU package (Ho et al. 2016). LZIFU performs single and multiple Gaussian component fits to the emission lines. Corrections for instrumental broadening are performed by subtracting the LSF from the velocity dispersion in quadrature. Effects of beam smearing are not considered.

A comparison between inferences for the global velocity dispersion between the single component LZIFU data products and our method are shown in Fig. 11. We compare the uniformly weighted ($\bar{\sigma}_v$) and Hα flux-weighted ($\bar{\sigma}_{v,{\rm H}\alpha}$) mean velocity dispersion across the FoV. We calculate both $\bar{\sigma}_v$ and $\bar{\sigma}_{v,{\rm H}\alpha}$ as these methods can find different velocity dispersions, with $\bar{\sigma}_{v,{\rm H}\alpha}$ typically resulting in higher velocity dispersions than $\bar{\sigma}_v$ (Davies et al. 2011). We only consider spaxels with Hα signal-to-noise > 10 as estimated by LZIFU. This was primarily due to the increased scatter in the LZIFU estimates for the Hα gas velocity dispersion in the low signal-to-noise regions.

Estimates of the global velocity dispersion using our method are in the range ~[7, 30] km s^{-1} using both the unweighted and Hα flux-weighted mean. This is in comparison to estimates using the single component LZIFU data products of ~ [10, 45] km s^{-1}.

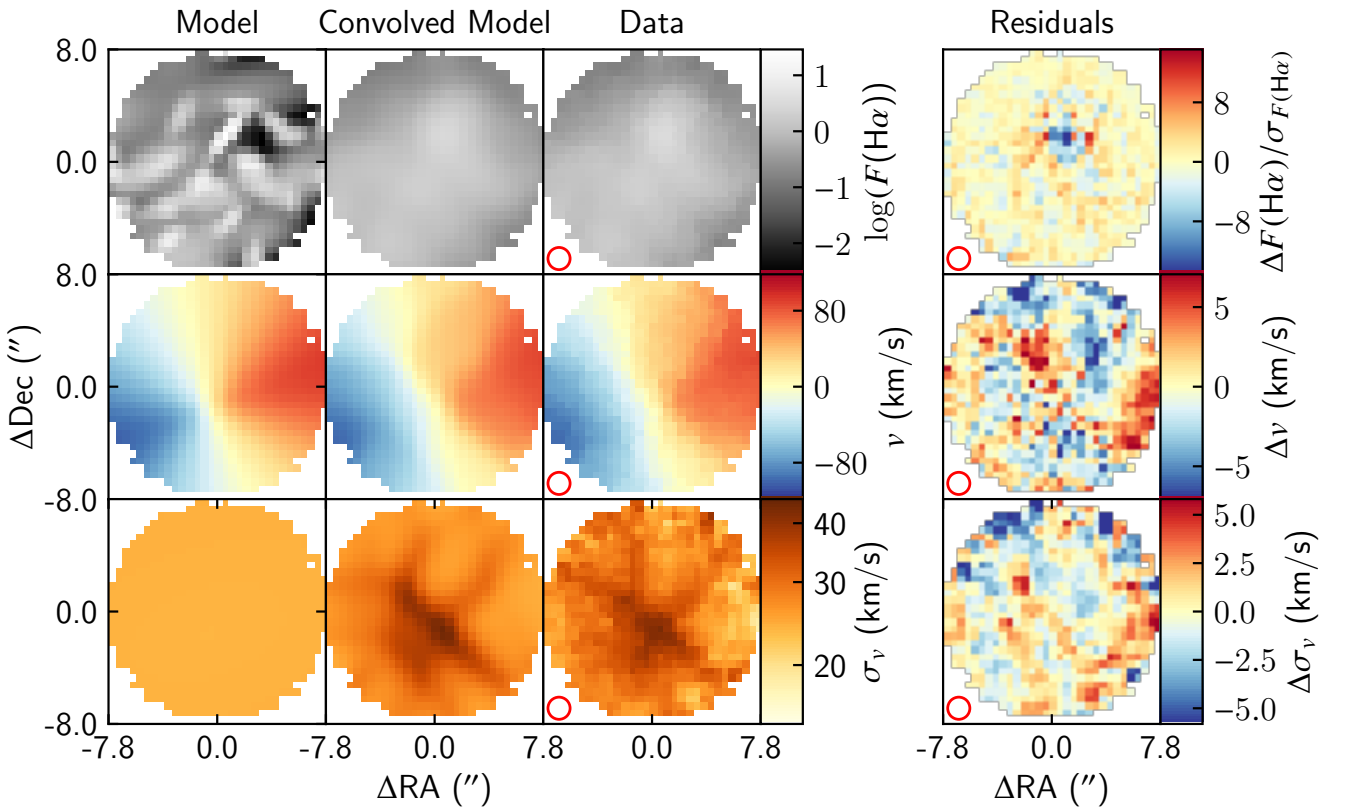

Figure 10. Same as Fig. 9 for GAMA 30890. This galaxy exhibits asymmetric substructure in the Hα gas kinematic maps. BLOBBY3D partially recovers the kinematic asymmetries despite only introducing asymmetric substructure in the Hα gas distribution. This is similar to the asymmetries modelled for our toy model with gas substructure in Fig. 8. This suggests that beam smearing can play a role in the observed substructure for the Hα gas kinematics.

The mean relative corrections per galaxy ($\Delta\bar{\sigma}_v/\bar{\sigma}_V$) from our method is -0.33 ± 0.19 and -0.29 ± 0.18 when comparing $\bar{\sigma}_v$ and $\bar{\sigma}_{v,\mathrm{H}\alpha}$, respectively. Absolute corrections for the Hα flux-weighted mean velocity dispersion were -9^{+7}_{-13} km s^{-1}.

In Fig. 11, the data are colour-coded by $\mathrm{FWHM_{PSF}}$ (left) and v_c (right). Qualitatively, we do not find significant trends for our corrections as a function of either of these parameters. We did expect to see a relationship between these parameters and our velocity dispersion corrections as that would be consistent with our toy model results. A larger sample of galaxies is probably required to find clear relationships between these variables and our corrections.

5 DISCUSSION

5.1 Estimating global velocity dispersion

Beam smearing is well-known to researchers that study spatially resolved spectroscopy. As such, there have been a number of approaches to correct for beam smearing in the literature. Most of this focus has been on correcting for the global velocity dispersion.

5.1.1 Heuristic Approaches

A number of heuristic approaches have been developed in an effort to estimate the intrinsic global velocity dispersion. A popular approach is to calculate an estimator of the velocity dispersion in regions away from the centre of the galaxy where beam smearing is expected to be negligible (eg. Johnson et al. 2018).

Another approach is to perform corrections for a global velocity dispersion estimator as a function of factors that drive beam smearing. For example, Johnson et al. (2018) derived corrections for the median velocity dispersion and the velocity dispersion in the outskirts of the galaxy as a function of the rotational velocity and the PSF width compared to the disk width. The functional form was estimated using a grid of toy models. Using this method, they estimated relative corrections for the median velocity dispersion as $\Delta\bar{\sigma}_v/\bar{\sigma}_v = 0.2^{+0.3}_{-0.1}$ for a sample of star-forming galaxies at $z \sim 1$ using data from the KMOS Redshift One Spectroscopic Survey (KROSS). Their relative corrections for the velocity dispersion are similar to those found in this paper. However, the median seeing for KROSS was 0.7″ corresponding to 5.4 kpc at the median redshift of their sample. In comparison, the mean seeing for the SAMI Galaxy Survey is 2.06″ (Scott et al. 2018), corresponding to 1.75 kpc at the mean redshift of $z = 0.043$ of the full SAMI Galaxy Survey sample. As such, the effect due to beam smearing on the observed velocity dispersion are expected to be greater for KROSS.

Johnson et al. (2018) also studied a sample of star-forming galaxies from the SAMI Galaxy Survey. They estimated global velocity dispersions for individual galaxies in

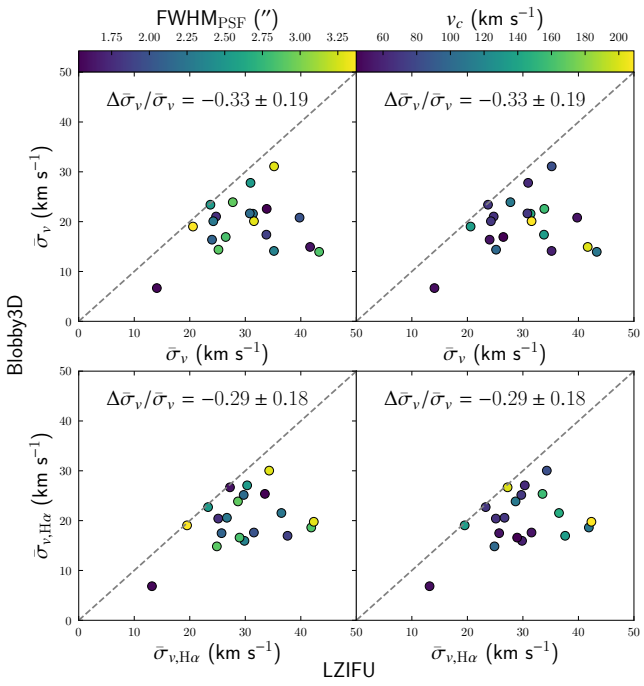

Figure 11. Comparing estimates for the mean velocity dispersion using maps from the LZIFU data products and 2D maps of our method. The comparisons calculated for the unweighted (top) and Hα flux-weighted (bottom) mean of the 2D velocity dispersion maps. $\Delta\bar{\sigma}_v/\bar{\sigma}_v$ is the arithmetic mean relative correction. We found that Blobby3D made significant corrections to the velocity dispersion estimates inferred by LZIFU.

the range $\sigma_v \sim [20, 60]$ km s^{-1} with one galaxy scattering as high as ~ 90 km s^{-1}. We find no examples of galaxies with $\sigma_v \gtrsim 30$ km s^{-1}. However, given that we have only studied a small sample of galaxies from the SAMI Galaxy Survey, we cannot definitively rule out such high global velocity dispersions.

Global velocity dispersions as high as 60 km s^{-1} may suggest that they have not fully accounted for beam smearing across all of the galaxies within their sample of galaxies from the SAMI Galaxy Survey. However, given that we have only studied a small sample of galaxies from the SAMI Galaxy Survey, we cannot definitively rule out such high global velocity dispersions.

Another approach to correct for the effects of beam smearing on the observed velocity dispersion is to perform corrections based on the local velocity gradient ($v_{\rm grad}$). Varidel et al. (2016) proposed calculating the local velocity gradient using a finite-difference scheme and then performed a regression analysis to estimate the observed velocity dispersion when the local velocity gradient is zero. Zhou et al. (2017) and Federrath et al. (2017b) have also used the finite-difference scheme method to remove spaxels where the velocity gradient is much greater than the observed velocity dispersion. We note that Zhou et al. (2017) used this approach to estimate the global Hα gas velocity dispersion in the range $\sigma_v \sim [20, 30]$ km s^{-1} with an outlier (GAMA 508421) estimated to be $\sigma_v = 87 \pm 44$ km s^{-1}. We note that GAMA 508421 has observed velocity dispersion of ~ 100 km s^{-1} in the galaxy centre that that has not been removed. It's possible that this peak is associated with beam smearing. Similarly, Oliva-Altamirano et al. (2018) subtract a disc-fitted local velocity gradient from the observed velocity dispersion in quadrature.

We reproduce these methods on our toy models. First, we revisit the finite-difference scheme and note that the magnitude of the local 1D gradient for a non-boundary spaxel is,

$$\left|\frac{\partial v}{\partial y}\right|_{y_i} \approx \left|\frac{v_{i+1} - v_{i-1}}{2\Delta y}\right|, \tag{26}$$

where i is the index and Δy is the width of the spaxel in the y-direction. The boundary pixels are estimated using the boundary pixel and the adjacent pixel. For a left-sided boundary, the estimated velocity gradient is then,

$$\left|\frac{\partial v}{\partial y}\right|_{y_0} \approx \left|\frac{v_1 - v_0}{\Delta y}\right|. \tag{27}$$

The total absolute magnitude of the velocity gradient is calculated by adding the orthogonal gradients in quadrature,

$$v_{\rm grad}(i,j) = \sqrt{\left|\frac{\partial v}{\partial x}\right|^2_{(i,j)} + \left|\frac{\partial v}{\partial y}\right|^2_{(i,j)}}. \tag{28}$$

This expands the previous method to include estimates for the boundary pixels. We also note that within the central pixels the division by $2\Delta y$ was omitted previously by Varidel et al. (2016). Strictly speaking, this is incorrect as the gradient will be over-estimated by a factor of 2. Note that the velocity gradient is in units km s^{-1} arcsec^{-1}. To make appropriate comparisons between σ_v and $v_{\rm grad}$, we must convert these to the same units. The most natural scale parameter is the width of the PSF, we choose the FWHM$_{\rm PSF}$ and multiply it by $v_{\rm grad}$.

We then repeat the analyses performed previously with the above alterations. We show our results in Fig 12, including comparison to a single-component Gaussian model per spaxel and our methodology. These methods provide significant corrections from the naive single-component Gaussian fits. However, our method still outperforms these methodologies across our set of toy models, as the heuristic methods can differ by up to ~20%.

Over-estimates in regions where beam smearing is high occur for estimates of the mean velocity dispersion where $\sigma_v \gg v_{\rm grad}$FWHM$_{\rm PSF}$. Increasing the cutoff did not result in significantly different estimates of the mean velocity dispersion. Over-estimation is unsurprising as the effect of beam smearing on the observed velocity dispersion occur for several factors of the FWHM$_{\rm PSF}$ where the observed velocity gradient is negligible as seen in Fig. 4.

For the parametric regression estimates we fit a cubic to σ_v vs. $v_{\rm grad}$ and then estimated the line at $v_{\rm grad} = 0$ km s^{-1} arcsec^{-1}. We fit a cubic instead of a first-order line in contrast to Varidel et al. (2016) as there were clear residuals observed by-eye in the linear and quadratic fits to the data. This method suffered from over-estimates of the mean velocity dispersion similar to that observed using the estimates in regions where $\sigma_v \gg v_{\rm grad}$FWHM$_{\rm PSF}$. We suspect this is driven by the observed velocity gradient being shallower than the underlying velocity gradient.

The in quadrature estimates under-estimate the mean velocity dispersions for $5 \lesssim v(R_{\rm opt})$FWHM$_{\rm PSF} \lesssim 30$. Adjusting a correction parameter α such that the corrections were of

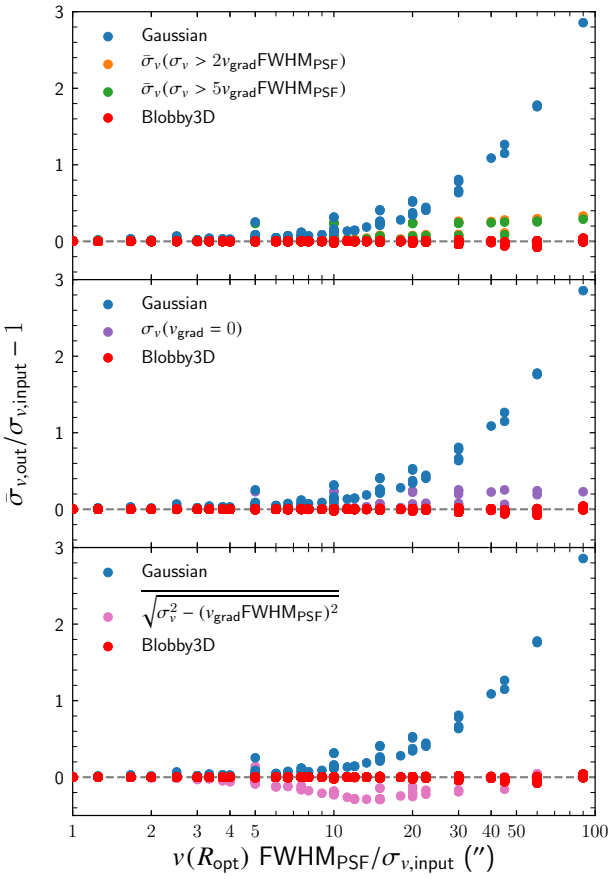

Figure 12. Using heuristic approaches to estimating the mean velocity dispersion for the toy models convolved by a Gaussian PSF using corrections from the observed local velocity gradient ($v_{\rm grad}$). Top: estimates in regions where the velocity dispersion is greater than a cutoff value of ${\rm FWHM_{PSF}}v_{\rm grad}(i,j)$. Middle: estimates the velocity dispersion at $v_{\rm grad} = 0$ by fitting a cubic to σ_v vs $v_{\rm grad}$. Bottom: in quadrature subtraction of $v_{\rm grad}$ from the observed velocity dispersion. In all cases, these approaches provide significant corrections for the intrinsic mean velocity dispersion compared to the single component Gaussian fits. However, the results from Blobby3D provide the most robust estimates for the intrinsic velocity dispersion.

the form $\sqrt{\sigma_v^2 - \alpha(v_{\rm grad}{\rm FWHM_{PSF}})^2}$ did not yield significant improvement. We note that Oliva-Altamirano et al. (2018) estimated the local velocity gradient after using GBKFit to estimate the underlying velocity gradient. As such, their estimate for the velocity profile should be less affected by beam smearing, and their velocity gradient will be smooth following a parametric radial profile. They also focused on differences from the mean velocity dispersion, which may not be effected by the precision of the estimate for the global velocity dispersion.

We also note that this is an idealised toy model with negligible noise. In practice, the noise will increase the uncertainties on the local velocity dispersion, which will cause significant deviations in the estimates of the mean velocity dispersion. This could be improved by fitting a velocity profile across the galaxy and using the local velocity gradient derived from that profile similar to (Oliva-Altamirano et al. 2018).

Furthermore, we only applied the velocity gradient approaches to toy models with no gas substructure. As we showed in Fig. 8 and 10, beam smearing complex gas substructure can have significant effects on the observed gas kinematics. This will effect the estimates for the $v_{\rm grad}$, and thus will affect the ability to estimate the underlying velocity dispersion.

These heuristic approaches still provide corrections to the observed velocity dispersion. They are also easy to implement as they use a small number of related parameters (eg. velocity gradient, width of the PSF, and distance from the centre of the galaxy). As such, they may be appropriate for particular research purposes.

As with any heuristic approaches, they often suffer from their simplicity in application. In this case, these methods cannot simultaneously model the beam smearing effect as it acts on the underlying gas and kinematic profiles. They also suffer from not fully taking into account the shape-parameters of the PSF, instead using a single measure of the PSF width such as the FWHM. 3D cube fitting algorithms are the only known approach to the authors that can perform such self-consistent modelling.

5.1.2 3D cube fitting algorithms

There are several 3D cube fitting approaches that have been proposed in the literature. Three of those are publicly available and are specifically designed to work for optical observations. Those are GalPak3D (Bouché et al. 2015), GBKFit (Bekiaris et al. 2016), and $^{\rm 3D}$Barolo (Di Teodoro & Fraternali 2015).

As seen in Section 3, $^{\rm 3D}$Barolo has issues resolving the kinematic profiles in low-resolution observations. This leads to over-estimated velocity dispersion and shallower velocity gradients. Our testing showed no significant difference in the inferred kinematics when running $^{\rm 3D}$Barolo with a differing number of rings.

We have no reason to believe that GalPak3D or GBKFit suffer from similar problems. Limitations of GalPak3D and GBKFit are due to the inflexibility of the model parameterisation which will lead to significant residuals for galaxies where complex substructure can be observed. The example galaxies from the SAMI Galaxy Survey seen in Fig. 9 and 10 are good examples of such galaxies. An inability to model these complex structures can lead to two potential problems:

(i) The galaxy substructure can be underfit. This can lead to the substructure systematically driving the estimates in indeterminate directions. Underfitting also leads to underestimates of uncertainties (Taranu et al. 2017).

(ii) Beam smearing is driven by the smearing of the underlying flux profile. If the underlying flux profile is clumpy it can lead to irregular kinematic profiles as seen in our examples in Fig. 8 and 10. As such, to get a full understanding of the effects of beam smearing, adequately modelling the gas substructure is important.

We also note that simplifications exist in our current methodology. In particular, assuming the kinematics follow radial profiles is likely to be too simplistic to model a large sample of galaxies. Also, modelling the gas substructure as a

hierarchical Gaussian mixture model is also imperfect. We understand that this could lead to similar problems as above.

The above reasoning led to the introduction of the additional σ_0 noise term. This term should help account for simple systematic noise between the model and data.

Also the flexibility of using a hierarchical Gaussian mixture model does provide much better fits to the data. To formalise this we performed a Bayesian model comparison between our current methodology with varying number of blobs and setting $N = 1$. Setting $N = 1$ is similar to a single-component disk model assuming a Gaussian flux profile. In both cases, we calculated the evidence (Z) using DNest4. Assuming no prior preference for either model, the odds ratio for our current methodology (M) compared to a single component model (M_0) is given by $O = p(D|M)/p(D|M_0) = Z/Z_0$. We found $\log(Z/Z_0) = 1.9 \pm 1.2 \times 10^4$ with $\log(Z/Z_0) > 0$ for all galaxies in our sample from the SAMI Galaxy Survey. Therefore, the variable blob model is preferred compared the single Gaussian component flux model using this measure.

5.2 Effects of beam smearing on kinematic asymmetries

We showed that a toy model with an asymmetric flux distribution, a radial velocity profile, and constant velocity dispersion leads to asymmetries in the velocity dispersion profile once convolved by the PSF (see Section 3.2). We also saw that modelling of asymmetries in the velocity dispersion profiles of GAMA 30890 can be partially performed by using a flexible gas distribution with radial kinematic profiles plus beam smearing. These observations have implications for the study of asymmetries in observed galaxies.

For example, a popular field of analysis is to estimate the kinematic asymmetries observed in the 2D maps (Shapiro et al. 2008). Analysis of kinematic asymmetries and their drivers have been performed on the SAMI Galaxy Survey previously (Bloom et al. 2017a,b, 2018). In those studies they used Kinemetry (Krajnović et al. 2006) to estimate the asymetries in the 2D kinematic maps. Kinemetry constructs kinematic maps by interpolating between a series of ellipses. Each ellipse is decomposed into a Fourier series of the form,

$$K(a,\psi) = A_0(a) + \sum_{n=1}^{N}(A_n(a)\sin(n\psi) + B_n(a)\cos(n\psi)), \quad (29)$$

where a is the semi-major axis length and ψ is the azimuthal angle. This is usually manipulated to the form,

$$K(a,\psi) = A_0(a) + \sum_{n=1}^{N} k_n(a)\cos(n(\psi - \phi_n(a))) \quad (30)$$

where

$$k_n = \sqrt{A_n^2 + B_n^2} \qquad \text{and} \qquad \phi_n = \arctan\left(\frac{A_n}{B_n}\right). \quad (31)$$

For n is odd the contribution to the 2D map is an even functional contribution. Similarly, for n is even the contribution is an odd functional contribution. The asymmetric contribution to a kinematic moment per spaxel is typically calculated using a ratio of the sum of $k_{n,\mathrm{mom}}$ for n > 1 compared to the first-order velocity moment $k_{1,v}$. In previous works on data from the SAMI Galaxy Survey, the following has been used,

$$v_{\mathrm{asym}} = \frac{k_{3,v} + k_{5,v}}{2k_{1,v}} \qquad \text{and} \qquad \sigma_{v,\mathrm{asym}} = \frac{k_{2,\sigma_v} + k_{4,v}}{2k_{1,v}}. \quad (32)$$

The odd moments were ignored for v_{asym} and the even moments were ignored for σ_{asym} as they were estimated to be negligible.

Analysing a sample of 360 galaxies Bloom et al. (2017a) estimated the mean asymmetry across the FoV to be $\bar{v}_{\mathrm{asym}} = 0.044^{+0.044}_{-0.017}$ and $\bar{\sigma}_{v,\mathrm{asym}} = 0.10^{+0.17}_{-0.04}$. This suggests greater asymmetries in the velocity dispersion compared to the velocity maps. However, the effect of beam smearing on the kinematic asymmetries has not been investigated.

Expanding our method to account for asymmetries in the velocity and velocity dispersion profiles would allow for simultaneous fitting of the kinematic asymmetries while taking into account the effects of beam smearing. This could be achieved by adopting the Fourier series decomposition of the moments similar to Kinemetry. A natural way to do so would be to parameterise k_n and ϕ_n as radial functions across the disk.

We also note that Bloom et al. (2017a) assigned $23 \pm 7\%$ of 360 galaxies from the SAMI Galaxy Survey as perturbed. In their analysis, they assigned galaxies to be perturbed when $\bar{v}_{\mathrm{asym}} > 0.065$. Thus, accounting for asymmetries is an important factor in accurately modelling a larger sample of galaxies at similar resolutions to the SAMI Galaxy Survey.

5.3 Implications for the study of gas turbulence within galaxies

Observations have established that galaxies at $z > 1$ exhibit higher velocity dispersion as well as clumpier gas and velocity dispersion profiles (Genzel et al. 2011; Wisnioski et al. 2011) compared to local galaxies. As the PSF width relative to the observed galaxy size is greater at higher redshift, the effects of beam smearing will typically be greater. As such, it is possible to mistakenly draw correlations across epochs if the effects of beam smearing on the gas velocity dispersion have not been corrected.

One relevant claim has been that star-formation feedback processes play an important role as a driver of gas turbulence across epochs (Green et al. 2010, 2014). In contrast, there have been several studies of the localised star-formation rate and gas turbulence in nearby galaxies which have not found a significant correlation (Varidel et al. 2016; Zhou et al. 2017). Another recent claim has been that gas turbulence may be driven by the interaction between clumps and the interstellar medium (Oliva-Altamirano et al. 2018). Inferring these relationships requires an ability to accurately determine the intrinsic gas distribution and kinematics. In such studies, our approach would provide a measure for the intrinsic velocity dispersion while taking into account the potentially complex gas distribution.

In particular, inferring relationships between gas clumps and the local kinematics should be much easier in our approach. For example, the study of the residuals in the velocity dispersion map could indicate clear peaks in the velocity dispersion that are correlated with the intrinsic gas distribution. A more natural way within the Bayesian framework, would be to parameterise the velocity dispersion as a function of the

gas flux. The simplest approach would be to assume a velocity dispersion component of the form $\log(\sigma_v) \propto F(x, y)$, where the proportionality constant would be a free parameter.

5.4 Potential applications for the study of gas outflows

Gas outflows play an important role as a star-formation feedback mechanism (Elmegreen 2009; Federrath et al. 2017a). As such, the identification of gas outflows in star-forming galaxies has received considerable attention (eg. Ho et al. 2014).

A difficulty in studying gas outflows is to distinguish between the gas rotation, gas outflows, and contributions of beam smearing on the observed emission line profiles. We suggest that applications of forward fitting modelling approaches, such as Blobby3D, are ideal to study these galaxies as the rotation and beam smearing contributions can be taken into account simultaneously.

In ideal circumstances, it will be possible to identify outflows as residuals from the 3D model. However, an ideal extension to Blobby3D for the study of gas outflows, would be to construct a parametric model for the gas outflows. This parameterisation would need to be carefully constructed as winds do not follow the rotational gas kinematics. As such, gas outflows would introduce asymmetries in the emission line profiles with different geometries to the galaxy plane.

This may require the introduction of higher-order moments for the emission line profiles. Functional forms for the emission lines that could be used are skewed Gaussian or Hermite-Gaussian profiles. An alternative approach would be to add a secondary gas velocity and velocity dispersion profile which has characteristics that represent an outflow. A simplistic model would likely require a parameterisation for the gas component moving radially outwards in a cone-like shape with a given velocity and velocity dispersion profile.

5.5 A note on run time

Other 3D fitting algorithms take $\mathcal{O}$(seconds - minutes) to run a typical SAMI Galaxy Survey sized cube cut around the Hα emission line. The current C++ implementation of Blobby3D took the equivalent of ~450 Central Processing Unit (CPU) hours for a single galaxy within our SAMI Galaxy Survey sample. Wall time was reduced significantly by running DNest4 in multi-threaded mode.

The run time is a function of the complexity of the gas substructure, the signal-to-noise, and the number of samples saved. The run time is a considerable disadvantage for researchers that have very large data sets or are low in computing resources. We have been able to work around this issue by using the Artemis cluster provided by The University of Sydney HPC Service. This gave us access to a large number of cores, such that we could run our methodology for several galaxies simultaneously.

The bottleneck is primarily driven by the number of blobs required to construct the flux profile. Thus decreasing the maximum number of blobs ($N_{\rm max}$) will decrease the run time significantly. Of course, this will lead to posterior distributions for N being abruptly cut-off at $N_{\rm max}$ for some galaxies. We could also implement non-uniform priors for the number of blobs. Similarly, some researchers may find that decomposing the gas distribution into a fixed number of blobs will be adequate to model the gas substructure. In these cases, the prior space will be significantly decreased, and thus will result in significantly faster convergence. We have not explored these possibilities in this work, but it may be important as we scale the methodology to larger samples.

Another approach would be to use an optimisation routine compared to a sampling algorithm. In this case, the user would only get an optimised point estimate, but such algorithms are typically much quicker. We note that there is an ability to optimise using DNest4. We have avoided optimisation techniques as we prefer to perform the full inference in order to estimate uncertainties.

Despite the improvements in speed that could be made, we still expect that our method will be significantly slower than other similar 3D fitting algorithms. However, the time restrictions implicit in our method are offset by the improvements in modelling the complex gas substructure that is apparent in typical IFS observations. Furthermore, due to the effects on kinematics that were discussed in Section 5.2, we suggest that researchers should consider using such flexible modelling approaches for the gas substructure in order to accurately infer the intrinsic gas kinematics in their observations.

6 CONCLUSIONS

Beam smearing occurs due to the flux profile being spread-out across the FoV by the seeing. For rotating disks this has significant effects on the observed kinematics. It has been well known that the observed LoS velocity profiles are typically flattened and the LoS velocity dispersion is increased when assuming single flux component galaxy models (Davies et al. 2011).

However, the observed gas distribution often exhibits complex structure including clumps, rings, or spiral arms. Considering this fact, we developed a methodology referred to as Blobby3D. Blobby3D can model complex gas substructure by using a hierarchical Gaussian mixture model. The kinematics are modelled assuming radial profiles. We take into account the effect of beam smearing by convolving the model by the seeing per spectral slice before comparing it to the data.

Blobby3D was applied to a sample of 20 star-forming galaxies from the SAMI Galaxy Survey. We estimated the global gas velocity dispersions for all galaxies in the range $\bar{\sigma}_v$ ~[7, 30] km s^{-1}. This is in comparison to estimates using a single Gaussian component per spaxel that were in the range $\bar{\sigma}_v$ ~[10, 45] km s^{-1}. The relative corrections per galaxy were $\Delta\sigma_v/\sigma_v = -0.29 \pm 0.18$. This has implications for galaxies observed at $z > 1$ that have observed gas velocity dispersions typically much greater than nearby galaxies.

We also show that resolving the gas substructure is important as the gas substructure can lead to asymmetries in the kinematic profiles. A toy model was constructed with asymmetric gas substructure with radial kinematic profiles plus beam smearing to show that asymmetric substructure was observable in the observed gas velocity dispersion. We also found that asymmetries in the velocity dispersion maps for GAMA 30890 can be partially recovered using our methodol-

ogy, that only introduces asymmetries in the gas distribution. This implies that studies of asymmetries within galaxies should consider the effects of beam smearing on their results.

To accurately infer the intrinsic gas kinematics both the gas flux and kinematic profiles plus beam smearing should be considered. With this in mind, methods such as BLOBBY3D, that are capable of performing such inferences should be an important step in analysing the kinematics for IFS observations of gas disks.

ACKNOWLEDGEMENTS

The SAMI Galaxy Survey is based on observations made at the Anglo-Australian Telescope. The Sydney-AAO Multi-object Integral field spectrograph (SAMI) was developed jointly by the University of Sydney and the Australian Astronomical Observatory. The SAMI input catalogue is based on data taken from the Sloan Digital Sky Survey, the GAMA Survey and the VST ATLAS Survey. The SAMI Galaxy Survey is supported by the Australian Research Council Centre of Excellence for All Sky Astrophysics in 3 Dimensions (ASTRO 3D), through project number CE170100013, the Australian Research Council Centre of Excellence for All-sky Astrophysics (CAASTRO), through project number CE110001020, and other participating institutions. The SAMI Galaxy Survey website is http://sami-survey.org/.

The authors acknowledge the University of Sydney HPC service at The University of Sydney for providing HPC and database resources that have contributed to the research results reported within this paper. URL: http://sydney.edu.au/research_support/

BJB acknowledges funding from New Zealand taxpayers via the Marsden Fund of the Royal Society of New Zealand. JBH is supported by an ARC Laureate Fellowship that funds JvdS and an ARC Federation Fellowship that funded the SAMI prototype. EDT acknowledges the support of the Australian Research Council (ARC) through grant DP160100723. JJB acknowledges support of an Australian Research Council Future Fellowship (FT180100231). CF acknowledges funding provided by the Australian Research Council (Discovery Projects DP170100603 and Future Fellowship FT180100495), and the Australia-Germany Joint Research Cooperation Scheme (UA-DAAD). BG is the recipient of an Australian Research Council Future Fellowship (FT140101202). Support for AMM is provided by NASA through Hubble Fellowship grant #HST-HF2-51377 awarded by the Space Telescope Science Institute, which is operated by the Association of Universities for Research in Astronomy, Inc., for NASA, under contract NAS5-26555. MSO acknowledges the funding support from the Australian Research Council through a Future Fellowship (FT140100255). NS acknowledges support of a University of Sydney Postdoctoral Research Fellowship.

REFERENCES

Aumer M., Burkert A., Johansson P. H., Genzel R., 2010, ApJ, 719, 1230
Bekiaris G., Glazebrook K., Fluke C. J., Abraham R., 2016, MNRAS, 455, 754
Bland-Hawthorn J., et al., 2011, Optics Express, 19, 2649
Bloom J. V., et al., 2017a, MNRAS, 465, 123
Bloom J. V., et al., 2017b, MNRAS, 472, 1809
Bloom J. V., et al., 2018, MNRAS, 476, 2339
Bouché N., Carfantan H., Schroetter I., Michel-Dansac L., Contini T., 2015, AJ, 150, 92
Bournaud F., Elmegreen B. G., Martig M., 2009, ApJ, 707, L1
Bournaud F., Elmegreen B. G., Teyssier R., Block D. L., Puerari I., 2010, MNRAS, 409, 1088
Brewer B. J., 2014, preprint (arXiv:1411.3921)
Brewer B., Foreman-Mackey D., 2018, Journal of Statistical Software, Articles, 86, 1
Brewer B. J., Pártay L. B., Csányi G., 2011a, Statistics and Computing, 21, 649
Brewer B. J., Lewis G. F., Belokurov V., Irwin M. J., Bridges T. J., Evans N. W., 2011b, MNRAS, 412, 2521
Brewer B. J., Foreman-Mackey D., Hogg D. W., 2013, AJ, 146, 7
Brewer B. J., Huijser D., Lewis G. F., 2016, MNRAS, 455, 1819
Bryant J. J., Bland-Hawthorn J., Fogarty L. M. R., Lawrence J. S., Croom S. M., 2014, MNRAS, 438, 869
Bryant J. J., et al., 2015, MNRAS, 447, 2857
Cappellari M., Emsellem E., 2004, PASP, 116, 138
Ceverino D., Dekel A., Bournaud F., 2010, MNRAS, 404, 2151
Cid Fernandes R., Stasińska G., Mateus A., Vale Asari N., 2011, MNRAS, 413, 1687
Contini T., et al., 2016, A&A, 591, A49
Courteau S., 1997, AJ, 114, 2402
Croom S. M., et al., 2012, MNRAS, 421, 872
Davies R., et al., 2011, ApJ, 741, 69
Dekel A., et al., 2009a, Nature, 457, 451
Dekel A., Sari R., Ceverino D., 2009b, ApJ, 703, 785
Di Teodoro E. M., Fraternali F., 2015, MNRAS, 451, 3021
Di Teodoro E. M., Fraternali F., Miller S. H., 2016, A&A, 594, A77
Di Teodoro E. M., et al., 2018, MNRAS, 476, 804
Dobbs C. L., Bonnell I. A., 2007, MNRAS, 374, 1115
Driver S. P., et al., 2011, MNRAS, 413, 971
Elmegreen B. G., 2009, in Andersen J., Nordströara m B., Bland-Hawthorn J., eds, IAU Symposium Vol. 254, The Galaxy Disk in Cosmological Context. pp 289–300 (arXiv:0810.5406), doi:10.1017/S1743921308027713
Epinat B., Amram P., Balkowski C., Marcelin M., 2010, MNRAS, 401, 2113
Federrath C., et al., 2017a, in Crocker R. M., Longmore S. N., Bicknell G. V., eds, IAU Symposium Vol. 322, The Multi-Messenger Astrophysics of the Galactic Centre. pp 123–128 (arXiv:1609.08726), doi:10.1017/S1743921316012357
Federrath C., et al., 2017b, MNRAS, 468, 3965
Förster Schreiber N. M., et al., 2009, ApJ, 706, 1364
Genzel R., et al., 2006, Nature, 442, 786
Genzel R., et al., 2011, ApJ, 733, 101
Glazebrook K., 2013, Publications of the Astronomical Society of Australia, 30, e056
Green A. W., et al., 2010, Nature, 467, 684
Green A. W., et al., 2014, MNRAS, 437, 1070
Ho I. T., et al., 2014, MNRAS, 444, 3894
Ho I.-T., et al., 2016, Ap&SS, 361, 280
Iorio G., Fraternali F., Nipoti C., Di Teodoro E., Read J. I., Battaglia G., 2017, MNRAS, 466, 4159
Johnson H. L., et al., 2018, MNRAS, 474, 5076
Józsa G. I. G., Kenn F., Klein U., Oosterloo T. A., 2007, A&A, 468, 731
Kauffmann G., et al., 2003, MNRAS, 346, 1055
Kelvin L. S., et al., 2012, MNRAS, 421, 1007
Krajnović D., Cappellari M., de Zeeuw P. T., Copin Y., 2006, MNRAS, 366, 787
Law D. R., Steidel C. C., Erb D. K., Larkin J. E., Pettini M., Shapley A. E., Wright S. A., 2007, ApJ, 669, 929
Oliva-Altamirano P., Fisher D. B., Glazebrook K., Wisnioski E.,

Bekiaris G., Bassett R., Obreschkow D., Abraham R., 2018, MNRAS, 474, 522
Persic M., Salucci P., Stel F., 1996, MNRAS, 281, 27
Richards S. N., et al., 2014, MNRAS, 445, 1104
Scott N., et al., 2018, MNRAS, 481, 2299
Shapiro K. L., et al., 2008, ApJ, 682, 231
Sharp R., et al., 2006, in Society of Photo-Optical Instrumentation Engineers (SPIE) Conference Series. p. 62690G (arXiv:astro-ph/0606137), doi:10.1117/12.671022
Sicking F. J., 1997, PhD thesis, PhD Thesis, University of Groningen, (1997)
Skilling J., 2004, in Fischer R., Preuss R., Toussaint U. V., eds, American Institute of Physics Conference Series Vol. 735, American Institute of Physics Conference Series. pp 395–405, doi:10.1063/1.1835238
Suyu S. H., Marshall P. J., Hobson M. P., Blandford R. D., 2006, MNRAS, 371, 983
Tamburro D., Rix H. W., Leroy A. K., Mac Low M. M., Walter F., Kennicutt R. C., Brinks E., de Blok W. J. G., 2009, AJ, 137, 4424
Taranu D. S., et al., 2017, ApJ, 850, 70
Varidel M., Pracy M., Croom S., Owers M. S., Sadler E., 2016, Publ. Astron. Soc. Australia, 33, e006
Walmswell J. J., Eldridge J. J., Brewer B. J., Tout C. A., 2013, MNRAS, 435, 2171
Wisnioski E., et al., 2011, MNRAS, 417, 2601
Zhou L., et al., 2017, MNRAS, 470, 4573
van de Sande J., et al., 2017, ApJ, 835, 104
van der Hulst J. M., Terlouw J. P., Begeman K. G., Zwitser W., Roelfsema P. R., 1992, in Worrall D. M., Biemesderfer C., Barnes J., eds, Astronomical Society of the Pacific Conference Series Vol. 25, Astronomical Data Analysis Software and Systems I. p. 131

This paper has been typeset from a TEX/LATEX file prepared by the author.

3 Applications of Blobby3D: The Drivers of Ionised Gas Turbulence in Low-z Galaxies

The second paper in this thesis is an application of BLOBBY3D to two samples of disc galaxies at $z \sim 0.1$. The samples include star-forming galaxies from the SAMI Galaxy Survey and the DYnamics of Newly Assembled Massive Objects (DYNAMO) survey. The gas kinematics inferred using BLOBBY3D were then analysed to understand the typical velocity dispersions of disc galaxies at $z \sim 0.1$, correlations of the velocity dispersion with other galaxy properties, as well as comparisons to models for the drivers of gas turbulence. The paper is titled *The SAMI Galaxy Survey: Gas velocity dispersions in low-z star-forming galaxies and the driver of turbulence*, that appeared in MNRAS in May 2020.

MNRAS **000**, 1–27 (2020) Preprint 11 June 2021 Compiled using MNRAS LATEX style file v3.0

The SAMI Galaxy Survey: Gas velocity dispersions in low-z star-forming galaxies and the drivers of turbulence

Mathew R. Varidel[1,2]★, Scott M. Croom[1,2], Geraint F. Lewis[1], Deanne B. Fisher[2,3], Karl Glazebrook[2,3], Barbara Catinella[2,4], Luca Cortese[2,4], Mark R. Krumholz[2,5,6,7], Joss Bland-Hawthorn[1,2], Julia J. Bryant[1,2,8], Brent Groves[2,4,5], Sarah Brough[2,9], Christoph Federrath[5], Jon S. Lawrence[10], Nuria P. Lorente[11], Matt S. Owers[12,13], Samuel N. Richards[14], Ángel R. López-Sánchez[8,12], Sarah M. Sweet[2,15], Jesse van de Sande[1,2], and Sam P. Vaughan[1,2]

[1]*Sydney Institute for Astronomy (SIfA), School of Physics, A28, The University of Sydney, NSW 2006, Australia*
[2]*ARC Centre of Excellence for All Sky Astrophysics in 3 Dimensions (ASTRO 3D)*
[3]*Centre for Astrophysics and Supercomputing, Swinburne University of Technology, PO Box 218, Hawthorn, VIC 3122, Australia*
[4]*International Centre for Radio Astronomy Research, University of Western Australia, 35 Stirling Highway, Crawley WA 6009, Australia*
[5]*Research School of Astronomy and Astrophysics, Australian National University, Canberra, ACT 2611, Australia*
[6]*Universität Heidelberg, Zentrum für Astronomie, Institut für Theoretische Astrophysik, 69120 Heidelberg, Germany*
[7]*Max Planck Institute for Astronomy, Königstuhl 17, 69117 Heidelberg, Germany*
[8]*Australian Astronomical Optics, AAO-USydney, School of Physics, University of Sydney, NSW 2006, Australia*
[9]*School of Physics, University of New South Wales, NSW 2052, Australia*
[10]*Australian Astronomical Optics, Macquarie University, 105 Delhi Rd, North Ryde, NSW 2113, Australia*
[11]*Faculty of Science & Engineering, Macquarie University. 105 Delhi Rd, North Ryde, NSW 2113, Australia*
[12]*Department of Physics and Astronomy, Macquarie University, NSW 2109, Australia*
[13]*Astronomy, Astrophysics and Astrophotonics Research Centre, Macquarie University, Sydney, NSW 2109, Australia*
[14]*SOFIA Science Center, USRA, NASA Ames Research Center, Building N232, M/S 232-12, P.O. Box 1, Moffett Field, CA 94035-0001, USA*
[15]*School of Mathematics and Physics, University of Queensland, Brisbane, QLD 4072, Australia*

Accepted XXX. Received YYY; in original form ZZZ

ABSTRACT

We infer the intrinsic ionised gas kinematics for 383 star-forming galaxies across a range of integrated star-formation rates (SFR $\in [10^{-3}, 10^{2}]$ M$_\odot$ yr^{-1}) at $z \lesssim 0.1$ using a consistent 3D forward-modelling technique. The total sample is a combination of galaxies from the SAMI Galaxy Survey and DYNAMO survey. For typical low-z galaxies taken from the SAMI Galaxy Survey, we find the vertical velocity dispersion ($\sigma_{v,z}$) to be positively correlated with measures of star-formation rate, stellar mass, H I gas mass, and rotational velocity. The greatest correlation is with star-formation rate surface density ($\Sigma_{\rm SFR}$). Using the total sample, we find $\sigma_{v,z}$ increases slowly as a function of integrated star-formation rate in the range SFR $\in [10^{-3}, 1]$ M$_\odot$ yr^{-1} from 17 ± 3 km s^{-1} to 24 ± 5 km s^{-1} followed by a steeper increase up to $\sigma_{v,z} \sim 80$ km s^{-1} for SFR $\gtrsim 1$ M$_\odot$ yr^{-1}. This is consistent with recent theoretical models that suggest a $\sigma_{v,z}$ floor driven by star-formation feedback processes with an upturn in $\sigma_{v,z}$ at higher SFR driven by gravitational transport of gas through the disc.

Key words: galaxies: kinematics and dynamics, galaxies: evolution, techniques: imaging spectroscopy, methods: statistical, methods: data analysis

★ E-mail: mathew.varidel@sydney.edu.au

1 INTRODUCTION

Galaxies at $z > 1$ typically have velocity dispersions greater than nearby galaxies (Kassin et al. 2012; Wisnioski et al. 2015; Johnson et al. 2018; Übler et al. 2019). While observations of galaxies at $z > 1$ reveal a significant proportion of galaxies with velocity dispersions in the range 50 – 100 km s^{-1} (e.g. Genzel et al. 2006; Law et al. 2007; Förster Schreiber et al. 2009; Law et al. 2009; Epinat et al. 2010; Jones et al. 2010; Lemoine-Busserolle et al. 2010), nearby galaxies typically have velocity dispersions of < 50 km s^{-1} (Epinat et al. 2008; Moiseev et al. 2015; Varidel et al. 2016; Yu et al. 2019). Although this has been observed, the process by which galaxies settle to lower velocity dispersions across epochs is not well understood.

Another important observation is that galaxies at all epochs exhibit velocity dispersions that are greater than expected by the thermal contribution of the gas alone. In the case of ionised gas measured using the Hα emission line, the characteristic temperature of 10^4 K corresponds to an expected velocity dispersion of ~9 km s^{-1} (Glazebrook 2013). Galaxies have velocity dispersions > 9 km s^{-1} at all epochs.

Studies suggest that turbulent motions above the thermal contribution dissipate on timescales of the order of the flow crossing time (Mac Low et al. 1998; Stone et al. 1998; Mac Low 1999). The crossing time for a galaxy with Toomre stability (Toomre 1964) of $Q \sim 1$ will be of order the dynamical time, which is typically O(100 Myr) (Krumholz et al. 2018). If the turbulent motions are on the scale of Giant Molecular Clouds (GMCs), it will decay on O(< 10 Myr). Therefore, we should rarely see galaxies with velocity dispersions greater than the thermal contribution, unless there is an ongoing driving mechanism to sustain the observed gas turbulence.

Numerous energetic sources have been proposed to contribute to the non-thermal turbulence observed in galaxies. These drivers can typically be split into star-formation feedback processes (Norman & Ferrara 1996; Mac Low & Klessen 2004; Krumholz & Matzner 2009; Murray et al. 2010), gravitational transport of gas onto (Elmegreen & Burkert 2010; Hopkins et al. 2013) or through (Krumholz & Burkert 2010) the disc, dynamical drivers such as shear and differential rotations across the disc (Federrath et al. 2016, 2017), or interactions between galaxy components (e.g. Dobbs & Bonnell 2007; Dekel et al. 2009; Ceverino et al. 2010; Aumer et al. 2010; Oliva-Altamirano et al. 2018). In this paper, we will be focusing primarily on differentiating star-formation feedback processes and gravitational transport of gas through the disc due to the clear predictions that have been made in the integrated star-formation rate (SFR) and global velocity dispersion (σ_v) plane (Krumholz & Burkhart 2016; Krumholz et al. 2018).

Star-formation feedback is thought to be dominated by the energy imparted by supernovae (Norman & Ferrara 1996; Mac Low & Klessen 2004). However, other drivers such as stellar winds, expansion of H II regions (Chu & Kennicutt 1994; Matzner 2002), and radiation pressure in high density star clusters (Krumholz & Matzner 2009; Murray et al. 2010) will also inject momentum into the interstellar medium. Observational evidence for star-formation feedback as the primary driver of gas turbulence has been argued by observing that SFR is correlated with σ_v. The SFR – σ_v correlation has been shown both within a single sample at constant redshift (Green et al. 2010, 2014; Moiseev et al. 2015; Yu et al. 2019) and by combining multiple samples across epochs (Green et al. 2010, 2014).

Assuming that star-formation feedback processes are a significant driver of the turbulence, it would be natural to expect a relation between local star-formation rate surface density ($\Sigma_{\rm SFR}$) and local velocity dispersion. There are conflicting results in the literature regarding the relationship between these local quantities. Some studies have found a significant relationship (Lehnert et al. 2009, 2013), whereas others have found the localised relationship to be weak (Genzel et al. 2011; Varidel et al. 2016; Zhou et al. 2017; Übler et al. 2019).

Furthermore, the physical mechanism for an energetic source to account for velocity dispersions due to star-formation feedback of several tens of km s^{-1} is not well established. Constructing equilibrium solutions between gravitational infall of the disc supported by outward pressure solely by supernovae leads to $\sigma_v \lesssim 25$ km s^{-1} with little variation as a function of SFR (Ostriker & Shetty 2011; Krumholz et al. 2018). An alternative approach that can account for increased turbulence is to assume that the star-formation efficiency per free-fall time ($\epsilon_{\rm ff}$) changes as a function of galaxy properties, thus changing the energetic input from star-formation feedback processes (Faucher-Giguère et al. 2013). However, numerous observations suggest that $\epsilon_{\rm ff}$ is approximately constant across a wide range of galaxy properties (Krumholz & Tan 2007; Krumholz et al. 2012; Federrath 2013; Salim et al. 2015; Krumholz et al. 2019).

An alternative set of driving mechanisms are due to gravitational effects. This includes the initial gravitationally unstable formation of the disc (Aumer et al. 2010), that can account for short-lived supersonic turbulence on the order of the disc formation time, O(100 Myr). It is thought that the supersonic turbulence that is initially set at disc formation can be maintained by the gravitational transport of gas through the disc (Krumholz & Burkert 2010). Krumholz & Burkhart (2016) also argued that the gravitational transport model predicts an increase in velocity dispersion at increased SFR that is more consistent with the data than models assuming star-formation feedback processes.

A further complication involved in inferring the ongoing drivers of turbulence across epochs is the effects of the spectral and spatial resolution on the observed velocity dispersion. The spectral resolution broadens the observed emission line often on order of the intrinsic velocity dispersion. This is typically accounted for by convolving the modelled emission line profile by the known Line-Spread Function (LSF) while fitting to the data (e.g. Förster Schreiber et al. 2009; Davies et al. 2011; Green et al. 2014; Varidel et al. 2019). This is a reasonable approximation as long as the model assumptions regarding the LSF are well known.

The spatial resolution is more difficult to account for as it acts to blur the emission line flux spatially per spectral slice. The observed velocity dispersion is then a complex function of the intrinsic flux distribution, line of sight (LoS) velocity profile, and LoS velocity dispersion profile. This effect is usually referred to as beam smearing.

In general, beam smearing acts to increase the observed velocity dispersion particularly where the velocity gradient is steepest (Davies et al. 2011; Glazebrook 2013), and in detail can result in spurious substructure in the velocity dispersion profile (Varidel et al. 2019). Furthermore, beam smearing could result in spurious correlations such as the SFR – σ_v correlation, as SFR is related to the mass which shapes the gravitational potential, and thus increases the velocity gradient at the centre of galaxies with higher SFR. Similarly, the width of the Point-Spread Function (PSF) relative to the galaxy size increases for increasing z, thus resulting in higher observed velocity dispersions if beam smearing is not corrected for appropriately.

The SFR – σ_v relation has been used to distinguish between the different energetic sources of turbulence (Krumholz & Burkhart 2016; Krumholz et al. 2018). However, comparisons between theoretical models and observations have typically been performed by combining several studies with different redshift ranges and beam

smearing corrections. In this paper, we improve comparisons of the observed velocity dispersion to theoretical models by studying a sample of nearby galaxies using a single technique to mitigate the effects of beam smearing. The data encompasses a wide range of SFR $\in [10^{-3}, 10^{2}]$ $M_\odot$ yr^{-1} of local galaxies at $z \lesssim 0.1$. The combined sample is comprised of observations from the SAMI Galaxy Survey Data Release Two (SAMI Galaxy Survey DR2, Croom et al. 2012; Scott et al. 2018) and the DYNAMO survey (Green et al. 2014). We use a consistent disc-fitting routine referred to as Blobby3D (Varidel et al. 2019), for all the galaxy gas kinematic modelling in this paper. Blobby3D is a disc fitting code that constructs a regularly rotating thin-disc galaxy model in 3D (position – position – wavelength space) that is then convolved by the PSF and LSF prior to comparing the model to the data. In that way it can account for the effect of beam smearing when inferring the velocity dispersion of the galaxy.

The outline of this paper is as follows. In Section 2 we describe the SAMI Galaxy Survey and DYNAMO surveys, as well as our sample selection criteria. In Section 3 we outline the methods used to measure the key gas kinematic properties. In Section 4, we will discuss our results. In Section 5 we compare our results to theoretical models of the drivers for turbulence. We summarise our conclusions in Section 6. Throughout this paper we assume the concordance cosmology ($\Omega_\Lambda = 0.7$, $\Omega_m = 0.3$, $H_0 = 70$ km s^{-1} Mpc^{-1}; Hinshaw et al. 2009) and a Chabrier (2003) Initial Mass Function (IMF).

2 DATA SELECTION

2.1 The SAMI Galaxy Survey

The SAMI Galaxy Survey was conducted with the Sydney-AAO Multi-object Integral field Spectrograph (SAMI, Croom et al. 2012). SAMI was mounted at the Anglo-Australian Telescope (AAT), that provided a 1 degree diameter Field-of-View (FoV). SAMI used 13 fused fibre bundles, known as Hexabundles (Bland-Hawthorn et al. 2011; Bryant et al. 2014), with a 75% fill factor. Each bundle contains 61 fibres of 1.6″ diameter, resulting in an approximately 15″ diameter FoV. The IFUs as well as 26 sky fibres were attached to pre-drilled plates using magnetic connectors. SAMI fibres were fed to the double-beam AAOmega spectrograph (Sharp et al. 2006). The 580V grating at 3750–5750 Å provides a resolution of $R = 1808$ ($\sigma = 70.4$ km s^{-1} at 4800 Å) and the 1000R grating from 6300–7400 Å providing a resolution of $R = 4304$ ($\sigma = 29.6$ km s^{-1} at 6850 Å) (Scott et al. 2018).

During the survey, observations of over 3000 galaxies were obtained. Target selection for the SAMI Galaxy Survey are provided in Bryant et al. (2015). The redshift range for the observed galaxies was $0.004 < z < 0.113$ and a stellar mass range of $7.5 < \log(M_*/M_\odot) < 11.6$. The Full-Width Half-Maximum (FWHM) of the seeing distribution was $1.10'' < \mathrm{FWHM_{PSF}} < 3.27''$. Relevant data used for the analysis in this paper are from the SAMI Galaxy Survey DR2 (Scott et al. 2018). This includes the aperture spectra, emission line products (Green et al. 2018), data cubes (Sharp et al. 2015), and input catalogue (Bryant et al. 2015).

2.2 Sample selection from the SAMI Galaxy Survey

Our aim was to select galaxies on the star-forming main sequence within the SAMI Galaxy Survey. As such, we performed the following selection criteria cuts to the sample from the SAMI Galaxy Survey DR2 (Scott et al. 2018).

Star-forming galaxies are selected by applying a cutoff integrated Hα equivalent width of $EW > 3$ Å (Cid Fernandes et al. 2011). The equivalent width is calculated as the total Hα flux compared to the total continuum flux across the SAMI FoV. The continuum flux in the region around Hα is estimated by calculating the mean continuum in the wavelength range [6500, 6540] Å. The integrated Hα flux estimates is sourced from the SAMI Galaxy Survey DR2 emission line data products.

We remove galaxies with ionised emission from non star-forming sources such as Active Galactic Nuclei (AGN) and Low-Ionisation Nuclear Emission-line Regions (LINERs). To implement this criteria, we remove galaxies where the AGN classification criteria proposed by Kauffmann et al. (2003) is met,

$$\log([\mathrm{O\,III}]/\mathrm{H}\beta) > \frac{0.61}{\log([\mathrm{N\,II}]/\mathrm{H}\alpha) - 0.05} + 1.3. \quad (1)$$

[O III] and [N II] represent the emission line fluxes at 5007 Å and 6583 Å, respectively. The line fluxes are estimated for the central region of the galaxy where AGN and LINER contamination should be greatest, using the 1.4″ aperture spectra from the SAMI Galaxy Survey DR2.

We retain galaxies that are face-on up to $e = 1 - b/a = 0.5$ ($0° < i < 60°$, assuming a thin disc). We avoid galaxies observed at high inclination as the intrinsic velocity dispersion is more difficult to constrain due to beam smearing. Plus galaxies are optically thick such that edge-on observations limit the ability to observe the integrated LoS from the entire galaxy. Furthermore, a thin disc model is assumed in Blobby3D, such that the galaxies will not be well modelled when observed close to edge-on.

We apply the following signal-to-noise cut on the spaxels in the data. We first apply a mask to spaxels with Hα flux signal-to-noise < 3. Spatially resolved Hα flux and it's error are obtained from the SAMI Galaxy Survey DR2 pipeline. We then construct groups of unmasked spaxels that are adjacent and meet the signal-to-noise criteria. The largest unmasked group is retained, whereas the remaining spaxels are masked. We retain galaxies that had at least 300 unmasked spaxels.

The above masking routine only finds the largest group of spaxels, which in principle could reject clumpy flux profiles. In practice, the effect of removing Hα clumps originating from the galaxy was negligible. Instead, it primarily removed spurious spaxels that were reported to have high signal-to-noise, yet by eye did not appear to be legitimate detections of flux originating from the galaxy.

We also remove mergers or galaxies with clearly disturbed gas kinematics from our final sample. Potential mergers were determined by eye from observations of the gas kinematic maps. 9 galaxies were removed from our final sample due to this criteria.

There are 1523 galaxies in the SAMI Galaxy Survey DR2 where all of the above diagnostic criteria are measurable. 342 galaxies remain once our criteria is applied. Figure 1 shows that we are selecting galaxies along the star-forming main sequence. We see a clear bimodal distribution in the log equivalent width, where we have selected those galaxies with $EW > 3$ Å. The equivalent width cut removes massive galaxies that are typically passive, which can be seen when plotting the equivalent width compared to M_* and R_e. There are a limited number of galaxies in our sample with 3 Å < $EW \lesssim 10$ Å as many of those galaxies are removed due to being classified as LINER/AGN or having < 300 spaxels that meet our signal-to-noise masking criteria.

Removing highly inclined galaxies results in a large cut to our sample, but does not bias our sample along any galaxy properties. Also, the selection of galaxies with at least 300 unmasked spaxels

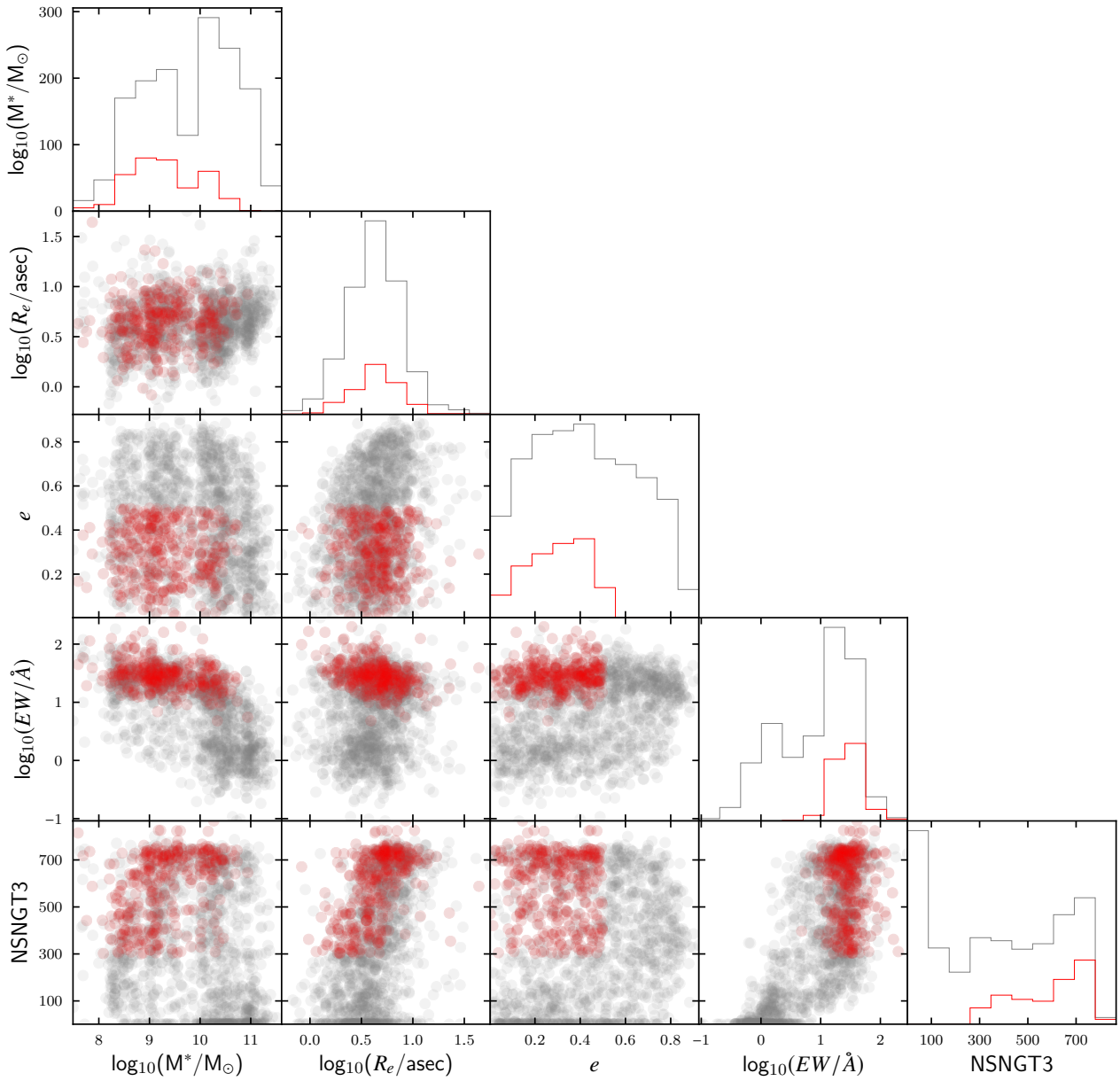

Figure 1. Galaxy parameters for our sample of 342 galaxies (red) selected from the total SAMI Galaxy Survey (grey). We show the marginalised (diagonal) and conditional (off-diagonal) distributions for the stellar mass ($\log_{10}(M^*/M_\odot)$), effective radius ($\log_{10}(R_e/\mathrm{asec})$), ellipticity ($e = 1 - b/a$), H$\alpha$ equivalent width ($\log_{10}(EW/\text{Å})$), and NSNGT3. NSNGT3 corresponds to the number of spaxels that meet our signal-to-noise masking criteria. We select a sample of star-forming galaxies from the SAMI Galaxy Survey with inclination and signal-to-noise cuts that can be adequately modelled using Blobby3D.

does remove galaxies with $R_e \lesssim 1''$, but there are very few of these galaxies in the underlying SAMI Galaxy Survey DR2 sample.

2.3 DYNAMO sample

The DYnamics of Newly Assembled Massive Objects (DYNAMO, Green et al. 2014) survey consists of a sample of star-forming galaxies in the local Universe ($z \lesssim 0.1$). These galaxies were classified as star-forming in the MPA-JHU Value Added Catalog from the Sloan Digital Sky Survey (SDSS, York et al. 2000). The galaxies comprising the DYNAMO survey were chosen primarily based on Hα luminosity. The aim was to include both high Hα luminious galaxies, that are rare in the local Universe, as well as a sample of typical galaxies in the local Universe. The resulting galaxy sample ranged SFR $\in [1, 100]$ $M_\odot$ yr^{-1}.

The data for the DYNAMO samples was obtained via observations using the 3.9 m Anglo-Australian Telescope (AAT) and the ANU 2.3 m Telescope at Siding Spring Observatory. The AAT

was equiped with the SPIRAL Integral-Field Unit (IFU) with the AAOmega Spectrograph (Sharp et al. 2006). SPIRAL is an array of 32×16 square, $0.7''$ lenslets with a contiguous integral field of $22.4'' \times 11.2''$. The 1700I grating was used on the red spectrograph providing a nominal resolution power of $R \sim 12000$. The ANU 2.3 m Telescope was equiped with the Wide-Field Spectrograph (WiFeS, Dopita et al. 2007). WiFeS has a $25'' \times 38''$ FoV with either $1.0'' \times 0.5''$ or $1.0'' \times 1.0''$ spaxels. The I7000 grating was chosen for the red arm, which has a 6893 – 9120 Å wavelength range with a spectral resolving power of $R \sim 7000$.

A total of 67 galaxies comprised the original DYNAMO sample. We remove galaxies observed at $i > 60°$, where i has been measured using the SDSS photometric pipeline using an exponential disc fit to the r-band. We perform the same masking criteria as described for the galaxies from the SAMI Galaxy Survey. We also remove galaxies with less than 30 unmasked spaxels. 41 galaxies were retained from the original DYNAMO sample.

3 METHODS

3.1 Modelling the gas disc kinematics

We use Blobby3D (Varidel et al. 2019) to infer the intrinsic gas kinematics for the observed galaxies. Blobby3D is a forward-fitting disc modelling procedure. It assumes that the gas lies in a regularly rotating thin-disc. The prior for the spatial gas distribution within the disc allows for clumpy gas profiles using a hierarchical Gaussian mixture-model. The model is constructed in 3D (position – position – wavelength space) and then convolved in accordance with the PSF and instrumental broadening by the LSF. The convolved model is then compared to the observed data cube.

The advantage of Blobby3D is that it is capable of performing inference for the spatial gas distribution, including substructure, plus the gas kinematics simultaneously. This is important as the effect of beam smearing is a function of the spatial gas distribution being blurred per spectral slice. As such, the observed gas kinematics is a complex function of the intrinsic spatial gas distribution, the velocity profile, and the velocity dispersion plus instrumental broadening and beam smearing. For example, Varidel et al. (2019) found that it is possible to observe spurious substructure in the gas kinematics in a symmetric regularly rotating disc with an asymmetric spatial gas distribution plus beam smearing.

Previous testing of Blobby3D has found that it is well optimised to infer the intrinsic velocity dispersion of galaxies (Varidel et al. 2019). Blobby3D was compared to an alternative forward-fitting methodology known as ^{3D}Barolo (Di Teodoro & Fraternali 2015). It was also compared to other heuristic modelling approaches that have been used in the literature, such as estimating the velocity dispersion in the outskirts of the galaxy (e.g. Zhou et al. 2017), correcting the observed velocity dispersion as a function of the velocity gradient (e.g. Varidel et al. 2016), and subtracting the velocity gradient in quadrature from the observed velocity dispersion (e.g. Oliva-Altamirano et al. 2018). Blobby3D was found to infer the intrinsic velocity dispersion more accurately than these alternative methods, particular for galaxies where the PSF or velocity gradient were greatest.

The parameterisation for Blobby3D is set within the Bayesian framework. The joint prior distribution for the parameters, hyperparameters, and data were defined in Varidel et al. (2019). We only make minor changes to the priors that were previously proposed. We outline the motivation for changing some of the prior distributions below.

The joint prior distribution used for this work performs inferences for the Hα flux plus the [N II]/Hα emission flux ratio for each spatial Gaussian flux profile (often referred to as a 'blob' in Blobby3D). The gas kinematics have been assumed to be consistent across the different gas components. Therefore, the inferences for the kinematics are constrained using extra information from the [N II] emission lines at 6548.1 Å and 6583.1 Å. The ratio of the flux between the [N II] emission lines is assumed to be $F_{6583.1}/F_{6548.1} = 3$.

To simplify the inference for the velocity dispersion, we assume a constant velocity dispersion across the disc ($\sigma_{v,0}$). We assume no radial gradient as the results for some galaxies returned large positive gradients when using the prior suggested by Varidel et al. (2019). The large spatial gradients in velocity dispersion after convolution appeared to be over-fitting for wider-tailed non-Gaussian emission line profiles. Therefore, we removed the velocity dispersion gradient from the inference in order to robustly infer the constant velocity dispersion component for the large sample of galaxies that were studied in this work.

We have also widened the bounds for our priors for the systemic velocity ($v_{\rm sys}$) and the asymptotic velocity (v_c) in order to model a larger set of galaxies than was performed by Varidel et al. (2019). Our new priors are,

$$v_{\rm sys} \sim \text{Cauchy}(0, 30 \text{ km s}^{-1})T(-300 \text{ km s}^{-1}, 300 \text{ km s}^{-1}), \quad (2)$$

$$v_c \sim \text{Loguniform}(1 \text{ km s}^{-1}, 1000 \text{ km s}^{-1}). \quad (3)$$

Where $T(a, b)$ represents the distribution being truncated to the interval $[a, b]$.

3.1.1 *Mitigating the effects of beam smearing*

The effect of beam smearing by the PSF is accounted for in Blobby3D by convolving the underlying model constructed by the PSF, prior to calculating the likelihood function. The PSF profile assumed in Blobby3D is a superposition of 2D concentric circular Gaussian profiles. Therefore, the PSF needs to first be modelled assuming this flux profile.

The SAMI Galaxy Survey pipeline provides estimates for the PSF by fitting a profile to a star that was observed simultaneously with the galaxy. We have used the Moffat profile estimates, where the PSF is described as,

$$p(r) = \frac{\beta - 1}{\pi\alpha^2}\left(1 + \frac{r^2}{\alpha^2}\right)^{-\beta}. \quad (4)$$

α is the FWHM and β is a shape parameter that controls the tails of the Moffat profile.

To refactor the Moffat profile parameters into a set of concentric Gaussians, we construct the 1D Moffat profile, then fit it with two 1D Gaussians. Two Gaussians were enough to adequately model the PSF profile. The estimated Gaussian parameters are then passed to Blobby3D.

For the DYNAMO sample, the FWHM of the PSF was measured during observations. As such, we assumed a 2D circular Gaussian profile to be representative of the PSF for the DYNAMO sample. Thus, the underlying model in Blobby3D was convolved with a Gaussian profile prior to comparing the model to the data for our galaxies from the DYNAMO survey.

3.1.2 *Continuum substraction*

Blobby3D requires the data to be continuum subtracted. For galaxies from the SAMI Galaxy Survey, we use the continuum models

made available in the SAMI Galaxy Survey DR2 pipeline. The full description for the continuum modelling routine is described in Owers et al. (2019). We estimate the continuum for the galaxies from the DYNAMO survey using a 300 bin moving median filter as also implemented by Green et al. (2014).

It is possible for the continuum modelling to introduce systematics in the resulting continuum subtracted data cube. These systematics may not be well accounted for in the BLOBBY3D approach. We make the assumption that the stellar continuum will be adequately modelled in regions of high Hα signal-to-noise. This is a significant motivation for implementing the Hα signal-to-noise masking outlined in Section 2.2.

3.1.3 *Posterior optimisation*

We use DNEST4 (Brewer et al. 2011; Brewer & Foreman-Mackey 2018) to get a point estimate of the maxima for the posterior Probability Density Function (PDF). DNEST4 is a sampling algorithm based on nested sampling (Skilling 2004), where the new levels are constructed by exploring a weighted mixture of the previous levels. Exploration of the levels is performed using a Metropolis Markov Chain Monte Carlo (MCMC). The multi-level exploration allows DNEST4 to be significantly more robust to local maxima compared to typical nested sampling, allowing for the exploration of high parameter spaces and multi-modal posterior distributions. Estimated values throughout this paper are of the maximum posterior PDF value in the chain sampled using DNEST4.

3.2 Global velocity dispersion

3.2.1 *Beam smearing corrections*

Assuming that BLOBBY3D accurately corrects for beam smearing, there should be no residual correlation between the PSF profile parameters and the inferred intrinsic velocity dispersion ($\sigma_{v,0}$). The distribution of $\sigma_{v,0}$ is consistent with our expectations for a beam smearing corrected sample. Figure 2 shows a comparison between the PSF Moffat profile parameters and $\sigma_{v,0}$ for our sample from the SAMI Galaxy Survey. For both α and β, zero remains inside the 68% shortest credible intervals for the Spearman-rank correlation coefficients.

For galaxies from the DYNAMO survey, the Spearman-rank correlation coefficient is estimated as $\rho(\mathrm{FWHM}, \sigma_v) = 0.10^{+0.17}_{-0.17}$. As zero remains within the 68% confidence interval, this result is also consistent with a beam smearing corrected sample.

We also compare $\sigma_{v,0}$ to an estimate of the velocity dispersion that was not corrected for beam smearing ($\sigma_{v,\mathrm{uncorrected}}$). The uncorrected estimator is calculated as the arithmetic mean velocity dispersion across the FoV, when fitting a single Gaussian component to each spaxel. Spaxels with Hα signal-to-noise < 3 are masked in this process to eliminate the effects of poorly constrained spaxels on the final estimate.

Estimates for $\sigma_{v,0}$ are significantly lower than $\sigma_{v,\mathrm{uncorrected}}$ (see Figure 3). Using the sample of galaxies from the SAMI Galaxy Survey, typical corrections were $\Delta\sigma_v = -5.3^{+4.0}_{-7.0}$ km s^{-1} and $\Delta\sigma_v/\sigma_{v,0} = -0.20^{+0.14}_{-0.18}$, where $\Delta\sigma_v = \sigma_{v,0} - \sigma_{v,\mathrm{uncorrected}}$. The typical beam smearing corrections are consistent with the results found by Varidel et al. (2019) on a sample of 20 star-forming galaxies in the SAMI Galaxy Survey using BLOBBY3D.

All estimated values have $\sigma_{v,0} > \sigma_{v,\mathrm{thermal}} = 9$ km s^{-1}. $\sigma_{v,\mathrm{thermal}}$ is the typical emission line width expected for a H II

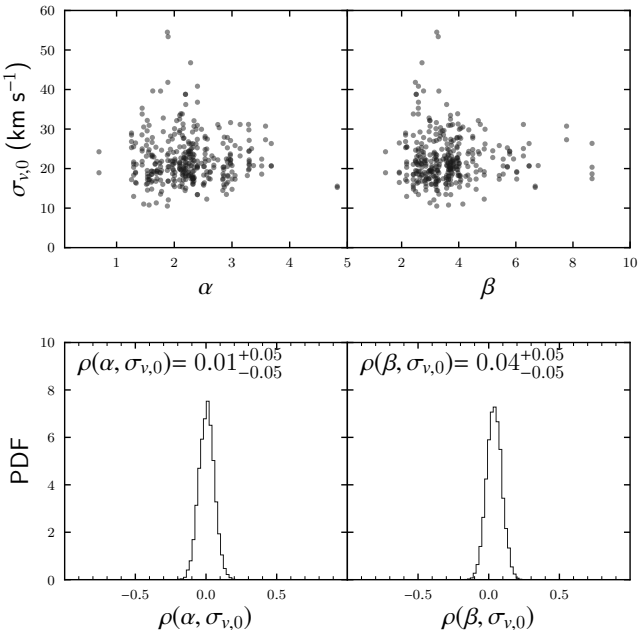

Figure 2. Comparing the PSF Moffat profile parameters α and β to the inferred global velocity dispersion for galaxies in our sample from the SAMI Galaxy Survey. We also show the PDF of the Spearman-rank correlation coefficients estimated using 10^4 bootstrap samples (bottom). $\rho = 0$ lies within the 68% shortest credible intervals suggesting that $\sigma_{v,0}$ is adequately corrected for beam smearing.

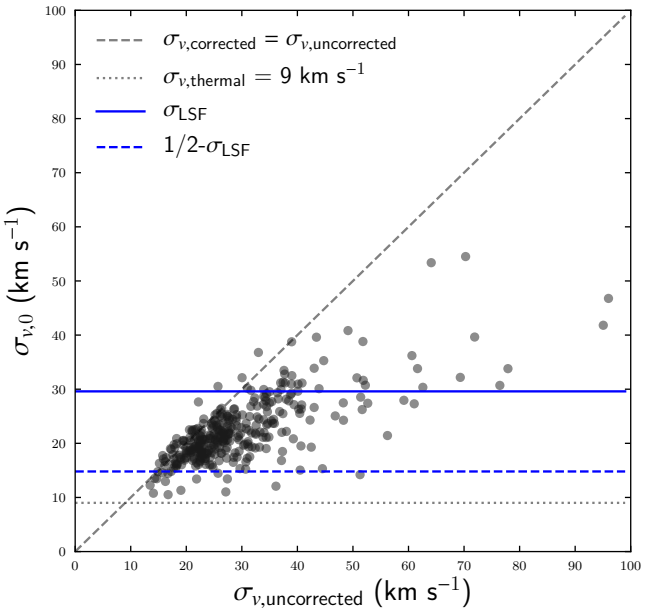

Figure 3. $\sigma_{v,0}$ estimated using BLOBBY3D compared to the arithmetic mean of the single-component fits per spaxel ($\sigma_{v,\mathrm{uncorrected}}$) to each galaxy from the SAMI Galaxy Survey sample. Estimates for the velocity dispersion are typically lower using BLOBBY3D as it mitigates the effects of beam smearing.

region at $\sim 10^4$ K (Glazebrook 2013). As such, $\sigma_{v,\mathrm{thermal}}$ sets a physically motivated lower bound.

3.2.2 *Considerations of the effects of the LSF on the velocity dispersion estimates*

The SAMI instrument has the spectral resolution of $\sigma_{\mathrm{LSF}} = 0.68$ Å ($\sigma_{v,\mathrm{LSF}} = 29.6$ km s^{-1}) in the red arm. For reference, we show the 1-$\sigma_{v,\mathrm{LSF}}$ and 1/2-$\sigma_{v,\mathrm{LSF}}$ on Figure 3. 89% of our galaxies have estimated intrinsic velocity dispersions less than $\sigma_{v,\mathrm{LSF}}$ and 4.6% of our sample were estimated to have intrinsic velocity dispersion less than $\sigma_{v,\mathrm{LSF}}/2$.

We correct for the LSF by convolving the emission line by a Gaussian profile with $\sigma_{v,\mathrm{LSF}}$ during the fitting procedure in Blobby3D. This procedure assumes that the observed emission line is a convolution of two Gaussians. Therefore, the estimated velocity dispersion can be affected by non-Gaussianities in the shape of the LSF, particularly when the velocity dispersion is significantly less than the width of the LSF. However, deviations of the SAMI LSF from a Gaussian profile are minor (van de Sande et al. 2017). Also 95.4% of our sample were estimated to be $\sigma_{v,0} > \sigma_{v,\mathrm{LSF}}/2$, as such the effects of minor systematic differences of the LSF from a Gaussian profile is unlikely to have significant effects on our inferences.

Similarly, the effect of variations in the LSF FWHM are minor for the SAMI Galaxy Survey. The LSF FWHM varied at the ∼5% level as a function of fibre, time, and wavelength during the SAMI Galaxy Survey (Scott et al. 2018). For the velocity dispersions values that we estimate, this should result in uncertainties on the level of $\Delta\sigma_v \sim 1$ km s^{-1}. As such, the variation of the LSF FWHM is not expected to have any significant effect on the conclusions drawn in this paper.

3.2.3 *Estimating the vertical velocity dispersion*

Our disc modelling approach calculates a global estimate for the intrinsic line-of-sight (LoS) velocity dispersion ($\sigma_{v,0} \equiv \sigma_{v,\mathrm{LoS}}$). Most studies using IFS observations report $\sigma_{v,\mathrm{LoS}}$. However, $\sigma_{v,\mathrm{LoS}}$ is a mixture of the radial ($\sigma_{v,R}$), azimuthal ($\sigma_{v,\phi}$), and vertical ($\sigma_{v,z}$) velocity dispersion components.

At any point in the sky, $\sigma_{v,\mathrm{LoS}}$ is given by (e.g. Equation 27a, Cappellari 2019),

$$\sigma^2_{v,\mathrm{LoS}} = \left(\sigma^2_{v,R}\sin^2\phi + \sigma^2_{v,\phi}\cos^2\phi\right)\sin^2 i + \sigma^2_{v,z}\cos^2 i. \quad (5)$$

Observed $\sigma_{v,\mathrm{LoS}}$ is the luminosity-weighted integral along the LoS. To calculate the average velocity dispersion, we make the following approximations. We assume that the flux is constant across a thin disc with finite radial extent. We also assume spatially constant velocity dispersion components and that $\sigma^2_{v,\perp} \equiv \sigma^2_{v,R} \approx \sigma^2_{v,\phi}$ then the average LoS velocity dispersion is given by,

$$\bar{\sigma}^2_{v,\mathrm{LoS}} = \sigma^2_{v,\perp}\sin^2 i + \sigma^2_{v,z}\cos^2 i. \quad (6)$$

Setting $\gamma^2 = \sigma^2_{v,z}/\sigma^2_{v,\perp}$, and rearranging, then

$$\sigma_{v,\mathrm{LoS}} = \sigma_{v,z}\sqrt{\sin^2 i/\gamma^2 + \cos^2 i} \quad (7)$$

The above model predicts changing $\sigma_{v,\mathrm{LoS}}$ as a function of i if $\gamma \neq 1$. For $\gamma > 1$, $\sigma_{v,\mathrm{LoS}}$ increases with increasing i, whereas $\sigma_{v,\mathrm{LoS}}$ decreases with i when $\gamma < 1$.

To estimate γ we assume that $\sigma_{v,\mathrm{LoS}}$ follows a loguniform distribution with mean $\sigma_{v,z,0}$ and log variance τ^2. The generating function for a single data point $\sigma_{v,z,i}$ is then,

$$p(\sigma_{v,\mathrm{LoS},j}|\sigma_{v,z,0},\tau^2,\gamma) \sim \mathrm{lognormal}(\sigma_{v,z,0}\sqrt{\sin^2 i/\gamma^2 + \cos^2 i},\tau^2). \quad (8)$$

We assume the following priors,

$$p(\sigma_{v,z,0}) \sim \mathrm{loguniform}(1,100) \quad (9)$$

$$p(\tau) \sim \mathrm{loguniform}(10^{-3},1) \quad (10)$$

$$p(\gamma) \sim \mathrm{loguniform}(0.1,10). \quad (11)$$

The posterior distribution is then given by,

$$p(\sigma_{v,z0},\tau,\gamma|\mathbf{D}) = p(\sigma_{v,z,0})p(\tau)p(\gamma)\prod_{j=1}^{N} p(\sigma_{v,\mathrm{LoS},j}|\sigma_{v,z,0},\tau^2,\gamma). \quad (12)$$

The above formulation assumes independence of the prior distribution between $\sigma_{v,z,0}$, τ, γ, as well as all $\sigma_{v,\mathrm{LoS},j}$. The above posterior distribution can now be sampled using typical techniques. We used emcee to sample the posterior distribution (Foreman-Mackey et al. 2013).

We estimate $\gamma = 0.80^{+0.06}_{-0.05}$ as shown in Figure 4, suggesting that the vertical velocity dispersion is less than the averaged azimuthal and radial components. This analysis was consistent with other approaches that we applied. For example, the bootstrapped Spearman-rank correlation coefficient distribution between the inclination and $\sigma_{v,\mathrm{LoS}}$ was $\rho(i,\sigma_{v,\mathrm{LoS}}) = 0.18^{+0.05}_{-0.05}$, where the uncertainties for the Sperman-rank correlation coefficient is estimated as the 68% shortest credible interval after bootstrap resampling. We also performed the above analysis using uniform priors for $\sigma_{v,z,0}$ and γ with the same ranges, yet we still find $\gamma = 0.80^{+0.06}_{-0.06}$.

Previous studies have suggested that $\sigma_{v,z}/\sigma_{v,R} \sim 0.6$ (Section 1.2.2, Glazebrook 2013) for stars. Mean H I gas velocity dispersion was reported up to ∼ 3 times higher for galaxies observed at $i > 60°$ compared to $i < 60°$ by Leroy et al. (2008), also suggesting that the contribution of $\sigma_{v,R}$ and $\sigma_{v,\phi}$ dominates.

Studies of ionised gas kinematics have typically not reported or found evidence that $\sigma_{v,z}$ is related to the inclination. For example, studies of high-z galaxies in the KMOS3D Survey have found no significant correlation between the axis ratio $q = b/a$ and $\sigma_{v,\mathrm{LoS}}$ (Wisnioski et al. 2015; Übler et al. 2019). However, such a relation may be difficult to identify in high-z galaxies with lower signal-to-noise and spatial resolution.

We estimate the vertical velocity dispersion ($\sigma_{v,z}$) for individual galaxies by inverting Equation 7 and using $\gamma = 0.8$. We estimated the Spearman-rank correlation between the inclination and $\sigma_{v,z}$ to be $\rho(i,\sigma_{v,z}) = 0.00^{+0.05}_{-0.05}$ after performing the correction per galaxy, suggesting that our analysis appropriately removed the correlation as a function of the inclination angle (see Figure 5).

Converting from $\sigma_{v,\mathrm{LoS}}$ to $\sigma_{v,z}$ adjusts the reported values by a couple of km s^{-1}. The marginalised distributions yield $\sigma_{v,\mathrm{LoS}} = 21.1^{+3.9}_{-5.2}$ km s^{-1} and $\sigma_{v,z} = 18.8^{+3.4}_{-4.8}$ km s^{-1} (see Figure 6). Typical differences are $\sigma_{v,\mathrm{LoS}} - \sigma_{v,z} = 2.4^{+0.9}_{-1.3}$ km s^{-1}, with the greatest correction being $\sigma_{v,\mathrm{LoS}} - \sigma_{v,z} = 7.9$ km s^{-1}.

For the remainder of this paper, we will report the values of $\sigma_{v,z}$. The subsequent analysis and results do not change qualitatively whether we use $\sigma_{v,z}$ or $\sigma_{v,\mathrm{LoS}}$, but $\sigma_{v,z}$ is preferred as it is an estimator free from effects from the viewing angle. It is also more appropriate to compare $\sigma_{v,z}$ to theoretical models, as they are

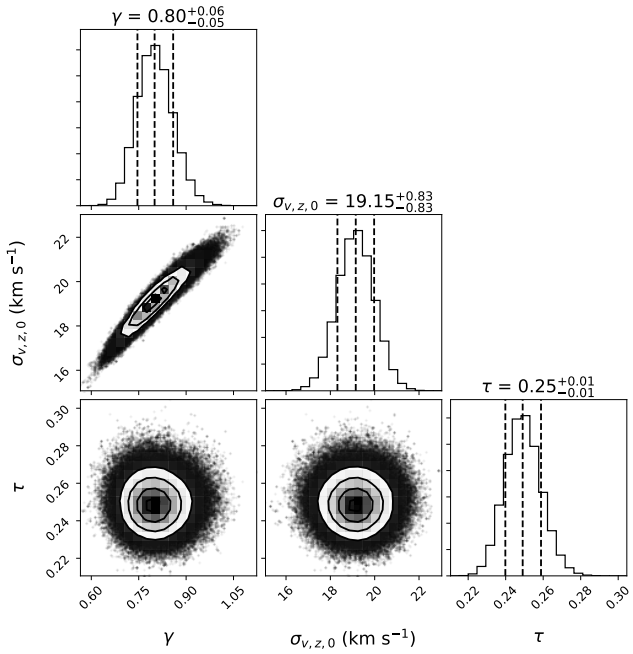

Figure 4. Corner plot (Foreman-Mackey 2016) showing the marginalised (diagonal) and joint (off-diagonal) posterior distributions for the parameter estimation for the inclination dependence model. There is evidence for a dependence of $\sigma_{v,\mathrm{LoS}}$ on inclination for our sample of galaxies from the SAMI Galaxy Survey. This suggests that the vertical velocity dispersion ($\sigma_{v,z}$) is less than the averaged azimuthal and radial velocity dispersion ($\sigma_{v,\perp}$).

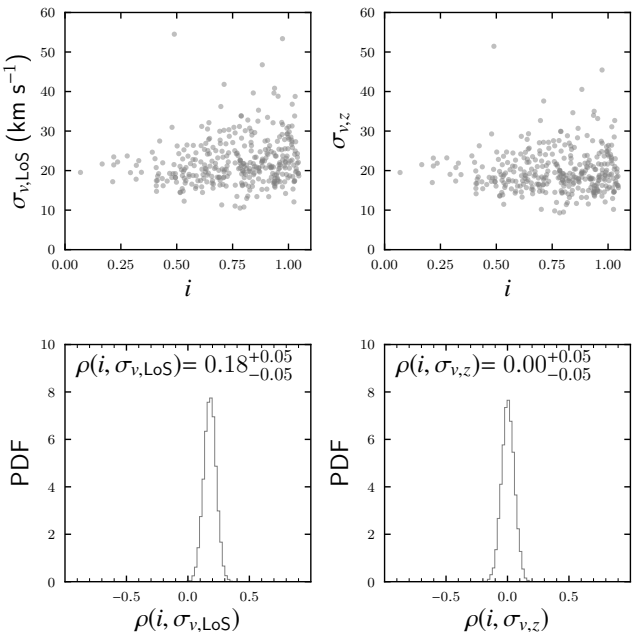

Figure 5. The relationship between the inclination (i) and inferred velocity dispersion estimates. We also show the PDF of the Spearman-rank correlation coefficients using bootstrap resampling (bottom). There is evidence for a weak positive correlation between the LoS velocity dispersion $\sigma_{v,\mathrm{LoS}}$ and i. Whereas the distribution for the vertical velocity dispersion after applying a correction factor yields no relation with i.

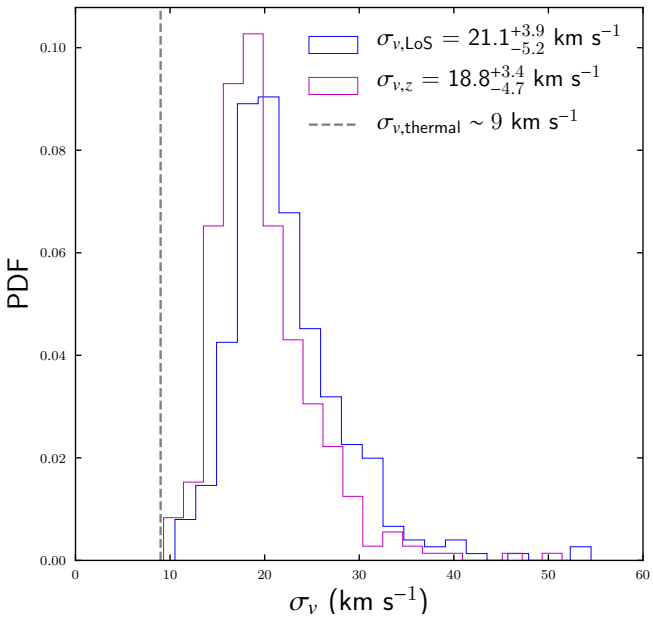

Figure 6. The distribution of the LoS ($\sigma_{v,\mathrm{LoS}}$, blue) and vertical ($\sigma_{v,z}$, red) velocity dispersion for our sample of galaxies from the SAMI Galaxy Survey. The estimated vertical velocity dispersion is adjusted down with respect to $\sigma_{v,\mathrm{LoS}}$ by a couple of km s^{-1} in accordance with the inclination correction described in Section 3.2.3.

typically framed with respect to $\sigma_{v,z}$. We report both values in Appendix A.

We have not applied the inclination correction for galaxies observed in the DYNAMO survey. This is due to finding no significant relation with $\rho(i, \sigma_{v,\mathrm{los}}) = -0.09^{+0.15}_{-0.15}$ for our galaxies from the DYNAMO survey. This suggests that there is no inclination effect to correct for within this sample. It may be that the sample from the DYNAMO survey is too small to infer the inclination effect. In this case, we choose not to apply the inclination effect found from the SAMI Galaxy Survey, as it is still possible that the inferred effect is methodological rather than physical across all galaxies.

3.3 Circular velocity estimates

Blobby3D estimates the LoS velocity profile using the empirical model proposed by Courteau (1997),

$$v(r) = v_c \frac{(1 + r_t/r)^{\beta}}{(1 + (r_t/r)^{\gamma})^{1/\gamma}} \sin(i) \cos(\theta) + v_{\mathrm{sys}}. \quad (13)$$

Where v_c is the asymptotic velocity and v_{sys} is the systemic velocity. r is defined by the distance to the kinematic centre. r_t is the turnover radius. β is a shape parameter that controls the gradient for $r > r_t$, where the velocity gradient increases for $\beta < 0$, and decreases when $\beta > 0$. γ is a shape parameter that controls how sharply the velocity profile turns over. i is the inclination of the galaxy. Then θ is the polar angle in the plane of the disc.

We intend to estimate the circular velocity from our inferred parameters. While v_c is a natural choice, it is difficult to get a strong constraint on v_c across our complete sample due to the FoV for the SAMI Galaxy Survey typically extending out to ~1.5 R_e. Instead, we estimate the absolute circular velocity at 2.2 R_e denoted as $v_{2.2}$ following (Bloom et al. 2017a).

For low values of i, small differences in the estimated i can result in large difference of $v_{2.2}$. Therefore, for low values of i,

incorrect estimates for the observed ellipticity can result in large changes in our estimates for the inclination. As such, we restrict our calculated values for $v_{2.2}$ to galaxies in the range $i \in [30°, 60°]$ ($e \in [0.13, 0.5]$ assuming a thin disc).

Similarly, galaxies with $R_e < 3.0''$ tended to have very large scatter on their $v_{2.2}$. At these limits, the spatial resolution of our observations are likely playing a role in increasing the scatter in the rotational velocity estimates. 230 galaxies meet the above inclination and R_e criteria. We only reference $v_{2.2}$ for galaxies that meet that inclination for the remainder of this paper.

3.4 Integrated star-formation rates

We used the best fit SFRs from the GAMA Survey (Gunawardhana et al. 2013; Davies et al. 2016; Driver et al. 2018). The SFRs are estimated using full spectral energy distribution (SED) fitting of 21 bands of photometry across the UV, optical, and far infrared ranges with MAGPHYS (da Cunha et al. 2008). MAGPHYS fits the observed photometry using a library that includes stellar spectral and dust emission profiles. In this way, the SFRs are corrected for dust emission. These estimates for the SFR were used instead of the SAMI Hα luminosity maps as there are known aperture affects given the limited FoV of the SAMI instrument (Appendix A, Medling et al. 2018).

For the galaxies from the DYNAMO survey, we used the SFR values reported by Green et al. (2014). SFRs were estimated using the Hα luminosity estimated from their observations. The SFR estimate includes a dust correction using the Balmer decrement from the ratio between their measured Hα and Hβ measurements. The SFR was then calculated using the dust-corrected Hα luminosity maps that were converted to SFR maps using the Kennicutt et al. (1994) conversion assuming a Chabrier (2003) IMF.

3.5 Integrated H I gas measurements

Follow-up 21 cm observations of SAMI galaxies were obtained as part of the SAMI-HI survey, carried out with the Arecibo radio telescope (Catinella et al. in prep.). Observations and data reduction were analogous to those of the xGASS survey (Catinella et al. 2018), with the only difference that these were not gas fraction-limited observations. We observed each galaxy until detected, but moved to another target if there was no hint of H I signal within the first 20-25 minutes of on-source integration.

H I emission-line spectra were obtained for 153 galaxies with these dedicated follow-up observations; on-source integration times ranged between 2 and 50 minutes, with an average of 15 minutes. Together with an additional 143 good HI detections (i.e., classified as detection code '1') in the Arecibo Legacy Fast ALFA (ALFALFA Giovanelli et al. 2005; Haynes et al. 2018) survey, SAMI-H I includes global H I spectra for 296 SAMI galaxies from the SAMI Galaxy Survey catalogue. 95 galaxies overlap with our sample selection from the SAMI Galaxy Survey.

4 RESULTS

4.1 Low gas velocity dispersion in the SAMI Galaxy Survey

We find vertical velocity dispersions lower than previously reported for studies of the gas kinematics in the SAMI Galaxy Survey. The median vertical velocity dispersion is $\sigma_{v,z} = 18.8$ km s^{-1} for our sample as shown in Figure 6. The 68-th shortest credible interval is [14.1, 22.1] km s^{-1} and the 95-th shortest credible interval is [11.4, 30.0] km s^{-1}. The maximum inferred vertical velocity dispersion for a single galaxy is $\sigma_{v,z} = 51$ km s^{-1}. We now compare this to two other studies of the gas kinematics of galaxies from the SAMI Galaxy Survey by Zhou et al. (2017) and Johnson et al. (2018).

Analysing 8 star-forming galaxies in the SAMI Galaxy Survey, Zhou et al. (2017) found that 7 out of 8 galaxies had $\sigma_{\rm gas} \in [20, 31]$ km s^{-1}. Their remaining galaxy (GAMA 508421) was reported as $\sigma_{\rm gas} = 87 \pm 44$ km s^{-1}. GAMA 508421 exhibits a high circular velocity in the outskirts of the SAMI FoV ($v \sim 130$ km s^{-1}) and a clear centralised peak in velocity dispersion that is typical of beam smearing affected galaxies. Our estimate for GAMA 508421 is $\sigma_{v,z} = 22$ km s^{-1}. As such, we suspect that the reported velocity dispersion for GAMA 508421 is greater than it's intrinsic velocity dispersion.

The discrepancy between Zhou et al. (2017) and our estimates, particularly with GAMA 508421, is most likely due to the different beam smearing corrections. Zhou et al. (2017) report the flux-weighted mean velocity dispersion using spaxels where $\sigma_v > 2v_{\rm grad}$. $v_{\rm grad}$ is an estimate for the local velocity gradient using adjacent spaxels defined as (Varidel et al. 2016),

$$v_{\rm grad}(x, y) = \sqrt{(v(x+1) - v(x-1))^2 + (v(y+1) - v(y-1))^2}. \quad (14)$$

See Section 5.1.1 by Varidel et al. (2019) for a revised calculation of the velocity gradient using a finite-difference scheme.

The approach used by Zhou et al. (2017) usually removes the centre of the galaxies, where the velocity gradient is steepest. This approach results in a significant downward correction compared to the uncorrected velocity dispersion estimates. However, the outskirts of galaxies can still be affected by beam smearing. Also, it is possible that the centre of the galaxy may be effected by beam smearing, yet not reach the $\sigma_v > 2v_{\rm grad}$ criteria, which is likely to have occurred in the case of GAMA 508421. The approach of Zhou et al. (2017) was also shown previously to over-estimate the intrinsic velocity dispersion in toy models (Section 5.1.1., Varidel et al. 2019)

Another study of a sample of 274 star-forming galaxies from the SAMI Galaxy Survey was performed by Johnson et al. (2018). They removed galaxies with $M_* > 8 \times 10^{10}$ M$_\odot$ and Sérsic index of $n > 2$. They also removed galaxies that they deem to be spatially unresolved or have kinematic uncertainties greater than 30%. While they do not provide summary statistics for their inferred velocity dispersion values from the SAMI Galaxy Survey, their plots show a typical range of $\sigma_0 \in [20, 60]$ km s^{-1}, plus one galaxy at $\sigma_0 \sim 90$ km s^{-1}. This is slightly above our range of velocity disperisions.

To estimate the intrinsic velocity dispersion, Johnson et al. (2018) calculated the median velocity dispersion across the kinematic maps or at the outskirts of their galaxy. They then apply a further correction on their estimated velocity dispersion by using a lookup table of toy galaxies that have been constructed with beam smearing effects. The slight difference between our studies may be driven solely by their choice of using a single FWHM estimate for the PSF rather than the Moffat profile used in this paper. Also, increased scatter may occur in their estimator due to being affected by low signal-to-noise spaxels in the outskirts of the galaxies.

4.2 Correlation of global velocity dispersion and integrated star-formation rate

Correlation analysis between the global velocity dispersion and several global galaxy properties from the SAMI Galaxy Survey

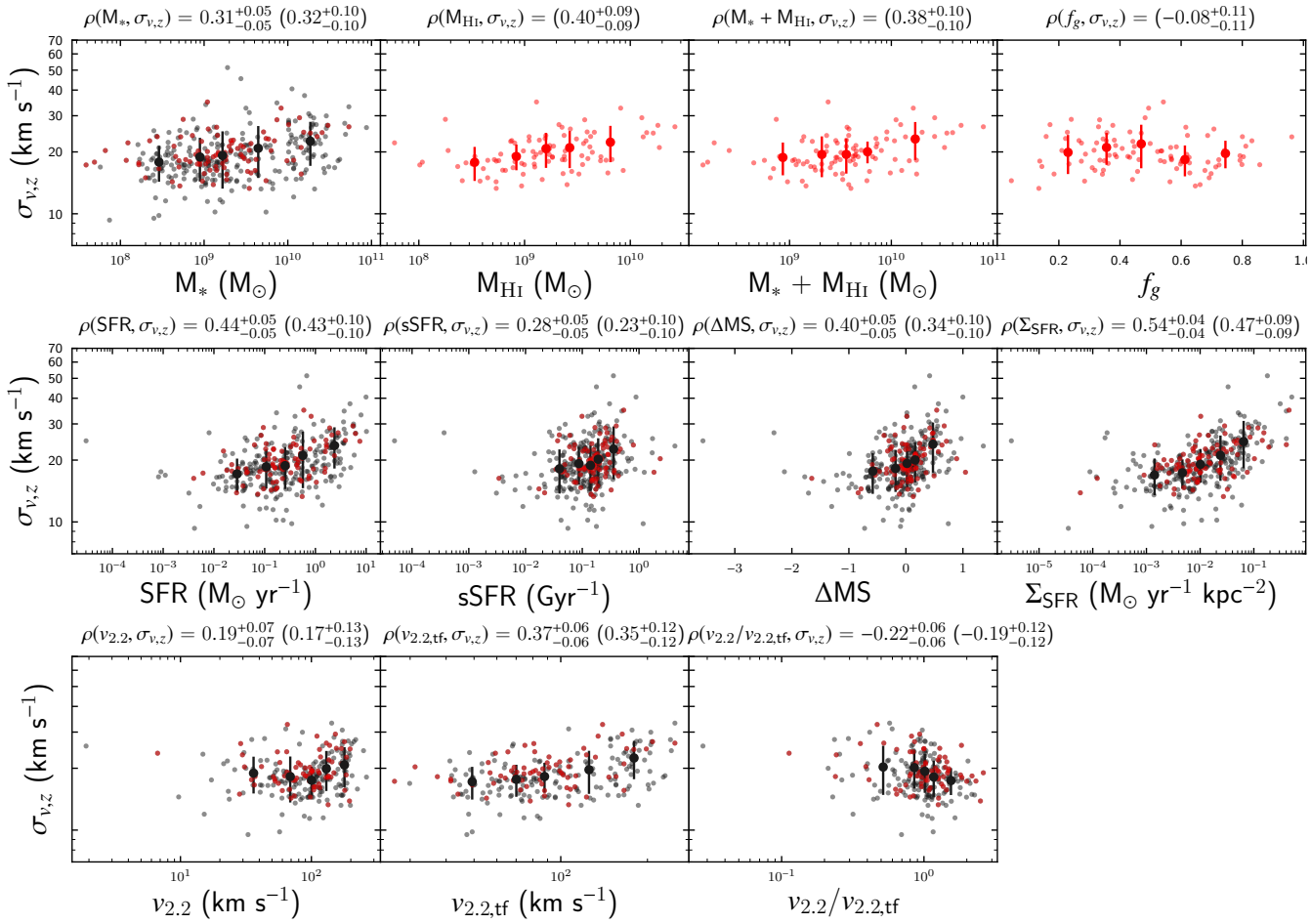

Figure 7. Comparing global intrinsic vertical velocity dispersion ($\sigma_{v,z}$) to global properties for galaxies from the SAMI Galaxy Survey. We show the relation of $\sigma_{v,z}$ with measures of mass (top), star-formation rate (middle), and rotational velocity (bottom), respectively. Red points indicate the galaxies with observed integrated H I masses. The Spearman-rank correlation coefficients are shown at the top of each plot, with brackets indicating the correlation coefficient for galaxies with measured H I masses. The uncertainties for the Spearman-rank correlation coefficients are estimated as the 68% shortest credible interval from 10^4 bootstrapped samples. We find significant positive correlations with measures of mass, star-formation rate, and rotational velocity. The greatest positive correlation we find is with star-formation rate surface density (Σ_{SFR}).

reveals that $\sigma_{v,z}$ has the greatest positive correlation with star-formation rate measures (Figure 7). We estimate the Spearman-rank correlation between the SFR and $\sigma_{v,z}$ to be $\rho(\mathrm{SFR}, \sigma_{v,z}) = 0.44^{+0.05}_{-0.05}$. We control for several factors in order to investigate this relationship further.

The correlation between $\sigma_{v,z}$ and star-formation rate increases when accounting for the galaxy size. To do this, we estimate the average star-formation rate surface density, $\Sigma_{SFR} = SFR/\pi R_e^2$ where R_e is the effective radius. The Spearman-rank correlation is then $\rho(\Sigma_{SFR}, \sigma_{v,z}) = 0.54^{+0.04}_{-0.04}$. Velocity dispersion is expected to increase with star-formation rate surface density assuming that star-formation feedback processes are acting as a driver of turbulence (e.g. Ostriker & Shetty 2011; Faucher-Giguère et al. 2013). As such, this does provide support that star-formation feedback processes is acting as a driver of turbulence within this sample of galaxies.

Figure 7 also shows a positive correlation between $\sigma_{v,z}$ and integrated stellar mass (M_*), H I gas mass ($M_{H\,I}$), as well as the sum of M_* and $M_{H\,I}$. Interestingly, there is a suggestion that $M_{H\,I}$ is slightly more correlated than M_* with $\sigma_{v,z}$, although the uncertainties are wide enough that we cannot confirm that is the case. SFR is well known to be correlated with M_*, which adds a further complication in determining the relation between $\sigma_{v,z}$ and SFR.

To account for the SFR – M_* relation, we calculated the specific star-formation rate (sSFR = SFR/M_*) and ΔMS. ΔMS is calculated as the log difference between the SFR and the star-forming main sequence relation as proposed by Renzini & Peng (2015). We find that the correlation between $\sigma_{v,z}$ and star-formation rate decreased after accounting for stellar mass. This suggests that the relation between $\sigma_{v,z}$ and star-formation rate is a combination of both SFR and stellar mass related quantities.

Despite the correlation between $\sigma_{v,z}$ and star-formation rate estimators, the absolute change in $\sigma_{v,z}$ as a function of SFR remains slight across the dynamic range of SFR $\in [10^{-3}, 10]$ $M_\odot$ yr^{-1}. We report the change in velocity dispersion in 5 SFR bins in Table 1. The change in mean velocity dispersion between the end bins from SFR = 0.029 $M_\odot$ yr^{-1} to SFR = 2.4 $M_\odot$ yr^{-1} is only 6.41 km s^{-1}. A similarly shallow gradient was found by Johnson et al. (2018) using data from the SAMI Galaxy Survey.

Galaxies are often kinematically classified as either rotationally or turbulence dominated by comparing the ratio of rotational and

Table 1. Comparing summary statistics of the vertical velocity dispersion in other samples compared to those in this work. Each sample was split into 5 bins of equal percentile widths. We show the mean ($\bar{\sigma}_{v,z}$), standard deviation ($\Delta\sigma_{v,z}$), the standard error ($\Delta\bar{\sigma}_{v,z}$), median (med($\sigma_{v,z}$)), and bootstrap resampled standard deviation of the median (Δmed($\sigma_{v,z}$)). The groups of galaxies are as follows: Low-z (Hα) (Epinat et al. 2008; Moiseev et al. 2015), H I surveys where 15 km s^{-1} has been added in-quadrature (Leroy et al. 2008; Walter et al. 2008; Ianjamasimanana et al. 2012; Stilp et al. 2013), high-z analogues from Varidel et al. (2016) plus the re-analysed galaxies from the DYNAMO survey, plus high-z (Hα) (Cresci et al. 2009; Epinat et al. 2009; Jones et al. 2010; Wisnioski et al. 2011, 2015; Wuyts et al. 2016; Di Teodoro et al. 2016; Johnson et al. 2018).

Group	Bin	SFR (M$_\odot$ yr^{-1})	$\bar{\sigma}_{v,z}$ (km s^{-1})	$\Delta\sigma_{v,z}$ (km s^{-1})	$\Delta\bar{\sigma}_{v,z}$ (km s^{-1})	med($\sigma_{v,z}$) (km s^{-1})	Δmed($\sigma_{v,z}$) (km s^{-1})
SAMI (Hα)	1	0.029	17.12	3.21	0.39	17.13	0.29
	2	0.11	18.54	3.99	0.49	18.31	0.41
	3	0.25	18.79	4.34	0.53	18.52	0.43
	4	0.57	21.07	6.47	0.79	19.72	0.71
	5	2.4	23.54	5.35	0.65	23.54	0.64
Low-z (Hα)	1	0.0047	19.46	2.89	0.43	18.84	0.72
	2	0.046	20.77	4.33	0.65	19.21	0.41
	3	0.18	20.57	3.86	0.58	19.21	0.6
	4	0.37	21.66	4.55	0.68	19.85	0.44
	5	1.0	23.5	7.0	1.0	21.21	0.81
Low-z (HI)	1	0.0014	16.95	0.55	0.18	16.86	0.15
	2	0.005	17.39	0.64	0.20	17.44	0.25
	3	0.066	18.65	2.98	0.99	17.81	0.6
	4	0.58	19.18	1.36	0.43	18.78	0.57
	5	2.2	20.82	2.58	0.82	19.9	1.4
High-z	1	0.96	27.0	3.2	1.1	26.23	0.94
Analogues (Hα)	2	3.2	39.4	12.6	4.4	40.0	4.9
	3	9.1	40.7	14.3	5.0	41.2	7.8
	4	17	43.0	15.2	5.4	42.9	7.6
	5	27	55.9	15.6	5.2	54.8	5.4
High-z (Hα)	1	3.4	44.0	20.5	1.6	39.8	1.9
	2	6.4	45.8	18.2	1.5	43.1	1.2
	3	10	44.3	20.3	1.6	42.8	3.2
	4	20	48.3	20.2	1.6	45.0	1.5
	5	82	53.2	20.0	1.6	51.0	2.6

random velocities (v/σ). In a similar vain to such analysis, we also investigated the relation between $\sigma_{v,z}$ and rotational velocity. $\sigma_{v,z}$ is shown compared to the rotational velocity measures using Bloбby3D ($v_{2.2}$) as outlined in Section 3.3 and using the Tully-Fisher relation ($v_{2.2,\mathrm{tf}}$, Bloom et al. 2017b), where

$$\log_{10}(v_{2.2}/\mathrm{km\ s^{-1}}) = 0.31\log(M_*/M_\odot) - 0.93. \quad (15)$$

We find a positive correlation between $\sigma_{v,z}$ and the rotational velocity estimators. This is to be expected as rotational velocity is also correlated with stellar mass. To control for that effect, we calculated the ratio between $v_{2.2}$ and $v_{2.2,\mathrm{tf}}$. We then find a negative correlation between $\sigma_{v,z}$ and $v_{2.2}/v_{2.2,\mathrm{tf}}$. As such, we observe that galaxies exhibit greater rotation than their mass predicts when $\sigma_{v,z}$ is lesser, and lesser rotation when $\sigma_{v,z}$ is greater.

4.3 Comparisons with other surveys

In this section we aim to describe our results from the SAMI Galaxy Survey in the context of other studies. In Table 1 and Figure 8 we show comparisons of velocity dispersion compared to SFR. The data is shown in four groups of galaxies; low-z measured using Hα (Epinat et al. 2008; Moiseev et al. 2015), low-z measured using H I (Leroy et al. 2008; Walter et al. 2008; Ianjamasimanana et al. 2012; Stilp et al. 2013), High-z analogues from Varidel et al. (2016) plus the galaxies that we re-analysed from the DYNAMO sample, and high-z galaxies at z $\gtrsim$ 1 (Johnson et al. 2018; Cresci et al. 2009; Wisnioski et al. 2011; Epinat et al. 2009; Law et al. 2009; Jones et al. 2010; Di Teodoro et al. 2016). Table 2 also outlines qualitative ranges for the galaxy parameters for galaxies at low-z measured using the Hα emission line, including other studies of the SAMI and DYNAMO samples.

The comparative data sets have been measured using both ionised and neutral gas. For ionised gas, there are two additional contributions to the velocity dispersion. One is the thermal broadening of $\sigma_{\mathrm{thermal}} \sim 9$ km s^{-1}, corresponding to the typical temperature of an H II region. There is also a contribution from the expansion speed of the H II region. Studies of the expansions speed reveal $\sigma_{\mathrm{expand}} \sim 10$ km s^{-1} for small regions, up to $\sigma_{\mathrm{expand}} \sim 13 - 17$ km s^{-1} for larger regions (Chu & Kennicutt 1994).

Given the contributions of $\sigma_{\mathrm{thermal}}$ and σ_{expand} to the observed ionised gas kinematics, we perform several adjustments to the comparative velocity dispersion estimates. For ionised gas estimates, we remove any corrections for the additional contributions. For H I studies, we assume a nominal contribution due to these effects of 15 km s^{-1}, that we add in quadrature to the published velocity dispersion estimates. We note that in other studies, 15 km s^{-1} has been subtracted in quadrature from the ionised gas measurements for comparisons between different studies. We prefer the alternative as 15% of our galaxies have $\sigma_{v,z} < 15$ km s^{-1}.

4.3.1 *Comparison with surveys at low-z*

The SAMI Galaxy Survey has similar selection criteria to the Mapping Nearby Galaxies at Apache Point Observatory (MaNGA, Bundy et al. 2015) survey in terms of fundamental galaxy properties (see Table 2). Our data have similar ranges in redshifts, stellar mass,

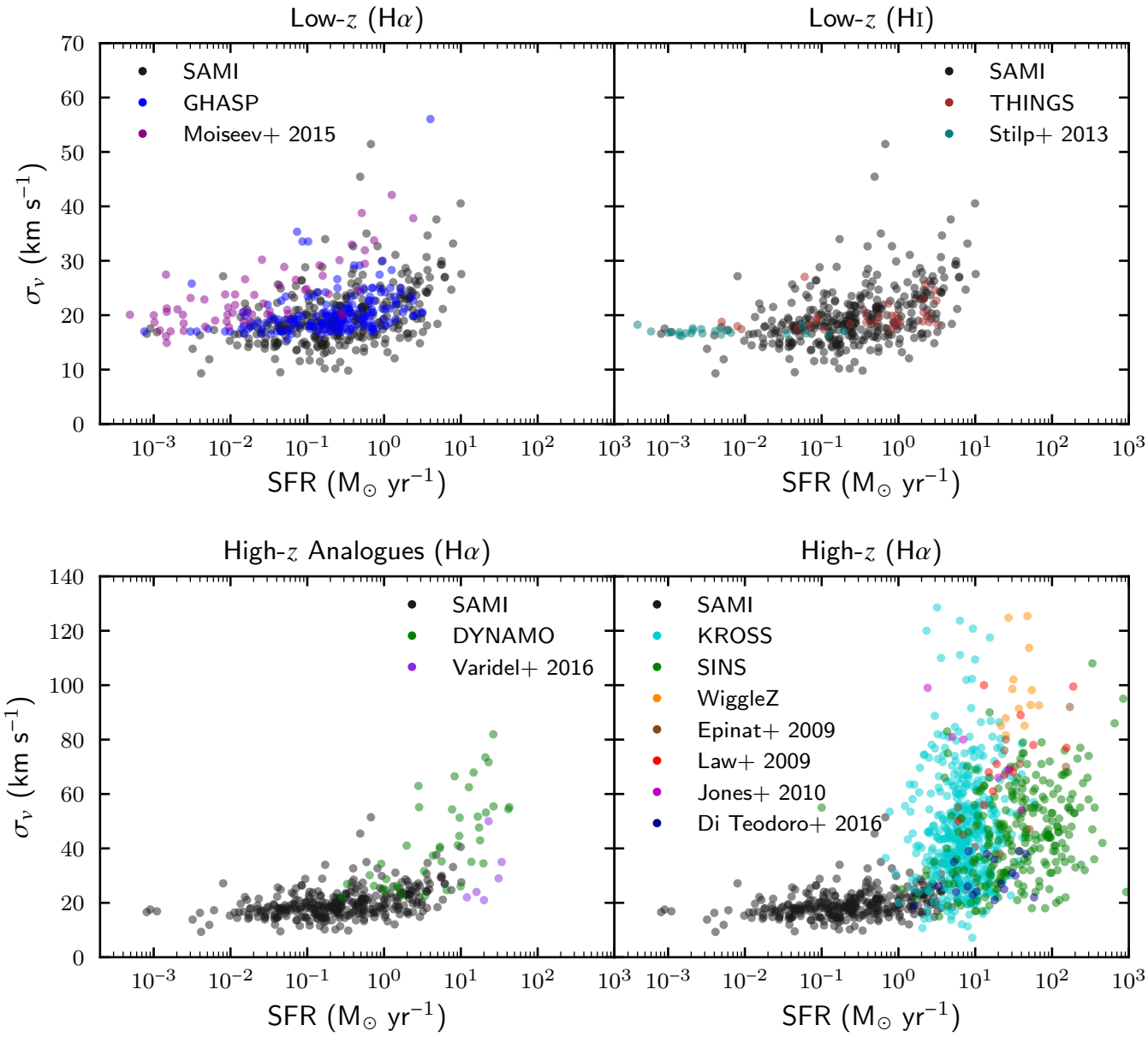

Figure 8. Comparison of the SFR – velocity dispersion (σ_v) relation compared to others surveys in the literature. The sets of galaxies that constitute each subplot are the same as outlined in Table 1. We find the SFR – σ_v relation increases slightly across the range SFR $\in [10^{-3}, 1]$ M$_\odot$ yr^{-1}, then turns up significantly at SFR $\gtrsim 1$ M$_\odot$ yr^{-1}. This relation is approximately consistent across all surveys.

and SFR. As such, we would naively expect the gas turbulence within our sample to be similar to the MaNGA survey estimates.

We find systematically lower velocity dispersions than those estimated by Yu et al. (2019). They estimated mean velocity dispersions of $\sigma \in [20, 50]$ km s^{-1} across various galaxy property ranges (Figure 6, Yu et al. 2019). Specifically for SFR vs. velocity dispersion they found mean $\sigma \in [30, 50]$ km s^{-1} across 4 bins in the range SFR $\in [10^{-2}, 10]$ M$_\odot$ yr^{-1}. Whereas we estimate mean $\bar{\sigma}_{v,z} \in [17, 24]$ km s^{-1} across 5 bins of SFR $\in [10^{-3}, 10]$.

Yu et al. (2019) also reported galaxies with velocity dispersion of $\sigma_v \gtrsim 50$ km s^{-1} up to $\sigma_v \sim 130$ km s^{-1}. This is similar to σ_v estimates for galaxies at high redshift (see high-z galaxies, Table 1). However, we see very little evidence for a significant fraction of galaxies with $\sigma_v \gtrsim 50$ km s^{-1}.

The spectral resolution of $\sigma_{\rm LSF} \in [50, 80]$ km s^{-1} (Bundy et al. 2015; Yu et al. 2019) may be an issue for MaNGA. The variability in the MaNGA spectral resolution could correspond to a large scatter in their estimated velocity dispersion, that may explain their upper limit of $\sigma_v \sim 100$ km s^{-1}. We also show that the velocity dispersion is significantly less than their spectral resolution, thus their assumptions regarding the LSF will be important.

Instead, our results are closer to the velocity dispersion estimates found in the Gassendi HAlpha survey of SPirals (GHASP, Epinat et al. 2008), where their galaxies overlap in SFR. We can see in Figure 8 that our samples match well with the work of Epinat et al. (2008)

Table 2. Qualitative ranges of galaxy parameters for low-z samples in the literature, where gas kinematics were estimated using the Hα emission line.

Sample	z	$\log_{10}(M_*/M_\odot)$	$\log_{10}(SFR / M_\odot\ yr^{-1})$	σ_v (km s^{-1})
SAMI (this work)	[0.005, 0.08]	[7.5, 11]	[-3, 1]	[10, 60]
SAMI (Johnson et al. 2018)	< 0.1	[7.5, 11]	[-3, 1]	[20, 90]
SAMI (Zhou et al. 2017)	< 0.1	[9.8, 10.8]	-	[20, 90]
DYNAMO (this work)	[0.06, 0.15]	[9, 11]	[-1, 2]	[10, 80]
DYNAMO (Green et al. 2014)	[0.06, 0.15]	[9, 11]	[-1, 2]	[10, 90]
GHASP (Epinat et al. 2008)	~ 0.01	-	[-3, 1]	[15, 30]
Moiseev et al. (2015)	$<$ 90 Mpc	-	[-3, 1]	[15, 40]
Varidel et al. (2016)	[0.01, 0.04]	[10.5, 11]	[1, 1.6]	[20, 50]
MaNGA (Yu et al. 2019)	[0.01, 0.15]	[8.5, 11.5]	[-2, 1]	[10, 130]

both in terms of mean velocity dispersion and gradient as a function of SFR. We only disagree slightly in terms of the intrinsic scatter, which could be sample selection, methodology, or signal-to-noise dependent.

We highlight that Epinat et al. (2008) estimated their velocity dispersion using the residuals in spatially resolved mean velocity compared to a rotational velocity model. As such, their measurements are fundamentally different and should not be affected by $\sigma_{\rm thermal}$ and $\sigma_{\rm expand}$. So we added 15 km s^{-1} in quadrature to their published velocity dispersion estimates for comparison purposes.

Our results are also qualitatively similar to those published by Moiseev et al. (2015), who studied a sample of nearby dwarf galaxies. Their results agree with the higher end of our velocity dispersion estimates, although there is still an offset in the mean velocity dispersion. We note that Moiseev et al. (2015) do not explicitly correct for beam smearing, but due to studying nearby galaxies at $<$ 90 Mpc, the effects of beam smearing should be minimal.

Combining the results of Moiseev et al. (2015) and Epinat et al. (2008), we find differences of the mean and median velocity dispersion estimates compared to our sample of $\sim 1-3$ km s^{-1} (see Table 1), where our results were systematically lower. The difference of ~ 2 km s^{-1} could be explained due to calculating $\sigma_{v,z}$ rather than $\sigma_{v,\rm LoS}$, which resulted in a downward shift in our velocity dispersion estimates by ~ 2 km s^{-1} as described in Section 3.2.3.

We find little difference in the intrinsic scatter between our sample and the combined samples of Moiseev et al. (2015) and Epinat et al. (2008). Calculating the 1-sigma standard deviation for the sample ($\Delta\sigma_{v,z}$), sample mean ($\Delta\bar{\sigma}_{v,z}$), and median (Δmed($\sigma_{v,z}$)), we find that all variance estimates were of similar magnitude (see Table 1). As such, we conclude that our results are approximately consistent with the analyses of Moiseev et al. (2015) and Epinat et al. (2008) at low-z using ionised gas, albeit with different selection and methodologies in inferring the intrinsic velocity dispersion. The only exception in inferred velocity dispersions at low-z using the ionised gas is the results of Yu et al. (2019) using MaNGA data where we estimate systematically lower σ_v.

Comparisons to the H I observations suggest that we get the same approximately flat SFR – σ_v relation across the range SFR $\in [10^{-3}, 10]$ M$_\odot$ yr^{-1}. While there are only slight differences between the mean velocity dispersion of $\sim 1-4$ km s^{-1} across varying SFR ranges, it is important to reiterate that the H I results have 15 km s^{-1} added in quadrature, which is the typical difference between H I and Hα estimates for the velocity dispersion. The varying contributions of $\sigma_{\rm thermal}$ and $\sigma_{\rm expand}$ may cause a larger scatter than the neutral hydrogen estimates.

4.3.2 *Comparisons with surveys at high-z and high-z analogues*

We now compare our results to those at high-z and high-z analogues. The data sets included are from the DYNAMO survey, which we have re-analysed using Blobby3D. We also include the beam-smearing corrected estimates denoted as $\sigma_{\rm m,uni,}{}_{v_g=0}$ from Varidel et al. (2016). These samples are of galaxies at low-z with SFR $\gtrsim 1$ M$_\odot$ yr^{-1}, that are similar to galaxies at high-z (see Table 1). As such, high-z analogues are likely to have similar properties to our galaxy sample at similar SFR.

Our re-analysis of the galaxies from the DYNAMO survey find results consistent with Green et al. (2014). The difference between our results and those of Green et al. (2014) are $\sigma_{v,z} - \sigma_{v,\rm green} = 0.0^{+4.9}_{-6.5}$ km s^{-1}. Follow-up studies of galaxies from the DYNAMO survey have also found similar results including re-analysis using alternative beam smearing corrections (Bekiaris et al. 2016) and observations using adaptive optics (Oliva-Altamirano et al. 2018).

There is a slight increase in σ_v when comparing SAMI with the high-z analogues at overlapping SFR. At SFR ~ 3 M$_\odot$ yr^{-1}, we estimate $\bar{\sigma}_{v,\rm SAMI} = 23.54 \pm 0.65$ km s^{-1} compared to $\bar{\sigma}_{v,\rm HzA} = 27.0 \pm 1.1$ km s^{-1} at SFR ~ 2.4 M$_\odot$ yr^{-1} and $\bar{\sigma}_{v,\rm HzA} = 39.4 \pm 4.4$ km s^{-1} at SFR ~ 3.2 M$_\odot$ yr^{-1} for the high-z analogues. The highest velocity dispersions are primarily from the DYNAMO survey. We note that while Blobby3D was applied to both samples, the PSF for DYNAMO was assumed to be a Gaussian profile compared to a Moffat profile for the SAMI Galaxy Survey. This may result in an increased beam smearing correction in the SAMI Galaxy Survey compared to the DYNAMO survey. Also, the inclination correction was only applied to SAMI, which resulted in a ~ 2 km s^{-1} subtraction to the initially inferred velocity dispersion from Blobby3D. As such, a difference of ~ 10 km s^{-1} may not be significant given limitations of comparing the two samples.

The high-z analogues extend the trend of increasing σ_v with SFR (see Figure 8). This trend starts to increases within the sample from SAMI Galaxy Survey at SFR $\gtrsim 1$ M$_\odot$ yr^{-1}. Expanding the star-formation rate range up to SFR ~ 100 M$_\odot$ yr^{-1} using the high-z analogues, we see that trend increases dramatically with σ_v up to 80 km s^{-1} in the range SFR $\in [10, 100]$ M$_\odot$ yr^{-1}, which is qualitatively consistent with samples at high-z.

The high-z galaxies exhibit a wide range of $\sigma_v \in [10, 150]$ km s^{-1}. Some of this extent is likely to be driven by lower signal-to-noise at higher redshift. Furthermore, systematic biases such as beam smearing effects, that act to increase σ_v, will be greater due to the lower spatial resolution. Instead, the high-z galaxies still exhibit similar σ_v as the high-z analogues when studied as a group.

The high-z galaxies still exhibit a trend of increasing velocity dis-

persion as function of SFR. There is a change from $\sigma_v \sim 40$ km s^{-1} to ~ 50 km s^{-1} for SFR of 3 to 82 M$_\odot$ yr^{-1} (see Table 1). We estimated the correlation to be $\rho(\mathrm{SFR}, \sigma_v) = 0.17^{+0.03}_{-0.04}$. This is a weaker correlation between SFR and σ_v than observed in low-z galaxies. Lesser correlation is likely linked to increased scatter for observations of galaxies at high-z. The increase in scatter may be driven by signal-to-noise, beam smearing effects due to lower spatial resolution, or a change in the physical drivers of gas turbulence at high-z.

There is evidence for increased σ_v at high-z compared to the high-z analogues at similar SFRs. In Table 1, we show binned estimators for dynamic ranges of SFR $\in [3, 30]$ M$_\odot$ yr^{-1} for these two samples. σ_v is $\sim$5 km s^{-1} higher at similar SFRs for the high-z galaxies compared to the high-z analogues.

5 THE DRIVERS OF TURBULENCE WITHIN LOW-Z GALAXIES

Turbulence in the Interstellar Medium (ISM) is expected to dissipate on the order of the disc crossing time (Mac Low et al. 1998; Stone et al. 1998). Thus, an ongoing energy source is required to maintain supersonic gas turbulence across epochs. Two proposed drivers are star-formation feedback process and gravity driven turbulence.

5.1 Star formation feedback driven turbulence

Star-formation feedback processes inject momentum into the ISM through several mechanisms. These mechanisms include supernova, stellar winds, expanding H II regions, and radiation pressure from highly dense star clusters. Therefore, there has been a claim that star-formation feedback processes could provide an ongoing source of energy for the supersonic turbulence in the ISM.

Observational studies have routinely found that there is a positive correlation between global σ_v and SFR, that has been used as evidence to support star-formation feedback processes as a driver of turbulence (Green et al. 2010, 2014; Moiseev et al. 2015; Johnson et al. 2018; Übler et al. 2019; Yu et al. 2019). In Section 4.2 we showed that this correlation exists in our sample of galaxies. We also showed that this correlation extends to higher SFR when connecting our sample to other galaxy surveys.

The relationship between SFR and σ_v has also been considered in theoretical and computational studies. Typically, the energy contribution from supernovae is considered to dominate, and therefore, has been the primary focus of most of these studies. The momentum injection per mass of stars is often assumed to be on the order of $\langle p_*/m_* \rangle = 3000$ km s^{-1}. Incorporating this momentum injection into theoretical models results in assuming that the rate of momentum injection is proportional to the star-formation rate surface density, thus $\dot{P} \propto \langle p_*/m_* \rangle \, \Sigma_{\mathrm{SFR}}$ (e.g. Ostriker & Shetty 2011; Faucher-Giguère et al. 2013; Krumholz et al. 2018). Therefore, we expect the velocity dispersion to be positively correlated with star-formation rate surface density, if star-formation feedback processes is playing a role in driving turbulence in the ISM.

We showed in Section 4.2 that $\sigma_{v,z}$ has a strong positive correlation with the galaxy averaged star-formation rate surface density. This is consistent with other analyses of the star-formation rate density and velocity dispersion (e.g. Lehnert et al. 2009; Yu et al. 2019; Übler et al. 2019). In some cases, this has been used as evidence for star-formation feedback processes acting as a primary driver of turbulence (Lehnert et al. 2009, 2013). Yet if star-formation feedback processes are acting as a driver of turbulence, we should expect that the localised Σ_{SFR} and σ_v are correlated, yet some analyses have found this relation (Lehnert et al. 2009, 2013), and other studies have found a weak or statistically insignificant relation between these localised properties (Genzel et al. 2011; Varidel et al. 2016; Zhou et al. 2017; Übler et al. 2019). Another approach to compare the observed velocity dispersion to the star-formation rate is to construct a bottom-up approach whereby Σ_{SFR} is modeled on the local scale and then integrated across the disc to estimate SFR.

To estimate Σ_{SFR} as a function of galaxy properties, it is first noted that the star-formation rate surface density is a function of the star-forming molecular gas fraction (f_{sf}) of the gas surface density (Σ_{gas}), that is then converted to stars at a star-formation rate efficiency per free-fall time (ϵ_{ff}). Following Krumholz et al. (2018) this can be written as,

$$\Sigma_{\mathrm{SFR}} = \frac{\epsilon_{\mathrm{ff}}}{t_{\mathrm{ff}}} f_{\mathrm{sf}} \Sigma_{\mathrm{gas}}, \tag{16}$$

where the remaining undefined quantity is the free-fall time (t_{ff}). This can then be incorporated into models to make predictions for the velocity dispersion.

One approach is to assume that the star-formation law is retained on the subgalactic scale. This assumes that ϵ_{ff} is approximately constant across the galaxy, which is broadly in agreement with the literature (Krumholz & Tan 2007; Krumholz et al. 2012; Federrath 2013; Salim et al. 2015; Krumholz et al. 2019). While some studies have found evidence for varying ϵ_{ff} as a function of galaxy properties (Hirota et al. 2018; Utomo et al. 2018), the results and implications for the value of ϵ_{ff} remains in dispute. Furthemore, studies using the above approximation have found that $\sigma_{v,z} \lesssim 25$ km s^{-1}, with little variation of $\sigma_{v,z}$ as a function of star-formation rate (Ostriker & Shetty 2011; Krumholz et al. 2018). As noted in the above samples, there is a large population of galaxies with $\sigma_{v,z} \gtrsim 25$ km s^{-1}, particularly at high redshifts. As such, it is unlikely that this model is able to explain the full range of observed $\sigma_{v,z}$. Furthermore, such models allow for the variation of the Toomre Q stability parameter, which leads to disagreements with observations. Hereafter, we will use the 'No Transport, Fixed ϵ_{ff}' model constructed by Krumholz et al. (2018) as representative of such models.

Another approach is to assume that ϵ_{ff} can vary as a function of galaxy properties. One such approach was developed by Faucher-Giguère et al. (2013), which assumes that the Toomre stability criteria Q self-regulates to 1. In their model, when $Q < 1$ the rate of constructing giant molecular clouds (GMCs) increases, thus increasing star-formation efficiency, driving Q upwards to 1. When $Q > 1$ the rate of GMC construction is limited and thus star-formation slows, leading to Q decreasing to 1. The Faucher-Giguère et al. (2013) model predicts that ϵ_{ff} increases with molecular gas content of the galaxy, leading to a correlation between SFR and velocity dispersion, thus potentially providing an explanation for the SFR – σ_v relation. Hereafter, we will refer to this model as 'No Transport, Fixed Q' and use the analytical model proposed by Krumholz et al. (2018) for comparison in the following sections.

5.2 Gravity driven turbulence

An alternative to star-formation feedback processes is driving of turbulence due to gravitational mechanisms. In such models, the gravitational potential energy of the gas is converted to kinetic energy, thus driving the turbulence in the ISM. Several mechanisms for this to occur are via accretion onto the disc, accretion through the disc, gravitational instabilities in the disc, or gravitational interactions between components of the disc.

During the initial formation of the disc, there is evidence that accretion onto the disc can cause the high levels of gas turbulence. However, this can only be sustained on the order of the accretion time (Aumer et al. 2010; Elmegreen & Burkert 2010). After initial disc formation, the effect of accretion onto the disc is unlikely to have a significant contribution on the gas turbulence (Hopkins et al. 2013).

Instead, it has been shown that the supersonic turbulence initially set in the ISM during galaxy formation will quickly approach a steady-state solution (Krumholz & Burkert 2010). Such a steady state solution can be found where the sole driving force is due to the accretion of gas through the disc balanced by the loss of turbulence primarily by shocks. This yields prescriptions for radial models of the gas surface density and $\sigma_{v,z}$. Making simplifying assumptions whereby the entire ISM is assumed to be a single star-forming region, and integrating the models over the radial extent of the disc, they derive a relationship that simplifies to SFR $\propto \sigma_{v,z}$, assuming other disc parameters are constant.

The above model is an instantaneous steady state solution, that is a function of the gas accretion rate and energy loss at the time. As the gas accretion rate has decreased over epochs, this model predicts lower gas turbulence in the ISM of galaxies at low-z. In Section 4.3.2 we highlighted that velocity dispersions were ~ 5 km s^{-1} higher in the high-z sample compared to the high-z analogues sample at similar SFR. This is consistent with the velocity dispersion decreasing as a function of decreasing gas accretion rate over time. Numerous other studies have also found that gas turbulence increases as a function of z (Kassin et al. 2012; Wisnioski et al. 2015; Johnson et al. 2018; Übler et al. 2019).

5.3 Combining star-formation feedback and gravity driven turbulence

Krumholz et al. (2018) recently pointed out that star-formation feedback processes can be added as an extra source of energy to the transport equation derived in Krumholz & Burkert (2010). Similar to the previously mentioned models for star-formation feedback processes, they only assume the contribution of supernovae on the gas turbulence.

Their full 'Transport + Feedback' model gives a SFR – $\sigma_{v,z}$ relation of the form,

$$\mathrm{SFR} = \frac{2}{1+\beta}\frac{\phi_a f_{\rm sf}}{\pi G Q} f_{g,Q} v_c^2 \sigma_{v,z} \times \max\left[\sqrt{\frac{2(1+\beta)}{3 f_{\rm g,P}}}\phi_{\rm mp}\frac{8\epsilon_{\rm ff} f_{g,Q}}{Q}, \frac{t_{\rm orb,out}}{t_{\rm sf,\,max}}\right] \quad (17)$$

$f_{\rm sf}$ is the fraction of the gas in the molecular star-forming phase. $f_{g,P}$ is the fractional contribution of the gas to the self-gravitation pressure at the mid-plane. $f_{g,Q}$ is the fractional gas contribution to the toomre-Q parameter. β describes the slope of the rotation curve ($\beta = d\ln v_c / d\ln r$). $t_{\rm sf,\,max}$ corresponds to the maximum star-formation timescale. $t_{\rm orb,\,out}$ corresponds to the orbital period at the edge of the star-forming dominated disc. ϕ_a is a constant that accounts for an offset due to observing global rather than local properties, with $\phi_a = 1$ for local galaxies. $\phi_{\rm mp} = 1.4$ corresponds to the assumed ratio of total pressure compared to turbulent pressure at the mid-plane.

This model results in a SFR – $\sigma_{v,z}$ relation with a floor at 10 km s^{-1} $\lesssim \sigma_{v,z} \lesssim$ 20 km s^{-1} (including the expansion and thermal contributions) for the lower SFR region, thus reproducing gas turbulence that is consistent with the 'No Transport, Fixed $\epsilon_{\rm ff}$' model.

Table 3. Parameter values for Krumholz et al. (2018) theoretical model tracks used for Figure 9.

Parameter	Local dwarf	Local Spiral	High-z
$f_{\rm sf}$	0.2	0.5	1.0
v_c (km s^{-1})	100	220	200
$t_{\rm orb}$ (Myr)	100	200	200
β	0.5	0.0	0.0
$f_{g,Q} = f_{g,P}$	0.9	0.5	0.7
ϕ_a	1	1	3
SFR$_{\rm min}$ (M$_\odot$ yr^{-1})	-	-	1
SFR$_{\rm max}$ (M$_\odot$ yr^{-1})	0.5	50	-

The SFR – $\sigma_{v,z}$ relation then transitions to SFR $\propto \sigma_{v,z}$ for higher SFR, consistent with the 'No Feedback' model.

Another important contribution of Krumholz et al. (2018) is that after deriving the transport equation, they can use it to find the steady state solutions making various assumptions. The above model assumes that there is a contribution of star-formation driven turbulence ($\sigma_{v,\rm sf}$) to the total turbulence ($\sigma_{v,z}$), where

$$\sigma_{v,\rm sf} = \frac{4 f_{\rm sf}\epsilon_{\rm ff}\langle p_*/m_*\rangle}{\sqrt{3 f_{g,P}}\pi\eta\phi_{\rm mp}\phi_Q\phi_{\rm nt}^{3/2}} \times \max\left[1, \sqrt{\frac{3 f_{g,P}}{8(1+\beta)}}\frac{Q_{\rm min}\phi_{\rm mp}}{4 f_{g,Q}\epsilon_{\rm ff}}\frac{t_{\rm orb}}{t_{\rm sf,\,max}}\right]. \quad (18)$$

Here $\eta = 1.5$ is a scaling parameter for the dissipation rate. $\phi_{\rm mp} = 1.4$ is the ratio of total to turbulent pressure at the midplane. $\phi_Q = 2$ is the gas to stellar Q plus one. By setting $\sigma_{v,\rm sf} = 0$, Krumholz et al. (2018) derive the 'No Feedback' model. In that case, the disc must remain stable, such that $Q = 1$.

Krumholz et al. (2018) derive the 'No Transport, Fixed $\epsilon_{\rm ff}$' model by setting $\sigma_{v,z} = \sigma_{v,\rm sf}$. In that case, the contribution is purely driven by the balance between gravitational collapse and star-formation driven by supernovae outwards. The model is similar to the model proposed by Ostriker & Shetty (2011).

The 'No Transport, Fixed Q' model, is derived by revisiting their transport equation and looking for solutions where Q is set as a constant. They derive a slightly different relation given by,

$$\mathrm{SFR} = \frac{4\eta\sqrt{\phi_{\rm mp}\phi_{\rm nt}^3}\phi_Q}{GQ^2}\left(\frac{p_*}{m_*}\right)^{-1}\frac{f_{g,Q}^2}{f_{g,P}} v_c^2\sigma_{v,z}^2. \quad (19)$$

The formulation of different drivers using the same theoretical backing allows for a relatively easy comparison between the observations and different model assumptions.

5.4 Comparison with theoretical model tracks

We now compare our observations to the theoretical models described above. We compare our data to the Krumholz et al. (2018) theoretical model tracks for various galaxy groups; low-z dwarfs, low-z spirals, and high-z galaxies. For each galaxy group we use the set of parameters suggested by Krumholz et al. (2018), which are shown in Table 3. To account for the thermal and expansion contributions to the velocity dispersion of the H II regions, 15 km s^{-1} was added in quadrature to the theoretical models.

We find the best agreement between our data and the 'Transport + Feedback' model (Figure 9). The lower-end of the SFR – $\sigma_{v,z}$ relation in the range SFR $\in [10^{-3}, 1]$ M$_\odot$ yr^{-1} is explained by the floor of the 'Transport + Feedback' model tracks, which is driven by star-formation feedback processes. Importantly, the slight increase

in $\sigma_{v,z}$ can be explained by a change in galaxy properties across the dynamic range of SFR. The upturn in the SFR – $\sigma_{v,z}$ relation at SFR $\gtrsim 1$ M$_\odot$ yr^{-1} is also consistent with 'Transport + Feedback' model tracks. This is in contrast to the alternative models, that cannot account for the relation across the full dynamic range of SFR.

The 'No Feedback' model is able to model the upturn in the SFR – $\sigma_{v,z}$ relation, but it cannot account for the lower-end of the relation. At the lower end of the relation, this model assumes $\sigma_{v,z}$ approaches the thermal and expansion contributions alone. We observed that most of our galaxies lie above the assumed $\sigma_{v,z} > 15$ km s^{-1} contributions from the thermal and expansion broadening. Furthermore, there is a positive correlation of $\sigma_{v,z}$ with SFR even at SFR $\lesssim 10$ M$_\odot$ yr^{-1} that the 'No Feedback' model does not appear to account for. Despite the 'No Feedback' model appearing to be a better model, we note that it is difficult to distinguish between the 'No Feedback model' and 'Transport + Feedback' model, as the thermal and expansion broadening contribution is not well known.

The 'No Transport, Fixed $\epsilon_{\rm ff}$' model accounts well for the lower-end SFR – $\sigma_{v,z}$ relation in our sample. However, it predicts very little evolution in $\sigma_{v,z}$ across galaxy properties for low-z galaxies. This is in contrast to the observations that do appear to have an upturn in $\sigma_{v,z}$ for increasing SFR. This suggests that there must be an additional energetic input to the 'No Transport, Fixed $\epsilon_{\rm ff}$' to account for increase $\sigma_{v,z}$ across SFR.

The 'No Transport, Fixed Q' model provides an alternative SFR – $\sigma_{v,z}$ relation (SFR $\propto \sigma_{v,z}^2$). The upturn in the theoretical relation qualitatively matches the observed upturn. However, the model tracks are lower than the observed $\sigma_{v,z}$. Similar to the 'No Feedback' model, increasing the thermal and expansion contributions to $\sigma_{v,z}$ would result in better agreement. The 'No Transport, Fixed Q' cannot account for the increased scatter in $\sigma_{v,z}$ for increasing SFR, due to estimating very little variation in $\sigma_{v,z}$ across most of our dynamic range of SFR.

To distinguish between the 'Transport + Feedback' and 'No Transport, Fixed Q' models, we also compare the theoretical model tracks while varying the circular velocity (see Figure 10). We see generally good agreement between the 'Transport + Feedback' model tracks and the observed velocity dispersion. The upturn in the velocity dispersion occurs approximately at the expected circular velocity.

To quantify the differences, we calculate the relative residuals between the data and the models. To do this, we used the 'local spiral' tracks for SFR < 10 M$_\odot$ yr^{-1} and a model with intermediate parameters between the 'local spiral' and 'high-z' models ($f_{\rm sf} = 0.8$, $t_{\rm orb} = 200$ M$_\odot$ yr^{-1}, $\beta = 0$, $f_{g,Q} = f_{g,P} = 0.6$, $\phi_a = 2$) for SFR ≥ 10 M$_\odot$ yr^{-1}. The relative residuals between the model tracks and data reveal $\Delta\sigma_{v,z}/\sigma_{v,z} = -0.02 \pm 0.32$ for the 'Transport + Feedback' model compared to $\Delta\sigma_{v,z}/\sigma_{v,z} = 0.29 \pm 0.42$ for the 'No Transport, Fixed Q' model. In particular, the relative residuals for the 'No Tranport, Fixed Q' model increase to $\Delta\sigma_{v,z}/\sigma_{v,z} = 1.16 \pm 0.52$ for SFR > 10 M$_\odot$ yr^{-1}. Thus, suggesting that the 'Transport + Feedback' model provides a better fit to the data than the 'No Transport, Fixed Q' model.

For galaxies at SFR $\gtrsim 10$ M$_\odot$ yr^{-1}, we require a transition to values more representative of the high-z galaxy model tracks, with higher $f_{\rm sf}$, $f_{g,Q}$, and $f_{g,P}$ to explain the SFR – $\sigma_{v,z}$ relation. This is not surprising given that those galaxies were selected from the DYNAMO sample. Many of these galaxies exhibit similar properties to those of high-z galaxies (Green et al. 2014; Fisher et al. 2017) including increased molecular gas fractions (Fisher et al. 2014).

A similar conclusion was reached by Übler et al. (2019), when comparing the 'Transport + Feedback' model tracks as a function of circular velocity for high-z galaxies. They found ~60% of their galaxies could be explained by varying the circular velocity alone.

Increasing the molecular gas fraction ($f_{\rm sf}$) and the gas gravitational contribution at the mid-plane ($f_{g,Q}$, $f_{g,P}$) also shifts the base $\sigma_{v,z}$ by a few km s^{-1}. As galaxies shift to higher $f_{\rm sf}$, $f_{g,Q}$, $f_{g,P}$ as a function of SFR, this provides a mechanism to explain the increase in $\sigma_{v,z}$ seen in the SAMI Galaxy Survey (see Section 3.2.1).

In comparison, the 'No Transport, Fixed Q' model predicts an increase in $\sigma_{v,z}$ as a function of SFR at a slower rate than the 'Transport + Feedback' model. Comparing the model tracks when varying the circular velocity and gas properties, we find that the $\sigma_{v,z} \gtrsim 30$ km s^{-1} are not predicted unless assuming a much lower circular velocity ($v_{2.2,\rm tf} \lesssim 50$ km s^{-1}) than expected given the stellar masses of the galaxies. Increasing the molecular gas content and gas gravitational contribution at the mid-plane as in the high-z galaxies only shifts the model tracks to higher SFR.

The above analysis suggests that the 'Transport + Feedback' model provides a better agreement with the data than those dominated by star-formation feedback processes. This does not completely rule out star-formation feedback processes as the primary driver, instead it may suggest that the assumed energy momentum due to star-formation feedback is too low. The assumed energy source is purely from single supernova, with momentum injection per unit of stars of $\langle p_*/m_* \rangle = 3000$ km s^{-1}. However, $\langle p_*/m_* \rangle$ may be significantly higher if other sources are incorporated. For example, Gentry et al. (2017) argue that $\langle p_*/m_* \rangle$ could be up to an order of magnitude higher when incorporating the effects of clustered supernova. As such, further studies will be required to understand the energetic sources of star-formation feedback processes to incorporate in these models.

As a further caveat to the above analysis, we note that the theoretical models assume that we are observing the star-forming molecular gas, rather than the ionised gas. The full set of differences between the kinematics of the molecular star-forming gas compared to the ionised gas is not complete. For example, there is evidence that ionised gas may have systematically lower rotation and higher velocity dispersions compared to the molecular gas (Levy et al. 2018). However, there is limited research into these differences at this time, as such we make the assumption that these differences are minimal. Further research into the differences in molecular gas and ionised gas kinematics will be required.

5.5 Comparing the correlation analysis to the theoretical models

The above theoretical models (Equations 17 and 19) suggest that SFR $\propto v_c^2$, all else being set equal. Thus, we should expect a strong inverse relationship between $\sigma_{v,z}$ and v_c. In Figure 7 we showed that there is a negative correlation between velocity dispersion and rotational velocity after accounting for the stellar mass contribution. We are forced to control for the stellar mass using the Tully-Fisher relation as both $\sigma_{v,z}$ and v_c increase for increasing stellar mass.

As such, the rotational velocity is a significant factor in prescribing the intrinsic turbulence within the galaxy. This is consistent with the theoretical models of Krumholz et al. (2018). However, the relationship between the turbulence and rotational velocity does not distinguish between star-formation feedback or gravitational driven mechanisms of turbulence.

The proposed models also suggest a dependence of the SFR – $\sigma_{v,z}$ relation on the mid-plane gas fraction ($f_{g,P}$), the mid-plane gas contribution to the toomre-Q parameter ($f_{g,Q}$), and on the molecular

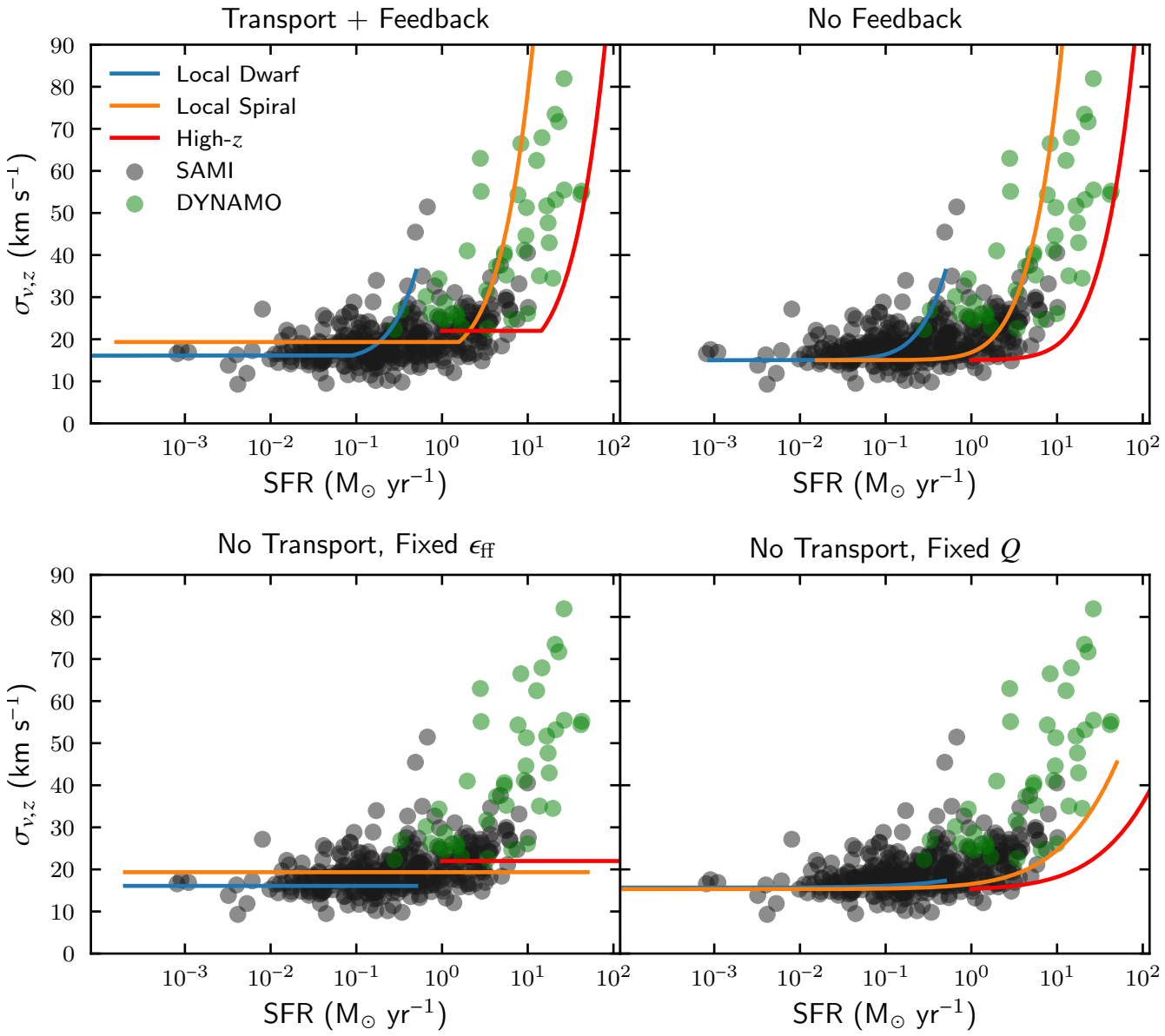

Figure 9. Comparison of the intrinsic vertical velocity dispersion compared to the theoretical model proposed by Krumholz et al. (2018). We show the 'Transport + Feedback', 'No Feedback', 'No Transport, Fixed $\epsilon_{\rm ff}$', and 'No Transport, Fixed Q' models. The individual tracks use a set of parameters (see Table 3) that represent typical galaxies for each galaxy type. We find that our observations are the most consistent with the 'Transport + Feedback' model.

to neutral gas fraction ($f_{\rm sf}$). Krumholz et al. (2018) also showed that galaxy turbulence driven solely by star-formation feedback has the relation SFR $\propto \sigma_v f_{g,Q}^2 / f_{g,P}$ whereas solely driven by gravitational mechanisms has SFR $\propto \sigma_v f_{g,Q}^2$.

The contribution of the gas content to the velocity dispersion is difficult to determine in our sample. We have measurements of the integrated H I mass for 95 galaxies in our sample from the SAMI Galaxy Survey. We showed a slight negative but still consistent with zero correlation between the total H I gas fraction (f_g) and $\sigma_{v,z}$ in Section 3.2.1.

A negative correlation between integrated H I mass and $\sigma_{v,z}$ could be due to the expected negative correlation expected between $\sigma_{v,z}$ and $f_{g,Q}$ in the 'Transport + Feedback' model. However, it could also be a result of increasing molecular gas fraction ($f_{\rm sf}$) for increasing SFR and M$_*$ that are also positively correlated with $\sigma_{v,z}$. We also note that the integrated H I measurements are not the ideal measurement as we cannot determine the mid-plane H I gas content within each galaxy. To accurately determine the relation between $\sigma_{v,z}$ and the gas content of the galaxy, we expect that resolved measurements of the H I and H_2 masses are required. In that way, we would be able to more precisely determine the mid-plane gravitational contribution of the galaxy gas content. We note that recent work by Sun et al. (2020) has begun to shed light on the mid-plane gas contributions to the observed turbulence, although further studies will be required.

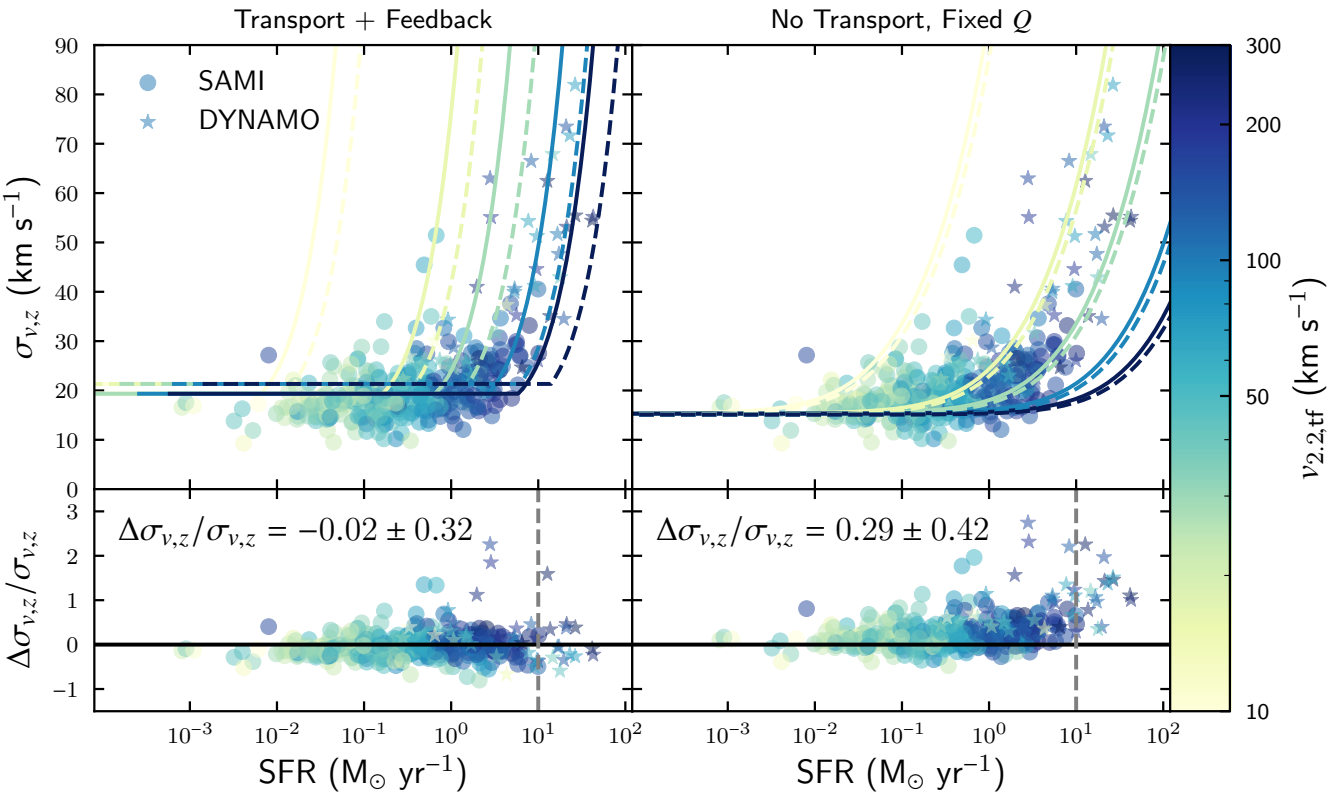

Figure 10. Comparison of the velocity dispersions for the total galaxy sample to the 'Transport + Feedback' (left) and 'No Transport, Fixed Q' (right) models proposed by Krumholz et al. (2018). The top two panels show the data compared to the model tracks, where the data and model tracks are colour coded by $v_{2.2,tf}$. For all other input parameters to the model tracks, the solid lines use the 'local spiral'. The dashed lines use intermediate values between the 'local spiral' and 'high-z' models; $f_{sf} = 0.8$, $t_{orb} = 200$ M$_\odot$ yr^{-1}, $\beta = 0$, $f_{g,Q} = f_{g,P} = 0.6$, $\phi_a = 2$. See Table 3 for the 'local spiral' and 'high-z' parameters. The bottom two panels show the relative residuals, where $\Delta\sigma_{v,z} = \sigma_{v,z} - \sigma_{v,z,\mathrm{model}}$. We use the models represented by the solid lines for SFR < 10 M$_\odot$ yr^{-1} and the dashed lines for SFR $\geq$ 10 M$_\odot$ yr^{-1}. We also show the mean and standard deviation of the relative residuals for each model. Both theoretical models predict an increase in $\sigma_{v,z}$ as a function of SFR, however, 'Transport + Feedback' provides a better fit as a function of circular velocity ($v_{2.2,tf}$).

6 CONCLUSIONS

We studied the intrinsic kinematic properties of the ionised gas in 383 low-z star-forming galaxies. 342 galaxies were obtained from the SAMI Galaxy Survey DR2 plus another 41 were from the DYNAMO survey. The total galaxy sample spans a wide range of galaxy properties with SFR $\in [10^{-3}, 10^{2}]$ M$_\odot$ yr^{-1}. The intrinsic gas kinematics were estimated using Blobby3D. Blobby3D is a flexible galaxy modelling approach that assumes that the galaxy is regularly rotating with spatially clumpy ionised gas distributions. In order to mitigate the effects of beam smearing and instrumental broadening, a convolution by the PSF and LSF on the underlying model is performed prior to calculating the likelihood function. We also performed a minor inclination correction for the sample from the SAMI Galaxy Survey to estimate the intrinsic vertical velocity dispersion ($\sigma_{v,z}$) as described in Section 3.2.1.

The sample of galaxies from the SAMI Galaxy Survey is a representation of typical galaxies at $z \lesssim 0.1$. As such, we only used that galaxy sample to determine the typical gas kinematics in galaxies at $z \lesssim 0.1$. We find the following:

- Low velocity dispersions of $\sigma_{v,z} \in [14.1, 22.1]$ km s^{-1} for the 68% shortest credible interval. This is $\sim$ 10 km s^{-1} lower than previous studies of the SAMI Galaxy Survey. The difference in results is likely driven by our beam smearing correction technique using Blobby3D, compared to the heuristic approaches applied by Zhou et al. (2017) and Johnson et al. (2018). We also find little evidence for a significant population of galaxies with $\sigma_{v,z} \gtrsim 50$ km s^{-1} as found by Yu et al. (2019) in a sample of galaxies of similar galaxy properties from the MaNGA Survey. In contrast, our velocity dispersions are approximately consistent with other studies of nearby galaxies (Moiseev et al. 2015; Epinat et al. 2008).
- There is a significant positive correlation between $\sigma_{v,z}$ and star-formation rate measures. The greatest correlation was with Σ_{SFR}. Although, the correlation is significant, the average $\sigma_{v,z}$ only increased by $\sim$ 6 km s^{-1} for a dynamic range of SFR $\in [10^{-3}, 10]$ M$_\odot$ yr^{-1}.
- We also find positive correlations of $\sigma_{v,z}$ with integrated stellar and H I gas mass as well as absolute rotational velocity.
- After controlling for stellar mass, there is a negative correlation between $\sigma_{v,z}$ and rotational velocity. This is consistent with theoretical models proposed by Krumholz et al. (2018) for both star-formation feedback processes and gravitational driving mechanisms of turbulence.
- We find a weak, but still consistent with zero, negative trend between $\sigma_{v,z}$ and the integrated H I gas fraction. Theoretical models

have suggested that there should be a relation between the gravitational contributions of the gas at the mid-plane and $\sigma_{v,z}$. We suspect that the signal between gas fraction and $\sigma_{v,z}$ is lost when using the integrated H I mass. Accurately determining the gravitational contributions of both H I and H_2 at the mid-plane is likely required to observe the proposed relations.

The combined SAMI Galaxy Survey and DYNAMO data sets span a wide range of SFR, allowing for improved comparisons to the theoretical models proposed by Krumholz et al. (2018). The SFR – $\sigma_{v,z}$ relation for our sample of galaxies is the most consistent with the 'Transport + Feedback' model proposed by Krumholz et al. (2018). We find that the SFR – $\sigma_{v,z}$ relation can be approximately explained by a transition of increasing circular velocity and molecular gas at higher SFR.

ACKNOWLEDGEMENTS

The SAMI Galaxy Survey is based on observations made at the Anglo-Australian Telescope. The Sydney-AAO Multi-object Integral field spectrograph (SAMI) was developed jointly by the University of Sydney and the Australian Astronomical Observatory. The SAMI input catalogue is based on data taken from the Sloan Digital Sky Survey, the GAMA Survey and the VST ATLAS Survey. The SAMI Galaxy Survey is supported by the Australian Research Council Centre of Excellence for All Sky Astrophysics in 3 Dimensions (ASTRO 3D), through project number CE170100013, the Australian Research Council Centre of Excellence for All-sky Astrophysics (CAASTRO), through project number CE110001020, and other participating institutions. The SAMI Galaxy Survey website is `http://sami-survey.org/`.

The authors acknowledge the University of Sydney HPC service at The University of Sydney for providing HPC and database resources that have contributed to the research results reported within this paper. URL: `http://sydney.edu.au/research_support/`

DBF and KG acknowledge support from the Australian Research Council Discovery Program grant DP160102235. DBF acknowledges support from Australian Research Council Future Fellowship FT170100376. LC is the recipient of an Australian Research Council Future Fellowship (FT180100066) funded by the Australian Government. MRK acknowledges support from Australian Research Council Future Fellowship FT180100375, and from a Humboldt Research Award from the Alexander von Humboldt Foundation. JJB acknowledges support of an Australian Research Council Future Fellowship (FT180100231). CF acknowledges funding provided by the Australian Research Council (Discovery Projects DP170100603 and Future Fellowship FT180100495), and the Australia-Germany Joint Research Cooperation Scheme (UA-DAAD). BG is the recipient of an Australian Research Council Future Fellowship (FT140101202). MSO acknowledges the funding support from the Australian Research Council through a Future Fellowship (FT140100255). JvdS is funded under JBH's ARC Laureate Fellowship (FL140100278).

REFERENCES

Aumer M., Burkert A., Johansson P. H., Genzel R., 2010, ApJ, 719, 1230
Bekiaris G., Glazebrook K., Fluke C. J., Abraham R., 2016, MNRAS, 455, 754
Bland-Hawthorn J., et al., 2011, Optics Express, 19, 2649
Bloom J. V., et al., 2017a, MNRAS, 465, 123
Bloom J. V., et al., 2017b, MNRAS, 472, 1809
Brewer B., Foreman-Mackey D., 2018, Journal of Statistical Software, Articles, 86, 1
Brewer B. J., Pártay L. B., Csányi G., 2011, Statistics and Computing, 21, 649
Bryant J. J., Bland-Hawthorn J., Fogarty L. M. R., Lawrence J. S., Croom S. M., 2014, MNRAS, 438, 869
Bryant J. J., et al., 2015, MNRAS, 447, 2857
Bundy K., et al., 2015, ApJ, 798, 7
Cappellari M., 2019, arXiv e-prints, p. arXiv:1907.09894
Catinella B., et al., 2018, MNRAS, 476, 875
Ceverino D., Dekel A., Bournaud F., 2010, MNRAS, 404, 2151
Chabrier G., 2003, PASP, 115, 763
Chu Y.-H., Kennicutt Robert C. J., 1994, ApJ, 425, 720
Cid Fernandes R., Stasińska G., Mateus A., Vale Asari N., 2011, MNRAS, 413, 1687
Courteau S., 1997, AJ, 114, 2402
Cresci G., et al., 2009, ApJ, 697, 115
Croom S. M., et al., 2012, MNRAS, 421, 872
Davies R., et al., 2011, ApJ, 741, 69
Davies L. J. M., et al., 2016, MNRAS, 461, 458
Dekel A., et al., 2009, Nature, 457, 451
Di Teodoro E. M., Fraternali F., 2015, MNRAS, 451, 3021
Di Teodoro E. M., Fraternali F., Miller S. H., 2016, A&A, 594, A77
Dobbs C. L., Bonnell I. A., 2007, MNRAS, 374, 1115
Dopita M., Hart J., McGregor P., Oates P., Bloxham G., Jones D., 2007, Ap&SS, 310, 255
Driver S. P., et al., 2011, MNRAS, 413, 971
Driver S. P., et al., 2018, MNRAS, 475, 2891
Elmegreen B. G., Burkert A., 2010, The Astrophysical Journal, 712, 294
Epinat B., Amram P., Marcelin M., 2008, MNRAS, 390, 466
Epinat B., et al., 2009, A&A, 504, 789
Epinat B., Amram P., Balkowski C., Marcelin M., 2010, MNRAS, 401, 2113
Faucher-Giguère C.-A., Quataert E., Hopkins P. F., 2013, MNRAS, 433, 1970
Federrath C., 2013, MNRAS, 436, 3167
Federrath C., et al., 2016, ApJ, 832, 143
Federrath C., et al., 2017, in Crocker R. M., Longmore S. N., Bicknell G. V., eds, IAU Symposium Vol. 322, The Multi-Messenger Astrophysics of the Galactic Centre. pp 123–128 (`arXiv:1609.08726`), doi:10.1017/S1743921316012357
Fisher D. B., et al., 2014, ApJ, 790, L30
Fisher D. B., et al., 2017, MNRAS, 464, 491
Foreman-Mackey D., 2016, The Journal of Open Source Software, 1, 24
Foreman-Mackey D., Hogg D. W., Lang D., Goodman J., 2013, PASP, 125, 306
Förster Schreiber N. M., et al., 2009, ApJ, 706, 1364
Gentry E. S., Krumholz M. R., Dekel A., Madau P., 2017, MNRAS, 465, 2471
Genzel R., et al., 2006, Nature, 442, 786
Genzel R., et al., 2011, ApJ, 733, 101
Giovanelli R., et al., 2005, AJ, 130, 2613
Glazebrook K., 2013, Publications of the Astronomical Society of Australia, 30, e056
Green A. W., et al., 2010, Nature, 467, 684
Green A. W., et al., 2014, MNRAS, 437, 1070
Green A. W., et al., 2018, MNRAS, 475, 716
Gunawardhana M. L. P., et al., 2013, MNRAS, 433, 2764
Haynes M. P., et al., 2018, ApJ, 861, 49
Hinshaw G., et al., 2009, ApJS, 180, 225
Hirota A., et al., 2018, PASJ, 70, 73
Hopkins P. F., Kereš D., Murray N., 2013, Monthly Notices of the Royal Astronomical Society, 432, 2639
Ianjamasimanana R., de Blok W. J. G., Walter F., Heald G. H., 2012, AJ, 144, 96
Johnson H. L., et al., 2018, MNRAS, 474, 5076
Jones T. A., Swinbank A. M., Ellis R. S., Richard J., Stark D. P., 2010, MNRAS, 404, 1247
Kassin S. A., et al., 2012, The Astrophysical Journal, 758, 106

Kauffmann G., et al., 2003, MNRAS, 346, 1055
Kelvin L. S., et al., 2012, MNRAS, 421, 1007
Kennicutt Robert C. J., Tamblyn P., Congdon C. E., 1994, ApJ, 435, 22
Krumholz M., Burkert A., 2010, ApJ, 724, 895
Krumholz M. R., Burkhart B., 2016, MNRAS, 458, 1671
Krumholz M. R., Matzner C. D., 2009, ApJ, 703, 1352
Krumholz M. R., Tan J. C., 2007, ApJ, 654, 304
Krumholz M. R., Dekel A., McKee C. F., 2012, ApJ, 745, 69
Krumholz M. R., Burkhart B., Forbes J. C., Crocker R. M., 2018, MNRAS, 477, 2716
Krumholz M. R., McKee C. F., Bland -Hawthorn J., 2019, ARA&A, 57, 227
Law D. R., Steidel C. C., Erb D. K., Larkin J. E., Pettini M., Shapley A. E., Wright S. A., 2007, ApJ, 669, 929
Law D. R., Steidel C. C., Erb D. K., Larkin J. E., Pettini M., Shapley A. E., Wright S. A., 2009, ApJ, 697, 2057
Lehnert M. D., Nesvadba N. P. H., Le Tiran L., Di Matteo P., van Driel W., Douglas L. S., Chemin L., Bournaud F., 2009, ApJ, 699, 1660
Lehnert M. D., Le Tiran L., Nesvadba N. P. H., van Driel W., Boulanger F., Di Matteo P., 2013, A&A, 555, A72
Lemoine-Busserolle M., Bunker A., Lamareille F., Kissler-Patig M., 2010, MNRAS, 401, 1657
Leroy A. K., Walter F., Brinks E., Bigiel F., de Blok W. J. G., Madore B., Thornley M. D., 2008, AJ, 136, 2782
Levy R. C., et al., 2018, ApJ, 860, 92
Mac Low M.-M., 1999, ApJ, 524, 169
Mac Low M.-M., Klessen R. S., 2004, Reviews of Modern Physics, 76, 125
Mac Low M.-M., Klessen R. S., Burkert A., Smith M. D., 1998, Phys. Rev. Lett., 80, 2754
Matzner C. D., 2002, ApJ, 566, 302
Medling A. M., et al., 2018, MNRAS, 475, 5194
Moiseev A. V., Tikhonov A. V., Klypin A., 2015, MNRAS, 449, 3568
Murray N., Quataert E., Thompson T. A., 2010, ApJ, 709, 191
Norman C. A., Ferrara A., 1996, ApJ, 467, 280
Oliva-Altamirano P., Fisher D. B., Glazebrook K., Wisnioski E., Bekiaris G., Bassett R., Obreschkow D., Abraham R., 2018, MNRAS, 474, 522
Ostriker E. C., Shetty R., 2011, ApJ, 731, 41
Owers M. S., et al., 2019, ApJ, 873, 52
Renzini A., Peng Y.-j., 2015, ApJ, 801, L29
Salim D. M., Federrath C., Kewley L. J., 2015, ApJ, 806, L36
Scott N., et al., 2018, MNRAS, 481, 2299
Sharp R., et al., 2006, in Society of Photo-Optical Instrumentation Engineers (SPIE) Conference Series. p. 62690G (arXiv:astro-ph/0606137), doi:10.1117/12.671022
Sharp R., et al., 2015, MNRAS, 446, 1551
Skilling J., 2004, in Fischer R., Preuss R., Toussaint U. V., eds, American Institute of Physics Conference Series Vol. 735, American Institute of Physics Conference Series. pp 395–405, doi:10.1063/1.1835238
Stilp A. M., Dalcanton J. J., Skillman E., Warren S. R., Ott J., Koribalski B., 2013, ApJ, 773, 88
Stone J. M., Ostriker E. C., Gammie C. F., 1998, ApJ, 508, L99
Sun J., et al., 2020, ApJ, 892, 148
Taylor E. N., et al., 2011, MNRAS, 418, 1587
Toomre A., 1964, ApJ, 139, 1217
Übler H., et al., 2019, ApJ, 880, 48
Utomo D., et al., 2018, ApJ, 861, L18
Varidel M., Pracy M., Croom S., Owers M. S., Sadler E., 2016, Publ. Astron. Soc. Australia, 33, e006
Varidel M. R., et al., 2019, MNRAS, 485, 4024
Walter F., Brinks E., de Blok W. J. G., Bigiel F., Kennicutt Robert C. J., Thornley M. D., Leroy A., 2008, AJ, 136, 2563
Wisnioski E., et al., 2011, MNRAS, 417, 2601
Wisnioski E., et al., 2015, ApJ, 799, 209
Wuyts S., et al., 2016, ApJ, 831, 149
York D. G., et al., 2000, AJ, 120, 1579
Yu X., et al., 2019, MNRAS, 486, 4463
Zhou L., et al., 2017, MNRAS, 470, 4573
da Cunha E., Charlot S., Elbaz D., 2008, MNRAS, 388, 1595
van de Sande J., et al., 2017, ApJ, 835, 104

APPENDIX A: GALAXY SAMPLE PROPERTIES

Table A1: Galaxy properties for the sample from the SAMI Galaxy Survey analysed in this work. We present the (*a*) spectroscopic redshift ($z_{\rm spec}$, Driver et al. 2011; Bryant et al. 2015), (*b*) the stellar mass (M_*, Taylor et al. 2011; Bryant et al. 2015), (*c*) effective radius (R_e, Taylor et al. 2011; Bryant et al. 2015), (*d*) photometric ellipticity ($e = 1 - b/a$, Kelvin et al. 2012; Bryant et al. 2015), and (*e*) SFR (Gunawardhana et al. 2013; Davies et al. 2016; Driver et al. 2018) from the GAMA Survey. We also show the (f) Tully-Fisher circular velocity at $r = 2.2R_e$ calculated using the relationship proposed by Bloom et al. ($v_{2.2,\rm tf}$, 2017b). The Blobby3D inferred (*f*) circular velocity at $r = 2.2R_e$ ($v_{2.2}$) and (*g*) the LoS velocity dispersion ($\sigma_{v,\rm LoS}$). We also report the (*h*) vertical velocity dispersion ($\sigma_{v,z}$) using the inclination correction outlined in Section 3.2.1.

GAMA ID	RA	Dec	$z^a_{\rm spec}$	$\log_{10}(M_*)^b$	R^c_e	e^d	$\log_{10}(\rm SFR)^e$	$v^f_{2.2,\rm tf}$	$v^g_{2.2}$	$\sigma^h_{v,\rm LoS}$	$\sigma^i_{v,z}$
	(°)	(°)		($M_\odot$)	(kpc)		($M_\odot$ yr^{-1})	(km s^{-1})	(km s^{-1})	(km s^{-1})	(km s^{-1})
8353	182.01649	0.69761	0.020	9.44	2.43	0.37	-0.35	99	112	22	19
8562	182.79067	0.78576	0.020	8.42	2.09	0.28	-1.4	48	15	13	12
8570	182.83286	0.80475	0.021	9.27	2.27	0.35	-0.84	88	60	18	16
8913	184.22040	0.76587	0.029	8.79	1.78	0.45	-4.5	62	-	29	25
9163	185.14066	0.78806	0.007	9.22	2.01	0.45	-1.1	85	35	21	18
9352	185.97719	0.83053	0.024	8.97	1.12	0.47	-0.83	71	-	27	23
14555	212.11498	0.70029	0.026	8.92	2.54	0.46	0.18	68	72	21	17
14812	212.93002	0.72011	0.025	9.99	2.72	0.24	-0.04	147	141	20	18
15218	214.59860	0.73213	0.026	9.11	5.22	0.45	-0.68	78	115	22	19
16948	221.10413	0.78286	0.026	8.89	2.98	0.17	-0.57	67	120	17	16
22932	179.63289	1.13192	0.039	9.47	4.06	0.02	-0.28	101	-	21	21
23337	181.22757	1.21561	0.021	9.74	3.02	0.30	-1.0	123	98	16	14
24414	185.53729	1.11275	0.023	8.35	2.52	0.30	-1.6	46	99	17	15
28654	211.81607	1.06503	0.035	9.14	2.38	0.20	-0.56	80	102	21	19
28738	213.15055	1.05790	0.046	10.05	2.60	0.42	0.077	153	-	27	23
30346	174.63865	-1.18449	0.021	10.45	5.33	0.32	0.43	204	184	22	19
30377	174.82286	-1.07931	0.027	8.22	2.29	0.35	-1.4	42	96	20	17
30890	177.25796	-1.10260	0.020	9.79	3.45	0.43	-0.28	127	123	25	22
32249	183.95869	-1.23808	0.021	8.51	2.72	0.12	-1.2	51	-	18	17
32274	184.15297	-1.08234	0.021	8.79	2.18	0.41	-0.89	62	74	19	16
32362	184.53565	-1.06411	0.019	10.41	6.02	0.44	-0.024	198	197	29	25
37050	215.90251	-1.06030	0.031	9.12	3.75	0.30	-0.7	79	100	19	17
39108	175.13410	-0.66962	0.027	8.35	1.63	0.17	-0.98	46	-	25	23
39145	175.43607	-0.68800	0.050	10.20	2.22	0.24	0.68	171	-	42	38
40283	180.46207	-0.65541	0.019	8.90	3.62	0.23	-1.8	67	50	16	15
40420	181.10961	-0.63196	0.020	9.21	3.62	0.36	-1.6	84	108	25	22
40765	182.89697	-0.69958	0.035	9.04	0.64	0.41	-0.23	75	-	41	35
40916	183.54716	-0.83157	0.025	9.82	6.33	0.45	-0.07	130	128	22	19
41173	184.54418	-0.74498	0.021	8.39	2.25	0.41	-1.4	47	23	18	15
47224	211.86055	-0.74540	0.035	9.16	1.14	0.40	-0.59	81	-	19	17
47500	213.25280	-0.83100	0.026	9.49	1.66	0.46	-0.25	103	-	26	22
47652	213.60344	-0.82934	0.040	9.43	2.64	0.14	0.00043	98	61	21	19
49730	222.29648	-0.70189	0.043	9.51	2.31	0.01	-0.29	104	-	22	22
49753	222.49249	-0.63135	0.026	8.76	3.27	0.40	-1.5	61	90	18	16
49755	222.38983	-0.78424	0.027	8.55	1.46	0.34	-0.92	53	-	20	18
49840	222.72006	-0.67251	0.042	9.22	4.17	0.31	-0.57	85	97	13	11
53809	175.11901	-0.39364	0.027	9.05	1.74	0.44	-0.64	75	-	21	18
53977	176.01840	-0.21097	0.048	10.01	4.04	0.20	0.43	149	122	28	26
54102	176.75303	-0.29422	0.005	8.89	1.21	0.48	-1.5	67	76	17	15
54359	177.74299	-0.36795	0.043	10.30	4.90	0.13	0.18	183	-	20	19
54382	177.89815	-0.37489	0.019	8.54	1.02	0.44	-1.2	52	-	23	19
54455	178.22625	-0.23571	0.026	9.13	5.43	0.49	-0.4	79	36	20	17
55160	180.63455	-0.38942	0.022	8.43	2.45	0.38	-0.93	48	31	28	24
55227	180.94630	-0.33660	0.020	8.33	3.04	0.33	-1.4	45	80	17	15
55346	181.69378	-0.27375	0.034	9.10	2.70	0.45	-0.76	78	68	17	15
55367	181.79334	-0.25959	0.022	8.40	3.36	0.30	-1.4	47	33	11	10
55648	183.00180	-0.37212	0.035	8.97	2.06	0.41	-0.68	71	-	16	14
56061	184.42641	-0.22620	0.041	9.13	2.22	0.31	-1.0	79	-	17	15
62435	212.84807	-0.30051	0.026	9.00	1.68	0.18	-0.95	72	-	20	19
63210	215.01946	-0.31480	0.051	10.30	2.91	0.43	-0.28	183	-	32	27

GAMA ID	RA	Dec	$z^a_{\rm spec}$	$\log_{10}(M_*)^b$	R^c_e	e^d	$\log_{10}(SFR)^e$	$v^f_{2.2,tf}$	$v^g_{2.2}$	$\sigma^h_{v,LoS}$	$\sigma^i_{v,z}$
	(°)	(°)		($M_\odot$)	(kpc)		($M_\odot$ yr^{-1})	(km s^{-1})	(km s^{-1})	(km s^{-1})	(km s^{-1})
63389	215.75063	-0.25454	0.055	10.07	5.45	0.42	0.31	155	162	20	17
63855	217.29079	-0.35168	0.035	9.56	5.16	0.13	0.37	108	-	21	20
64087	218.09196	-0.22671	0.055	10.37	3.39	0.49	0.33	193	-	27	23
65237	222.08657	-0.32651	0.044	9.15	5.22	0.30	-0.59	81	132	20	18
69620	175.72473	0.16189	0.018	9.30	1.91	0.25	-0.24	90	79	24	21
69653	175.85485	0.01404	0.018	8.64	2.84	0.40	-0.91	56	57	25	21
71099	183.06138	0.07230	0.008	8.46	0.74	0.23	-1.1	49	37	18	17
71146	183.25125	0.04376	0.021	9.15	4.04	0.32	-0.6	81	94	21	18
71269	183.97349	0.08162	0.041	9.09	2.32	0.48	0.02	77	-	21	18
71382	184.62741	0.01323	0.021	8.95	1.90	0.19	-1.0	70	129	20	18
77373	212.98003	0.07655	0.040	9.00	4.76	0.50	-0.77	72	104	19	16
77446	213.26064	0.14638	0.055	10.33	5.85	0.16	0.36	187	157	26	24
77754	214.64775	0.15772	0.053	10.48	8.20	0.44	0.79	208	179	32	27
78406	216.98714	0.02259	0.024	8.99	3.09	0.15	-0.86	72	111	19	17
78425	217.06865	0.00231	0.053	10.05	2.49	0.36	1.0	153	-	47	41
78667	218.09082	0.17812	0.055	10.16	8.25	0.22	0.37	166	170	23	21
78921	219.16095	0.11740	0.030	9.44	5.78	0.45	-0.43	99	112	19	16
79601	222.34769	0.04231	0.044	9.05	2.21	0.09	-0.27	75	-	18	17
79710	222.74198	0.09219	0.042	9.18	2.78	0.40	-1.1	82	54	21	18
79712	222.80757	0.02796	0.023	8.57	0.99	0.28	-1.4	53	-	25	22
84048	175.78879	0.55890	0.019	8.66	2.10	0.33	-1.6	57	149	22	19
84107	175.99843	0.42801	0.029	9.71	3.21	0.23	0.21	120	155	28	25
85481	182.70962	0.59591	0.020	9.02	1.99	0.41	-2.5	73	114	16	14
86116	185.27934	0.46134	0.007	7.69	0.51	0.38	-1.7	28	-	21	18
91627	212.81851	0.48944	0.053	10.31	7.86	0.29	0.49	185	179	22	19
99511	183.12848	0.89422	0.021	8.71	2.68	0.13	-1.1	59	-	15	14
99513	183.15825	0.89339	0.020	8.42	2.19	0.10	-1.9	48	-	17	16
99795	184.23281	0.91977	0.029	8.95	2.11	0.05	-0.48	70	-	18	17
100162	185.79312	0.93489	0.026	9.15	1.57	0.50	-0.65	81	-	19	16
100192	185.92766	0.96219	0.024	9.33	3.04	0.08	-0.66	92	-	23	22
105573	212.54694	0.86584	0.026	8.54	1.14	0.39	-1.1	52	-	13	12
105962	214.14784	0.88664	0.026	8.96	3.37	0.36	-0.84	70	65	22	19
106042	214.56214	0.89109	0.026	10.14	7.81	0.20	0.74	163	152	32	29
106331	215.51320	0.86205	0.036	9.61	5.54	0.44	-0.13	112	107	19	16
106376	215.81121	0.97834	0.040	10.27	7.46	0.15	0.88	179	115	26	25
106717	217.01889	1.00631	0.026	10.19	2.93	0.30	0.59	169	170	28	25
107594	221.07590	0.85401	0.026	8.93	3.53	0.47	-0.67	69	115	22	19
136917	176.35594	-1.73764	0.029	9.11	1.87	0.42	-0.87	78	-	18	16
136980	176.53583	-1.82683	0.027	8.63	4.07	0.44	-1.1	56	75	16	14
137071	177.07578	-1.64035	0.013	8.71	0.84	0.20	-0.052	59	-	28	25
137155	177.21879	-1.84390	0.028	8.39	3.61	0.22	-1.5	47	62	21	19
137789	179.57125	-1.72809	0.019	8.57	1.57	0.30	-1.2	53	64	22	19
137847	179.79836	-1.70706	0.020	9.16	2.63	0.33	-0.49	81	46	25	22
138066	180.72149	-1.77911	0.035	9.85	4.29	0.41	-0.61	133	102	19	16
138094	180.74242	-1.70226	0.021	8.77	2.24	0.32	-2.3	61	60	14	12
144197	179.32270	-1.37420	0.026	9.13	1.08	0.21	-0.61	79	-	26	24
144236	179.35020	-1.31321	0.026	8.61	0.99	0.45	-0.93	55	-	23	20
144320	179.73348	-1.43043	0.052	10.27	1.96	0.30	-0.03	179	-	34	30
144402	179.96120	-1.38195	0.036	10.25	3.25	0.35	0.55	177	172	35	31
144497	180.37719	-1.43612	0.035	9.28	1.09	0.12	-0.17	88	-	55	51
144682	181.03465	-1.41719	0.035	9.02	1.03	0.41	-0.77	73	-	40	34
145267	183.70061	-1.34594	0.032	9.12	1.37	0.47	-1.1	79	-	31	26
145583	185.32451	-1.25413	0.022	9.39	3.61	0.41	-0.8	96	85	17	14
176955	174.94289	-1.87526	0.058	10.62	9.09	0.34	0.7	230	204	21	18
177081	175.53937	-1.90905	0.020	8.92	1.47	0.33	-0.34	68	81	30	26
177481	176.91006	-1.92285	0.027	8.84	1.61	0.30	-1.4	65	-	22	19
178481	180.44250	-1.93475	0.025	9.00	4.51	0.29	-0.72	72	109	20	18
178580	180.81309	-1.95678	0.021	8.43	1.75	0.00	-1.4	48	-	20	20
183932	174.27021	-1.60977	0.022	8.27	1.86	0.16	-1.2	43	26	21	20

GAMA ID	RA (°)	Dec (°)	$z^a_{\rm spec}$	$\log_{10}(M_*)^b$ ($M_\odot$)	R^c_e (kpc)	e^d	$\log_{10}(SFR)^e$ ($M_\odot$ yr^{-1})	$v^f_{2.2,tf}$ (km s^{-1})	$v^g_{2.2}$ (km s^{-1})	$\sigma^h_{v,LoS}$ (km s^{-1})	$\sigma^i_{v,z}$ (km s^{-1})
184234	175.68429	-1.48754	0.029	9.01	4.37	0.05	-0.62	73	-	21	21
184370	176.21728	-1.53212	0.026	9.65	2.55	0.14	-0.56	115	36	20	19
184415	176.34198	-1.56521	0.028	9.56	2.28	0.24	-0.26	108	111	20	18
185190	179.49465	-1.55768	0.020	9.01	2.45	0.32	-0.86	73	83	16	14
185252	179.54589	-1.64745	0.022	8.46	3.57	0.39	-1.7	49	48	21	18
185291	179.80472	-1.60447	0.022	8.83	2.38	0.41	-1.1	64	53	24	21
185532	180.69427	-1.59343	0.020	9.28	3.45	0.12	-0.91	88	-	17	16
185557	180.75343	-1.63802	0.019	9.62	1.13	0.24	-	113	-	23	21
185622	181.08444	-1.53028	0.005	7.87	6.13	0.29	-2.4	32	43	11	9
197419	135.20729	-0.71429	0.041	9.30	3.62	0.40	-0.58	90	103	17	14
198503	139.76575	-0.81766	0.017	8.58	0.93	0.46	-1.3	54	-	29	25
198817	140.97499	-0.68263	0.055	10.09	4.75	0.20	0.16	158	184	24	22
203148	132.84017	-0.39516	0.043	9.27	1.77	0.12	-0.26	88	-	26	25
203684	134.79005	-0.27214	0.042	9.19	3.54	0.46	-0.48	83	117	18	15
203729	135.04616	-0.30183	0.042	9.44	2.17	0.44	-0.31	99	-	53	45
203998	136.14023	-0.31481	0.028	8.93	1.60	0.09	-0.78	69	-	16	15
204096	136.52107	-0.26037	0.040	9.98	3.82	0.17	0.0099	146	158	16	15
204868	139.84670	-0.21330	0.039	9.49	1.10	0.19	-0.27	103	-	21	20
208520	129.40912	0.05067	0.035	9.65	4.74	0.16	-0.45	115	121	17	15
208892	130.75455	0.16933	0.029	9.39	7.04	0.48	-0.81	96	100	17	15
209181	132.12520	0.17087	0.058	10.30	5.53	0.23	0.79	183	173	30	27
209414	133.20974	0.15797	0.026	9.04	3.84	0.45	-1.0	75	90	24	20
209743	134.67676	0.19143	0.041	10.16	6.20	0.48	0.018	166	180	18	16
210060	136.40777	0.00327	0.019	8.98	4.92	0.21	-1.0	71	99	17	15
210567	138.74414	0.20803	0.057	9.48	5.79	0.13	-0.37	102	-	14	14
210781	139.64824	0.05988	0.055	10.22	5.31	0.24	-0.089	173	168	18	16
210808	139.75689	0.17252	0.017	8.41	1.47	0.13	-1.9	48	95	15	14
210909	140.28626	0.08058	0.024	8.44	1.73	0.49	-1.9	49	55	23	20
214245	129.52446	0.60896	0.014	9.40	1.35	0.32	-1.6	96	75	20	17
214860	131.89667	0.56184	0.058	9.75	7.03	0.49	0.003	124	104	25	21
216843	140.19242	0.60472	0.024	9.26	4.06	0.29	-0.68	87	93	21	18
220275	180.92608	1.45729	0.021	9.14	2.69	0.02	-0.89	80	-	17	17
220319	180.99245	1.48278	0.021	8.57	2.33	0.21	-1.8	53	24	16	14
220371	181.23715	1.50824	0.020	9.53	3.23	0.35	-0.93	106	134	21	18
220372	181.28939	1.55929	0.021	9.06	1.86	0.12	-1.3	76	-	18	17
220439	181.63159	1.61663	0.019	9.54	2.54	0.18	-0.26	107	134	14	13
220578	182.17817	1.45636	0.019	8.98	1.28	0.41	-0.78	71	-	17	14
220687	182.83299	1.49227	0.007	9.27	3.36	0.43	-0.75	88	74	17	15
220750	182.98977	1.48925	0.021	8.62	2.42	0.30	-0.87	55	70	16	14
221369	185.83472	1.61648	0.027	8.64	1.26	0.34	-0.56	56	-	23	20
227036	211.82817	1.28196	0.035	9.56	4.02	0.39	0.19	108	136	25	22
227223	212.67106	1.33941	0.055	10.31	4.44	0.11	0.75	185	-	31	29
227289	212.82231	1.35262	0.026	9.17	4.75	0.08	-0.68	82	-	21	20
227673	214.53595	1.22412	0.026	9.35	3.15	0.13	-0.28	93	-	24	23
227970	215.60459	1.19760	0.054	10.16	5.19	0.24	0.47	166	174	16	15
228086	216.08084	1.12442	0.039	9.18	4.21	0.20	-0.38	82	60	19	17
230174	178.74753	1.85812	0.021	8.48	1.85	0.19	-1.9	50	51	18	17
238328	213.96582	1.58638	0.025	8.82	1.36	0.36	-1.3	64	-	20	17
238395	214.24319	1.64043	0.025	9.87	2.26	0.18	0.28	135	110	31	29
238406	214.20244	1.75963	0.056	10.45	8.32	0.37	0.25	204	194	27	24
239490	217.99757	1.58140	0.030	9.21	3.68	0.19	-0.58	84	68	21	19
240108	220.62338	1.50040	0.007	9.02	1.20	0.42	-1.3	73	75	20	17
240202	221.12828	1.52201	0.005	8.66	1.29	0.21	-2.0	57	41	17	15
250277	214.43384	1.98131	0.058	10.01	5.72	0.29	0.23	149	35	31	28
251297	218.11956	1.91052	0.030	9.52	4.10	0.30	-0.31	105	116	18	16
251367	218.23409	1.89580	0.030	9.04	2.25	0.30	-0.85	75	87	21	19
252074	221.96823	1.80223	0.028	8.58	3.14	0.42	-1.3	54	30	18	15
271562	174.75468	1.33657	0.005	7.82	0.70	0.41	-0.81	31	31	24	20
272996	181.66757	1.33397	0.022	8.76	1.88	0.49	-1.3	61	58	21	17

GAMA ID	RA (°)	Dec (°)	$z^a_{\rm spec}$	$\log_{10}(M_*)^b$ ($M_\odot$)	R^c_e (kpc)	e^d	$\log_{10}(SFR)^e$ ($M_\odot$ yr^{-1})	$v^f_{2.2,tf}$ (km s^{-1})	$v^g_{2.2}$ (km s^{-1})	$\sigma^h_{v,LoS}$ (km s^{-1})	$\sigma^i_{v,z}$ (km s^{-1})
273092	181.99998	1.39593	0.037	10.07	6.27	0.25	0.19	155	37	20	18
273242	182.79525	1.44168	0.019	8.68	2.78	0.15	-1.3	58	83	19	18
273296	182.99771	1.35004	0.021	9.56	5.31	0.46	-0.28	108	68	19	16
273309	183.03839	1.31149	0.020	9.24	3.60	0.11	-1.1	86	-	19	18
273951	185.93037	1.31109	0.026	8.72	2.53	0.45	-0.38	59	7	28	24
278074	211.96000	1.13692	0.025	9.78	4.56	0.17	-1.4	126	60	15	14
278554	132.30501	0.78322	0.043	9.00	4.05	0.09	-0.68	72	-	19	18
278684	133.13103	0.85357	0.011	8.09	0.48	0.20	-1.8	38	-	24	22
278804	133.85939	0.85818	0.042	9.82	2.45	0.38	-0.97	130	-	15	13
278909	134.42490	0.81731	0.041	9.33	2.37	0.48	-0.78	92	-	15	13
279066	135.13286	0.97642	0.018	8.25	4.71	0.28	-	42	10	16	15
279818	139.43876	1.05542	0.027	9.54	4.35	0.21	-0.26	107	42	22	20
279917	139.99533	0.96084	0.018	9.32	3.88	0.44	-0.34	91	76	24	20
289107	181.04059	1.82596	0.017	9.68	3.73	0.36	-0.75	118	168	15	13
296639	212.67738	1.40807	0.046	10.22	3.13	0.18	0.17	173	132	22	20
296742	213.20535	1.48923	0.018	9.15	1.38	0.46	-1.1	81	29	31	26
296934	214.04425	1.54141	0.053	10.21	3.82	0.20	0.28	172	174	25	23
297633	216.56453	1.49149	0.055	10.43	6.88	0.25	0.38	201	175	19	17
297694	216.86676	1.33773	0.025	9.11	12.31	0.14	-1.6	78	195	15	14
298114	218.40091	1.30590	0.056	10.25	5.93	0.41	0.49	177	175	24	20
298738	221.59337	1.22840	0.050	10.06	5.64	0.43	0.15	154	154	22	19
300350	129.16480	1.13610	0.014	8.32	1.49	0.22	-3.1	45	41	18	17
300372	129.29410	1.00136	0.039	9.16	1.23	0.18	-0.86	81	-	26	24
300477	129.70677	1.12101	0.029	9.25	3.53	0.26	-0.64	87	130	22	20
300787	130.93495	1.07919	0.044	10.32	2.97	0.32	0.045	186	199	15	13
300821	131.03734	1.21435	0.013	8.82	0.98	0.29	-0.64	64	88	23	20
301346	133.52459	1.19186	0.044	10.16	3.33	0.46	0.42	166	170	28	24
301885	135.53948	1.22605	0.057	10.60	11.86	0.40	0.56	227	263	21	18
318936	212.94107	1.94731	0.018	8.90	2.77	0.36	-0.61	67	100	22	19
319150	213.62262	1.81263	0.025	8.56	1.06	0.38	-1.0	53	-	23	20
320068	216.87191	1.85175	0.029	9.17	2.38	0.28	-0.59	82	102	22	20
320281	217.63635	1.85328	0.034	9.84	3.02	0.39	-0.11	132	185	26	23
322910	129.39531	1.57389	0.031	9.74	3.61	0.19	-0.48	123	30	25	23
323194	130.81630	1.48410	0.013	8.61	0.81	0.37	-1.4	55	-	17	15
323224	130.98705	1.58429	0.013	8.61	1.02	0.11	-0.78	55	-	18	17
323242	131.00309	1.67133	0.028	9.50	1.38	0.23	-0.4	104	-	36	33
323504	131.95082	1.53447	0.063	10.94	11.71	0.09	0.41	289	-	27	26
323507	132.03504	1.56604	0.040	9.44	2.92	0.14	-0.3	99	144	23	21
323874	133.49341	1.66407	0.058	10.56	4.42	0.08	-0.61	221	-	17	17
324323	135.50044	1.78604	0.053	9.74	2.64	0.48	-0.63	123	-	12	10
325533	140.92832	2.00336	0.053	10.10	6.79	0.48	-0.12	159	172	17	15
345646	130.40960	1.96809	0.014	8.44	3.75	0.08	-1.2	49	-	25	24
346257	133.04215	1.98304	0.029	8.63	1.21	0.50	-1.1	56	-	22	19
346440	133.74686	2.13436	0.020	8.37	0.50	0.11	-1.2	46	-	19	18
346718	134.86958	2.06157	0.057	9.46	1.77	0.19	0.33	101	-	27	25
346861	135.29644	2.07820	0.055	9.82	5.15	0.33	-0.26	130	132	16	14
347263	136.99176	2.27055	0.026	9.48	2.92	0.46	-0.55	102	184	22	19
375904	131.27015	1.40141	0.014	8.07	1.06	0.35	-1.5	37	51	21	18
376165	132.17024	1.49956	0.029	8.70	2.94	0.12	-1.4	58	-	19	18
376185	132.35194	1.38501	0.034	9.07	2.16	0.30	-0.75	76	-	21	19
377348	137.33399	1.61430	0.004	7.59	0.44	0.17	-2.2	26	53	19	17
378060	140.38950	1.58462	0.017	8.70	3.10	0.34	-1.6	58	56	19	17
382152	135.42424	1.85215	0.057	10.12	6.77	0.28	-0.22	161	120	24	21
382631	137.71356	2.02189	0.055	10.09	2.92	0.16	-0.015	158	-	19	17
382764	138.26745	2.03871	0.013	9.05	1.18	0.34	-0.43	75	138	30	26
383033	139.59121	2.17020	0.027	8.47	2.22	0.31	-1.4	50	49	20	18
383259	140.67041	2.11154	0.057	10.73	6.74	0.42	0.9	249	143	39	33
383318	140.95009	2.11275	0.024	9.92	5.05	0.48	-0.085	140	66	39	33
386286	131.34372	2.19006	0.006	8.22	1.11	0.24	-1.6	42	52	20	18

GAMA ID	RA (°)	Dec (°)	$z^a_{\rm spec}$	$\log_{10}(M_*)^b$ ($M_\odot$)	R^c_e (kpc)	e^d	$\log_{10}(SFR)^e$ ($M_\odot$ yr^{-1})	$v^f_{2.2,tf}$ (km s^{-1})	$v^g_{2.2}$ (km s^{-1})	$\sigma^h_{v,LoS}$ (km s^{-1})	$\sigma^i_{v,z}$ (km s^{-1})
386898	134.40439	2.23945	0.054	10.44	8.66	0.21	0.31	202	225	17	16
388603	140.78384	2.48607	0.017	9.80	5.50	0.12	-0.4	128	-	22	20
418624	137.09716	2.54414	0.055	10.01	4.72	0.30	-0.15	149	176	20	18
418795	137.76469	2.57229	0.039	9.13	1.62	0.24	-0.77	79	-	11	10
419632	140.75064	2.86863	0.025	8.85	1.80	0.13	-3.0	65	17	19	18
422355	130.50504	2.52837	0.028	9.26	3.18	0.04	-0.63	87	-	19	19
422359	130.55488	2.62461	0.050	10.07	2.72	0.45	0.14	155	-	14	12
422366	130.59560	2.49733	0.029	9.62	5.58	0.49	-0.35	113	90	22	18
422486	131.18034	2.57274	0.026	8.78	2.15	0.42	-0.79	62	135	21	18
422619	131.78175	2.62180	0.029	9.63	4.52	0.14	-1.8	114	97	17	16
463660	213.92314	-1.15695	0.038	9.02	3.18	0.08	-1.4	73	-	15	14
485504	216.10103	-1.76490	0.056	10.20	6.57	0.23	0.21	171	184	18	16
485529	216.24765	-1.86856	0.030	9.07	1.83	0.46	-0.36	76	-	30	25
485834	217.57879	-1.78770	0.056	10.69	6.41	0.43	0.54	242	250	29	24
485885	217.75790	-1.71721	0.055	10.25	6.09	0.16	0.76	177	167	23	21
487010	222.52592	-1.61157	0.043	9.01	2.93	0.19	-0.9	73	67	17	16
487027	222.67911	-1.71488	0.026	10.09	3.58	0.35	0.57	158	149	33	28
487175	223.33977	-1.59495	0.042	9.73	3.48	0.28	0.32	122	127	24	22
492384	216.39461	-1.37612	0.055	10.46	4.59	0.45	0.12	205	172	31	26
492414	216.50320	-1.41180	0.055	10.10	5.31	0.02	0.33	159	-	23	23
493621	221.83561	-1.30299	0.029	9.03	3.37	0.23	-1.3	74	109	20	18
493812	222.52657	-1.16131	0.043	9.54	4.59	0.45	-0.97	107	136	26	22
493825	222.43912	-1.17427	0.027	8.23	1.91	0.39	-1.3	42	51	21	18
508421	216.98916	-1.63118	0.055	10.39	4.55	0.26	-0.2	195	192	25	22
508680	217.90221	-1.59247	0.030	9.25	3.54	0.25	-0.51	87	93	16	14
509397	221.19366	-1.51910	0.056	10.24	6.82	0.19	-0.053	176	109	20	19
509444	221.32078	-1.56930	0.034	9.05	3.65	0.35	-1.2	75	88	21	18
509557	221.96775	-1.57005	0.027	8.87	0.56	0.38	-0.81	66	-	33	29
509576	221.97272	-1.37673	0.027	8.26	2.72	0.32	-0.65	43	66	20	17
509670	222.34731	-1.55925	0.027	8.95	4.31	0.43	-0.71	70	118	22	18
509852	223.13292	-1.34509	0.043	10.07	7.69	0.34	0.29	155	105	19	17
511867	216.38846	-1.11394	0.055	10.68	7.47	0.40	1.0	240	218	32	28
511921	216.67460	-1.14927	0.031	9.16	1.19	0.38	-0.46	81	-	24	21
512524	219.06927	-1.13120	0.040	9.27	5.47	0.08	-0.59	88	-	16	16
513108	221.71563	-1.14686	0.042	9.64	7.81	0.14	-0.5	114	135	25	24
514029	214.13351	-1.18215	0.050	10.49	6.38	0.30	0.51	210	187	19	17
517167	131.16137	2.41098	0.030	9.24	2.41	0.31	-0.12	86	114	19	17
517249	131.55101	2.41047	0.028	9.40	3.38	0.38	-0.29	96	83	24	21
517306	131.71344	2.56971	0.030	9.38	3.07	0.37	-0.34	95	90	22	19
517960	134.27689	2.66458	0.013	8.30	2.59	0.39	-1.4	44	28	17	15
521736	130.67894	2.87319	0.050	9.87	1.71	0.33	0.57	135	-	40	35
521768	131.07263	2.88117	0.050	10.19	4.78	0.22	0.036	169	160	22	20
521894	131.65458	2.82703	0.013	8.77	1.58	0.26	-1.5	61	106	19	17
521898	131.68612	2.79428	0.028	8.46	1.19	0.09	-1.1	49	-	22	21
534654	174.35287	-0.96382	0.050	10.31	3.84	0.03	-0.0073	185	-	22	22
534753	175.02585	-0.90142	0.029	10.35	1.14	0.33	0.22	190	-	27	24
535283	177.25575	-0.88835	0.020	8.50	0.72	0.50	-1.3	51	-	19	16
535974	179.96350	-0.85869	0.036	9.27	1.96	0.40	-0.28	88	-	21	18
537399	185.08379	-0.88202	0.040	9.63	4.51	0.32	-0.33	114	116	18	16
537476	185.39249	-1.00951	0.021	8.21	1.49	0.42	-0.56	41	23	25	22
543752	212.63639	-0.84186	0.025	8.92	5.06	0.47	-1.3	68	53	23	19
543763	212.75337	-0.90393	0.026	8.49	2.01	0.49	-1.8	50	76	20	17
543860	213.15467	-1.01222	0.054	10.01	4.94	0.20	0.31	149	44	31	28
544084	213.89591	-1.03869	0.038	9.04	5.12	0.42	-0.81	75	169	17	15
544812	216.98074	-1.00818	0.029	9.32	3.42	0.41	-1.1	91	116	17	15
544853	217.37900	-0.88385	0.035	9.54	7.30	0.18	-1.4	107	96	16	15
546043	222.74183	-0.88154	0.027	9.43	3.01	0.25	-0.36	98	104	21	19
551192	139.33882	-0.45421	0.017	8.75	0.61	0.32	-1.0	61	-	33	29
551368	140.01779	-0.50248	0.026	8.88	1.09	0.04	-1.2	66	-	24	23

GAMA ID	RA (°)	Dec (°)	$z^a_{\rm spec}$	$\log_{10}(M_*)^b$ ($M_\odot$)	R^c_e (kpc)	e^d	$\log_{10}(SFR)^e$ ($M_\odot$ yr^{-1})	$v^f_{2.2,tf}$ (km s^{-1})	$v^g_{2.2}$ (km s^{-1})	$\sigma^h_{v,LoS}$ (km s^{-1})	$\sigma^i_{v,z}$ (km s^{-1})
558887	174.37404	-0.47340	0.029	8.83	2.28	0.40	-0.97	64	77	21	18
559292	176.41768	-0.57082	0.028	8.71	2.52	0.47	-0.58	59	41	26	22
559300	176.53218	-0.45799	0.013	8.64	1.23	0.23	-1.7	56	46	18	16
559495	177.34230	-0.62371	0.040	9.05	3.20	0.43	-0.18	75	138	21	18
560333	179.98443	-0.54822	0.022	9.90	5.52	0.18	-0.18	138	154	17	16
560718	181.33290	-0.48020	0.005	7.76	0.50	0.14	-3.0	30	63	18	17
560946	182.33179	-0.52747	0.035	9.19	3.44	0.35	-0.97	83	88	13	12
561143	183.01351	-0.60685	0.035	9.54	4.33	0.47	0.15	107	64	37	31
567676	212.76660	-0.54511	0.026	8.57	2.42	0.17	-1.8	53	21	23	21
567736	213.05273	-0.61270	0.025	8.69	1.81	0.47	0.32	58	15	28	23
567760	213.07541	-0.56930	0.025	8.46	4.69	0.28	-0.47	49	57	11	10
570119	222.13518	-0.57531	0.043	9.56	5.51	0.48	0.43	108	134	24	20
570174	222.60503	-0.46932	0.042	9.81	9.83	0.29	-0.76	129	104	23	20
573586	129.12557	-0.08624	0.052	10.03	4.42	0.24	0.027	151	148	25	22
574008	131.02735	-0.10350	0.051	10.18	6.14	0.47	0.56	168	144	28	24
574029	131.07729	-0.04921	0.051	10.04	3.17	0.23	0.56	152	-	27	24
574193	134.43437	-0.04481	0.044	8.73	5.02	0.18	-0.63	60	123	19	17
574572	136.33633	-0.03700	0.019	8.76	0.79	0.08	-1.6	61	-	17	17
574617	136.43827	-0.19325	0.076	10.33	4.12	0.15	0.46	187	-	24	22
574692	136.73747	-0.12355	0.019	9.31	1.82	0.37	-0.41	90	36	23	20
583443	174.88168	-0.15990	0.028	8.93	1.99	0.15	-0.92	69	97	22	20
583637	175.82494	-0.18161	0.056	10.01	4.10	0.05	0.11	149	-	23	22
584013	177.87898	-0.07776	0.048	10.46	3.79	0.29	0.75	205	85	34	30
585121	181.19288	-0.01538	0.040	9.55	2.68	0.27	-0.42	107	139	31	28
585231	181.78147	-0.02019	0.021	8.76	2.15	0.41	-1.6	61	72	17	15
592863	214.33856	-0.16910	0.044	9.46	6.05	0.14	-0.37	101	98	20	19
592999	215.06156	-0.07938	0.053	10.26	4.92	0.47	0.3	178	197	27	23
593526	216.81878	-0.09008	0.031	9.32	1.64	0.49	-0.55	91	-	24	20
594059	218.90933	-0.09702	0.029	9.48	4.95	0.31	-0.87	102	96	21	19
594906	222.36208	-0.16420	0.041	9.77	1.66	0.31	0.22	126	-	26	23
594990	222.80149	-0.06085	0.044	10.34	3.72	0.26	-2.1	189	191	30	27
598911	129.30130	0.38743	0.042	9.39	6.87	0.21	-0.27	96	81	19	17
598968	129.56040	0.35208	0.042	10.06	6.74	0.20	0.12	154	121	19	18
599095	130.13599	0.26201	0.035	9.44	2.72	0.34	-1.0	99	115	23	20
599134	130.26050	0.39590	0.037	9.09	2.21	0.38	-0.63	77	-	25	22
599329	131.10371	0.34289	0.015	8.40	0.71	0.33	-1.1	47	-	29	25
599862	132.74012	0.23892	0.041	9.04	4.62	0.14	-0.83	75	123	12	11
600026	133.48520	0.21557	0.051	10.28	5.00	0.28	0.46	181	203	30	26
600312	134.81541	0.39164	0.011	8.86	0.76	0.25	-0.97	66	55	27	24
601323	139.34146	0.32191	0.054	10.73	8.32	0.31	0.32	249	130	30	27
601395	139.56851	0.38503	0.017	8.91	8.81	0.26	-1.4	68	2	29	26
610474	180.39356	0.34748	0.039	10.01	2.40	0.24	0.45	149	-	30	27
610997	182.86904	0.37865	0.020	9.32	2.55	0.22	-0.83	91	118	25	23
611629	185.50338	0.31504	0.034	9.46	1.38	0.33	-0.5	101	-	26	23
617655	212.63506	0.22418	0.029	9.07	3.24	0.14	-2.4	76	104	17	16
617945	213.72345	0.40730	0.028	8.47	0.91	0.22	-1.0	50	-	21	19
618071	214.01854	0.21626	0.026	8.94	5.14	0.37	-0.8	69	62	21	18
618116	214.40555	0.32910	0.051	10.25	6.47	0.27	0.37	177	179	27	24
618152	214.52287	0.22739	0.053	10.01	4.18	0.29	-0.15	149	32	23	20
619095	218.03502	0.41114	0.053	10.47	3.69	0.32	0.6	207	211	31	27
622333	132.56179	0.75988	0.043	9.03	3.61	0.24	-	74	42	18	17
622394	133.06978	0.68110	0.041	9.22	3.17	0.28	-0.57	85	173	24	22
622744	134.82995	0.79776	0.013	9.16	1.58	0.46	-0.43	81	65	28	24
622770	134.98662	0.78816	0.052	10.01	2.36	0.48	-0.4	149	-	34	29
623366	138.54711	0.81821	0.055	10.42	6.71	0.06	0.26	200	-	20	19
623712	140.13867	0.72106	0.017	9.16	2.83	0.08	-1.4	81	-	19	18

This paper has been typeset from a TEX/LATEX file prepared by the author.

4 Applications of Blobby3D: The Drivers of Ionised Gas Turbulence Across Epochs

The research in this chapter aims to understand the change in kinematics across epochs. Blobby3D is applied to a sample of galaxies from the KMOS Redshift One Spectroscopic Survey (KROSS). The results from this analysis at $z \sim 1$ is then compared to the SAMI and DYNAMO galaxies at $z \sim 0.1$. This chapter is a research paper in preparation, and thus has not undergone peer review.

Declaration of work:

- Mathew Varidel performed the modelling including the data preparation for the running of Blobby3D for galaxies from KROSS selected for this paper.
- Alfred Tiley from the KROSS team contributed to the paper by providing and organising the KROSS data for use by Mathew Varidel. We also note that this work builds on the observations and pipelines built by the KROSS team.
- Analysis including plots and calculations were performed by Mathew Varidel.
- This work was written by Mathew Varidel in consultation with supervisors Scott Croom and Geraint Lewis.

MNRAS 000, 1–14 (In Preparation) Preprint 11 June 2021 Compiled using MNRAS LATEX style file v3.0

SAMI-KROSS: The gas kinematics from $z \sim 1$ to $z \sim 0.1$ using disc modelling

Mathew R. Varidel[1,2]⋆ Scott M. Croom[1,2], and Geraint F. Lewis[1],
[1]*Sydney Institute for Astronomy (SIfA), School of Physics, A28, The University of Sydney, NSW 2006, Australia*
[2]*ARC Centre of Excellence for All Sky Astrophysics in 3 Dimensions (ASTRO 3D)*

Accepted XXX. Received YYY; in original form ZZZ

ABSTRACT

We study the evolution of gas kinematics in disc galaxies from at $z \sim 1$ and $z \sim 0.1$ using a consistent forward modelling technique. Our sample of galaxies include 193 galaxies from the KMOS Redshift One Spectroscopic Survey (KROSS) at $z \sim 1$ that have been modelled for this paper. The distribution of gas velocity dispersions is $\sigma_v = 41.4^{+14.9}_{-18.2}$ km s^{-1} in KROSS, represented by the median and 68% shortest-credible interval. Our estimates for σ_v are in agreement with previous analyses of galaxies with similar galaxy properties. Comparing the KROSS sample to galaxies from the SAMI Galaxy Survey and DYNAMO survey finds that all galaxies have kinematics that are consistent with being marginally stable discs. Furthermore, the gas kinematics across all three samples is consistent with theoretical models that suggest turbulence driven by a combination of star-formation feedback via supernovae plus gas transport through the disc.

Key words: galaxies: kinematics and dynamics, galaxies: evolution, techniques: imaging spectroscopy, methods: statistical, methods: data analysis

1 INTRODUCTION

Studies have shown that significant settling of the gas within galactic discs has occurred since $z \sim 1$ (Kassin et al. 2013; Wisnioski et al. 2015). Observations of the ionised gas using the Hα emission line find typical velocity dispersion of galaxies at $z \lesssim 0.1$ to be $\sigma_v \sim 10 - 30$ km s^{-1} (Epinat et al. 2008; Moiseev et al. 2015; Zhou et al. 2017; Varidel et al. 2020), whereas studies at $z \sim 1$ find typical mean velocity dispersions of $20 - 50$ km s^{-1} (Kassin et al. 2013; Wisnioski et al. 2015; Johnson et al. 2018; Übler et al. 2019). Similarly, for nearby galaxies where neutral hydrogen can be observed, galaxies have typical velocity dispersions of $\sigma_v \sim 10$ km s^{-1}, with scatter on the order of km s^{-1} (Leroy et al. 2008; Walter et al. 2008; Ianjamasimanana et al. 2012; Stilp et al. 2013). Therefore, it has been argued that the drivers of turbulence across this epoch must decrease significantly.

Numerous galaxy properties are also known to evolve from $z \sim 1$ to today. This includes fundamental parameters such as galaxy mass, size, and star-formation. Some of these parameters are related to the turbulence in the galaxy. For example, galaxies are thought to be in approximate equilibrium between gravitational collapse due to their mass and outward forces driven by centrifugal forces and turbulence as suggested by Toomre (1964) and found to be consistent with observations (Wisnioski et al. 2015). Furthermore, the gas accretion rate and star-formation rate is known to decrease over this epoch (Hopkins & Beacom 2006; Noeske et al. 2007a,b) which are both linked with potential drivers of turbulence including gravitational instabilities (Krumholz & Burkert 2010; Krumholz & Burkhart 2016) and star-formation feedback processes (Norman & Ferrara 1996; Mac Low & Klessen 2004; Lehnert et al. 2009; Green et al. 2014). We note that large scale dynamics, gravitational instabilities resulting from interactions between different components (e.g. Dobbs & Bonnell 2008; Tasker & Tan 2009; Aumer et al. 2010), as well as thermal instabilities due to interactions between various phases of the gas (Piontek & Ostriker 2004) have also been suggested to energetically contribute to gas turbulence. The role that each of these drivers may play in the ongoing gas turbulence within the disc is still highly debated, but an accurate measure of the velocity dispersion is a vital step towards improving our understanding.

The spatial resolution also plays an important part in inferring the gas kinematics. At increasing redshift the galaxy disc is less spatially resolved than galaxies nearby. Due to the blurring of the rotational velocity across the spatial resolution element, this results in broader observed emission line profiles at earlier redshifts. This effect, known as beam smearing, is well known but can be difficult to correct for as it depends on a complex function of the spatial luminosity, velocity, and velocity dispersion profiles (Davies et al. 2011; Varidel et al. 2019). As such, when comparing analyses across epochs it is preferable to do so using similar techniques.

In this paper, we take that approach by studying galaxies at $z \lesssim 0.1$ and $z \sim 1$ using a single disc fitting model

⋆ E-mail: mathew.varidel@sydney.edu.au

known as Blobby3D (Varidel et al. 2019). Disc fitting has become a popular method to estimate the velocity dispersion while limiting the effects of beam smearing. These methods construct a model of the underlying galaxy and then convolve the model by the spatial and spectral resolution prior to comparing to the observations. This approach has been used for a significant period of time with HI observations (e.g. Roberts 1968; Begeman 1987) at low redshifts. There has also been an increasing tendency to use disc modelling to infer the gas kinematics in Hα observations (e.g. Cresci et al. 2009; Übler et al. 2018, 2019; Varidel et al. 2019, 2020). Also see the interesting application of disc modelling with strong gravitational lensing by Rizzo et al. (2020).

Blobby3D provides an ability to infer the gas kinematics using a flexible galaxy model. In particular, the flexibility in the spatial gas profile allows for the modelling of galaxies with complex spatial substructure such as clumps and spirals. Blobby3D does this by allowing the flux profile to be decomposed into several two-dimensional (2D) Gaussian components. The 2D profiles for the rotational velocity and velocity dispersion are assumed to be well modelled by axisymmetric radial profiles. The model for the galaxy is then convolved by the PSF and compared to the data.

It was shown by Varidel et al. (2019) that spatially resolved clumpy gas flux profiles result in observations of spurious gas kinematic substructures. As such, Blobby3D is an appropriate approach in cases where gas flux substructure can be observed. In low-z galaxies this is often the case as the spatial resolution in IFS observations is sufficient to observe clumps. In high-z galaxies it is often harder to observe individual clumps as the spatial resolution is often comparable to the disc scale length in many large scale surveys. Although, we also know that galaxies at high-z have clumpy and irregular profiles with regularly rotating kinematics (Genzel et al. 2011; Wisnioski et al. 2011) consistent with the assumptions in Blobby3D. As such, Blobby3D is an appropriate tool to study the kinematics of galaxies for many IFS observations.

Our data consists of a sample at $z \sim 1$ from the KMOS Redshift One Survey (KROSS, Stott et al. 2016) that we have modelled using Blobby3D for this paper. This sample is compared to two samples that have previously been modelled using Blobby3D at $z \lesssim 0.1$ from the SAMI Galaxy Survey (Croom et al. 2012; Bryant et al. 2015) and the DYnamics of Newly Assembled Massive Objects (DYNAMO, Green et al. 2014) survey. This approach provides us with a consistent methodology of modelling gas kinematics for galaxies spanning an important epoch in galaxy evolution where galaxy kinematics are thought to have settled significantly.

The structure of this paper is as follows. In Section 2 we outline our data selection. In Section 3 we outline the modelling approach to infer the gas kinematics as well as the checks performed for this approach. In Section 4 we describe the inferences for the sample of galaxies from KROSS. In Section 5 we describe the evolution of velocity dispersion from $z \sim 1$ to $z \sim 0.1$. In Section 6 we compare the three samples to theoretical models for the drivers of turbulence. We summarise the conclusions drawn throughout our analysis in Section 7. Throughout this paper we assume the concordance cosmology ($\Omega_\Lambda = 0.7$, $\Omega_m = 0.3$, $H_0 = 70$ km s^{-1} Mpc^{-1}; Hinshaw et al. 2009) as well as a Chabrier (2003) initial mass function (IMF).

2 DATA SELECTION

2.1 KMOS Redshift One Survey

KROSS was designed to study typical star-forming galaxies at $z \sim 1$ (Stott et al. 2016). Galaxy selection for KROSS is constructed from several catalogues with known redshifts in the range $z \in [0.8, 1]$. A cut on an observed magnitude of $K_{\rm AB} < 22.5$ corresponding to $\log_{10}(\mathrm{M}_* \ / \ \mathrm{M}_\odot) \gtrsim 9.3$ for the given redshift range was applied in order to observe the Hα emission line. The parent sample for KROSS consists of $\gtrsim$ 17000 galaxies but the final sample was limited to galaxies with high local density in order to observe multiple objects simultaneously. A total of 795 galaxies were observed using the above criteria during the survey.

KROSS galaxies were observed using the K-band Multi-Object Integral Field Spectrograph (KMOS, Sharples et al. 2004, 2013). KMOS is on the European Southern Observatory Very Large Telescope (ESO/VLT). It allows for the simultaneous observation of 24 objects across a 7.2′ total Field of View (FoV). Each IFU has a $2.8'' \times 2.8''$ FoV with typical spatial resolution during KROSS of $\mathrm{FWHM_{PSF}} = 0.7'' \pm 0.2''$.

The YJ-band grating for KMOS was used to observe the Hα emission line that is redshifted to 1.181 – 1.312 μm at $z \in [0.8, 1.0]$. The typical spectral resolution was $R = 3400$ at the Hα emission line. Although, it has been shown that the difference in spectral resolution is up to $\Delta R/R \sim 1000$ ($\sigma \sim 10$ km s^{-1}) across the different IFUs (Wisnioski et al. 2019).

During the survey up to 20 galaxies were observed simultaneously with the remaining observations made up of 3 IFUs for sky-subtraction and 1 for observing a star to determine the PSF. Three separate dithers are used for each galaxy that are combined into a single data cube. We use the final data cubes that have a uniform sampling of 0.2″ for the modelling and analysis in this paper (Stott et al. 2016).

The following sample selection criteria was used for this paper. 20 galaxies were removed due to being identified as having Active Galactic Nuclei (AGN) in the KROSS database (AGN_FLAG = 1, Harrison et al. 2017). These galaxies have an emission line ratio of [NII]/H$\alpha > 0.8$ or a broad line component in the Hα emission line profile of $\gtrsim 1000$ km s^{-1} which is consistent with AGN identification criteria proposed by Kewley et al. (2013). We only use galaxies where Harrison et al. (2017) were able to use the Hα emission line to determine the half-light radius and inclination. We also remove highly inclined galaxies ($i > 60°$) as it is difficult to estimate the intrinsic vertical velocity dispersion for those galaxies.. These are classified as QUALITY = 1 galaxies by Harrison et al. (2017).

We show global galaxy parameters from the KROSS data for our selection in Figure 1. There were 315 galaxies remaining after applying the above cuts. Our selection criteria does not appear to introduce any significant biases compared to the properties in the full sample from KROSS.

2.1.1 Auxilliary data from KROSS

Several data products from the publicly available KROSS catalogue are used throughout this paper. We use the redshift (z), integrated star-formation rates (SFR), integrated stellar mass (M_*), as well as the inferred deconvolved half-light radius (R_e), inclination angle (i), and redshift (z) which are

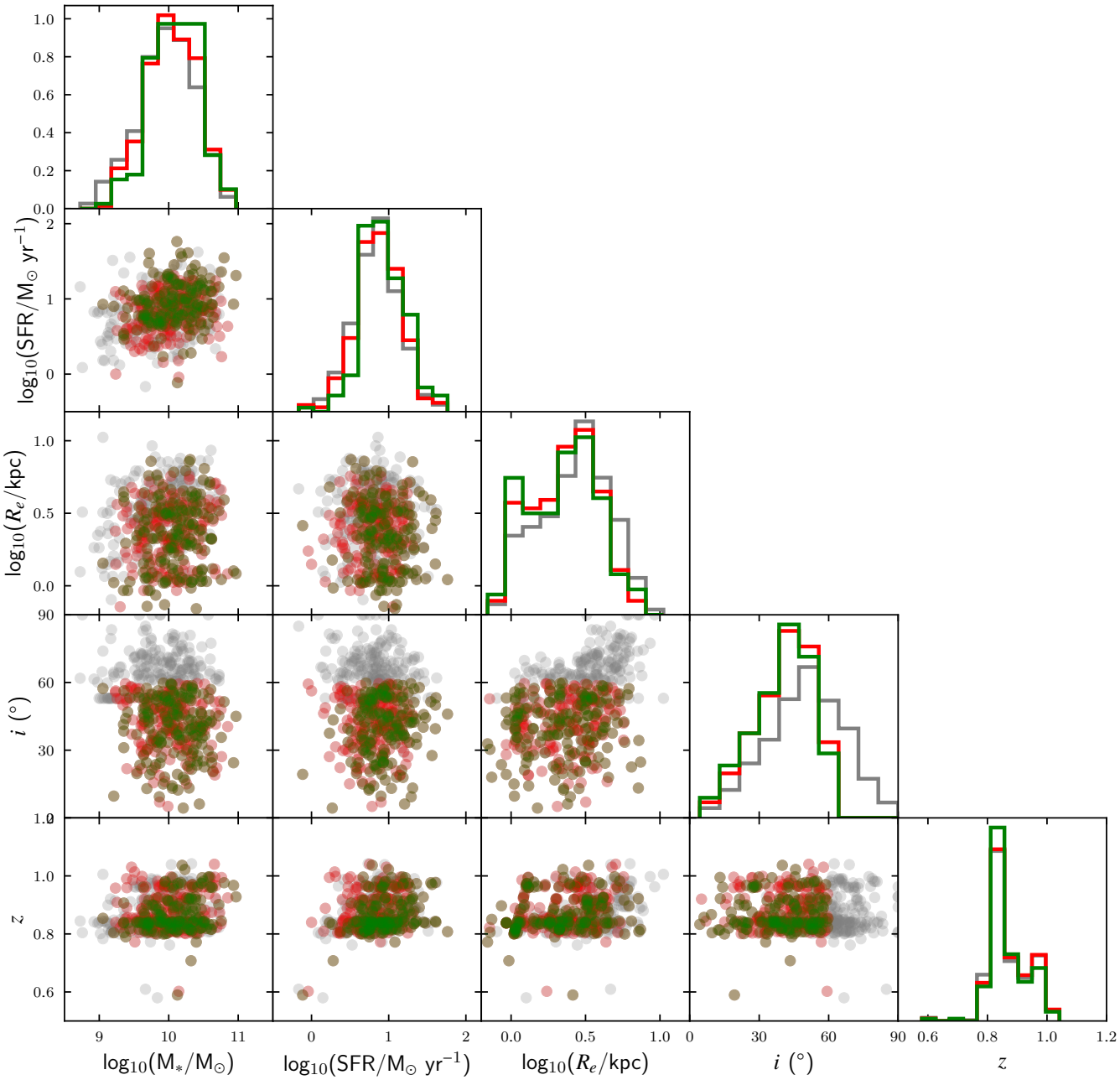

Figure 1. Data selection from KROSS. Galaxies selected as in Section 2.1 (red) and a final cut performed later as described in Section 3.1.1 (green) compared to the full sample (grey). Parameters shown are stellar mass (M_*), integrated star-formation rate (SFR), half-light radius (R_e), inclination (i), and redshift (z). Our sample selection does not appear to deviate significantly from in fundamental galaxy property distributions in KROSS.

denoted as 'SFR', 'MASS', 'R_IM', 'THETA_IM', and 'Z' by Harrison et al. (2017). We will provide a quick summary of these data products below, but please see Harrison et al. (2017) for a full explanation of these data products.

The redshift and SFR were calculated using the summed spectra of the Hα emission line. SFR was calculated using the integrated Hα luminosity in the KROSS data cube. The lumunosity is then converted to a SFR using the relation proposed by Kennicutt (1998) and converted to a Chabrier (2003) IMF. An extinction correction is applied in accordance with Wuyts et al. (2011).

Stellar masses were estimated by scaling the H-band AB magnitude by a constant mass-to-light ratio for all galaxies. Harrison et al. (2017) used the mass-to-light ratio of $\Upsilon_H = 0.2$, that was the median mass-to-light ratio for the KROSS sample using the HYPERZ spectral energy distribution (SED) fitting code with spectral templates provided by Bruzual & Charlot (2003) and fitted to the U-band via IRAC 4.5 μm photometry. The stellar mass is then calculated as $M_* = \Upsilon_H \times 10^{-0.4(M_H - 4.71)}$.

The half-light radius and inclinations are described by Johnson et al. (2018). The inclination is determined by fit-

ting a 2D Gaussian profile to the broad-band imaging from the Hubble Space Telescope or the UKIRT Infrared Deep Sky Survey (UKIDDS, Lawrence et al. 2007). Then the inclination ('THETA_IM', $\theta_{\rm im}$) is derived using the following assumption,

$$\cos^2\theta_{\rm im} = \frac{(b/a)^2 - q_0^2}{1 - q_0^2}, \quad (1)$$

with the intrinsic thickness of the galaxy assumed to be $q_0 = 0.2$. To determine the half-light radius the broad-band images were then fitted using a series of increasingly larger concentric 2D ellipses with constant position angle derived using a 2D Gaussian profile fit to the broad-band image. 'R_IM' $= R_e$ is the semi-major radius where half of the flux is encompassed within the ellipse.

2.2 Comparative Samples

In this paper, we will also compare our results from KROSS to galaxies from the SAMI Galaxy Survey (Croom et al. 2012; Bryant et al. 2015) and the DYNAMO (Green et al. 2014) survey. We use the inferred kinematic results of Varidel et al. (2020) from these data sets for our comparison. We use these results as they have been analysed in similar ways to the KROSS data in this paper. The motivation for the sample selection from the SAMI Galaxy Survey and DYNAMO survey are provided in Varidel et al. (2020) but we summarise the selection below for clarity.

The sample of galaxies from the SAMI Galaxy Survey is from Data Release 2 (Scott et al. 2018). Star-forming galaxies were selected by applying a cutoff of Hα equivalent width of of $EW > 3$ Å (Cid Fernandes et al. 2011). AGN and Low-Ionisation Nuclear Emission-line Regions (LINERs) were removed using the criteria proposed by (Kauffmann et al. 2003). In an effort to accurately infer the gas velocity dispersion, galaxies were selected with the semi-major to semi-minor axis ratio of $0.5 < b/a < 1$, corresponding to inclination of $i < 60°$ assuming a circular thin disc. A signal-to-noise cut was also applied by selecting only galaxies that have at least 300 connected spaxels with Hα signal-to-noise > 3. Nine galaxies were also removed that appeared to have disturbed kinematics that were suggestive of major mergers. Using the above criteria 342 galaxies remained.

Similar cuts were performed for the DYNAMO Survey. Galaxies were selected with inclination of $i < 60°$. A cut of galaxies with < 30 connected spaxels with Hα signal-to-noise > 3. A total of 41 galaxies were selected from a total of 67 galaxies in the DYNAMO survey.

We also use supplementary data from the catalogues for the SAMI Galaxy Survey (Bryant et al. 2015) and DYNAMO survey (Green et al. 2014). This includes stellar mass, inclination and redshift. The SFR for galaxies from the DYNAMO survey come from Green et al. (2014). The SFR for galaxies from the SAMI Galaxy Survey come from the best fit values from the GAMA Survey (Gunawardhana et al. 2013; Davies et al. 2016; Driver et al. 2018), which use SED fitting of 21 photometry bands with MAGPHYS (da Cunha et al. 2008). The values used throughout this paper are consistent with those used by Varidel et al. (2020).

3 METHODS

3.1 Modelling the gas kinematics

Blobby3D (Varidel et al. 2019) was used to model the gas kinematics for our sample of galaxies from KROSS. Blobby3D is a three-dimensional (3D, spatial–spatial–wavelength) data cube fitting code. The primary use case of Blobby3D is to model the gas kinematics of galaxies while limiting the effects of beam smearing. This is performed by constructing a galaxy model that is convolved by the point spread function (PSF) prior to comparing the model to the data via the likelihood function.

We start with the joint prior as outlined by Varidel et al. (2019) and modified slightly in Varidel et al. (2020). We make one further modification to the joint prior distribution, which is to restrict the minimum velocity dispersion to be equal to the expected thermal contribution from the gas of ∼9 km s^{-1} (Glazebrook 2013). The prior for the constant velocity dispersion term across the disc is then,

$$\sigma_{v,0} \sim \text{Loguniform}(9 \text{ km s}^{-1}, 200 \text{ km s}^{-1}). \quad (2)$$

The joint posterior distribution was sampled using DNest4 (Brewer et al. 2009; Brewer & Foreman-Mackey 2016). DNest4 is a diffusive nested sampling algorithm that performs a Markov-Chain Monte-Carlo (MCMC) sampling of a mixture of constrained likelihood levels. DNest4 routinely saves MCMC samples during the run. The post-processing in DNest4 estimates the posterior-weights for each level and outputs a sample of MCMC saves based on these posterior weights. We eliminate any runs of DNest4 where the posterior sample provided was less than 50. In cases where a mode is identifiable in the posterior PDF, we report the median of the posterior PDF as a point estimate, with upper and lower reported values estimated as the bounds of the 68% shortest credible interval (e.g. Chapter 2.2.2 in Sivia & Skilling 2012).

For our galaxies from KROSS we also choose to run Blobby3D in single component mode. In this case, the number of Gaussian components that represent the spatial flux profile is set to one. We did this to limit the run time. Also the spatial resolution of KROSS is such that the PSF is often a similar size to the disc, such that individual gas clumps are often smeared out. For the SAMI and DYNAMO galaxies we allowed the number of Gaussian clumps to vary. We ran a sample of 60 galaxies from KROSS allowing the number of components to vary between 1 and 10. We show the comparison between the single ($\sigma_{v,\rm single}$) to multiple ($\sigma_{v,\rm multi}$) component fits in Figure 2. We find the mean difference to be $\sigma_{v,\rm single}/\sigma_{v,\rm multi} = 1.04 \pm 0.03$. As such, we find little evidence for a difference between the two approaches. We suspect that the spatial resolution of KROSS may play a significant role in this. Furthermore, as we are calculating the average velocity dispersion rather than the localised velocity dispersion, the differences can average across the disc.

3.1.1 Beam smearing corrections

We show our inferred velocity dispersion estimates ($\sigma_{v,0}$) using Blobby3D for the sample of galaxies from KROSS compared to alternative approaches in Figure 3. Two alternative approaches have been estimated by (Johnson et al. 2018). They report an estimate of the velocity dispersion in the outskirts of the galaxy ($\sigma_{v,\rm obs}$) as well as a beam smearing cor-

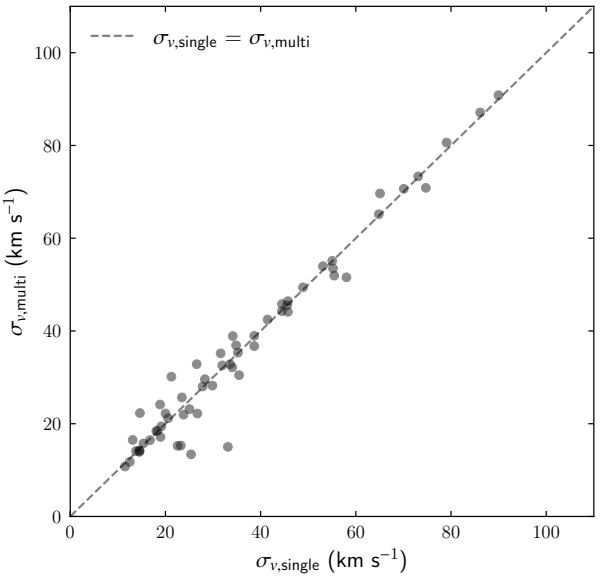

Figure 2. Comparing inferences for σ_v using Blobby3D for spatial flux assuming models with a single ($\sigma_{v,\mathrm{single}}$) and variable (between 1 and 10) Gaussian components ($\sigma_{v,\mathrm{multi}}$). This plot shows the comparison for 60 galaxies from our sample from KROSS. We find that there is no significant difference between $\sigma_{v,\mathrm{single}}$ and $\sigma_{v,\mathrm{multi}}$.

rection on that value as a function of the rotational velocity and disc scale length compared to the PSF width ($\sigma_{v,0,\mathrm{J18}}$).

The beam smearing corrected value for the velocity dispersion provided by Johnson et al. (2018) performs an explicit correction to the observed value. Therefore, $\sigma_{v,0,\mathrm{J18}}$ is strictly less than $\sigma_{v,\mathrm{obs}}$. The typical difference between these two values is minor with the median difference of $\sigma_{v,0,\mathrm{J18}}/\sigma_{v,\mathrm{obs}} = 5.8\%$. Although, some values are corrected as much as 80% difference. While corrections are often minor, some significant corrections occur as the velocity dispersion in the outskirts of an observed galaxy can still be elevated due to beam smearing effects (e.g. Figure B1 in Johnson et al. 2018).

Prior to establishing our final sample, we found an issue with estimated the velocity dispersion for some galaxies. Approximately 38% of galaxies have no clear mode in the distribution for $\sigma_{v,0}$ that is distinguishable above the $\sigma_{v,\mathrm{thermal}}$ limit. This suggests that those galaxies have unphysical velocity dispersions. This issue has been observed in galaxies observed using KMOS previously. A significant proportion of galaxies studied by Übler et al. (2019) using The KMOS^{3D} Survey data and fitted with a 3D disc modelling approach were found to have best-fit velocity dispersion values below the thermal limit. They found 28 of 175 of their total galaxy sample and 22 out of 80 at $z \sim 0.6 - 1.0$ had values below the thermal limit. They attribute this to the variation in the spectral resolution of up to $\Delta R = 1000$ on the KMOS instrument (Wisnioski et al. 2019). Given such significant uncertainty in the spectral resolution on KMOS it will be difficult to accurately infer the velocity dispersion below the spectral resolution of $\sigma_{\mathrm{LSF}} \sim 37$ km s^{-1}.

For this paper, we have decided to remove galaxies that do not have clear modes in their posterior PDF. Those galaxies are shown in green in Figure 1. There is no evidence to suggest that this introduces any biases from our underlying samples.

The final sample that we use in subsequent sections of this paper is shown in the furthest right panel in Figure 3. For this sample, there is a slight offset of $\sigma_{v,0}/\sigma_{v,0,J18} - 1 = -0.07^{+0.19}_{-0.41}$. However, the samples are broadly consistent after considering the uncertainties on both measures, as we find $z = (\sigma_{v,0} - \sigma_{v,0,\mathrm{J18}})/\sqrt{(\Delta\sigma_{v,0,\mathrm{J18}})^2 + (\Delta\sigma_{v,0})^2} = -0.11^{+0.54}_{-0.63}$. We consider this our most reliable sample of galaxies from KROSS to perform inferences on later in this paper.

The above results are consistent with the disc modelling tests performed by Johnson et al. (2018). They analysed a sample of 14 galaxies within KROSS using ^{3D}Barolo (Di Teodoro & Fraternali 2015). They found that the the velocity dispersion estimated using ^{3D}Barolo were typically 20% less than $\sigma_{v,0,\mathrm{J18}}$. However, they found 12 out of 14 galaxies were within 2σ agreement with $\sigma_{v,0,\mathrm{J18}}$.

3.1.2 Velocity dispersion checks

We compare our remaining sample of $\sigma_{v,0}$ to galaxy inclination (i) and the Full-Width Half-Maximum of the PSF ($\mathrm{FWHM_{PSF}}$) as a check (see Figure 4). We find that the PDF for the correlation between i and $\sigma_{v,0}$ is $\rho(i, \sigma_{v,0}) = 0.06 \pm 0.08$, which includes zero, consistent with a sample that has removed the inclination effects on $\sigma_{v,0}$. We do find $\rho(\mathrm{FWHM_{PSF}}, \sigma_{v,0}) = -0.16 \pm 0.07$ suggesting that there is a potential over-correction in $\sigma_{v,0}$ with respect to the $\mathrm{FWHM_{PSF}}$. We have not applied a further correction to $\sigma_{v,0}$ to remove this issue.

Blobby3D was tested with the focus on typical galaxies observed in the SAMI Galaxy Survey. Galaxies within SAMI are at $z \lesssim 0.1$ and have spatial resolution of $\Delta R/R = 4304$ ($\sigma \sim 29.6$ km s^{-1}) near Hα and spatial resolution of $\mathrm{FWHM_{PSF}} \sim 2$" with typical galaxy half-light radius ~ 1" (Scott et al. 2018). In comparison KROSS has spectral resolution $\Delta R/R = 4304$ ($\sigma \sim 37$ km s^{-1}) with galaxies at higher redshift with lower spatial resolution. Therefore, SAMI Galaxy Survey observations are typically at higher spatial and spectral resolution than KROSS. Therefore, Blobby3D may over-correct in this lower resolution regime.

3.1.3 Rotational Velocity

We use the rotational velocity profile inferred in the fitting of Blobby3D. The assumed velocity profile in Blobby3D is the empirical model assumed by (Courteau 1997),

$$v(r) = \frac{(1 + r_t/r)^{\beta}}{(1 + (r_t/r)^{\gamma})^{1/\gamma}} \sin(i)\cos(\theta) + v_{\mathrm{sys}}. \quad (3)$$

Where r is defined as the radial distance from the kinematic centre of the galaxy, r_t is the turnover radius, v_{sys} is the systemic velocity, v_c is the asymptotic velocity. β defines the shape for $r > r_t$, where $\beta < 0$ corresponds to a positive velocity gradient, and $\beta > 0$ corresponds to a decreasing velocity gradient. γ defines the sharpness of the velocity profile turnover at $r = r_t$. Then i corresponds to the inclination and θ corresponds to the polar angle in the plane of the disc.

We report the inclination corrected rotational velocity at

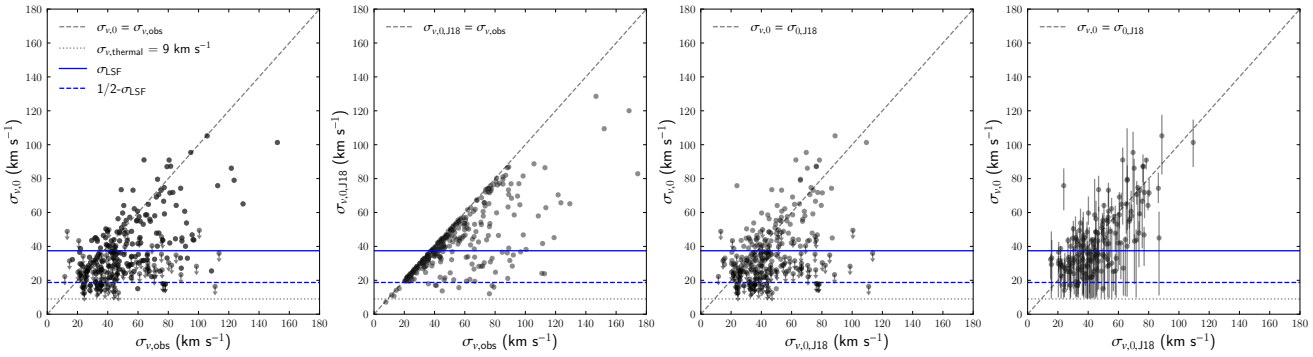

Figure 3. Comparisons of our estimates for the velocity dispersion for our sample of galaxies from KROSS. We show our estimates ($\sigma_{v,0}$) compared to two estimates from Johnson et al. (2018). The two comparison are the observed velocity dispersion in the outskirts of the galaxy ($\sigma_{v,\rm obs}$) and a beam smearing corrected estimated applied as a function of velocity and disc scale length compared to the PSF width ($\sigma_{v,0,\rm J18}$). For each panel we draw horizontal lines to show the typical instrumental broadening ($\sigma_{\rm LSF}$), half the instrumental broadening (1/2-$\sigma_{\rm LSF}$), and the thermal broadening for a HII region ($\sigma_{v,\rm thermal} = 9$ km s^{-1}). In the fourth panel we only show galaxies where there is a clear mode in the posterior PDF from our fits. We also show the 68% shortest credible interval in the fourth panel.

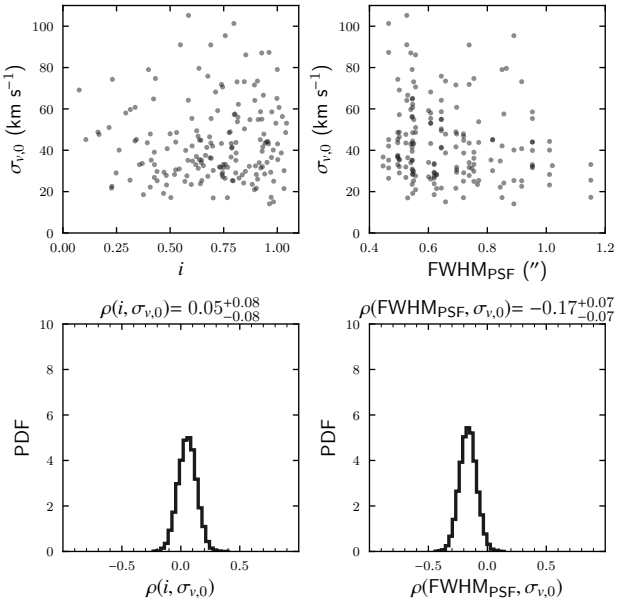

Figure 4. Our velocity dispersion estimates compared to the inclination (left column) and FWHM$_{\rm PSF}$ (right column). We find no significant correlation between $\sigma_{v,0}$ and i. We do find a negative correlation between FWHM$_{\rm PSF}$ and $\sigma_{v,0}$, suggesting a potential over-correction using BLOBBY3D.

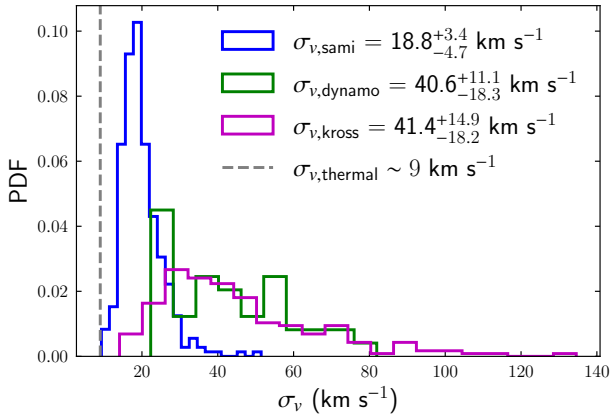

Figure 5. Velocity dispersion for samples from KROSS, SAMI and DYNAMO. We find similar distributions for the velocity dispersion for KROSS and DYNAMO, whereas SAMI has lower velocity dispersions.

$r = 2.2R_e$ for each galaxy. We note that the typical location to record the rotational velocity is $r = 2.2r_d$, where r_d is the exponential disc scale length. We use $r = 2.2R_e$ as it is consistent with the Tully-Fisher relation derived by Bloom et al. (2017) which was subsequently used to make comparisons with the SAMI and DYNAMO galaxies in Varidel et al. (2020). To limit the effect of the inclination corrections on the inferred rotational velocity we do not report galaxies that have $i < 30°$. The total number of galaxies where we report the $v_{2.2}$ value is 151. The choice of estimating the rotational velocity at $r = 2.2R_e$ and removing galaxies the inclination of $i < 30°$ is consistent with the estimated values for the galaxies from the SAMI Galaxy Survey and DYNAMO survey.

4 RESULTS

4.1 Typical velocity dispersions in KROSS

KROSS galaxies have velocity dispersions significantly above the thermal component for a HII region. The distribution of velocity dispersions is $\sigma_{v,\rm kross} = 41.4^{+14.9}_{-18.2}$ km s^{-1}, where the upper and lower bounds are estimated using the 68% shortest-credible interval. We estimate the median to be $\sigma_v = 41.4 \pm 1.2$ km s^{-1}, which is only slightly lower than $\sigma_0 = 43 \pm 1$ km s^{-1} reported by Johnson et al. (2018). These values are significantly higher than the thermal broadening of $\sigma_{v,\rm thermal} \sim 9$ km s^{-1} (Glazebrook 2013), which suggests turbulent motions in the ISM.

The KROSS velocity dispersions are typical of galaxies with similar global galaxy properties (see Figure 5). Their velocity dispersions are approximately consistent with the sample from DYNAMO with $\sigma_{v,\mathrm{dynamo}} = 40.6^{+11.1}_{-18.3}$ km s^{-1}. KROSS and DYNAMO both have $9.5 \lesssim \log_{10}(\mathrm{M}_*/\mathrm{M}_\odot) \lesssim 11$ and $0 \lesssim \log_{10}(\mathrm{SFR}/\mathrm{M}_\odot\ \mathrm{yr}^{-1}) \lesssim 2$, which are quantities well known to be correlated with velocity dispersion. Similarly, KROSS galaxies match well with other galaxies at similar redshift, for example Übler et al. (2019) derive a best fit value of $\sigma_0 \sim 34.3$ km s^{-1} at $z \sim 0.9$.

In contrast, SAMI has lower velocity dispersions than KROSS with $\sigma_{v,\mathrm{sami}} = 18.8^{+3.4}_{-4.7}$ km s^{-1}. SAMI galaxies have a wider range of galaxy properties with $8 \lesssim \log_{10}(\mathrm{M}_*/\mathrm{M}_\odot) \lesssim 11$, $-2 \lesssim \log_{10}(\mathrm{SFR}/\mathrm{M}_\odot\ \mathrm{yr}^{-1}) \lesssim 1$, and $z \sim 0.1$. This is consistent with the previously studies that have found higher velocity dispersions at higher redshift.

4.2 Velocity dispersion correlations in KROSS

We show our inference for σ_v in the KROSS sample compared to global galaxy properties in Figure 6. The properties we compare to are stellar mass (M_*), rotational velocity ($v_{2.2}$), and integrated star-formation measures. The integrated stellar masses come from the SAMI Galaxy Survey catalogue (Bryant et al. 2015). The rotational velocity measure, $v_{2.2}$, is estimated using the inferred profile by Blobby3D extrapolated to $2.2R_e$. The rotational estimate is corrected for the inclination angle. We only consider galaxies with $30° < i < 60°$ to limit the issue of estimating the rotational velocity for nearly face-on galaxies. For the star-formation rate we show the integrated star-formation rate (SFR) using the specific star-formation rate ($\mathrm{sSFR} = \mathrm{SFR}/\mathrm{M}_*$), the log difference between the SFR and expected SFR given it's stellar mass ($\Delta\mathrm{MS} = \log_{10}(\mathrm{SFR}/\mathrm{SFR}(\mathrm{M}_*, z))$) where $\mathrm{SFR}(\mathrm{M}_*, z)$ is estimated using the relation from Wuyts et al. (2011), and the star-formation rate density estimated as $\Sigma_{\mathrm{SFR}} = \mathrm{SFR}/\pi R_e^2$. Previous studies have found that these properties are positively correlated with velocity dispersion. However, we only find a significant relation with average star-formation rate density (Σ_{SFR}).

Correlations with global properties are difficult to find in the KROSS data set. This is explained by the limited dynamic range in galaxy properties. The stellar mass range in particular, which is well known to correlate with all of these global properties, ranges from $\log_{10}(\mathrm{M}_*/\mathrm{M}_\odot) \in [9.5, 10.5]$. It remains interesting that a clear correlation is shown with Σ_{SFR}. Σ_{SFR} has consistently been found to have a significant correlation with velocity dispersion across numerous studies (Lehnert et al. 2009, 2013; Yu et al. 2019; Übler et al. 2019; Varidel et al. 2020). In particular, the greatest correlation in SAMI galaxies was also Σ_{SFR}.

5 EVOLUTION IN GAS TURBULENCE SINCE $Z \sim 1$

We now compare our inferences for the gas kinematics in KROSS at $z \sim 1$ to galaxies from the SAMI Galaxy Survey and DYNAMO survey at $z \lesssim 0.1$. The goal is to show the change in gas kinematics across this range and compare those changes to predictive models that exist in the literature.

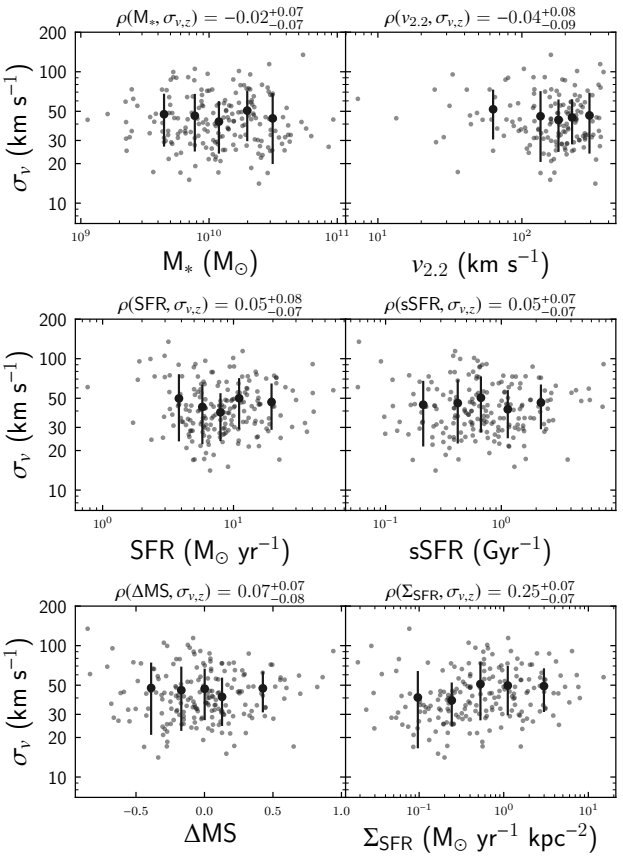

Figure 6. Correlation of velocity dispersion with global galaxy properties for KROSS. We show comparisons against stellar mass M_*, rotational velocity ($v_{2.2}$), integrated star-formation rate (SFR), specific star-formation rate ($\mathrm{sSFR} = \mathrm{SFR}/\mathrm{M}_*$), the offset between SFR and expected star-formation given stellar mass ($\Delta\mathrm{MS} = \log_{10}(\mathrm{SFR}/\mathrm{SFR}(\mathrm{M}_*, z))$) and average star-formation rate density ($\Sigma_{\mathrm{SFR}} = \mathrm{SFR}/\pi R_e^2$). We use the Spearman-rank correlation coefficients with upper and lower bounds estimated as the 68% shortest credible interval after 10^4 bootstrap resamples. The median in the galaxy properties, σ_v plus the 68% shortest credible interval upper and lower bounds for σ_v in 5 bins with equal number of data points are also shown. We only find a clear correlation between velocity dispersion and Σ_{SFR}.

5.1 Marginally stable Toomre discs

A gas disc is expected to be in marginally stable equilibrium between gravitational collapse and outward forces due to centrifugal forces and random motions. The Toomre (1964) stability criterion for a gas disc is,

$$Q_{\mathrm{g}} = \frac{\kappa \sigma_v}{\pi G \Sigma_{\mathrm{g}}}, \tag{4}$$

where κ is the epicyclic frequency and Σ_{g} is the gas surface density. Genzel et al. (2011) showed that this can be written in terms of the total and gas mass of the galaxy,

$$Q_{\mathrm{g}} = \frac{\sigma_v}{v} \frac{a M_{\mathrm{tot}}}{M_{\mathrm{g}}} = \frac{\sigma_v}{v} \frac{a}{f_{\mathrm{g}}}. \tag{5}$$

The parameter a defines the shape of the rotation curve of the galaxy. Rotational models that are typically assumed are Keplarian ($a = 1$), constant ($a = \sqrt{2}$), uniform density ($a = \sqrt{3}$), or solid-body ($a = 2$). $f_g \equiv \mathrm{M}_{\mathrm{tot}}/\mathrm{M}_*$ represents the

total gas fraction. There are several ways to compare this relation to the data.

We start by following the approach taken by Wisnioski et al. (2015), who constructed a predictive model for the kinematics based on estimating f_g as a function of z from scaling relations. They start by assuming that the molecular gas fraction dominates, such that $f_g = f_{g,\rm mol}$, which is true for typical high star-formation rate galaxies. Also, the relevant gas to determine Q_g is that within the disc radius and near the mid-plane such that it is typically molecular. The molecular gas fraction is defined as,

$$f_{g,\rm mol} \equiv \frac{1}{1 + (t_{\rm dep}{\rm sSFR})^{-1}} \quad (6)$$

where the depletion time of the molecular gas is $t_{\rm dep} \equiv {\rm M}_{g,\rm mol}/{\rm SFR}$ and the specfic star-formation rate as ${\rm sSFR} \equiv {\rm SFR}/{\rm M}_*$. They use the depletion rate scaling relation as defined by,

$$t_{\rm dep}[{\rm Gyr}] = 1.5(1+z)^{\alpha}, \quad (7)$$

where the range -1.5 $< \alpha <$ -0.7 has been proposed (Davé et al. 2012; Tacconi et al. 2013). We use $\alpha = -1$ as suggested by Wisnioski et al. (2015). The specific star-formation rate follows the scaling relation from Whitaker et al. (2014),

$${\rm sSFR}({\rm M}_*, z) = 10^{a({\rm M}_*)}(1+z)^{b({\rm M}_*)} \quad (8)$$

with the following relations substituted into the above equation,

$$a({\rm M}_*) = -10.73 + \frac{1.26}{1 + \exp((\log_{10}({\rm M}_*/{\rm M}_\odot) - 10.49)/0.25)} \quad (9)$$

$$b({\rm M}_*) = 1.85 + \frac{1.57}{1 + \exp((10.35 - \log_{10}({\rm M}_*/{\rm M}_\odot))/0.19)}. \quad (10)$$

We note that the above relations were constrained using data in the range $0.5 < z < 2.5$ and $9.2 < \log_{10}({\rm M}_*/{\rm M}_\odot) < 11.2$. The SAMI and DYNAMO galaxies are at $z \sim 0.1$, so the extrapolation may not be valid. We will address this shortly.

We put these relations back into Equation 5 and rearrange to yield redshift predictions for the kinematics of the galaxy. We show these results in Figure 7. The data plotted are limited to SFR > 0.05 M$_\odot$ yr^{-1} and $\log({\rm M}_*/{\rm M}_\odot) > 9.5$. The mass range is applied as the Toomre stability criterion is much more robust for higher mass galaxies. The SFR limit is applied to remove 3 galaxies that have outlying SFR compared to the remaining galaxies at $\log({\rm M}_*/{\rm M}_\odot) > 9.5$, that have low estimated molecular gas fractions using the above approach of $f_g < 0.01$.

The top panel in Figure 7 shows a grey band representing a range of realistic velocities for our galaxies of $v \in [100, 250]$ km s^{-1}. In the bottom panel the grey band represents $0.5 < Q_g < 2.0$, which are realistic values for Q_g. It is usually expected that Q_g will be close to the critical stability value ($Q_{\rm crit}$) that is required to maintain gravitational equilibrium. For a thin gas disc it is expected to be $Q_{\rm crit} = 1$. However, for thicker discs this decreases as low as $Q_{\rm crit} \sim 0.6$ (Kim et al. 2002; Kim & Ostriker 2007). Considering a combined stellar plus gas disc raises the expected value as high as $Q_{\rm crit} \sim 1.4$. Also, adding magnetic fields to the simulations increases $Q_{\rm crit}$ by an extra ∼50% (Kim et al. 2003).

The SAMI and KROSS data show approximate agreement

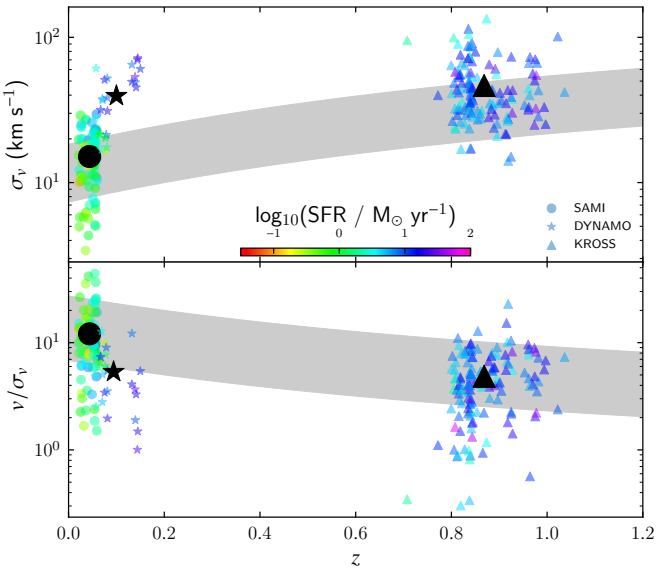

Figure 7. Kinematic redshift predictions as proposed by Wisnioski et al. (2015). In the top panel we show the velocity dispersion (σ_v) prediction within a band of 100 km s^{-1} < v < 250 km s^{-1}. In the bottom panel we show the ratio between rotational and random motions (v/σ_v) in a band $0.5 < Q_g < 2$. We assumed $a = \sqrt{2}$ in both panels. Also note that 15 km s^{-1} has been subtracted in quadrature from σ_v prior to plotting. We have also limited the galaxy ranges to $\log_{10}({\rm M}_*/{\rm M}_\odot) > 9.5$ and SFR > 0.05 M$_\odot$ yr^{-1}. The black points show the median values for each sample along both axes. We find approximate agreement between the predictions and our data from KROSS and SAMI, whereas the DYNAMO galaxies sit outside the predicted ranges.

with the predicted kinematic ranges. The exception are the DYNAMO galaxies that have higher velocity dispersion than predicted. DYNAMO galaxies have higher than average SFR, and thus higher molecular gas fraction than typical galaxies at $z \sim 0.1$. As such, it is not expected that they would follow the average evolution of kinematics.

To address this point, we show v/σ_v compared to the predicted molecular gas fractions in Figure 8. In this case, we also show the data compared to the gas fractions predicted by Tacconi et al. (2018), who have used a larger data set in the range $0 < z < 4$, which is more appropriate for the redshift range that we have studied. They show that the molecular to stellar gas mass ratio is dependent on z, ΔMS, and M$_*$. The relation they use is,

$$\log_{10}({\rm M}_{\rm mol}/{\rm M}_*) = 0.07 - 3.8(\log_{10}(1+z) - 0.63)^2 + 0.53\log_{10}({\rm sSFR}/{\rm sSFR}({\rm MS}, z, {\rm M}_*)) - 0.33\log_{10}({\rm M}_*/{\rm M}_\odot) - 10.7 \quad (11)$$

where we have substituted in the values in their Table 3b. They use the predicted sSFR relation estimated by Speagle et al. (2014), where

$$\log_{10}({\rm sSFR}/{\rm Gyr}^{-1}) = (-0.16 - 0.026t_c)(\log_{10}({\rm M}_*/{\rm M}_\odot) + 0.025) - (6.51 - 0.11t_c) + 9 \quad (12)$$

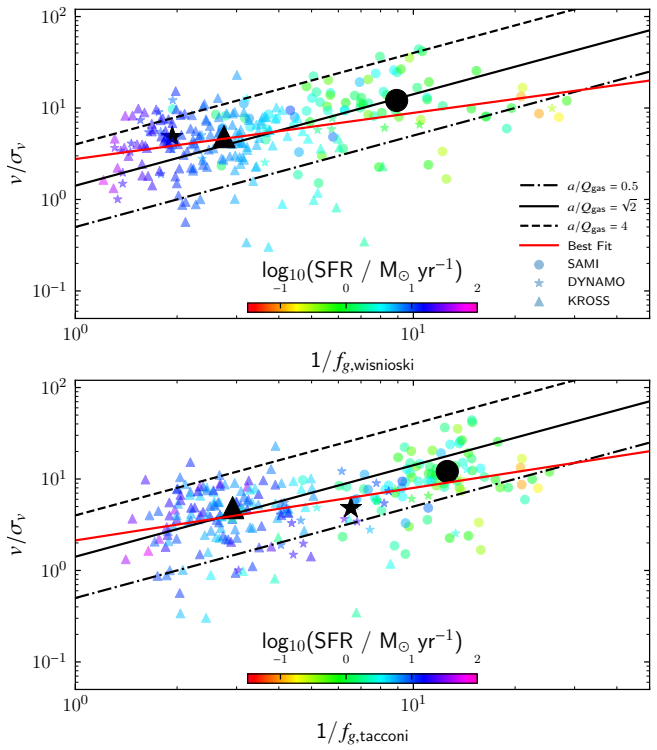

Figure 8. v/σ_v compared to the inverse of the molecular gas fraction f_g. Where f_g is estimated using the procedures outlined by Wisnioski et al. (2015) in the top panel and Tacconi et al. (2018) in the bottom panel. The same galaxy selection from our samples as Figure 7 has been applied. We plot three lines representing a/Q_g = 0.5, $\sqrt{2}$, and 4 encompassing the ranges $1 < a < 2$ and $0.5 < Q_g < 2$. Mean $1/f_g$ and v/σ_v are plotted in large black points for our samples from each survey. A linear fit of the form $v/\sigma_v = b - m\log_{10}(f_g)$ is also shown. We find that all samples lie in realistic ranges of a/Q_g. The fitted trend line and and mean values suggest that there is a decrease in a/Q_g (i.e. increase in Q_g assuming a is constant) from the KROSS to SAMI sample.

with,

$$\log_{10}(t_c) = 1.143 - 1.026\log_{10}(1+z) - 0.599\log_{10}^2(1+z) + 0.528\log_{10}^3(1+z). \quad (13)$$

We find that all galaxy samples lie in realistic ranges of a/Q_g. The mean values for a/Q_g lie in the $0.5 < a/Q_g < 4$ range which is constructed assuming $1 < a < 2$ and $0.5 < Q_g < 2$. For individual galaxies using the $f_{g,\mathrm{wisnioski}}$ (as defined in Equations 6 - 10) we find 75% of galaxies lie in the range $0.5 < a/Q_g < 4$. Similar results are found using $f_{g,\mathrm{tacconi}}$ (as defined in Equations 11 - 13) with 79% of galaxies in the range $0.5 < a/Q_g < 4$. As such, the results suggest that typical galaxies lie in the range $0.5 < a/Q_g < 4$.

In particular, DYNAMO galaxies are not significant outliers when plotted in the v/σ vs. $1/f_g$ space. A similar result was found by Green et al. (2014), where they used the relations proposed by Kennicutt (1998) to infer the total (HI + H_2) gas mass of the galaxy. As such, all three samples can be understood to be well explained by the Toomre stability criterion.

The predicted molecular gas fractions for DYNAMO galaxies vary depending on the scaling relation used. Using the predictions by Wisnioski et al. (2015) suggests that DYNAMO galaxies have similar f_g to the KROSS sample, whereas f_g predicted by Tacconi et al. (2018) lie between the KROSS and SAMI samples. As the DYNAMO galaxies are rare for their redshift it is likely that the scaling relation may not be ideal.

Several estimates of the molecular gas fraction have been performed for DYNAMO. Fisher et al. (2019) have compiled a sample of 17 DYNAMO galaxies with molecular gas measurements using CO(1-0) emission and infrared spectral energy density fitting. Their estimates give molecular gas fractions of $f_g \sim 0.14 - 0.44$. Our estimated ranges are 0.07 – 0.31 using Tacconi et al. (2018) and 0.03 – 0.77 using Wisnioski et al. (2015). For overlapping galaxies we find the relative difference between the scaling relations and those that have been measured to be $f_{g,\mathrm{tacconi}}/f_{g,\mathrm{fisher}} = 1.19^{+0.01}_{-0.14}$ and $f_{g,\mathrm{wisnioski}}/f_{g,\mathrm{fisher}} = 0.37^{+0.05}_{-0.14}$. Neither scaling relation results in appropriately consistent molecular gas relations with those measured, but the relation proposed by Tacconi et al. (2018) is closest.

A relative increase in a/Q_g is apparent from the KROSS sample at $z \sim 1$ to the SAMI galaxies at $z \sim 0.1$. This is shown both in the offsets in the mean v/σ_v compared to the a/Q_g = constant lines, as well as by a simple best fit line of the form $\log_{10}(\mathrm{v}\ /\ \sigma_v) = b - m\log_{10}(f_g)$ to all of our galaxies. The change in a/Q across the sample is suggestive of an increase in disc stability from $z \sim 1$ to $z \sim 0.1$. Assuming a = constant, we can infer the change in Q_g for our three samples. We show this in Figure 9. From redshift $z \sim 1$ to $z \sim 0.1$, the Q_g increases by a factor of ∼1.75 assuming the Tacconi et al. (2018) relation for the molecular gas fractions. The DYNAMO galaxies also show a higher stability criterion consistent with galaxies in the SAMI Galaxy Survey when using the Tacconi et al. (2018) relation. This suggests that galaxies increase their stability from $z \sim 1$ to $z \sim 0.1$.

An increase in Q_g is consistent with previous observations. Q_g is often found to be ∼1 for $z \gtrsim 1$ but $Q_g \sim 2$ is often found in local discs (van der Kruit & Freeman 1986; Wisnioski et al. 2015; Johnson et al. 2018; Übler et al. 2019). This may be due to local galaxies having a greater contribution from the stellar disc to their mass. It was also argued by Obreschkow et al. (2015) that the increase in specific angular momentum over time acts to stabilise discs and thus Q_{crit} is expected to be higher at lower redshift. As such, it has been suggested that we should observe slightly high Q_g in local galaxies.

6 DRIVERS OF TURBULENCE FROM $Z \sim 1$ TO $Z \sim 0.1$

The previous analysis suggests that galaxies are marginally stable with a slight increase in stability from $z \sim 1$ to $z \sim 0.1$. That analysis does not discriminate on the energetic contribution of various drivers to the gas turbulence. In this section, we endeavour to compare the gas kinematics in our galaxies to driver dependendent models of the gas kinematics.

There have been several proposed drivers of gas turbulence within the disc. These can generally be split into star-formation feedback mechanisms, gravitational mechanisms such as collapse of gas or interaction between galaxy com-

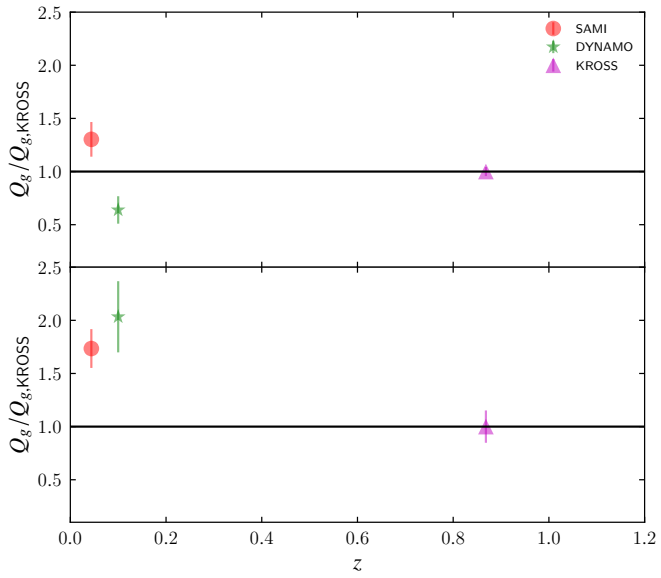

Figure 9. The redshift trend of the Toomre Q_g parameter as a function of redshift. In the top panel we show the estimates using the presciption by Wisnioski et al. (2015) and in the bottom panel we show the estimates using the prescription by Tacconi et al. (2018). We find that there is an increase in Q_g from KROSS at $z \sim 1$ to SAMI at $z \sim 0.1$.

ponents, or dynamical drivers such as shear and differential rotation across the disc. As we are studying the global gas kinematics, we aim to compare our inferences to models that have been proposed for global galaxy properties. These mainly consist of models that intend to differentiate between star-formation feedback processes driven primarily by supernovae and gravitational mechanisms due to the collapse of the gas through the disc.

6.1 Comparisons with theoretical models

Krumholz et al. (2018) provided a theoretical framework to understand gas kinematics of a marginally stable disc in vertical hydrostatic and energetic equilibrium with prescribed turbulence drivers. The drivers include energetic contributions to the turbulence from transport of gas through the disc as well as from supernovae. The model predicts turbulence at levels of $\sim$10 – 30 km s^{-1} can be sustained by supernovae alone. Turbulence at $\gtrsim$ 30 km s^{-1} can only be achieved via gravitational transport of gas through the disc leading to shocks.

We show comparisons between our inferences for the global intrinsic velocity dispersion and the models constructed by Krumholz et al. (2018) in Figure 10. We compare the intrinsic velocity dispersion to the turbulence driven models with star-formation feedback (denoted 'Feedback') and gas transport (denoted 'Transport'). Two different prescriptions are made for the star-formation feedback in the 'No Transport, Fixed $\epsilon_{\rm ff}$' and 'No Transport, Fixed Q' models. In the 'No Transport, Fixed $\epsilon_{\rm ff}$' model the star-formation rate per freefall time ($\epsilon_{\rm ff}$) is fixed, amounting to the assumption that the star-formation law is constant across galaxy properties as has been suggested by numerous studies (see Krumholz et al. (2019) for a summary). The 'No Transport, Fixed Q' model assumes that the gas self-regulates on the sub-galactic scale to maintain $Q \sim 1$ but that $\epsilon_{\rm ff}$ can vary with galaxy properties. These two models make strikingly different predictions with the 'No Transport, Fixed $\epsilon_{\rm ff}$' predicting very little correlation between star-formation rate and galaxy properties, whereas the 'No Transport, Fixed Q' model predicts SFR $\propto \sigma_v^2$. The 'No Feedback' model assumes that turbulence is only driven by the transport of gas through the disc. Whereas the 'Transport + Feedback' model assumes that turbulence is driven by both star-formation feedback with fixed $\epsilon_{\rm ff}$ and transport of gas through the disc. These models require prescriptions for various properties of the galaxies. Figure 10 we use the parameters suggested by Krumholz et al. (2018) to construct the tracks for 'Local Spiral', 'Local Dwarf', and 'High-z' galaxies.

All model tracks at SFR $\lesssim 1$ M$_\odot$ yr^{-1} predict similar velocity dispersion ranges at $\sigma_v \sim 15 - 25$ km s^{-1}. The data primarily from SAMI also yields velocity dispersions at this level. As such, there is less information that can be used to differentiate between the models at SFR $\lesssim 1$ M$_\odot$ yr^{-1}.

The difficulty in differentiating models at this level is driven by the lower limit in velocity dispersion in Hα at $\sigma_v \sim 15$ km s^{-1}. This lower limit has been found across various studies (e.g., Epinat et al. 2008; Varidel et al. 2020). It has also been shown that galaxies with similar SFR have an offset of ~ 15 km s^{-1} between Hα and HI observations (Krumholz et al. 2018; Varidel et al. 2020). A contribution of ~ 9 km s^{-1} is expected from the temperature of the ionised gas alone (Glazebrook 2013). A further contribution from the expansion of HII regions is also expected but the typical contribution is not well known. Studying individual HII regions yields a range of contributions with many $\sigma_{\rm expand} \lesssim 10$ km s^{-1} up to $\sigma_{\rm expand} \sim 13 - 17$ km s^{-1} for larger regions (Chu & Kennicutt 1994). As such, the lower limit of ~ 15 km s^{-1} in HII is expected with some variance on a per galaxy basis dependent on the contribution of the expansion term.

At SFR $\gtrsim 1$ M$_\odot$ yr^{-1} the models diverge such that the data can differentiate between the models. According to the models proposed by Krumholz et al. (2018) the gas transport through the disc can provide enough energy to drive turbulence up to $\sigma_v \sim 100$ km s^{-1}. The contribution from supernovae alone cannot explain velocity dispersions of $\sigma \gtrsim 30$ km s^{-1} at SFR ~ 10 M$_\odot$ yr^{-1} with either the 'No Transport, Fixed $\epsilon_{\rm ff}$' or 'No Transport, Fixed Q' model.

Many galaxies in KROSS are supersonic with σ_v up to 100 km s^{-1} in the region 1 M$_\odot$ yr^{-1} $\lesssim$ SFR $\lesssim 100$ M$_\odot$ yr^{-1}. This is qualitatively consistent with the 'Transport + Feedback' models that predict an upturn in velocity dispersion in this region. However, the fiducial assumptions of high-z galaxies do predict velocity dispersions to increase at SFR $\gtrsim 10$ M$_\odot$ yr^{-1}. We suspect that this is primarily driven by subtleties in the assumptions in the fiducial parameters.

These models have dependencies on several galaxy properties that we now endeavour to explore. A comparison between the 'Transport + Feedback' model and the observed kinematics is shown in Figure 11. In this case, we note that the model predicts,

$$\mathrm{SFR} = \sqrt{\frac{2}{1+\beta}} \frac{\phi_a f_{\rm sf} f_g}{\pi G} \frac{1}{Q} \frac{t_{\rm orb}}{t_{\rm sf,\ max}} f_g v_{2.2}^2 \sigma_v. \quad (14)$$

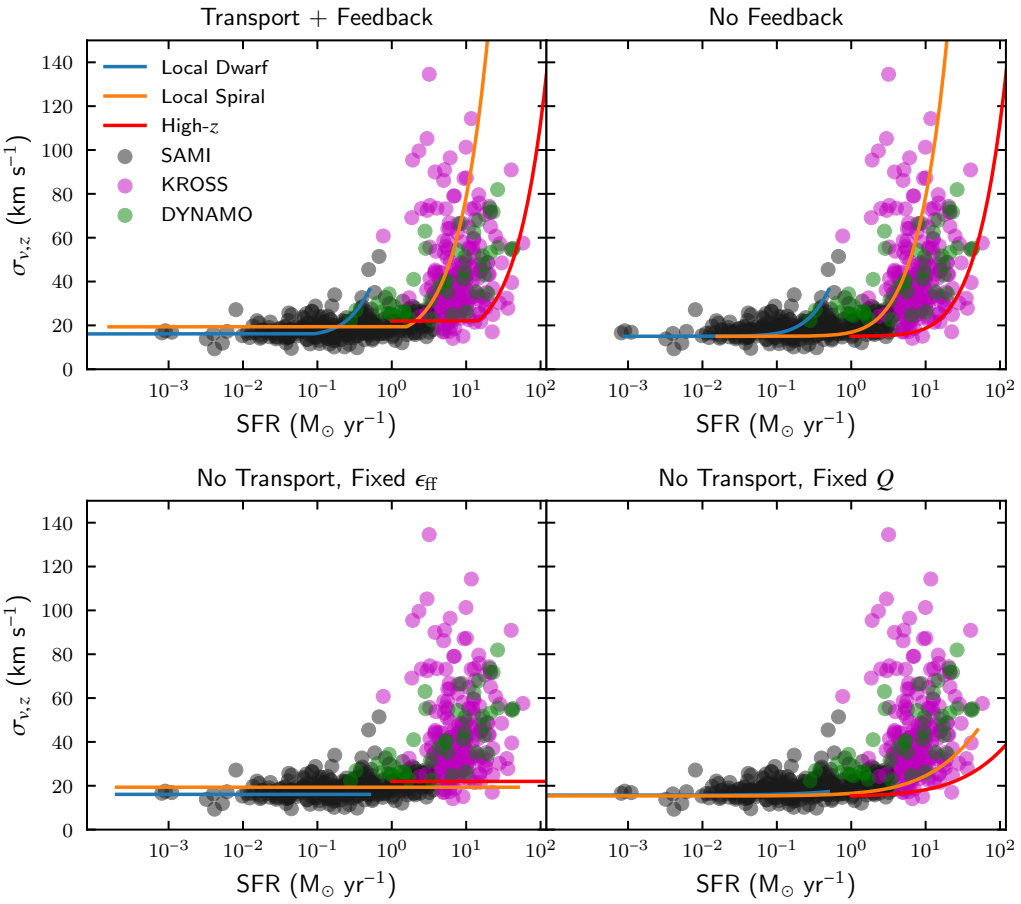

Figure 10. The SFR – σ_v relation compared to predictions made by the models proposed Krumholz et al. (2018). 'Transport' denotes turbulence driving by gravitational transport of the gas through the disc. Whereas 'Feedback' represents star-formation feedback due to supernovae explosions. We add 15 km s^{-1} in quadrature to the proposed models in order to account for the thermal and expansion contributions to the gas. The 'Local Dwarf', 'Local Spiral', and 'High-z tracks use typical galaxy properties suggested by Krumholz et al. (2018) to constrain the models.

We choose the following values as constant across our galaxies; the maximum star-formation timescale of $t_{\rm sf,\,max} = 2$ Gyr, and rotational parameter $\beta = 0$. These values are the fiducial values proposed for both high-z and low-z spiral galaxies by Krumholz et al. (2018). For simplification, we take intermediate values between the high-z and low-z spiral values for the following parameters; orbital period is $t_{\rm orb} =$ 210 Myr and the fraction of molecular gas forming stars is $f_{\rm sf} = 0.8$. Using those simplifications gives,

$$\mathrm{SFR} = 0.14 \frac{\phi_a}{\pi G} \frac{1}{Q} f_g v^2 \sigma_v. \quad (15)$$

The remaining parameter ϕ_a is an offset that takes into account the integration from spatially resolved to global star-formation laws. Krumholz et al. (2018) suggested $\phi_a = 2$ on an average but expected $\phi_a = 1$ for local galaxies and $\phi_a = 3$ for high-z galaxies.

Equation 15 predicts SFR $\propto f_g v^2 \sigma_v$ assuming ϕ_a and Q are constants. We plot this relation in Figure 11. In this case, we are required to subtract the non-turbulent contribution from the intrinsic velocity dispersion. As performed previously we subtract 15 km s^{-1} in quadrature due to to the thermal and expansion contributions to the Hα gas velocity dispersion. Unfortunately, this removes 39 galaxies from the SAMI Galaxy Survey with $\sigma_v < 15$ km s^{-1}. All of the removed galaxies have SFR < 3 M$_\odot$ yr^{-1} and $\log_{10}$(M$_*$/M$_\odot$) $<$ 10.4. We show in Appendix A that subtracting only the thermal contribution to the Hα velocity dispersion, which allows for all galaxies to be shown on the plot, does not qualitatively change our results.

For the purposes of Figure 11 we use the Tacconi et al. (2018) relation for the molecular gas fraction. We note that there are several caveats between the estimated gas fractions using the scaling relations and the models proposed by Krumholz et al. (2018). First, the gas fraction should be the total gas fraction, whereas we only take into account the molecular gas fraction. Also, the gas mass that contributes to the driving of turbulence is expected to be that in the mid-plane, whereas the scaling relations estimate the total molecular gas fraction.

Galaxies broadly follow the prescribed proportionality relation across the full range of SFR ($\log_{10}$(SFR / M$_\odot$ yr^{-1}) $\in$ [-3, 2]) for realistic values of Q and ϕ_a. Although several factors drive significant scatter. To exlore the factors that drive this scatter, we also colour code the plot using various galaxy

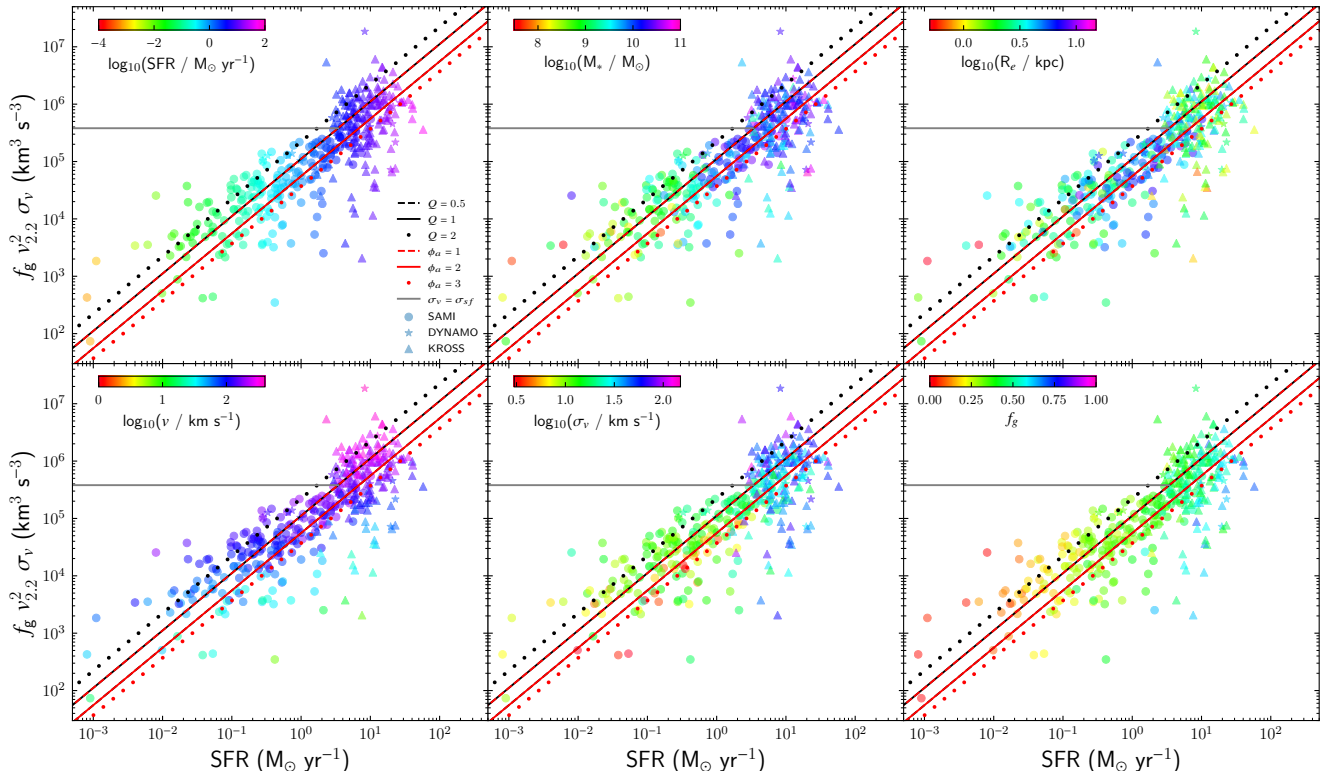

Figure 11. Comparison between the expected 'Transport + Feedback' relation between SFR and $f_g v_{2.2}^2 \sigma_v$. The expected relation is shown with varying Toomre stability $Q = 0.5$ (dashed black), 1 (solid black), 2 (dotted black) and star-formation integration correction $\phi_a = 1$ (dashed red), 2 (solid red), 3 (dotted red). The grey line is a representation of galaxy turbulence driven solely by star-formation feedback mechanisms with the assumption $\sigma_{\rm sf} = 18$ km s^{-1}, $f_g = 0.5$, and $v_{2.2} = 200$ km s^{-1}. It is expected that some galaxies will lie between the SFR $\propto f_g v_{2.2}^2 \sigma_v$ relations and the grey line assuming the 'Transport + Feedback' model. We subtract 15 km s^{-1} from σ_v represented of the thermal and HII region expansion terms. We find a good agreement between the expected relation and the data with $Q \sim 1$ and $\phi_a \sim 1$ across the three samples.

properties. We see very little unexpected residual correlation with most galaxy properties. Although the relationship on the y–axis is dominated by the rotational velocity.

The importance of the rotational velocity on the y–axis is due to $v_{2.2}^2$ dominating the dynamic range. The dynamic range for velocity is $v_{2.2} \in [10, 300]$ km s^{-1} corresponding to $v_{2.2}^2 \in [10^2, 10^5]$ km^2 s^{-2}. Whereas $\sigma_v \in [10, 100]$ km s^{-1} and $f_g \in [0.1, 0.8]$. As such, small differences or incorrect estimates for $v_{2.2}$ can cause galaxies to lie off the plane. The relation SFR $\propto v_{2.2}^2$ is also expected due to the correlation of those quantities with mass. As such, the relation is dominated by the correlation in galaxy properties given their mass.

One subtlety of the 'Transport + Feedback' model is that the velocity dispersion due to star-formation feedback is approximately constant for a wide range of galaxy parameters. Using the prescription provided by Krumholz et al. (2018) with the fiducial model values above, we get the star-formation feedback contribution to the velocity dispersion to be $\sigma_{\rm sf} = 18$ km s^{-1}. As a representation of this effect, we plot a grey line with $\sigma_{\rm sf} = 18$ km s^{-1}, $f_g = 0.5$, and $v_{2.2} = 200$ km s^{-1}. For galaxies with $\sigma_v = \sigma_{\rm sf}$ the Toomre stability can take values of $Q \geq 1$. This predicts lower values of SFR for a given f_g, v, and σ_v. As such, we expect some galaxies to lie in the region between the SFR $\propto f_f v_{2.2}^2 \sigma_v$ and the grey line. We do see a slight bias at SFR $\lesssim 1$ M$_\odot$ yr^{-1} that scatter into this region as expected.

We also explore the potential change in ϕ_a in the 'Transport + Feedback' model. We plot $\phi_a = 1$, 2, 3 for $Q = 1$. We see that for galaxies at SFR $\gtrsim 1$ M$_\odot$ yr^{-1}, the bulk of the galaxies sit close to the $\phi_a = 1$ model. Isolating ϕ_a without taking into account the other variables in the model is difficult. Despite this difficulty, we see little evidence for an integration constant deviating from $\phi_a = 1$ for in our sample.

Compare this to the 'No Transport, Fixed Q' model where the turbulence is assumed to be driven by star-formation feedback processes as shown in Figure 12. We see that at $\sigma_v \gtrsim 30$ km s^{-1} the data systematically lie above the expected SFR $\propto f_g v_{2.2}^2 \sigma_v^2$ relation. As such, we see that the 'Transport + Feedback' model provides a better fit to the data than the 'No Transport, Fixed Q'.

7 CONCLUSIONS

We studied the intrinsic gas kinematics for galaxies at $z \sim 1$ from KROSS. 315 galaxies from KROSS were modelled using a 3D forward modelling process referred to as BLOBBY3D. We found 38% of galaxies had no clear mode greater than the thermal contribution of the gas of 9 km s^{-1}. This issue is likely related to the variation in spectral resolution of up

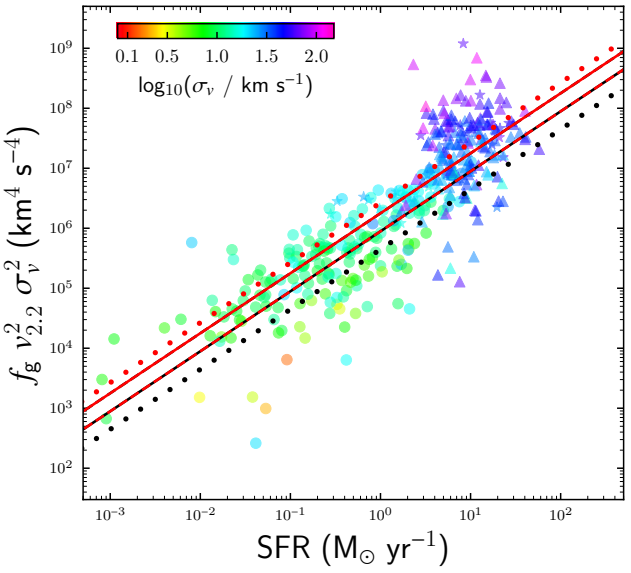

Figure 12. Comparison between the expected 'No Transport, Fixed Q' relation between SFR and $f_g v_{2.2}^2 \sigma_v^2$. The expected relation is shown with varying Toomre stability $Q = 0.1$, 1, 2 (black) and star-formation integration correction $\phi_a = 1$, 2, 3 (red). The 'No Transport, Fixed Q' provides a reasonable fit until $\sigma_v \gtrsim 30$ km s^{-1} at SFR ~ 10 M$_\odot$ yr^{-1}.

to $\Delta R = 1000$ across different IFUs on KMOS as it was also found by Übler et al. (2019) using data from KMOS^{3D}. These galaxies were removed from the sample leaving 193 galaxies to be further analysed.

The galaxies exhibit high velocity dispersions that are evidence for turbulent gas within the disc of most galaxies. This is consistent with previous estimates of the gas in KROSS (Johnson et al. 2018) as well as similar studies at $z \sim 1$ (Kassin et al. 2013; Wisnioski et al. 2015; Übler et al. 2019). We also note that the gas kinematics are consistent with those estimated in the DYNAMO survey using Blobby3D, which are a set of galaxies with similar galaxy properties, including stellar mass and SFR, but at $z \sim 0.1$.

We find that the samples in KROSS, DYNAMO, and SAMI exhibit gas kinematics consistent with galaxies that are marginally stable discs. These models suggest that the velocity dispersion decreases from high redshift till today in unison with the decreasing SFR and molecular gas fractions. Consistent with predictions we find that SAMI galaxies have Q_g that is ∼75% greater than that found in KROSS at $z \sim 1$.

We then compared the intrinsic velocity dispersion estimates to theoretical models that include turbulence driven by gas transport through the disc and from supernovae. Our estimates are consistent with the 'Transport + Feedback' model proposed by Krumholz et al. (2018) which suggests that the $\sigma_v \sim 15 - 30$ km s^{-1} at SFR $\lesssim 1$ M$_\odot$ yr^{-1} driven by supernovae explosions with galaxies at SFR $\gtrsim 1$ M$_\odot$ yr^{-1} increasing up to $\sigma_v \gtrsim 30$ km s^{-1} driven by gas transport through the disc.

ACKNOWLEDGEMENTS

This work is based on observations obtained at the Very Large Telescope of the European Southern Observatory. Programme IDs: 60.A-9460; 092.B-0538; 093.B-0106; 094.B-0061; 095.B-0035.

The SAMI Galaxy Survey is based on observations made at the Anglo-Australian Telescope. The Sydney-AAO Multi-object Integral field spectrograph (SAMI) was developed jointly by the University of Sydney and the Australian Astronomical Observatory. The SAMI input catalogue is based on data taken from the Sloan Digital Sky Survey, the GAMA Survey and the VST ATLAS Survey. The SAMI Galaxy Survey is supported by the Australian Research Council Centre of Excellence for All Sky Astrophysics in 3 Dimensions (ASTRO 3D), through project number CE170100013, the Australian Research Council Centre of Excellence for All-sky Astrophysics (CAASTRO), through project number CE110001020, and other participating institutions. The SAMI Galaxy Survey website is http://sami-survey.org/.

The authors acknowledge the University of Sydney HPC service at The University of Sydney for providing HPC and database resources that have contributed to the research results reported within this paper. URL: http://sydney.edu.au/research_support/

REFERENCES

Aumer M., Burkert A., Johansson P. H., Genzel R., 2010, ApJ, 719, 1230
Begeman K. G., 1987, PhD thesis, -
Bloom J. V., et al., 2017, MNRAS, 472, 1809
Brewer B. J., Foreman-Mackey D., 2016, arXiv e-prints, p. arXiv:1606.03757
Brewer B. J., Pártay L. B., Csányi G., 2009, arXiv e-prints, p. arXiv:0912.2380
Bruzual G., Charlot S., 2003, MNRAS, 344, 1000
Bryant J. J., et al., 2015, MNRAS, 447, 2857
Chabrier G., 2003, PASP, 115, 763
Chu Y.-H., Kennicutt Robert C. J., 1994, ApJ, 425, 720
Cid Fernandes R., Stasińska G., Mateus A., Vale Asari N., 2011, MNRAS, 413, 1687
Courteau S., 1997, AJ, 114, 2402
Cresci G., et al., 2009, ApJ, 697, 115
Croom S. M., et al., 2012, MNRAS, 421, 872
da Cunha E., Charlot S., Elbaz D., 2008, MNRAS, 388, 1595
Davé R., Finlator K., Oppenheimer B. D., 2012, MNRAS, 421, 98
Davies R., et al., 2011, ApJ, 741, 69
Davies L. J. M., et al., 2016, MNRAS, 461, 458
Di Teodoro E. M., Fraternali F., 2015, MNRAS, 451, 3021
Dobbs C. L., Bonnell I. A., 2008, MNRAS, 385, 1893
Driver S. P., et al., 2018, MNRAS, 475, 2891
Epinat B., Amram P., Marcelin M., 2008, MNRAS, 390, 466
Fisher D. B., Bolatto A. D., White H., Glazebrook K., Abraham R. G., Obreschkow D., 2019, ApJ, 870, 46
Genzel R., et al., 2011, ApJ, 733, 101
Glazebrook K., 2013, Publ. Astron. Soc. Australia, 30, e056
Green A. W., et al., 2014, MNRAS, 437, 1070
Gunawardhana M. L. P., et al., 2013, MNRAS, 433, 2764
Harrison C. M., et al., 2017, MNRAS, 467, 1965
Hinshaw G., et al., 2009, ApJS, 180, 225
Hopkins A. M., Beacom J. F., 2006, ApJ, 651, 142
Ianjamasimanana R., de Blok W. J. G., Walter F., Heald G. H., 2012, AJ, 144, 96
Johnson H. L., et al., 2018, MNRAS, 474, 5076

Kassin S. A., Weiner B. J., Faber S. M., Gardner J. P., DEEP2 Team 2013, in American Astronomical Society Meeting Abstracts #221. p. 304.06
Kauffmann G., et al., 2003, MNRAS, 346, 1055
Kennicutt Robert C. J., 1998, ApJ, 498, 541
Kewley L. J., Dopita M. A., Leitherer C., Davé R., Yuan T., Allen M., Groves B., Sutherland R., 2013, ApJ, 774, 100
Kim W.-T., Ostriker E. C., 2007, ApJ, 660, 1232
Kim W.-T., Ostriker E. C., Stone J. M., 2002, ApJ, 581, 1080
Kim W.-T., Ostriker E. C., Stone J. M., 2003, ApJ, 599, 1157
Krumholz M., Burkert A., 2010, ApJ, 724, 895
Krumholz M. R., Burkhart B., 2016, MNRAS, 458, 1671
Krumholz M. R., Burkhart B., Forbes J. C., Crocker R. M., 2018, MNRAS, 477, 2716
Krumholz M. R., McKee C. F., Bland -Hawthorn J., 2019, ARA&A, 57, 227
Lawrence A., et al., 2007, MNRAS, 379, 1599
Lehnert M. D., Nesvadba N. P. H., Le Tiran L., Di Matteo P., van Driel W., Douglas L. S., Chemin L., Bournaud F., 2009, ApJ, 699, 1660
Lehnert M. D., Le Tiran L., Nesvadba N. P. H., van Driel W., Boulanger F., Di Matteo P., 2013, A&A, 555, A72
Leroy A. K., Walter F., Brinks E., Bigiel F., de Blok W. J. G., Madore B., Thornley M. D., 2008, AJ, 136, 2782
Mac Low M.-M., Klessen R. S., 2004, Reviews of Modern Physics, 76, 125
Moiseev A. V., Tikhonov A. V., Klypin A., 2015, MNRAS, 449, 3568
Noeske K. G., et al., 2007a, ApJ, 660, L43
Noeske K. G., et al., 2007b, ApJ, 660, L47
Norman C. A., Ferrara A., 1996, ApJ, 467, 280
Obreschkow D., et al., 2015, ApJ, 815, 97
Piontek R. A., Ostriker E. C., 2004, ApJ, 601, 905
Rizzo F., Vegetti S., Powell D., Fraternali F., McKean J. P., Stacey H. R., White S. D. M., 2020, Nature, 584, 201
Roberts M. S., 1968, ApJ, 151, 117
Scott N., et al., 2018, MNRAS, 481, 2299
Sharples R. M., et al., 2004, in Moorwood A. F. M., Iye M., eds, Society of Photo-Optical Instrumentation Engineers (SPIE) Conference Series Vol. 5492, Ground-based Instrumentation for Astronomy. pp 1179–1186, doi:10.1117/12.550495
Sharples R., et al., 2013, The Messenger, 151, 21
Sivia D. S., Skilling J., 2012, Data analysis: a Bayesian tutorial, 2 edn. Oxford University Press
Speagle J. S., Steinhardt C. L., Capak P. L., Silverman J. D., 2014, ApJS, 214, 15
Stilp A. M., Dalcanton J. J., Skillman E., Warren S. R., Ott J., Koribalski B., 2013, ApJ, 773, 88
Stott J. P., et al., 2016, MNRAS, 457, 1888
Tacconi L. J., et al., 2013, ApJ, 768, 74
Tacconi L. J., et al., 2018, ApJ, 853, 179
Tasker E. J., Tan J. C., 2009, ApJ, 700, 358
Toomre A., 1964, ApJ, 139, 1217
Übler H., et al., 2018, ApJ, 854, L24
Übler H., et al., 2019, ApJ, 880, 48
van der Kruit P. C., Freeman K. C., 1986, ApJ, 303, 556
Varidel M. R., et al., 2019, MNRAS, 485, 4024
Varidel M. R., et al., 2020, MNRAS, 495, 2265
Walter F., Brinks E., de Blok W. J. G., Bigiel F., Kennicutt Robert C. J., Thornley M. D., Leroy A., 2008, AJ, 136, 2563
Whitaker K. E., et al., 2014, ApJ, 795, 104
Wisnioski E., et al., 2011, MNRAS, 417, 2601
Wisnioski E., et al., 2015, ApJ, 799, 209
Wisnioski E., et al., 2019, ApJ, 886, 124
Wuyts S., et al., 2011, ApJ, 738, 106
Yu X., et al., 2019, MNRAS, 486, 4463
Zhou L., et al., 2017, MNRAS, 470, 4573

APPENDIX A: FURTHER NOTES ON THE COMPARISON OF OUR DATA TO THE TRANSPORT + FEEDBACK MODEL

In Figure 11 we showed the comparison of the Transport + Feedback model proposed by Krumholz et al. (2018) compared to our data. In that case, we subtracted 15 km s^{-1} in quadrature from σ_v prior as a correction for the thermal and expansion contributions to the velocity dispersion. For completeness we show this same plot in Figure A1 subtracting only the 9 km s^{-1} expected due the thermal contribution to the Hα velocity dispersion.

Only correcting for the thermal component results in 39 extra galaxies at SFR < 3 M$_\odot$ yr^{-1}. We also see that galaxies at SFR $\lesssim 1$ M$_\odot$ yr^{-1} typically lie slightly above the Transport + Feedback relation assuming $\phi_a = 1$ and $Q = 1$. Although we note that in the case where star-formation feedback is the primary driver of the turbulence the Transport + Feedback model assumes $Q \geq 1$, as such galaxies can lie in this range while remaining consistent with the Transport + Feedback model.

This paper has been typeset from a TEX/LATEX file prepared by the author.

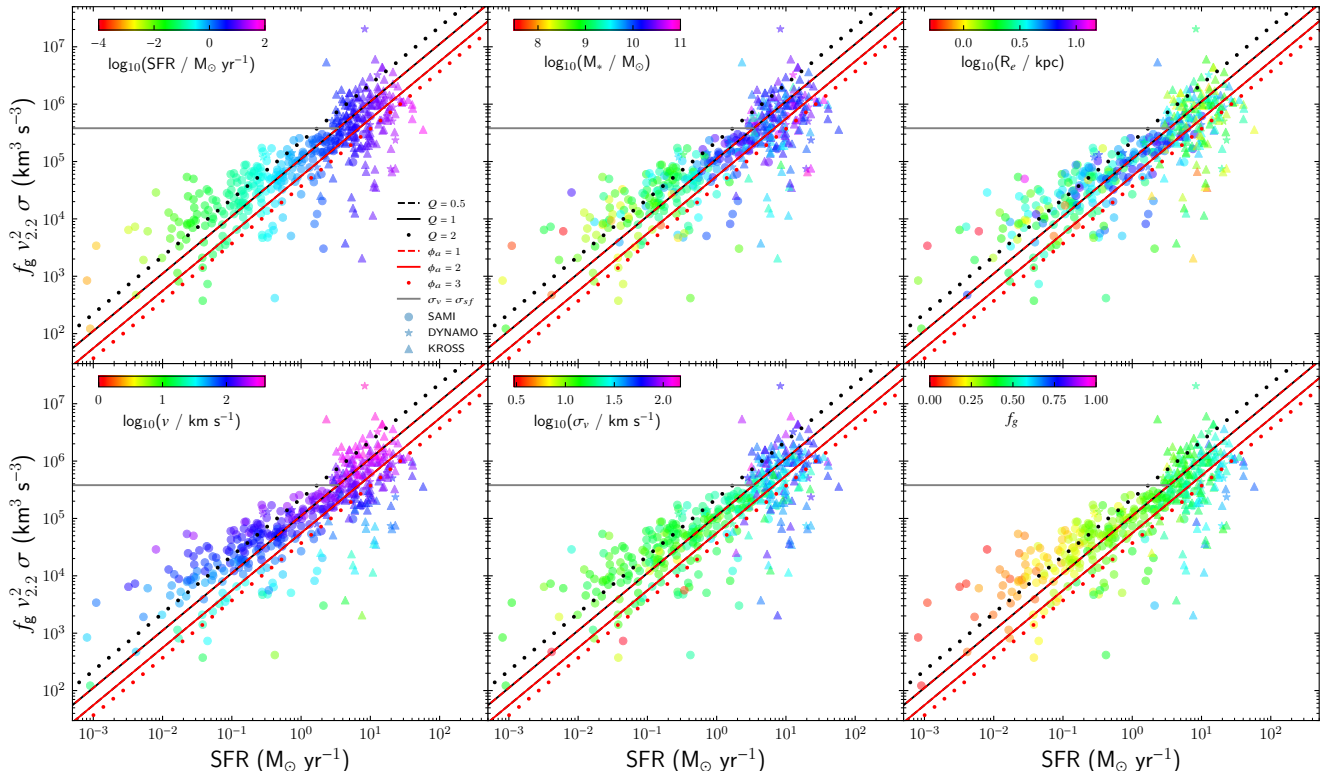

Figure A1. Same as Figure 11 but with only the thermal contribution to the Hα velocity dispersion subtracted. This change results in a qualitatively similar relation to seen previously although galaxies lie above the $\phi_a = Q = 1$ lines.

5 Conclusions

For this thesis I was concerned with determining the gas kinematic and their drivers in a wide range of galaxies. In Chapter 2 the problem of beam smearing was addressed. This chapter describes a unique 3D modelling approach for studying the gas kinematics of galaxies where Hα clumps can be observed. The motivation for this work was that Hα flux clumps are often visible in many observations of galaxies from the SAMI Galaxy Survey, plus we suspected that clumpier high-z galaxies would likely be affected.

The modelling approach, referred to as BLOBBY3D, is based on a thin disc model of the galaxy where the Hα flux profile is modelled using a number of 2D non-concentric Gaussians. The kinematic profiles are assumed to be azimuthally symmetric radial profiles. The model is then convolved by the PSF and LSF prior to being compared to the data. We tested BLOBBY3D on toy galaxies and observations from the SAMI Galaxy Survey. We found that the BLOBBY3D approach was able to recover toy modelled galaxy kinematics more accurately than several methods including an alternative 3D modelling algorithm known as ^{3D}BAROLO, as well as several heuristic approaches. We also showed that clumps in the Hα flux profile can lead to spurious observed substructures in the gas kinematics, which suggests that researchers could be misled when relating local Hα flux to gas kinematic properties from observed maps.

The remainder of this thesis describes the study of observed gas kinematics in several galaxy samples. These include galaxies with a wide range properties at $z \sim 0.1$, in particular $\log_{10}(M_*/M_\odot) \in$ [7.5, 11] and $\log_{10}(SFR/M_\odot\ yr^{-1}) \in$ [-3, 1] in Chapter 3. As well as studying galaxies across epochs from $z \sim 0.1$ to $z \sim 1$ in Chapter 4.

Chapter 3 describes the application of BLOBBY3D to galaxies from the SAMI Galaxy Survey and DYNAMO survey. To my knowledge this is the first case of applying a single 3D modelling technique to galaxies with such a wide range of SFR and stellar mass at a single epoch. In this work we found that the velocity dispersion remains in the range $\sigma_v \sim 15 - 25$ km s^{-1} with only a slight increase as a function of SFR across $\log_{10}(SFR/M_\odot\ yr^{-1}) \in$ [-3, 0]. The velocity dispersion increases significantly in the range $\sigma_v \in$ [30, 80] km s^{-1} at $\log_{10}(SFR/M_\odot\ yr^{-1}) \in$ [0, 2]. Comparing this to current theoretical models for the drivers of gas turbulence suggests that our results are consistent with star-formation driving turbulence at SFR $\lesssim 1\ M_\odot\ yr^{-1}$ and transport of gas through the disc driving turbulence at SFR $\gtrsim 1\ M_\odot\ yr^{-1}$.

The application of BLOBBY3D to galaxies at $z \sim 1$ to galaxies from KROSS was described in Chapter 4. We found that the velocity dispersion of galaxies at $z \sim 1$ was higher than typical galaxies at $z \sim 0.1$ as representative of galaxies from the SAMI Galaxy Survey. However, the velocity dispersions were consistent with galaxies from the DYNAMO survey that had similar stellar mass and SFR properties as those from KROSS. We were able to show that the galaxy kinematics across the three samples were consistent with the galaxies being marginally stable from gravitational collapse. Furthermore, it was shown that the turbulence is consistent with theoretical models for turbulence using a combination of star-formation feedback and gas transport is valid up to $z \sim 1$.

5.1 Future work

There are several avenues of further work that could be performed. First is further applications of the current BLOBBY3D approach. Code for BLOBBY3D has been made available at `github.com/SpaceOdyssey/Blobby3D` for this purpose. Further effort will be made to help others use and extend the code. The goal will be to apply it some of the above mentioned research.

To my knowledge a study of galaxies from $z \sim 0.1$ to $z > 1$ using a single disc modelling technique has not been completed. Übler et al. (2019) applied a similar disc modelling technique to galaxies from $z \sim 1$ to $z \sim 3$ using data from the KMOS^{3D} survey. This thesis includes research where disc modelling was applied from $z \sim 0.1$ to $z \sim 1$. However, given that the corrections for beam smearing can result in slightly different offsets, it would be preferable for a consistent approach to be applied to such a wide range of galaxies. Also, several observational studies are currently collecting data that will observe galaxies at different epochs including the Middle Ages Galaxy Properties with Integral Field Spectroscopy (MAGPI, Foster et al., 2020) survey at $0.25 < z < 0.35$ as well as an increasing prevalence of observations of disc galaxies at $z > 3$ (e.g. Neeleman et al., 2020; Rizzo et al., 2020).

BLOBBY3D could also be used to study the localised Hα and velocity dispersion relation. The localised relation has been studied in observational studies previously. These studies have often been inconclusive with some studies finding correlations between Hα flux and velocity dispersions (Lehnert et al., 2009, 2013) while others have found weak to no correlation (Varidel et al., 2016; Zhou et al., 2017; Übler et al., 2019). Oliva-Altamirano et al. (2018) made a more subtle argument for the localised Hα clumps being closer to regions of high velocity dispersion. However, as the results in Chapter 2 suggest, spurious substructures can be introduced into the velocity dispersion maps due to the substructure in the Hα flux maps. One approach to address this is to use very high spatial resolution data where beam smearing may be minimised (Sun et al., 2018, 2020; Oliva-Altamirano et al., 2018). Although such studies are limited to nearby galaxies or specific instruments, so approaches will still be needed to study other galaxy samples. As such, modelling the substructure in both Hα flux and velocity dispersion would help with this.

A possible extension of BLOBBY3D would be to assign an individual velocity dispersion per 'blob'. This will allow for spatial changes in the velocity dispersion that can then be convolved prior to comparing to the data. This was attempted during the work in Chapter 2, but it was deemed too unreliable to be applied to a large survey. Although I suspect that it still may be possible to do this on smaller samples of high quality data.

A current limitation to the observational comparisons made throughout this thesis are the comparisons that can be made to theoretical models. To further distinguish between the drivers of turbulence it will be preferable to have theoretical models that make predictions for the effects such as clustered star-formation, individual clumps, and large scale dynamics. That will allow approaches such as BLOBBY3D to be used to distinguish them, potentially on localised spatial scales. As such, further input from theoretical models to constrain the possible range of velocity dispersion for particular galaxies is also required.

No matter the future applications of BLOBBY3D, I suggest that the development and application of such a flexible disc modelling approach has its own merits. Pushing the flexibility of disc modelling coupled with advanced sampling algorithms is now possible with modern computational resources. As such, I hope to see researchers using techniques that take into account the effects of the substructure of the galaxy in the future.

Bibliography

Agertz O., Teyssier R., Moore B., 2009, MNRAS, 397, L64

Aiton E. J., 1975, The Mathematical Gazette, 59, 250

Aizu K., Tabara H., 1967, Progress of Theoretical Physics, 37, 296

Angel J. R. P., Adams M. T., Boroson T. A., Moore R. L., 1977, ApJ, 218, 776

Aumer M., Burkert A., Johansson P. H., Genzel R., 2010, ApJ, 719, 1230

Bacon R., et al., 2001, MNRAS, 326, 23

Balbus S. A., 1986, ApJ, 303, L79

Balbus S. A., Hawley J. F., 1991, ApJ, 376, 214

Baldry I. K., Glazebrook K., Brinkmann J., Ivezić Ž., Lupton R. H., Nichol R. C., Szalay A. S., 2004, ApJ, 600, 681

Balmer J. J., 1885, Annalen der Physik, 261, 80

Barden S. C., Wade R. A., 1988, in Barden S. C., ed., Astronomical Society of the Pacific Conference Series Vol. 3, Fiber Optics in Astronomy. pp 113–124

Bekiaris G., Glazebrook K., Fluke C. J., Abraham R., 2016, MNRAS, 455, 754

Bland-Hawthorn J., et al., 2011, Optics Express, 19, 2649

Blumenthal G. R., Faber S. M., Primack J. R., Rees M. J., 1984, Nature, 311, 517

Bohr N., 1913, Philosophical Magazine, 26, 1

Bouché N., Carfantan H., Schroetter I., Michel-Dansac L., Contini T., 2015, AJ, 150, 92

Bournaud F., Elmegreen B. G., Elmegreen D. M., 2007, ApJ, 670, 237

Bournaud F., Elmegreen B. G., Martig M., 2009, ApJ, 707, L1

Bryant J. J., Bland-Hawthorn J., Fogarty L. M. R., Lawrence J. S., Croom S. M., 2014, MNRAS, 438, 869

Bryant J. J., et al., 2015, MNRAS, 447, 2857

Buitrago F., Trujillo I., Conselice C. J., Bouwens R. J., Dickinson M., Yan H., 2008, ApJ, 687, L61

Cappellari M., et al., 2011, MNRAS, 413, 813

Chon S., Hosokawa T., 2019, MNRAS, 488, 2658

Chu Y.-H., Kennicutt Robert C. J., 1994, ApJ, 425, 720

Colless M., et al., 2001, MNRAS, 328, 1039

Conselice C. J., 2014, ARA&A, 52, 291

Conselice C. J., Wilkinson A., Duncan K., Mortlock A., 2016, ApJ, 830, 83

Content R., 1997, in Ardeberg A. L., ed., Society of Photo-Optical Instrumentation Engineers (SPIE) Conference Series Vol. 2871, Optical Telescopes of Today and Tomorrow. pp 1295–1305, doi:10.1117/12.269020

Courtes G., 1982, An Integral Field Spectrograph (IFS) for Large Telescopes. Springer, Dordrecht, p. 123, doi:10.1007/978-94-009-7787-7_16

Croom S. M., et al., 2012, MNRAS, 421, 872

Daddi E., et al., 2005, ApJ, 626, 680

Dekel A., et al., 2009, Nature, 457, 451

Di Teodoro E. M., Fraternali F., 2015, MNRAS, 451, 3021

Dobbs C. L., Bonnell I. A., 2008, MNRAS, 385, 1893

Driver S. P., Windhorst R. A., Ostrander E. J., Keel W. C., Griffiths R. E., Ratnatunga K. U., 1995, ApJ, 449, L23

Eggen O. J., Lynden-Bell D., Sandage A. R., 1962, ApJ, 136, 748

Einstein A., 1905, Annalen der Physik, 322, 132

Eisenhauer F., Raab W., 2015, ARA&A, 53, 155

Federrath C., 2015, MNRAS, 450, 4035

Field G. B., 1965, ApJ, 142, 531

Förster Schreiber N. M., et al., 2006, ApJ, 645, 1062

Förster Schreiber N. M., et al., 2009, ApJ, 706, 1364

Foster C., et al., 2020, arXiv e-prints, p. arXiv:2011.13567

Fraunhofer J., 1817, Annalen der Physik, 56, 264

Galilei G., 1653, Sidereus nuncius: magna longeque admirabilia spectacula pandens, suspiciendaÌĄque proponens unicuique, prsÌĘertim veroÌĂ philosophis, atque astronomis. Early English books online, Typis Jacobi Flesher, Londini

Gentry E. S., Krumholz M. R., Dekel A., Madau P., 2017, MNRAS, 465, 2471

Genzel R., et al., 2006, Nature, 442, 786

Genzel R., et al., 2011, ApJ, 733, 101

Glazebrook K., 2013, PASA, 30, e056

Glazebrook K., Ellis R., Santiago B., Griffiths R., 1995, MNRAS, 275, L19

Goldbaum N. J., Krumholz M. R., Forbes J. C., 2015, ApJ, 814, 131

Goldbaum N. J., Krumholz M. R., Forbes J. C., 2016, ApJ, 827, 28

Green A. W., et al., 2010, Nature, 467, 684

Green A. W., et al., 2014, MNRAS, 437, 1070

Green A. W., et al., 2018, MNRAS, 475, 716

Greif T. H., Bromm V., Clark P. C., Glover S. C. O., Smith R. J., Klessen R. S., Yoshida N., Springel V., 2012, MNRAS, 424, 399

Hamacher D. W., Banks K., 2018, arXiv e-prints, p. arXiv:1806.02462

Hamacher D. W., Fuller R. S., Norris R. P., 2012, Australian Archaeology, 75, 46

Hampton E. J., et al., 2017, MNRAS, 470, 3395

Harrison C. M., et al., 2017, MNRAS, 467, 1965

Heath T. L., Aristarchus of Samos 1913, Aristarchus of Samos, the ancient Copernicus; a history of Greek astronomy to Aristarchus, together With Aristarchus's Treatise on the sizes and distances of the sun and moon. Oxford, Clarendon Press

Herschel J. F. W., 1864, Philosophical Transactions of the Royal Society of London Series I, 154, 1

Hill J. M., Angel J. R. P., Scott J. S., Lindley D., Hintzen P., 1980, ApJ, 242, L69

Höglund B., Roberts M. S., 1965, ApJ, 142, 1366

Hopkins A. M., Beacom J. F., 2006, ApJ, 651, 142

Hubbard E. N., Angel J. R. P., Gresham M. S., 1979, ApJ, 229, 1074

Hubble E., 1926, Contributions from the Mount Wilson Observatory / Carnegie Institution of Washington, 324, 1

Hubble E. P., 1927, The Observatory, 50, 276

Hubble E. P., 1929, ApJ, 69, 103

Immeli A., Samland M., Gerhard O., Westera P., 2004, A&A, 413, 547

Johnson H. L., et al., 2018, MNRAS, 474, 5076

Jones D. H., et al., 2004, MNRAS, 355, 747

Kak S., 2003, arXiv e-prints, p. physics/0301078

Kassin S. A., et al., 2012, ApJ, 758, 106

Kereš D., Katz N., Weinberg D. H., Davé R., 2005, MNRAS, 363, 2

Kereš D., Katz N., Fardal M., Davé R., Weinberg D. H., 2009, MNRAS, 395, 160

Kim C.-G., Ostriker E. C., 2015, ApJ, 802, 99

Kirchhoff G., Bunsen R., 1860a, The London, Edinburgh, and Dublin Philosophical Magazine and Journal of Science, 20, 88

Kirchhoff G., Bunsen R., 1860b, Annalen der Physik, 186, 161

Koyama H., Inutsuka S.-i., 2002, ApJ, 564, L97

Kritsuk A. G., Norman M. L., 2002, ApJ, 569, L127

Krumholz M., Burkert A., 2010, ApJ, 724, 895

Krumholz M. R., Burkhart B., Forbes J. C., Crocker R. M., 2018, MNRAS, 477, 2716

Law D. R., Steidel C. C., Erb D. K., Larkin J. E., Pettini M., Shapley A. E., Wright S. A., 2007, ApJ, 669, 929

Le Tiran L., Lehnert M. D., van Driel W., Nesvadba N. P. H., Di Matteo P., 2011, A&A, 534, L4

Lehnert M. D., Nesvadba N. P. H., Le Tiran L., Di Matteo P., van Driel W., Douglas L. S., Chemin L., Bournaud F., 2009, ApJ, 699, 1660

Lehnert M. D., Le Tiran L., Nesvadba N. P. H., van Driel W., Boulanger F., Di Matteo P., 2013, A&A, 555, A72

Mac Low M.-M., 1999, ApJ, 524, 169

Mac Low M.-M., Klessen R. S., 2004, Reviews of Modern Physics, 76, 125

Mac Low M.-M., Klessen R. S., Burkert A., Smith M. D., 1998, Phys. Rev. Lett., 80, 2754

Masters K. L., et al., 2019, MNRAS, 487, 1808

Milne D. K., 1970, Proceedings of the Astronomical Society of Australia, 1, 333

Mortlock A., et al., 2013, MNRAS, 433, 1185

Neeleman M., Prochaska J. X., Kanekar N., Rafelski M., 2020, Nature, 581, 269

Noguchi M., 1999, ApJ, 514, 77

Norman C. A., Ferrara A., 1996, ApJ, 467, 280

Oesch P. A., et al., 2010, ApJ, 709, L21

Oesch P. A., et al., 2016, ApJ, 819, 129

Oliva-Altamirano P., Fisher D. B., Glazebrook K., Wisnioski E., Bekiaris G., Bassett R., Obreschkow D., Abraham R., 2018, MNRAS, 474, 522

Pasquini L., et al., 2002, The Messenger, 110, 1

Pease F. G., 1915, PASP, 27, 239

Pease F. G., 1916, PASP, 28, 33

Piontek R. A., Ostriker E. C., 2004, ApJ, 601, 905

Piontek R. A., Ostriker E. C., 2007, ApJ, 663, 183

Planck Collaboration et al., 2018, arXiv e-prints, p. arXiv:1807.06209

Poveda A., Woltjer L., 1968, AJ, 73, 65

Ptolemy C., Taliaferro R. C., 1948, The Almagest. Encyclopaedia Britannica

Rees M. J., Ostriker J. P., 1977, MNRAS, 179, 541

Rizzo F., Vegetti S., Powell D., Fraternali F., McKean J. P., Stacey H. R., White S. D. M., 2020, Nature, 584, 201

Roberts M. S., 1968, ApJ, 151, 117

Rubin V. C., Ford W. Kent J., 1970, ApJ, 159, 379

Rubin H. H., Mezger P. G., 1970, A&A, 5, 407

Rydberg J., 1890, Philosophical Magazine, 5, 331

Sachs A., 1974, Philosophical Transactions of the Royal Society of London Series A, 276, 43

Sánchez S. F., et al., 2012, A&A, 538, A8

Scott N., et al., 2018, MNRAS, 481, 2299

Sharp R., et al., 2006, in Society of Photo-Optical Instrumentation Engineers (SPIE) Conference Series. p. 62690G (arXiv:astro-ph/0606137), doi:10.1117/12.671022

Sharp R., et al., 2015, MNRAS, 446, 1551

Sharples R. M., et al., 2004, in Moorwood A. F. M., Iye M., eds, Society of Photo-Optical Instrumentation Engineers (SPIE) Conference Series Vol. 5492, Ground-based Instrumentation for Astronomy. pp 1179–1186, doi:10.1117/12.550495

Sharples R., et al., 2013, The Messenger, 151, 21

Sicking F. J., 1997, PhD thesis

Slipher V. M., 1917, Proceedings of the American Philosophical Society, 56, 403

Stone J. M., Ostriker E. C., Gammie C. F., 1998, ApJ, 508, L99

Stott J. P., et al., 2016, MNRAS, 457, 1888

Strateva I., et al., 2001, AJ, 122, 1861

Sun J., et al., 2018, ApJ, 860, 172

Sun J., et al., 2020, ApJ, 901, L8

Tasker E. J., Tan J. C., 2009, ApJ, 700, 358

Teuben P. J., 2002, in Athanassoula E., Bosma A., Mujica R., eds, Astronomical Society of the Pacific Conference Series Vol. 275, Disks of Galaxies: Kinematics, Dynamics and Peturbations. pp 217–228 (arXiv:astro-ph/0204471)

Tiley A. L., et al., 2019, MNRAS, 482, 2166

Trujillo I., et al., 2006, MNRAS, 373, L36

Trujillo I., Conselice C. J., Bundy K., Cooper M. C., Eisenhardt P., Ellis R. S., 2007, MNRAS, 382, 109

Übler H., et al., 2019, ApJ, 880, 48

van den Bergh S., Abraham R. G., Ellis R. S., Tanvir N. R., Santiago B. X., Glazebrook K. G., 1996, AJ, 112, 359

Vanderriest C., 1980, PASP, 92, 858

van der Wel A., et al., 2014, ApJ, 788, 28

van de Sande J., et al., 2017, ApJ, 835, 104

van Dokkum P. G., et al., 2010, ApJ, 709, 1018

Varidel M., Pracy M., Croom S., Owers M. S., Sadler E., 2016, PASA, 33, e006

Walch S., Naab T., 2015, MNRAS, 451, 2757

Weinzirl T., et al., 2011, ApJ, 743, 87

Wisnioski E., et al., 2011, MNRAS, 417, 2601

Wisnioski E., et al., 2015, ApJ, 799, 209

Wollaston W. H., 1802, Philosophical Transactions of the Royal Society of London, 92, 365âĂŞ380

Woltjer L., 1970, in Habing H. J., ed., IAU Symposium Vol. 39, Interstellar Gas Dynamics. p. 229

Woltjer L., 1972, ARA&A, 10, 129

York D. G., et al., 2000, AJ, 120, 1579

Zasov A. V., Saburova A. S., Khoperskov A. V., Khoperskov S. A., 2017, Physics Uspekhi, 60, 3

Zhou L., et al., 2017, MNRAS, 470, 4573